IS**FGM**s 2016

14th International Symposium

Functionally Graded Materials
Multiscale & Multifunctional Structures

PROCEEDINGS

Editor
Prof. Dr. Monika Willert-Porada

September 18-22, 2016, Bayreuth, Germany

Contents

History of MM&FGM Conference

This 14th International Symposium of the Functionally Graded Materials held at Bayreuth, Germany (2016) continues the series started with previous international symposia on FGM held in Sendai, Japan (1990), San Francisco, USA (1992), Lausanne, Switzerland (1994), Tsukuba, Japan (1996), Dresden, Germany (1998), Estes Park, USA (2000), Beijing, China (2002), Leuven, Belgium (2004), Hawaii, USA (2006), Sendai, Japan (2008), Guimaraes, Portugal (2010), Beijing, China (2012) and Sao Paulo, Brazil (2014).

Scope & Topics

The increasing demand for improved performance of materials under severe conditions, for expanding application areas of known materials and for reduction of the material and energy footprint of advanced products calls for materials with unique structures in addition to a specific chemical composition. Tailoring the structure with the help of *functional gradients* or *unique building blocks in metamaterials* enables specific functionalities at different geometrical scales. Such materials are designed with embodied continuous spatial variations in composition and microstructure for the specific purpose, e.g., for adjusting their mechanical, thermal, optical, electrical, biological or multi-functional response to specific application conditions.

The desired functional profile is often achieved with multi-material composites, characterized by a specific distribution of different materials and microstructures, with different sizes and shapes, with passive and active functionalities. Such materials can even include autonomous energy harvesting, storage and conversion properties, in addition to adequate mechanical, thermal, electromagnetic, chemical or biologic responses, configuring a so called multifunctional behavior. These structure-dominated multi-phase materials are best understood through a comprehensive multiscale modelling approach. Their processing and characterization requires new methodologies and techniques. They have a wide range of application including, for example, biomedical, automotive, aerospace, mechanical, civil, energy and transportation engineering applications.

The main objective of the 14th International Symposium on Functionally Graded Materials (ISFGMˢ) is to provide opportunities for exchange of ideas, discussion and improvement of the state of the art theory, modelling and synthesis techniques, applications and recent developments in the areas of functionally graded materials and metamaterials, through plenary lectures, oral presentations and posters.

The conference **topics** will include the following aspects of Functionally Graded Materials and Metamaterials for Multiscale and Multifunctional Structures:

- Material concepts & design criteria for FGMs and Metamaterials
- Synthesis and Processing
- Characterization, structure and functionality
- Mechanical and thermo-mechanical properties, other functionalities
- Modelling and Simulation
- Bio-inspired & Biomaterials
- Applications
- Life Cycle Analysis (LCA)

Organizers & Committees

Conference Chair

Prof. Dr. Monika Willert-Porada, University of Bayreuth, Germany

Co-Chair

Prof. Omer Van Der Biest, Katholieke University Leuven, Belgium

Local Organizing Committee

Dr.-Ing. Thorsten Gerdes, University of Bayreuth, Germany

Kerstin Söllner, University of Bayreuth, Germany

Dr.-Ing. Andreas Rosin, University of Bayreuth, Germany

Dipl.-Ing. Achim Schmidt-Rodenkirchen, InVerTec, Germany

Dr.-Ing. Daniel Leykam, University of Bayreuth, Germany

Technical Committee

Prof. Dr. Michael Gasik

Department of Materials Science and Engineering

Aalto University

Espoo, Finland

Prof. Dr.-Ing. Bernd Kieback

Institute of Materials Science

Technical University Dresden

Dresden, Germany

Prof. Evgeny Levashov

Scientific-Educational Center of SHS

Head of the Department "Powder Metallurgy and Functional Coatings"

National University of Science and Technology "Moscow Institute of Steel and Alloys"

Moscow, Russia

Prof. Dr. Thomas Scheibel

Chair of Biomaterials

Engineering Department

University of Bayreuth, Germany

Prof. Siegfried Schmauder

Institute of Materials Testing

University Stuttgart

Stuttgart, Germany

Prof. Filipe Samuel Silva

Departamento de Engenharia Mecânica (DEM)

Escola de Engenharia da Universidade do Minho

Campus de Azurém,

Guimarães, Portugal

Prof. Dr. Martin Wegener

Institute for Applied Physics

Karlsruher Institut für Technologie

Karlsruhe, Germany

Endorsing Society:

International Advisory Committee on FGM (IACFGM)

Chairman: Prof. Akira Kawasaki, Tohoku University, Japan

Co-Chairmen: Prof. Glaucio H. Paulino, University of Illinois, USA

Prof. Omer Van Der Biest, Katholieke Universiteit Leuven, Belgium

International Scientific Committee

[USA]

Prof. Glaucio H. Paulino, University of Illinois

Prof. Marek-Jerzy Pindera, University of Virginia

Prof. Jeong-Ho Kim, University of Connecticut

Assoc. Prof. Huming Yin, Columbia University

[Germany]

Prof. Dr. Monika Willert-Porada, University of Bayreuth

[Belgium]

Prof. Omer Van Der Biest, Katholieke Universiteit Leuven

[Finland]

Prof. Michael M. Gasik, Aalto University Foundation, School of Chemical Technology (Aalto CHEM)

[Slovenia]

Dr. Sasa Novak, Jožef Štefan Institute, Department for Nanostructured Materials – K7, Ljubljana

[Russia]

Prof. Evgeny Levashov, National University of Science and Technology "MISiS"

Dr. Vladimir Sanin, Institute of Structural Macrokinetics and Materials Science (ISMAN)

[China]

Prof. Lianmeng Zhang, Wuhan University of Technology

Prof. Qingjie Zhang, Wuhan University of Technology
Prof. Wei Pan, Tsinghua University
Prof. Chang-Chun Ge, University of Science and Technology Beijing
Prof. Jing-Feng Li, Tsinghua University
Prof.Zhangjian Zhou, University of Science and Technology Beijing

[Turkey]

Assoc. Prof. Serkan Dag, Middle East Technical University

[Brazil]

Prof. Fernando A. Rochinha, Federal University of Rio De Janeiro (UFRJ)
Prof. Emilio C.N.Silva, University of Sao Paulo
Prof. Luis Augusto Rocha, UNESP – Universidade Estadual Paulista "Júlio de Mesquita Filho"

[South Korea]

Assoc. Prof. Hansang Kwon, Pukyong National University

[Japan]

Prof. Akira Kawasaki, Tohoku University
Prof. Emeritus Yoshinari Miyamoto, Toyotanso, Co.
Prof. Ichiro Shiota, Salesian Polytechnic
Dr. Akinaga Kumakawa, Japan Aerospace Exploration Agency
Dr. Yoshikazu Shinohara, National Institute for Materials Science
Prof. Kiyotaka Matsuura, Hokkaido University
Prof. Takashi Goto, Tohoku University
Prof. Yoshimi Watanabe, Nagoya Institute of Technology
Prof. Kazuhiro Hasezaki, The University of Tokushima
Prof. Soshu Kirihara, Osaka University

Conference at a glance

Monday, September 19th, 2016

Welcome and Opening Ceremony	
Oral Session: Manufacturing and properties assessment of FG materials and structures I	*Oral Session:* Modelling of FG materials and structures I
Oral Session: Structure dominated Biomaterials I	*Oral Session:* Porous and ordered structures
Oral Poster Presentations	
Bavarian Evening	

Tuesday, September 20th, 2016

Opening of Industrial Exhibition	
Oral Session: Manufacturing and properties assessment of FG materials and structures II	*Oral Session:* Testing of FG materials and structures
Oral Session: FG amorphous and semi-crystalline materials	*Oral Session:* Modelling of FG materials and structures II
Oral Poster Presentations	
Conference Dinner at Eremitage Restaurant incl. Poster Award	

Wednesday, September 21st, 2016

Oral Session: Manufacturing and properties assessment of FG materials and structures III	*Oral Session:* Structure dominated Biomaterials II
Oral Session: Performance verification of FG materials and structures	
Panel discussion & closing ceremony, Introduction of next conference venue	
Farewell Barbecue	

Thursday, September 22nd, 2016

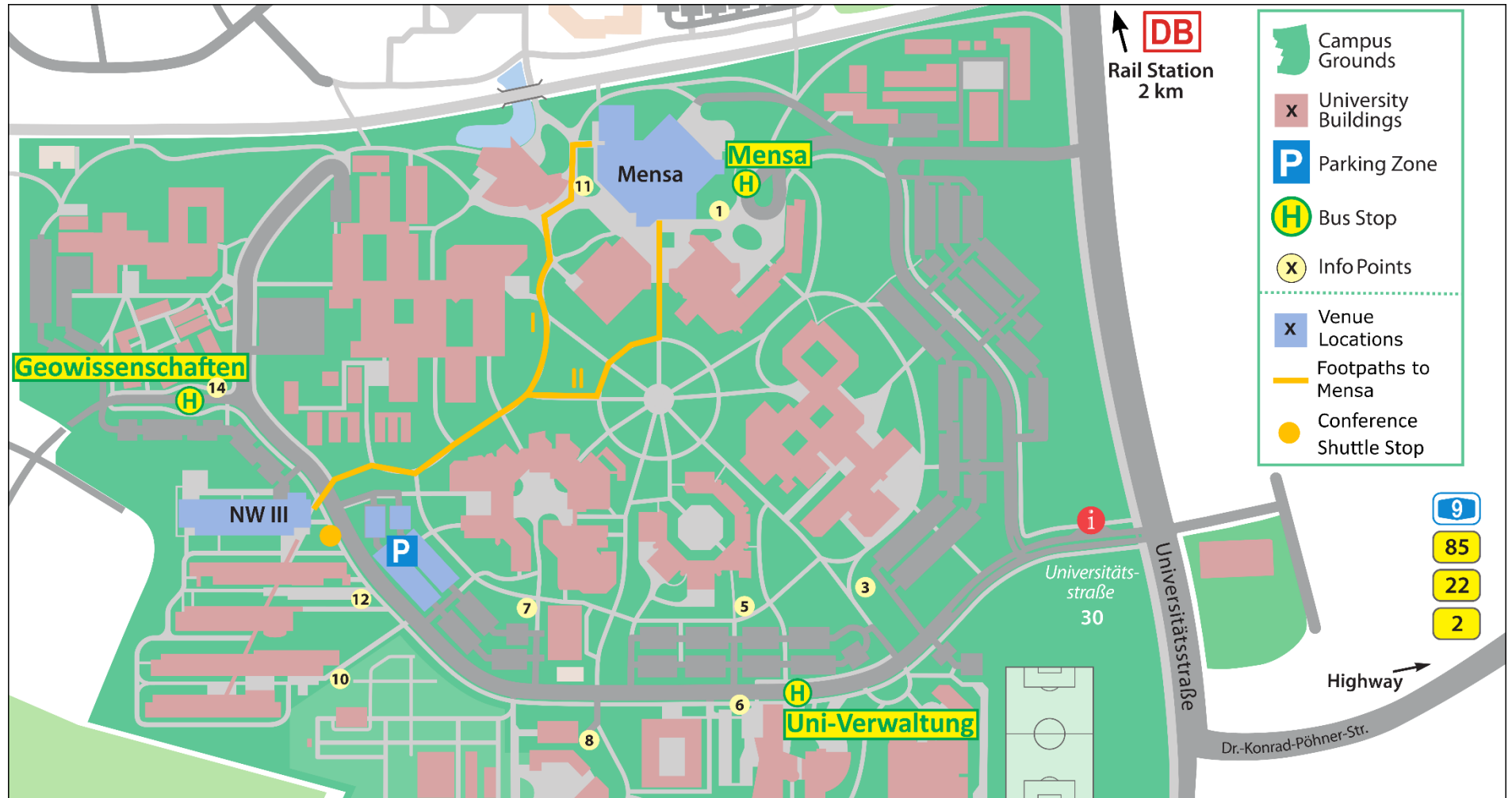| |
|---|
| Hands-on Training Additive Manufacturing |
| Visit of the neutron source Garching |
| Visit of Oktoberfest Munich |

Maps

Bayreuth
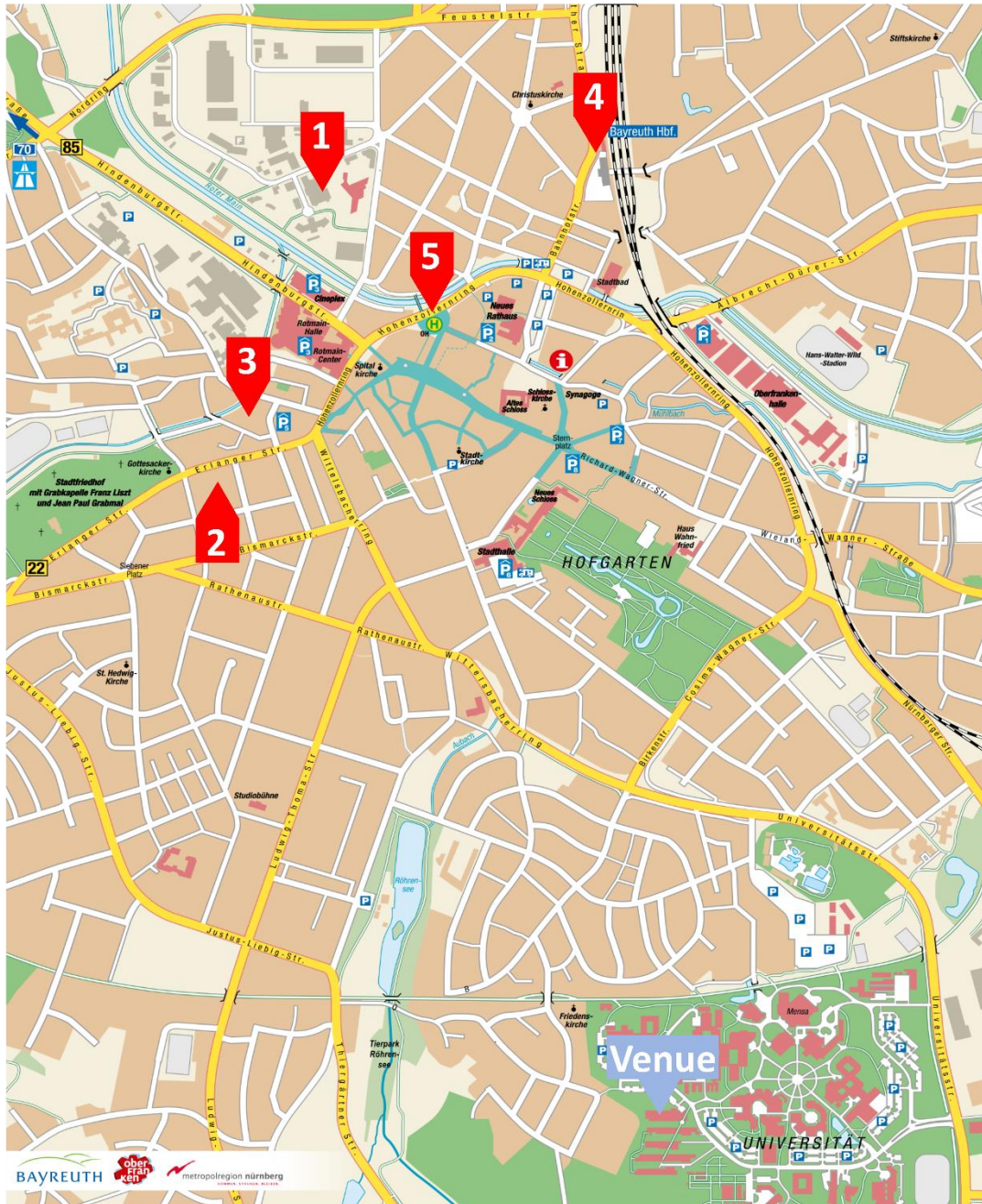
Accomodation

1 Arvena Kongress Hotel

2 H4 Hotel Residenzschloss
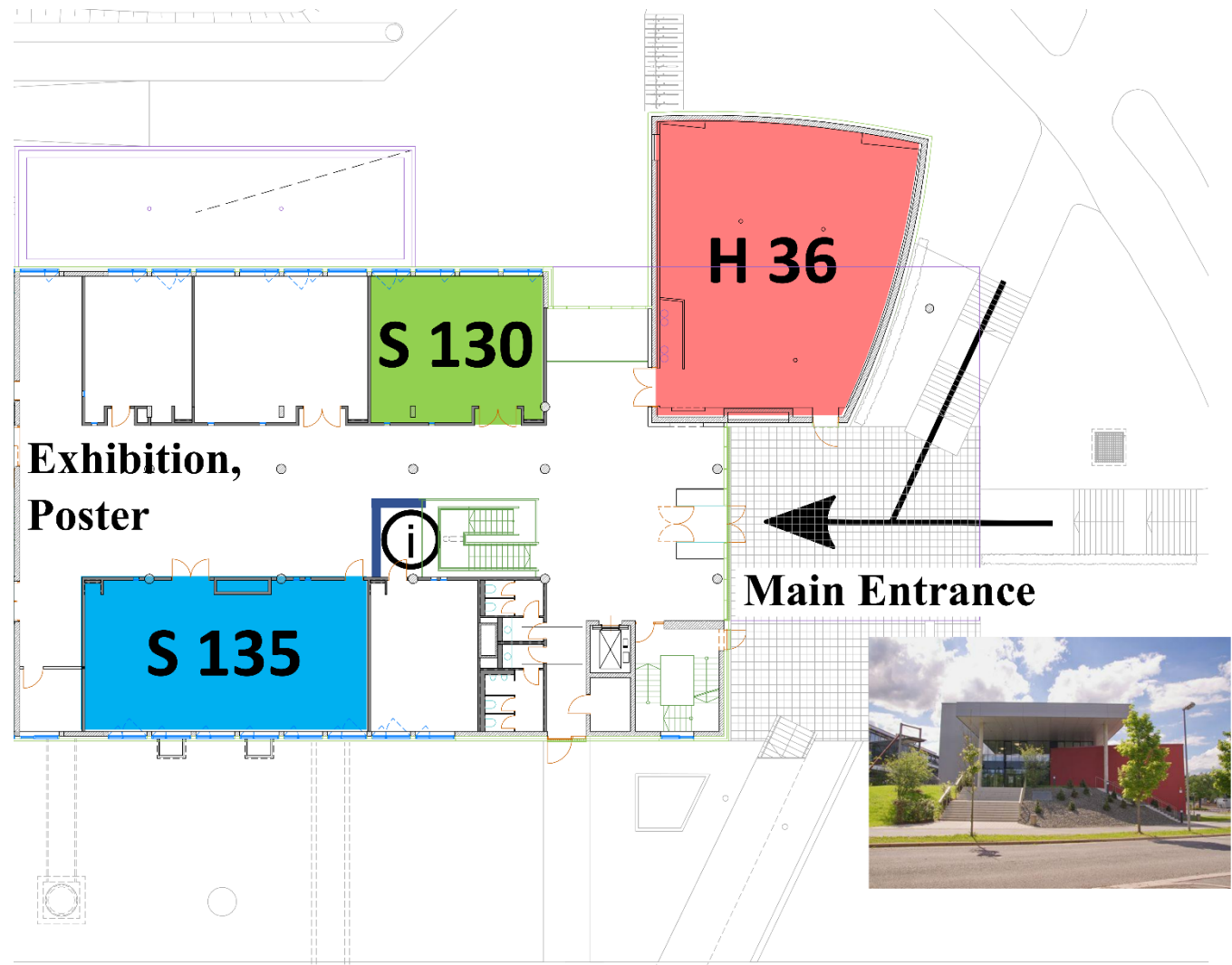
3 Hotel Rheingold

Public Transport

4 Main station

5 Central bus station

━━ Inner city

University of Bayreuth

DB
Rail Station
2 km

Mensa
11
Mensa
H
1

Geowissenschaften
H 14

NW III
P
12
10

7
5
3
i
Universitäts-
straße
30

6
Uni-Verwaltung
8

Universitätsstraße

Highway

Dr.-Konrad-Pöhner-Str.

9
85
22
2

Legend:
- Campus Grounds
- x University Buildings
- P Parking Zone
- H Bus Stop
- x Info Points
- x Venue Locations
- Footpaths to Mensa
- Conference Shuttle Stop

Symposium Venue

H 36

S 130

S 135

Exhibition,
Poster

Main Entrance

Oral sessions

Monday, September 19th, 2016

8:30 – 9:00	**Opening Ceremony** Venue: H36 / NW3

	Plenary Lecture I	M. van Hecke	
9:00 – 9:45	**Plenary Lecture I** Venue: H36 / NW3	**M. van Hecke** **Session Chair: O. Van Der Biest**	Combinatorial Design of Textured Mechanical Metamaterials

9:45 – 10:15	**Coffee break**

	Venue: S130 / NW III **Manufacturing and Properties Assessment of Functionally Graded Materials and Structures I** **Session Chair: I. Konyashin**	**Venue: S135 / NW III** **Modelling of Functionally Graded Structures and Materials and Structures I,** **Session Chair: S. Schmauder**
10:15 – 10:50	**I. Konyashin** – Functionally graded WC-Co cemented carbides: The state of the art	**V. Petrova** – Modeling of thermomechanical fracture of functionally graded coatings
10:50 – 11:15	**C.B. Wang** – Preparation and Properties of Nd-Substituted Bismuth Titanate Films with Gradient Composition	**M. Amirpour** – Stress and vibration analysis of FG plate with in-plane material properties variation
11:15 – 11:40	**D. Sidorenko** – Functionally graded diamond containing composite materials: manufacture, properties, performance	**R. Gunes** – Investigation on the Ballistic Limit of Functionally Graded Plates,
11:40 – 12:05	**B. Henriques –** Mechanical characterization of feldspathic porcelain-zirconia composites	**C. Mohcine** – Geometrically nonlinear free vibration of clamped-clamped functionally graded beam with an edge crack
12:05 – 12:30	**G. Luo** – Fabrication and Application of Mg-Cu Graded-Density Impactors from Powder Processing for Accurately Controlled Complex Loading Paths in Light-gas Gun,	**I. Comez** – The Contact Problem of a Rigid Punch Sliding over a Functionally Graded Bilayer

12:30 – 13:30	**Lunch break**

	Plenary Lecture II	S. Schmauder	
13:30 – 14:15	**Plenary Lecture II** Venue: H36 / NW3	**S. Schmauder** **Session Chair: O. Van Der Biest**	Challenges in multiscale materials modelling for FGMs

	Structure Dominated Biomaterials I, Session Chair: J. C. M. Souza	**Porous and Ordered Structures, Session Chair: V. Sanin**
14:20 – 14:55	**M. Lorenzetti** – Titania Surface Layer Can Prevent Adhesion of Bacteria to Titanium Implants	**O. Mondain-Monval** – Soft Porous Materials for Acoustics
14:55 – 15:20	**C. Ortmann** – Functionally Graded Ceramic Implant Materials for Joint Endoprotheses – Experiences and Outlook	**R. Zhang** – Fabrication and Characterization of Functionally Graded CNTs/PMMA Microcellular Foams with Designed Cell Structure
15:20 – 15:45	**J. C. M. Souza –** Applications of functionally graded materials in dentistry	**N. A. Sanina** – Multifunctional polymer composites and ordered nanostructures of photochromic molecular magnets: synthesis and properties

15:45 – 16:15	**Coffee break**

16:15 – 16:40	**A. Rosin –** In-vitro biocompatibility of Ti-implants with compositionally graded coatings	**M. Borovinšek** – Plastic wave propagation velocity in graded metallic foam materials
16:40 – 17:05	**B. Henriques** – FEM and analytical analysis of the bending stress distribution in graded zirconia-based dental ceramics	**K. Arslan** – Low Velocity Impact Performance of Honeycomb Sandwich Structures Reinforced by Functionally Graded Face Plates,

17:05 – 17:30	**Oral Poster presentations**
17:30 – 21:30	**Bavarian Evening & Poster Session Opening**

Tuesday, September 20th, 2016			
9:00 – 9:45	**Plenary Lecture III** Venue: H36 / NW3	**C. Körner** **Session Chair: A. Kawasaki**	From open-cellular materials to mechanical metamaterials by structural design and 3D-printing,
9:45 – 10:15	Coffee break & Poster presentations & Industrial exhibition		
10:15 – 11:00	**Plenary Lecture IV** Venue: H36 / NW3	**L.A. Rocha** **Session Chair: A. Kawasaki**	Multifunctional graded surfaces for osseointegrated implants: Combining tribocorrosion resistance with bone cells activity
	Venue: S130 / NW III **Manufacturing and Properties Assessment of Functionally Graded Materials and Structures II** **Session Chair: Y. Watanabe**		**Venue: S135 / NW III** **Testing of Functionally Graded Structures and Materials I** **Session Chair: C. Körner**
11:05 – 11:30	**S. Kirihra** – Stereolithographic Additive Manufacturing of Geometric Micro Patterns in Bulky Metal and Ceramic Components		**J. Zhang** – Microstructural Characterization of Mg/Al Diffusion Bonded Joint Using Al-Ni Interlayer
11:30 – 11:55	**M. Rauch** – Challenge for Additive Manufacturing of Functionally Graded Materials Parts		**C. Richter** – Hot corrosion behavior of 8Y-ZrO_2/$ZrSiO_4$ ceramic sealed by Laser-assisted Microwave Plasma Processing
11:55 – 12:20	**Y. Watanabe –** Microstructure and Wear Property of Al-Al_3Ti FGMs Fabricated by Centrifugal Solid-Particle and *in-situ* Methods		**S. Takahashi** – Measurement of Young's Modulus at Elevated Temperatures of Thermal Barrier Coating by Bending Resonance Method
12:20 – 12:45	**V.N. Sanin –** Hierarchical Structured Intermetallic Alloys Produced by Centrifugal SHS-Casting Technology		**Y. Shinohara** – Development of measurement system of thermoelectric properties of thin films in the thickness direction,
12:45 – 13:30	Lunch break & Industrial Exhibition		
13:45 – 14:30	**Plenary Lecture V** Venue: H36 / NW3	**C. Santangelo** **Session Chair: A. Kawasaki**	Self-Folding Structures By Programming Gradients in Polymer Sheets: Theory and Practice
	Functionally Graded Amorphous and Semi-Crystalline Materials **Session Chair: A.R. Boccaccini**		**Modelling of Functionally Graded Materials and Structures II** **Session Chair: C. Santangelo**
14:35 – 15:10	**S. Gerlach** - Gradient-Index Micro-Optics by Ion Exchange in Glass and its Applications to Optical Metrology and Biophotonic Imaging		**M. Gasik** - FGM Thermal Barrier Coatings Optimization under Hot Burner Testing Conditions
15:10 – 15:35	**A. Streicher** - Confocal chromatic sensor systems based on gradient index optics		**M. K. Apalak** - Stress wave propagation in a functionally graded cylinder
15:35 – 16:00	**T. Gerdes** - Compositionally graded glass by microwave field assisted ion exchange		**F. Yu -** Nonlinear Dynamic of Imperfect FGM Shallow Shell with Time Dependent Parameters in Temperature Field
16:00 – 16:25	**D. Leykam** - Glasceramics with graded photocatalytic activity		**K. Daszkiewicz** - Elastoplastic analysis of axially loaded FGM box section column
16:25 – 16:45	Coffee break & Poster presentations & Industrial exhibition		
16:45 – 17:30	**Plenary Lecture VI** Venue: H36 / NW3	**A. R. Boccaccini** **Session Chair: A. Kawasaki**	Functionally Graded Materials in Biomedical Applications: Progress and Challenges
19:00 – 22:00	Conference dinner at Eremitage Restaurant		

Wednesday, September 21st, 2016

Time	Venue: H36 / NW3		
9:00 – 9:45	**Plenary Lecture VII** Venue: H36 / NW3	**U. Gbureck** **Session Chair: M. Gasik**	3D Printing of Drug and Material Gradients in Bioceramic Implants
9:45 – 10:15	**Coffee break**		

Time	**Venue: S130 / NW III** **Manufacturing and Properties Assessment of Functionally Graded Materials and Structures III** **Session Chair: L.A. Rocha**	**Venue: S135 / NW III** **Structure Dominated Biomaterials II,** **Session Chair: G. Lang**
10:15 – 10:40	**C.-C. GE -** Research on FGM for Nuclear Applications	**E. DeSimone** - Recombinant spider silk proteins as bioinks
10:40 – 11:05	**M. Hamamci -** Experimental Investigation of Microstructural and Micromechanical Properties of Fe/B_4C-Fe/B Functionally Graded Materials	**C. Haynl** - Collagen-based gradient materials for tendon replacement
11:05 – 11:30	**H. Kohri** - Friction and Wear Characteristics of MoS_2/Cu-Sn Composite Film	**G. Lang** - Mechanical Testing of Engineered Spider Silk Filaments Provides Insights into Molecular Features on a Meso-Scale
11:30 – 11:55	**J. Park** - Functionally Graded Cu ZnS Phosphor and its Applications	**M. Miyaoka** - Study on the functionally graded characteristics of biofilms
11:55 – 12:20	**E. Zamulaeva -** Electrospark Deposited FGMs Coatings with Enhanced Characteristics	**A. Ohmukai** - Decomposition and Recovery Technology of Multi-Function Type Print Circuit Board with Substrate a Biodegradable Resin
12:20 – 13:30	**Lunch break**	

Time	Venue: H36 / NW3		
13:30 – 14:05	**Keynote** Venue: H36 / NW3	**B. Nacke** **Session Chair: M. Gasik**	Electromagnetic induced segregation of aluminum alloy cast parts,

Time	**Manufacturing and Properties Assessment of Functionally Graded Materials and Structures IV,** **Session Chair: B. Henriques**	**Performance Verification of Functionally Graded Materials and Structures,** **Session Chair: M. K. Apalak**
14:10 – 14:35	**R. Zhang** - Synthesis and Mechanical Properties of Graded TC4 Titanium Alloy via Plasma Activated Sintering	**M. Aydin** - Effect of Number of Layers on the Ballistics Performance of Functionally Graded Sandwich Plates
14:35 – 15:00	**X. Ren** - Innovative Preparation of Nano-sized WC/W2C/W Functionally Graded Material (FGM)	**S. Oetinger** - High pressure injection valve with magnetic gradient
15:00 – 16:00	Venue: H36 / NW3	Panel discussion & closing ceremony (Introduction of next conference venue)
16:00	**Farewell barbecue**	

Poster Program

Development of a functional glass having antimicrobial activity, non-irritant and low ion elution via silver or copper ion exchangehnique	Gyu-In Shim, Seong-Hwan Kim, Se-Young Choi	Department of Materials Science and Engineering, Yonsei University, Seoul, Republic of Korea
Fabrication of lightweight and thin bulletproof materials satisfying protective capacity of NIJ level III using strengthened-glass/polymer composite by ion exchange	Gyu-In Shim[1], Seong-Hwan Kim[1], Jong-Kyoo Park[2], Se-Young Choi[1]	[1]Department of Materials Science and Engineering, Yonsei University, Seoul, Republic of Korea [2]Agency for Defense Development, Daejeon, Republic of Korea
Fabrication of functionally graded materials with a high melting point difference for extreme environment application	Zhangjian Zhou, Changchun Ge	School of Materials Science and Engineering, Uniersity of Science and Technology, Beijing, China
Oxidation Resistance of MoSi$_2$/Mo FGMs Layer for Titanium Aluminide Intermetallic Compound	Masayuki Ohshima[1], Shohei Matsuda[1], Toshimitsu Tetsui[2], Kazuhiro Hasezaki[3]	[1]Intelligent Structures and Mechanics Systems Engineering, Graduate School of Advanced Science and Technology, Tokushima University, Tokushima, Japan [2]High Temperature Materials Center, National Institute for Materials Science, Tsukuba, Ibaraki, Japan [3]Department of Mechanical Science, Graduate School of Science and Technology, Tokushima University, Tokushima, Japan
Change in mechanical characterization according to the addition of graphene in functionally graded Cu-ZnO manufactured through spark plasma sintering	Kwangjae Park[1], Jehong Park[2], Seungchan Cho3, Akira Kawasaki[4], Kwonhoo Kim[1] Hansang Kwon[1,2]	[1]Pukyong National University, Republic of Korea [2]Next-Generation Materials Co., Ltd.(NGM), Republic of Korea [3]Korea Institute of Materials Science, Republic of Korea [4]Tohoku University, Japan
Si$_3$N$_4$-CMC reinforced with compositionally graded carbon fibers	Christian Richter[1], Karina Mees[1], Monika Willert-Porada[1], Viktor Heyer[2], Achim Schmidt-Rodenkirchen[3]	[1]Chair of Materials Processing, University of Bayreuth, Germany [2]Graduate School 1229, University of Bayreuth, Germany [3]InVerTec e.V., Bayreuth, Germany
Influence of ionic conductivity gradient in refractory lining for energy efficiency of electrically heated glass melting tanks	Andreas Rosin, Thorsten Gerdes, Monika Willert-Porada	Chair of Materials Processing, University of Bayreuth, Germany
Reactive Texturing of Y-TZP and Ce-TZP in Magnetic Field	O. Van der Biest[1], D. Vriami[1], E. Beaugnon[2]	[1]Department of Materials Engineering, K.U.Leuven, Heverlee, Belgium [2]Laboratoire National des Champs Magnétiques Intenses (LNCMI), Grenoble, France
Innovative Preparation of Nano-sized WC/W2C/W Functionally Graded Material (FGM)	Xiaona Ren, Min Xia, Qingzhi Yan, Changchun Ge	Institute of Nuclear Energy and New Energy System Materials, School of Materials Sciences and Engineering, University of Science and Technology Beijing (USTB), Beijing, China.

Workshop Program

Workshop: Additive manufacturing for multimaterials and functionally graded materials and hands-on training

Date: Thursday, September 22nd, 2016
Room: H36/ NW III

10:00	**Introduction into workshop topics**
10:30 – 11:00	**The LaserCUSING® Process**
	Peter Pontiller-Schymura
	Concept Laser GmbH, Lichtenfels, Germany
11:00 – 11:30	**Binder Jetting technology to 3D print complex parts in industrial-grade materials**
	Dr. Sarig Nachum
	Fraunhofer-Zentrum für Hochtemperatur-Leichtbau HTL, Bayreuth
11:30 – 12:30	**Lunch break**

Plenary Lectures

Prof. Dr.-Ing. habil. Aldo R. Boccaccini

Functionally Graded Materials in Biomedical Applications: Progress and Challenges

Aldo R. Boccaccini is Professor of Biomaterials and Head of the Institute of Biomaterials at the University of Erlangen-Nuremberg, Germany. He is also visiting Professor at Imperial College London, UK. He holds an engineering degree from Instituto Balseiro (Argentina), Dr-Ing. from RWTH Aachen University (Germany) and Habilitation from TU Ilmenau (Germany). The research activities of Prof. Boccaccini are in the field of glasses, ceramics and composites for biomedical, functional and/or structural applications. He is the author or co-author of more than 600 scientific papers and 15 book chapters. His work has been cited more than 15,000 times and he was named in the 2014 Thomson Reuters Highly Cited Researcher list. Boccaccini has been a visiting professor at different universities around the world, including Japan, Italy, Spain, Slovenia, Netherlands, Singapore, Argentina and Poland. His achievements have been recognized with several awards including, most recently, the Materials Prize of the German Materials Society (DGM) in 2015 and the Turner Award of the International Commission on Glass (2016). In 2015, he was elected member of the World Academy of Ceramics. Boccaccini is the editor-in-chief of the journal Materials Letters and serves in the editorial board of more than 10 international journals. In 2015 he was elected member of the Council of the European Society for Biomaterials (ESB). He also serves in the Review Panel of the German Science Foundation (DFG) and is an international advisor to the Ministry of Science and Technology of Argentina.

Functionally Graded Materials in Biomedical Applications: Progress and Challenges

Liliana Liverani, Aldo R. Boccaccini

[1]*Institute of Biomaterials, University of Erlangen-Nuremberg*
91058 Erlangen, Germany
aldo.boccaccini@ww.uni-erlangen.de

An overview on the applications of FGM in the biomedical field will be presented, with focus on the different uses that FGM (and stratified materials) are increasingly finding in tissue engineering and drug delivery applications. FGM, usually featuring porosity, are favorable to act as 3D scaffolds to induce the regeneration of tissues and organs because of their biomimetic structure resembling the anisotropic properties of native tissues. A variety of FGM-based scaffolds (and layered structures) are being investigated which exhibit graded properties in terms of composition, morphology, pore size and mechanical properties. An important area of application of such FGM is in the reconstruction of tissue interfaces, e.g. between soft and hard tissues. Scaffolds based on FGM can be obtained by integrating different fabrication techniques, like electrospinning, rapid prototyping, foam replica method, freeze drying, etc. A series of examples will be reviewed in this lecture highlighting the materials used, usually smart combinations of biopolymers, bioactive ceramics or glasses and porosity, and the relevant manufacturing technologies. For example, to reconstruct the osteochondral interface, a soft polymer fibrous layer (the cartilage side) can be deposited on the bone scaffolds, usually made of hydroxyapatite or bioactive glass foams [1]. In this context, electrospinning will be highlighted as an attractive technique to fabricate FGM-based (and layered) scaffolds, combining 3D patterned fibrous (nano)structures (Fig. 1 A-C) with zonal (biomimetic) mineralization utilizing bioactive nanoparticles embedded in the fibres. Remaining challenges in the field, especially in terms of understanding time dependent, long-term biological performance of FGM constructs in vivo will be discussed.
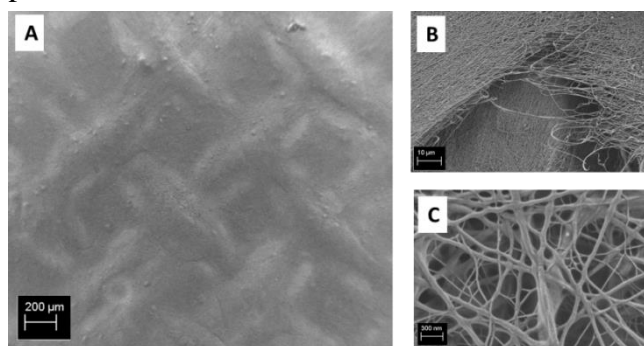
Fig. 1 (A-C) Patterned electrospun fibrous layers utilized to fabricate FGM scaffolds

[1] L. Liverani, et al., Mater. Sci. Eng. A 557 (2012) 54–58.

Keywords: scaffolds, tissue interfaces, stratified structures, electrospinning, composites

Prof. Dr. rer. nat. Uwe Gbureck

3D Printing of Drug and Material Gradients in Bioceramic Implants

Uwe Gbureck is a professor in the Department or Functional Materials in Medicine and Dentistry, University of Würzburg. He earned a PhD degree in chemistry from the University of Würzburg in 1999 about the synthesis of organically modified titaniumoxide coatings as coupling agents for hydrolysis resistant metal-polymer joints in dental applications. Afterwards, he investigated the use of injectable mineral biocements as bone replacement materials for low load bearing defect sites within his "Habilitation" thesis in 2005 and was later on appointed as "Priv.-Doz." (2005) and "Apl.-Prof." for Experimental Dentistry at the University Hospital Würzburg. His main research interests include the chemistry and material properties of mineral biocements based on calcium and magnesium phosphate chemistry, the use of such cement in rapid prototyping applications, as well as drug delivery systems based on inorganic structured materials.

3D Printing of Drug and Material Gradients in Bioceramic Implants

S. Meininger, E. Vorndran, U. Gbureck

Department for Functional Materials in Medicine and Dentistry, University Hospital Würzburg, Germany, uwe.gbureck@fmz.uni-wuerzburg.de

The classical application of bioceramics in the form of granules or monolithic implants is subsequently replaced by using tissue regeneration approaches based on macroporous scaffolds. The latter are seeded with cells either in vitro in a bioreactor or directly in vivo following implantation. The fabrication of such scaffolds by additive manufacturing approaches aims to produce defined microstructures with interconnecting, anisotropically aligned pores in the sub millimetre range from calcium or magnesium phosphate compounds. Here, 3D powder printing has been demonstrated to be a powerful tool for bioceramic fabrication, whereas a reactive binder liquid is selectively applied onto thin powder layers [1]. A major advantage of 3D printing technology is the ability to work at ambient temperature, e.g. the use of reactive cement systems enables the fabrication of low temperature, hydrated ceramics with a simultaneous local deposition of bioactive compounds to direct cellular response to the material. Such a spatial control of scaffold modification with various drugs was recently demonstrated by using a commercial multi-colour printer for sample preparation [2], in which the black channel was used for applying the binder, while the other three channels were filled with drug solutions (BMP-2, vancomycin, heparin) and polymer solution (chitosan hydrochloride) to produce graded material compositions. Drug release kinetics were shown to depend on the drug localisation (homogeneous, depot or graded) within the scaffolds; while homogeneously loaded scaffolds provided first order release kinetics, drug depots or gradients resulted in zero order release over a period of 3-4 days with release rates in the range 0.68-0.96 %/h.

[1] Vorndran E, Moseke C, Gbureck U. 3D printing of ceramic implants, MRS Bulletin 40 (2015), 127-136.
[2] Vorndran E, Klammert U, Ewald A, Barralet JE, Gbureck U. Similtaneous bioactive immobilisation during 3D powder printing of bioceramic drug release matrices, Adv Funct Mater 20 (2010), 1585-1591.

Keywords: Calcium phosphate scaffolds, 3D powder printing, drug release

Prof. Dr. Martin van Hecke

Combinatorial Design of Textured Mechanical Metamaterials

Martin van Hecke got his PhD in theoretical physics in 1996 at the University of Leiden. Since then he has worked on a broad range of topic in soft matter, including pattern formation and chaos, granular media, foams, rheology and jamming, combining experiments, simulations and theory. The common thread in all this works is the fascination for the emergence of complex behavior in seemingly simple systems. In 2008 Martin van Hecke was appointed as professor in the 'organization of disordered media' in Leiden, and after been awarded the Vici grant in 2011, he has refocused his research towards mechanical metamaterials, from patterned elastic media to origami. His main current fascination is the inverse problem: to design and make simple materials for which desired complex behavior emerges. Since Sept 2014 he works part-time at AMOLF, running a single group at two locations and spearheading the 'Designer Matter' initiative.

Combinatorial Design of Textured Mechanical Metamaterials

Corentin Coulais[1,2] Eial Teomy[3] Koen de Reus[1] Yair Shokef[3] and Martin van Hecke[1,2]

[1]*Huygens-Kamerlingh Onnes Lab, Universiteit Leiden, PObox 9504, 2300 RA Leiden, The Netherlands*
[2]*FOM Institute AMOLF, Science Park 104, 1098 XG Amsterdam, The Netherlands*
[3] *School of Mechanical Engineering and The Sackler Center for Computational Molecular and Materials Science, Tel Aviv University, Tel Aviv 69978, Israel*

The structural complexity of metamaterials is limitless, although in practice, most designs comprise periodic architectures which lead to materials with spatially homogeneous features. More advanced tasks, arising in e.g. soft robotics, prosthetics and wearable tech, involve spatially textured mechanical functionality which require aperiodic architectures. However, a naïve implementation of such structural complexity invariably leads to frustration, which prevents coherent operation and impedes functionality. Here we introduce a combinatorial strategy for the design of aperiodic yet frustration-free mechanical metamaterials, whom we show to exhibit spatially textured functionalities. We implement this strategy using cubic building blocks - voxels - which deform anisotropically, a local stacking rule which allows cooperative shape changes by guaranteeing that deformed building blocks fit as in a 3D jigsaw puzzle, and 3D printing. We show that these aperiodic metamaterials act as programmable shape shifters, morphing into spatially complex but predictable and designable shapes when uniaxially compressed. Moreover their mechanical response to compression by a textured surface reveals their ability to perform sensing and pattern analysis. Combinatorial design thus opens a new avenue towards mechanical metamaterials with machine-like functionalities.

Keywords: Mechanical Metamaterials, Combinatorics, Designer Matter

Prof. Dr.-Ing. habil. Carolin Körner

From open-cellular materials to mechanical metamaterials by structural design and 3D-printing

Carolin Körner has studied theoretical physics and graduated in the field of theoretical nuclear physics at the University of Erlangen-Nuremberg. Afterwards she changed to the Department of Materials Science and gained her PhD in the field of modelling of laser material interaction phenomena. She habilitated in the field of light-weight materials with focus on metal foams. Since 2011 she is full professor for Materials Science and head of the Chair Materials Science and Technology for Metals at the University of Erlangen-Nuremberg. In addition, she is head of the additive manufacturing groups at the Joint Institute of Advanced Materials and Processes in Fürth and at New Materials Fürth GmbH. Her research areas are additive manufacturing of high performance materials, casting technologies, metal matrix composites and process simulation.

From open-cellular materials to mechanical metamaterials by structural design and 3D-printing

C. Körner[1], F. Warmuth[2], M. Wormser[2], Y. Liebold-Ribeiro[1]

[1]Universität Erlangen-Nürnberg,
Chair of Materials Science and Technology for Metals,
carolin.koerner@fau.de
[2]Universität Erlangen-Nürnberg,
Joint Institute of Advanced Materials and Processes, Fürth,

Cellular metals or metal foams are an interesting class of material since they offer property combinations which go beyond that of compact materials. Now, the rapid development of 3D-printing technologies makes the realization of nearly all kind of open-cellular structures possible. Thus, the underlying cell architecture is no longer governed by a more or less stochastic production process like foaming but can be freely designed and optimized to fulfill specific properties. This new design freedom can now be used to create materials with completely unusual and new properties, e.g. materials showing a negative Poisson's ratio (auxetic material) or materials with full phononic band gaps. The properties of these printed materials are primarily governed by their structure and only secondarily by the underlying material. Hence they are named as mechanical metamaterials.

In order to fully exploit this new kind of fabrication freedom, a fundamental understanding of the physical mechanisms leading to specific properties, like a negative Poisson's ratio or full phononic band gaps, has to be developed. A systematic approach based on eigenmode analysis of basic cell topologies combined with static and dynamic numerical characterization allows to identify the governing mechanisms leading to specific properties. Based on this knowledge, a specific design of cellular materials showing certain properties can be performed.

Selective electron beam melting, a powder bed based additive manufacturing method, is used to fabricate specific cellular materials of high performance metallic alloys such as titanium. The comparison of the calculated properties of the printed materials with experimental results demonstrates the predictive power of the knowledge based design.

Keywords: Cellular metals, mechanical metamaterials, 3D-printing, selective electron beam melting

Prof. Luís Augusto Rocha

Multifunctional graded surfaces for osseointegrated implants: Combining tribocorrosion resistance with bone cells activity

Luís Augusto Rocha is Associated Professor at UNESP – Univ. Estadual Paulista, Faculdade de Ciências de Bauru. Formerly he was Associated Professor at the Department of Mechanical Engineering of University of Minho, in Portugal. He is the coordinator of the IBTN/Br, Brazilian branch of the Institute of Biomaterials, Tribocorrosion and Nanomedicine and member of the *MEMS-UMinho – Center MicroElectroMechanical Systems* at University of Minho.

His research interests are focused on biomaterials, namely on the development of functionally graded materials (FGM), surface functionalization of metallic biomaterials and on the investigation of the degradation mechanisms of those materials, essentially from the tribocorrosion point-of-view, and its influence on biological systems.

He is a member of WP18 on Tribocorrosion (European Federation of Corrosion), LGM-AS – Int. Assoc. for Layered and Graded Materials (World Academy of Ceramics) and International Advisory Board on Functionally Graded Materials (FGM Forum, Japan).

Multifunctional graded surfaces for osseointegrated implants: Combining tribocorrosion resistance with bone cells activity

L.A. Rocha[1,2], F.G. Oliveira[2,3], A.R. Ribeiro[2,4]

[1]*UNESP – Universidade Estadual Paulista, Fac. Ciências Bauru, Brazil, lrocha@fc.unesp.br*
[2]*IBTN/Br – Brazilian Branch of the Institute of Biomaterials, Tribocorrosion and Nanomedicine, Brazil*
[3]*CITEVE – Centro Tecnológico Indústria Têxtil e Vestuário, Vila Nova de Famalicão, Portugal, fernando.g86@gmail.com*
[4]*National Institute of Metrology Quality and Technology, Directory of Metrology Applied to Health Sciences, Rio de Janeiro, Brazil, arribeiro@inmetro.gov.br*

Titanium and its alloys are widely used in dental and orthopedic implants. Among other factors, lifetime of osseointegrated implants is influenced by the capability of the surface of the implant to induce osteoblasts (bone-forming cells) to adhere, proliferate and mineralize as fast as possible in order to anchor the implant in place. However, the intrinsic low resistance to wear of Ti-based materials may compromise its biological performance. In fact, degradation by tribocorrosion mechanisms (corrosion + mechanical wear) results in the modification of the surface characteristics of the material, but, at the same time, generates micro or nano-sized debris and/or metallic ions that may have a deleterious effect on the biological functions locally and systemically. Anyway, the surface properties of titanium can be tailored to ensure enhanced biological properties, corrosion and wear resistance.

Oxide films grown on titanium by micro-arc-oxidation (MAO) may be designed with graded properties for optimized performance. The incorporation of bioactive elements such as Ca, P and Mg can enhance the biological response of the surface, allowing better interaction with bone cells, enhancing at the same time the tribocorrosion resistance of the surfaces.

In this work an overview of the growth mechanisms of these multifunctional functionally graded doped titanium oxide films will be presented. Also, the influence of the chemical and structural characteristics of the film on the tribocorrosion mechanisms and biological interactions will be discussed.

Keywords: Functionally graded surfaces; osteoblasts; debris; tribocorrosion; nanotoxicity

Prof. Christian Santangelo

Self-Folding Structures By Programming Gradients in Polymer Sheets: Theory and Practice

Professor Santangelo is a theoretical physicist with a research interest in soft materials. He received his B.A. degree in Physics from Cornell University in 1997 and his Ph.D. in Physics from UC Santa Barbara in 2004, with Fyl Pincus. He did a post-doc at the University of Pennsylvania with Randy

Kamien, then joined the Physics Department at the University of Massachusetts in 2007. He is the recipient of the 2004 Glenn Brown Prize from the International Liquid Crystal Society and a CAREER award in 2008. His most recent work has been on using geometry to design shape and control the mechanical properties of thin elastic sheets.

Self-Folding Structures By Programming Gradients in Polymer Sheets: Theory and Practice

Christian Santangelo[1]

[1]Department of Physics, University of Massachusetts Amherst, csantang@physics.umass.edu

Recent advances in the fabrication of polymer hydrogel sheets have resulted in the fabrication of structures capable of reversibly folding and unfolding. This self-folding is achieved by imbuing the sheets with gradients in composition, either through photolithography or by careful chemistry, and by carefully tuning material properties. Yet, the theoretical tools to design such self-folding sheets lag behind experimental capabilities. I will discuss the work of our group and collaborators in developing tools to design self-folding structures by programming either gradients in cross-link density or material properties. Whether, and how, a particular structure can be "self-folded" depends crucially on the interplay between geometry and the mechanics thin sheets. Finally, I will discuss challenges in the design and fabrication of self-folding structures.

Keywords: self-folding, origami, geometry

Prof. Dr. rer. nat. Siegfried Schmauder

Challenges in multiscale materials modelling for FGMs

Professor Dr. Siegfried Schmauder is currently a Professor of Materials Science and Strength of Materials at the University of Stuttgart, Germany. He graduated in Mathematics from the University of Stuttgart in 1981, and received his Dr. rer. nat. degree from the same University in 1988. After his work as a research group leader at the Max-Planck-Institute for Metals Research and postdoctoral research stays at the University of Tokyo, Japan, and at the University of California at Santa Barbara (UCSB), USA, he accepted an offer to become a Professor at the State Materials Testing Agency (MPA), University of Stuttgart. Since 2003 he is working at the Institute for Materials Testing, Materials Science and Strength of Materials (IMWF) at the same University. He is author of more than 400 research papers in the field of nano- and micromechanics of composites and metals as well as on multiscale simulation of hierarchical materials.

Challenges in multiscale materials modelling for FGMs

Siegfried Schmauder

Institute for Materials Testing, Materials Science and Strength of Materials (IMWF)
University of Stuttgart, Pfaffenwaldring 32, D-70569 Stuttgart, Germany,
siegfried.schmauder@imwf.uni-stuttgart.de

In the recent past, multiscale materials modelling became a central idea in understanding present day complex composites and in making progress in the development of advanced materials [1]. There exists, however, a discrepancy between available results described in literature and the expression "multiscale modelling", because typically cases are treated with two length scales only and sometimes additional one or two time scales.

This presentation will describe several successfully running multiscale examples which are used in analyzing pipeline steel weldments, metal/ceramic interfaces, polymer composites, bionic materials and fatigue problems of metals which are employed for a better understanding of physical phenomena in these materials leading to their deformation and fracture behavior. The potential of these findings for modelling and development of FGMs in future applications will be shown in the present contribution.

In addition, studies will be shown which provide the basis for the development of new metallic alloys when taking ab initio, Monte Carlo or Molecular Dynamics modelling approaches into account. As examples solid solution hardening [2] is considered for Fe-base materials or fatigue loading for polycrystalline steels [3] where property predictions are in close agreement to experimental findings.

[1] S. Schmauder, I. Schäfer (Eds.), Multiscale Materials Modelling – Approaches to Full Multiscaling, de Gruyter, Berlin (2016) (to be published)
[2] S. Schmauder, C. Kohler, Comp. Mater. Sci., 50 (2011), 1238-1243
[3] Z. Bozic, S. Schmauder, M. Mlikota, M. Hummel, Fatigue Fract. Eng. Mater. Struct., 37(2014), 1043–1054

Keywords: multiscale modelling, fatigue, solid solution hardening, FGMs

Abstracts

Session: Manufacturing and Properties Assessment of Functionally Graded Materials and Structures I

Session Chair: I. Konyashin

Date: Monday, September 19th, 2016, Morning Session: 10:15-12:30
Room: S 130/ NW III

10:15 – 10:50	**Functionally graded WC-Co cemented carbides: The state of the art** I.Konyashin, S. Hlawatschek, B. Ries, E. Levashov, A. Zaitsev
10:50 – 11:15	**Preparation and Properties of Nd-Substituted Bismuth Titanate Films with Gradient Composition** C.B. Wang, D.Y. Guo, C.Y. Liu, Q. Shen, L.M. Zhang
11:15 – 11:40	**Functionally graded diamond-containing composite materials: manufacture, properties, performance** D. Sidorenko, E. Levashov, P. Loginov, N. Shvyndina, E. Skryleva
11:40 – 12:05	**Mechanical characterization of feldspathic porcelain-zirconia composites** B. Henriques, R. L.P Santos, R. M. Nascimento, J. C.M. Souza, F. Silva
12:05 – 12:30	**Fabrication and Application of Mg-Cu Graded-Density Impactors from Powder Processing for Accurately Controlled Complex Loading Paths in Light-gas Gun** Guoqiang Luo, Jiayu He, Lianmeng Zhang, Xiaozhuang Zhou, Qiang Shen, Meijuan Li, Chuanbin Wang, Jian Zhang, Jinsong Bai, Yuyin Yu
12:30 – 13:30	**Lunch**

Functionally graded WC-Co cemented carbides: The state of the art

I.Konyashin[1,2], S. Hlawatschek[1], B. Ries[1], E. Levashov[2], A. Zaitsev[2]

[1]*Element Six GmbH, Burghaun, Germany. Email: igor.konyashin@e6.com*
[2]*National University of Science and technology MISiS, Moscow, Russia. Email: levashov@shs.misis.ru*

The fabrication of cemented carbides with functionally graded composition, microstructure and properties has been an issue of great interest in the cemented carbide industry for a long time. The history of the development and fabrication of functionally graded cemented carbides is outlined. Different technologies employed for the manufacture of functionally graded WC-Co cemented carbides are reviewed. Various types of functionally graded WC-Co materials designed for specific applications and fabricated by tailored sintering techniques are described. The functionally graded cemented carbides are characterized by a unique combination of various properties including exceptionally high hardness and fracture toughness, which cannot be achieved in bulk WC-Co materials. Carbide articles are described in which functional gradients of hardness, cobalt content and WC grain size have been obtained as a result of creating Co drifts and regulating the WC grain growth by controlling the carbon content of the surface layer. Mechanisms of binder migration phenomena allowing one to produce the functionally graded cemented carbides by their self-assembly during sintering are presented. The mechanisms are based on considering capillary forces in parts of carbide articles with various carbon contents and/or different WC mean grain sizes. Different applications of the functionally graded cemented carbides with numerous examples illustrating the dramatic improvement of their wear-resistance and significant prolongation of tool lifetime are presented. Modern trends in the research and development of novel functionally graded WC-Co cemented carbides are outlined.

Preparation and Properties of Nd-Substituted Bismuth Titanate Films with Gradient Composition

C.B. Wang, D.Y. Guo, C.Y. Liu, Q. Shen, L.M. Zhang

State Key Lab of Advanced Technology for Materials Synthesis and Processing, Wuhan University of Technology, wangcb@whut.edu.cn

Nd-substituted bismuth titanate ($Bi_{4-x}Nd_xTi_3O_{12}$, abbreviated as BNT) films have been extensively investigated for the possibility of application in non-volatile ferroelectric memories. It is supposed that the properties of those films could be enhanced by changing their compositions gradually, as verified in the compositionally-graded V-doped bismuth titanate films. In this study, BNT films with gradient composition were prepared on $Pt(111)/Ti/SiO_2/Si$ substrates by sol-gel, and the microstructure, ferroelectric and dielectric properties of the films as a function of composition were investigated. At first, single-phased BNT films with compositions changing from x = 0 to x = 1.0, respectively, were obtained. With increasing Nd content, the preferred orientation of the films changed from random to (117), resulting in the improvement in properties. Then, the (117)-oriented BNT films with two kinds of gradient composition, i.e., upgraded and downgraded, were prepared. As compared with the homogeneous BNT films, the remanent polarization (P_r) and permittivity (ε_r) of the compositionally-graded BNT films were significantly enhanced, which were $2P_r = 34.9\ \mu C/cm^2$ and $\varepsilon_r = 509$.
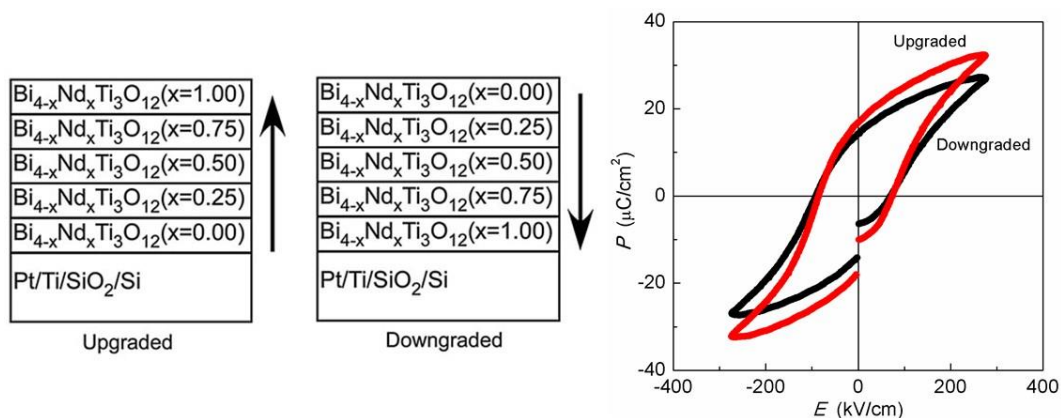
Figure 1 Structure and ferroelectric properties of BNT films with gradient composition

Keywords: BNT films, gradient composition, ferroelectric properties, dielectric properties

Functionally graded diamond-containing composite materials: manufacture, properties, performance

D. Sidorenko, E. Levashov, P. Loginov, N. Shvyndina, E. Skryleva

National University of Science and technology MISiS, Moscow, Russia. email: dsidorenko@inbox.ru

Diamond cutting tools with metal binders (saw blades, core drills and wire saws) are widely used to machine the most difficult to work with materials, such as reinforced concrete, stone and steel structures. In such operation conditions the tools wear down rather quickly, which has significant technical and economic implications. Currently, there are three main ways of improving the quality of diamond cutting tools: increasing (1) strength of binder (metal matrix), (2) diamond grain grade and (3) adhesion strength between the diamond and the binder. In present work a new approach to design of diamond containing composite material have been suggested: the simultaneous improvement of (1) and (3) during diamond composite material sintering. The mechanism of spontaneous formation of WC-based layer on diamond surface during sintering with metal binder in the presence of WC nanopowder as a reinforcing additive is studied. This intermediate layer provides a good adhesion between matrix and diamond. The layer is formed via a gas-phase transport mechanism leading to chemisorption of volatile tungsten oxide WO_3 onto diamond surface followed by WO_3 reduction and carbide formation. The simultaneous increase of the binder mechanical properties and formation of a protective WC-based layer on the diamond surface provide a synergistic effect, leading to the enhancement in operation performance of the diamond tool, in particular increasing productivity and cutting speed.

Keywords: diamond; interfacial layer; nanoparticles; metal matrix composite; cutting tool

Mechanical characterization of feldspathic porcelain – zirconia composites

B. Henriques[1,2], R. L.P Santos[3], R. M. Nascimento[3], J. C.M. Souza[4], F. Silva[2]

[1]Ceramic and Composite Materials Research Group (CERMAT), Federal University of Santa Catarina (UFSC), Campus Trindade, Florianópolis/SC, Brazil, brunohenriques@dem.uminho.pt
[2]CMEMS-UMinho, University of Minho, Campus de Azurém, 4800-058 Guimarães, Portugal, fsamuel@dem.uminho.pt
[3]Department of Materials Engineering, Federal University of Rio Grande do Norte (UFRN), Campus Lagoa Nova, 59078-970, Natal, Brazil, rubensmaribondo@gmail.com, raffitasantos8@hotmail.com
[4]CEPID, Department of Dentistry (DODT), Universidade Federal de Santa Catarina (UFSC), Florianópolis/SC, Brazil, julio.c.m.souza@ufsc.br

The purpose of this study was the production and mechanical characterization of feldspathic porcelain reinforced by zirconia particles aiming at a FGM application. Feldspathic porcelain specimens with different volume fractions (10, 20, 30, 40 or 50%) of zirconia particles (3YTZP) dispersed in the matrix were produced. The mixtures were heat pressed in vacuum at 970°C for 2 min. Flexural strength, Hardness, Young's modulus and fracture toughness were measured. The microstructure and fracture surfaces were characterized by FEG-SEM. Chemical analyses were performed by EDS and XRD. The highest flexural strength (218 ± 24 MPa) and fracture toughness (2.1 ± 0.1 MPa m$^{1/2}$) values were recorded for composites containing 30% zirconia particles. That corresponded to improvement in mechanical properties of about 2 times relative to those registered for feldspar-based porcelain. The Young's moduli increased with the addition of zirconia particles. The hardness values were not significantly different. The addition of zirconia particles to feldspathic porcelain improved significantly the mechanical properties of the base material.

Keywords: feldspathic porcelain, zirconia, heat pressing, composites, mechanical properties.

Fabrication and Application of Mg-Cu Graded-Density Impactors from Powder Processing for Accurately Controlled Complex Loading Paths in Light-gas Gun

Guoqiang Luo[1], Jiayu He[1], Lianmeng Zhang[1] *, Xiaozhuang Zhou[1], Qiang Shen[1], Meijuan Li[1], Chuanbin Wang[1], Jian Zhang[1], Jinsong Bai[2], Yuyin Yu[2]

[1]*State Key Laboratory of Advanced Technology for Materials Synthesis and Processing, Wuhan University of Technology, Wuhan 430070, China*
[2] *Laboratory of Shock Wave and Detonation Physics Research, Institute of Fluid Physics, P O Box 919-111, Mianyang, Sichuan 621900, China*
corresponding author, Tel.: +86 186-2706-0013; fax: +86 27 87879468. E-mail address: luogq@whut.edu.cn

Compositionally graded Mg-Cu structures for use as light-gas gun impactors were fabricated by powder processing and hot-press sintering. Layers of pressed metal powders were stacked in sequence according to designed density-thickness curves to attain desired thermodynamic loading paths. Powder processing was simple to operate and allowed excellent control of the composition and thickness. The samples were highly densified (≥98.7%) and contained no intermetallic compounds or magnesium oxides. Mg and Cu phases were dispersed homogeneously and well compacted and no obvious pores or voids between layers were found. The thickness of each layer deviated little from the designed values, with errors of 0.06-1.13%. Additionally, the parallelism and flatness of the samples were very good. In order to attain the dynamic loading paths, a 14 layer graded-density impactor was chosen randomly to shot target Al with a LiF window, and the resulting profile was measured with VISAR. The measured profile was compared with the designed that simulated by onedimensional hydrodynamic numerical model. These two profiles agreed well with each other, with both particle velocity and time scale accurately controlled. The Pressure-Time diagram was calculated and a complex applied-pressure profile combining shock loading, constant pressure, release, quasi-isentropic compression was attained. The mechanism of the Pressure-Volume diagram was explored extensively.

Keywords: Powder processing; Graded-density impactors; Complex applied-pressure profile

Session: Modelling of Functionally Graded Materials and Structures I

Session Chair: S. Schmauder

Date: Monday, September 19th, 2016, Morning Session: 10:15-12:30
Room: S 135/ NW III

10:15 – 10:50	**Modeling of thermomechanical fracture of functionally graded coatings** V. Petrova, S. Schmauder
10:50 – 11:15	**Stress and vibration analysis of FG plate with in-plane material properties variation** Maedeh Amirpour, Simon Bickerton, Raj Das, Brian Mace
11:15 – 11:40	**Investigation on the Ballistic Limit of Functionally Graded Plates** Recep Gunes, Mevlut Hakan, M. Kemal Apalak, J.N. Reddy
11:40 – 12:05	**Geometrically nonlinear free vibration of clamped-clamped functionally graded beam with an edge crack** Chajdi Mohcine, Merrimi El Bekkaye, El Bikri Khalid
12:05 – 12:30	**The Contact Problem of a Rigid Punch Sliding over a Functionally Graded Bilayer** Isa Comez, Mehmet Ali Guler
12:30 – 13:30	**Lunch**

Modeling of thermo-mechanical fracture of functionally graded coatings

Vera Petrova [1,2], Siegfried Schmauder [1]

[1]*IMWF, University of Stuttgart, Pfaffenwaldring 32, D-70569 Stuttgart, Germany*
[2]*Voronezh State University, University Sq.1, Voronezh 394006, Russia, veraep@gmail.com*

A model of fracture of functionally graded coatings on a homogeneous substrate (semiinfinite medium) subjected to thermo-mechanical loading (residual thermal stresses due to sudden cooling and/or tension) is presented. The material properties are continuous functions of a thickness coordinate (e.g., exponential function). The method of singular integral equations is used in this problem. The solution of the equations is obtained numerically. This method is applicable when the material gradation of the functionally graded coating is not steep.

Experimental investigations of thermal barrier coatings under thermal shock show that edge cracks appear first and then internal horizontal cracks are forming [1]. Besides, the tendency for horizontal crack initiation increases as the primary surface crack length increases. In this connection the interaction of a system of arbitrarily inclined edge cracks with internal cracks is investigated. Stress intensity factors at crack tips are determined and then, using an appropriate fracture criterion, the direction of crack propagation is derived as well as which crack starts to propagate first.

[1] A. Gilbert, K. Kokini, S. Sankarasubramanian, Surf. Coat. Technol. 202 (2008), 2152-2161

Keywords: fracture, functionally graded coatings, thermo-mechanical loading, stress intensity factors

Stress and Vibration analysis of the FG plate with in-plane material properties variation

Maedeh Amirpour[1], Simon Bickerton[1], Raj Das[1], Brian Mace[2]

[1] *Center of Advanced Composite Materials (CACM), Department of Mechanical Engineering, University of Auckland, New Zealand* maedeh.amirpourmolla@auckland.ac.nz
[2] *Department of Mechanical Engineering, University of Auckland, New Zealand*

This paper presents the bending and free vibration solution of functionally graded (FG) plates with variation of material properties through their length using higher order shear deformation theory (HSDT). The present theory accounts for both the shear deformation and thickness stretching effect by a sinusoidal variation of the displacement field across the thickness. The problem is then modelled using the finite element method (FEM) using graded solid element. This element has the spatially graded property distribution (at different Gauss points), which is implemented by the user subroutines UMAT and USDFLD for bending and vibration analysis, respectively. It can be concluded that the present exact formulation is not only accurate, but also simple in predicting the bending and vibration of the FG plates.

Also, the good agreement found between the exact solution and the numerical simulation demonstrates the effectiveness of graded solid element in the modelling of the FG plate. Moreover, the combination of the derived analytical and numerical results will enable us to understand the behaviour of new materials with controlled macro properties through the specific direction with potential relevance to biomedical and aerospace sectors.

Keywords: FG plates, In-plane properties variation, Stress, Vibration

Investigation on the Ballistic Limit of Functionally Graded Plates

Recep Gunes[1], Mevlut Hakan[2], M. Kemal Apalak[3], J.N. Reddy[4]

[1] *Department of Mechanical Engineering, Erciyes University, Kayseri 38039,*
recepg@erciyes.edu.tr
[2] *Department of Mechanical Engineering, Erciyes University, Kayseri 38039,*
mevluthakan@erciyes.edu.tr
[3] *Department of Mechanical Engineering, Erciyes University, Kayseri 38039,*
apalakmk@erciyes.edu.tr
[4] *Department of Mechanical Engineering, Texas A&M University,*
College Station, TX 77843-3123, USA, jnreddy@tamu.edu

Armor technologies are continuously improving against projectile threats which increasing ravage and destruction area. The use of composite materials as the armor structures provides high resistance against projectile, as well as facilitate the mobility by reducing the weight of structure. Besides, it is very important to design of composite armors both to disrupt the projectile tip geometry and to protect the structural integrity in ballistic applications. In this respect, functionally graded materials consisting of ceramic and metal are extremely suitable for ballistic applications due to their nature. Namely, the ceramic constituent provides high ballistic resistance against projectile while the metal constituent supplies the structural integrity of the FGM armor.

The aim of this study is to investigate the effect of through-thickness material properties of the FG plates and impact angle of the projectile on the ballistic limits of FGM armor system. MoriTanaka homogenization scheme is used as the micro-mechanical model to determine the through-thickness material properties in the graded region. Three-dimensional explicit finite element simulations are carried out for the FGM armor impacted at 0º, 15º, 30º, 45º and 60º obliquity by a 0.30 caliber Fragment Simulating Projectile (FSP). The ballistic limit, absorbed energy by the FGM armor, and the critical impact angle of the projectile are quantified.

Keywords: Functionally graded materials, Oblique impact, Ballistic limit, Explicit finite element method

The Contact Problem of a Rigid Punch Sliding over a Functionally Graded Bilayer

Isa Comez[1], Mehmet Ali Guler[2]

[1]Department of Civil Engineering, Karadeniz Technical University, Trabzon, Turkey,
isacomez@ktu.edu.tr
[2]Department of Mechanical Engineering, TOBB University of Economics and
Technology, Ankara, Turkey, mguler@etu.edu.tr

In this study the plane frictional sliding contact problem between a rigid cylindrical punch and a Functionally Graded (FG) bilayer is considered. The thicknesses and the material properties of the layers are different. The normal and tangential forces are applied to the upper layer via a rigid cylindrical stamp, and the lower layer is perfectly bonded to a rigid substrate.

Poisson's ratios are assumed to be constant and the elasticity moduli are assumed to vary exponentially through the thicknesses of the layers. Applying the Fourier integral transform technique, the plane contact problem is reduced to a singular integral equation of the second kind in which the unknowns are the contact pressure and the contact width. The singular integral equation is solved numerically utilizing Gauss-Jacobi integration formula. Numerical results include the contact pressure and the in-plane stress components for several geometrical and elastic parameters such as the material inhomogeneity, the friction coefficient, the height of the layers, the mismatch in the material properties at the interface and the contact width. The results obtained from this study would be helpful for the design engineers in developing wear resistant coatings and surfaces that would resist fatigue damage due to contact loading.

Keywords: Contact Mechanics, Sliding Contact, FGM, Friction, Singular Integral Equation
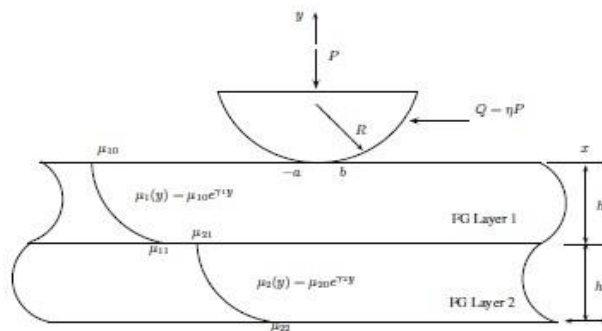
Geometrically nonlinear free vibration of clamped-clamped functionally graded beam with an edge crack

CHAJDI Mohcine [1], MERRIMI El Bekkaye [2], EL BIKRI Khalid [3]

¹Mohammed V University in Rabat. ENSET - Rabat, LaMIPI. Rabat, Morocco,
chajdimohcine@gmail.com
²Mohammed V University in Rabat. ENSET - Rabat, LaMIPI. Rabat, Morocco,
e.merrimi@um5s.net.ma
³Mohammed V University in Rabat. ENSET - Rabat, LaMIPI. Rabat, Morocco,
k.elbikri@um5s.net.ma

The present work concerns a homogenization procedure already studied in [1] developed to reduce the problem of geometrically nonlinear free vibrations of a clamped-clamped beam in functionally graded composite materials (FGM) containing an open crack in the center, to that of the homogeneous isotropic beam. The cracked section is modelled by an elastic spring and the material properties are expected to vary according to an exponential distribution through the thickness estimated by the mixture rule. The semi analytical model used in this approach is based on the theory of Euler-Bernoulli beam and assumptions Von Karman geometric nonlinearity, that is already treated in [2] subsequently reduced by the principle of Hamilton to link the depth of the crack at the fundamental frequency using fracture mechanics theory that has been done in [3]. Direct iterative method is presented for solving the eigenvalue equation for governing the frequency nonlinear vibration and form non-associated linear mode, in order to show the effect of the crack and the volume fraction of the dynamic response of the beam.

[1] *E. Merrimi, K. El bikri, R. Benamar, nonlinear free vibrations of laminated composite beams, An* Effective Formulation", Applied Mechanics and Materials, Vols. 105-107, pp. 1681-1684, Sep. 201

[2] Benamar R. Non-linear dynamic behaviour of fully clamped beams and rectangular isotropic and laminated plates, PhD Thesis, University of Southampton, 1990. p. 35–6.

[3] K.El Bikri, R.Benamar, M.M.Bennouna, Geometrically non-linear free vibrations of clamped– clamped beams with an edge crack. Computers &Structures 84 (2006) 485–502.

Keywords: nonlinear vibration, functionally graded material, beam, crack.

Session: Structure Dominated Biomaterials I

Session Chair: J. C. M. Souza

Date: Monday, September 19th, 2016, Afternoon Session: 14:20-17:05
Room: S 130/ NW III

14:20 – 14:55	**Titania Surface Layer Can Prevent Adhesion of Bacteria to Titanium Implants** Martina Lorenzetti, David Stopar, Saša Novak
14:55 – 15:20	**Functionally Graded Ceramic Implant Materials for Joint Endoprotheses – Experiences and Outlook** Claudia Ortmann, Karen Hans, Thomas Oberbach, Hannes Richter
15:20 – 15:45	**Applications of functionally graded materials in dentistry** Júlio C. M. Souza, Bruno Henriques, Márcio C. Fredel, Rubens M. Nascimento, Filipe S. Silva
15:45 – 16:15	**Coffee break**
16:15 – 16:40	**In-vitro biocompatibility of Ti-implants with compositionally graded coatings** A. Rosin, E. Rieß, M. Willert-Porada
16:40 – 17:05	**FEM and analytical analysis of the bending stress distribution in graded zirconia-based dental ceramics** Bruno Henriques, Douglas Fabris, Júlio C. M. Souza, Joana Mesquita-Guimarães, Yu Zhang, Márcio Fredel, Filipe Silva

Titania Surface Layer Can Prevent Adhesion of Bacteria to Titanium Implants

Martina Lorenzetti[1], David Stopar[2], Saša Novak[1]

[1]*Department of Nanostructured Materials, Jožef Stefan Institute, Ljubljana, Slovenia,*
martina.lorenzetti@ijs.si, sasa.novak@ijs.si
[2]*Biotechnical Faculty, University of Ljubljana, Ljubljana, Slovenia, david.stopar@bf.uni-lj.si*

Despites titanium alloys are considered suitable materials for hard tissue replacement, microbial pre-surgical infections are often the cause for implant failure, with subsequent need for revision surgeries. The demand for improving the cell attachment to the load-bearing orthopaedic implant, rather than the occurrence of bacterial colonization, has been driving the research towards the optimization of the biomaterials surface properties, being the key-point for the success of arthroplasties. Accordingly, several methods have been proposed to improve the implant-tissue interface, such as the fabrication of exterior coatings or layers. Among the possible approaches, hydrothermal treatment (HT) of Ti-based alloys allows the synthesis of fully-dense and stable nanocrystalline anatase-TiO_2 layers.

The adhesion of a green fluorescent protein-tagged bacterium *Escherichia coli* was largely reduced already after 1 h incubation in contact with the HT-substrates, which further decreased in combination of HT method with other surface treatments (i.e. highly reactive oxygen plasma). Such a behaviour depended on the physico-chemical properties of the HT titania layers. Namely, the layers exhibited peculiar topographical, mechanical and electrochemical surface properties, as well as photo-induced physical phenomena [1].

The outcomes suggested that the surface micro-/nano-topography and surface chemistry of the anatase-TiO_2 layers contributed the most in boosting the "race for the surface" in favor of osteogenesis [2] rather than bacterial adhesion [3], followed by a surface charge effect, and, least, wettability.

[1] Lorenzetti M. et al, Mat Sci Eng C, 37 (2014), 390-8

[2] Lorenzetti M. et al, J Biomater Appl, 30 (2015), 71-84

[3] Lorenzetti et al, ACS Appl Mater Interfaces, 7 (2014), 1644–51

Keywords: titania, anatase, layers, implants, bacterial adhesion

Functionally Graded Ceramic Implant Materials for Joint Endoprotheses – Experiences and Outlook

Claudia Ortmann[1], Karen Hans[2], Hannes Richter[3] Thomas Oberbach[4]

[1]Mathys Orthopaedie GmbH, claudia.ortmann@mathysmedical.com
[2]Mathys Orthopaedie GmbH, karen.hans@mathysmedical.com
[3]Fraunhofer Institut IKTS Hermsdorf, hannes.richter@ikts.fraunhofer.de
[4]Mathys Orthopaedie GmbH, thomas.oberbach@mathysmedical.com

Dispersion ceramics made of alumina and YTZP are known for high strength, high fracture toughness and low wear rates. Mathys Orthopaedie GmbH made different efforts to use functionally graded ceramic materials and their extraordinary properties to manufacture save, osseointegrative and innovative implants.

This lecture includes two research works on this area.

A: Alumina hip heads were prepared with YTZP gradient inside the head cone. The resulting graded ZTA (zirconia toughend alumina) material was made by salt infiltration. Fracture strength, infiltration depth, density and amount of zirconia were investigated.

B: ATZ (alumina toughend zirconia) ceramic implants with porous layers have been manufactured. The Aim of work is to generate a porous, osseointegrative and metal-free ceramic implant. Material was made by use of a spray coating method. It was characterized according to morphology, layer thickness, pore structure, roughness and adhesive tensile strength.

ZTA gradient material showed increased fracture strength, high th. density in case of and fine microstructure. Concerning ATZ material, a porous, but adhesive ATZ layer was created.

High efforts are required for the authorization procedure of such medical devices. We are convinced that in future new additive manufacturing technologies help and offer new design opportunities for functionally graded ceramic implant materials.

Keywords: gradient, alumina, Y-TZP, porous, implant

Applications of functionally graded materials in dentistry

Júlio C. M. Souza[1,2], Bruno Henriques[2,3], Márcio C. Fredel[3], Rubens M. Nascimento[4], Filipe S. Silva[2]

[1] CEPID, Department of Dentistry (DODT), Universidade Federal de Santa Catarina (UFSC), Florianópolis/SC, Brazil, jsouza@dem.uminho.pt
[2]Department of Mechanical Engineering (DEM), Campus Azurém, 4800-058, Guimarães, Portugal, fsamuel@dem.uminho.pt
[3] Department of Mechanical Engineering, Universidade Federal de Santa Catarina (UFSC), Florianópolis/SC, Brazil; m.fredel@ufsc.br
[4] Department of Materials Engineering, Universidade Federal do Rio Grande do Norte (UFRN), Natal/RN, Brazil; rmaribondo@ufrnet.br

In Dentistry, several authors have found different configurations based on functionally graded materials (FGM) to avoid failures in prosthetic infrastructures, abutments and implants. The main aim of this study was to describe recent studies of functionally graded materials in dentistry. An electronic Medline search was carried out to obtain the most relevant aspects of functionally graded materials in dentistry. The search items included layered materials based on metal-ceramic, all-ceramic and composite dental materials. Nowadays, many studies involving the FGM concept have been carried out on dental implants based on titanium and ceramic materials to improve bone osseointegration and mechanical behavior as well as in dental restoration interfaces (e.g. interlayers at porcelain fused to infrastructures systems). Such strategies have promoted a gradual transition between dissimilar materials decreasing residual stresses generated during fabrication and mastication, as well as mimicking optical properties of tooth structures.

[1] Y. Zhang. *Journal of the European Ceramic Society.* 32, 2623 (2012).
[2] Mesquita-Guimarães J, Henriques, Souza JCM, Volpato CA, Silva FS, Fredel MC. Functionally graded materials in dentistry. In: *Advances in Materials Science Research*. Nova Science Publishers 2015
[3] B. Henriques, D. Soares, F. S. Silva. *Journal of the Mechanical Behavior of Biomedical Materials.* 4, 1718 (2011)

Keywords: FGM; functionally graded materials;

In-vitro Biocompatibility of Ti Implants with Compositionally Graded Coatings

Andreas Rosin[1], Elke Rieß[2], Monika Willert-Porada[1]

[1]*Chair of Materials Processing, University of Bayreuth, Bayreuth, Germany,*
andreas.rosin@uni-bayreuth.de
[2]*FKI GmbH, Ahorntal, Germany, elke.riess@fki-gmbh.de*

Cementless titanium alloy implants are aiming at improved and long-lasting implant fixation due to combined bone ongrowth and ingrowth into a porous, foam-like metal surface (functional level I). For improved osseointegration on the porous implant surface a nanometer thin bioactive coating is provided, either from TiO_2 or bioactive glass, in order to inhibit biofilm formation and/or promote adhesion of osteoblasts (functional level II). Porous fillings of Ca/Ti phosphates or bioactive glass inside the void shall provide bioresorbable compounds for bone mineralization (functional level III). Above described compositionally graded implant coatings were approached and investigated in the frame of the EU funded project "Multifunctional bioresorbable biocompatible coatings with biofilm inhibition and optimal implant fixation" (Meddelcoat). Sol-gel, electrophoretic deposition, hydrothermal treatment and (microarc) anodization were the mainly used coating techniques. In vitro testing was focused on biofilm formation and cytoreactions like adhesion and proliferation of human osteogenic and endothelial cells, or expression of genetic markers. As a result, TiO_2 coatings were found to be most beneficial for biofilm inhibition, while bioactive glass coatings were beneficial for promoting cytoreactions. However, the porosity of the implant surface generally limits in vitro the adhesion and proliferation of osteogenic cells in comparison to blank surfaces. In vivo tests finally indicated that level II coatings with thin titania layer, and level III coatings of resorbable bioactive glass tend to be most beneficial for bone ingrowth [1-3].

[1] Drnovšek, N., Novak, S., Dragin, U. et al., International Orthopaedics (SICOT), Vol.36 (2012), pp. 1739-1745
[2] Chaudhari A, Braem A, Vleugels J, Martens JA et al., PLoS ONE, Vol. 6 [9] (2011), p. e24186.
[3] Braem, A., Neirinck, B., Van der Biest, O., Vleugels, J., Key Engineering Materials, Vol.654 (2015), pp. 144-148

Keywords: implants, biocompatibility, functionally graded coatings, in vitro, in vivo

FEM and analytical analysis of the bending stress distribution in graded zirconia-based dental ceramics

Bruno Henriques[1,2], Douglas Fabris[1], Júlio C.M. Souza[3], Joana MesquitaGuimarães[1], Yu Zhang[4], Márcio Fredel[1], Filipe Silva[2]

[1]*Ceramic and Composite Materials Research Group (CERMAT), Federal University of Santa Catarina (UFSC), Campus Trindade, Florianópolis/SC, Brazil, brunohenriques@dem.uminho.pt, m.fredel@ufsc.br, douglas.df1@gmail.com, mesquitaguimaraesjoana@gmail.com*
[2]*CMEMS-UMinho, University of Minho, Campus de Azurém, 4800-058 Guimarães, Portugal, fsamuel@dem.uminho.pt*
[3]*CEPID, Department of Dentistry (DODT), Universidade Federal de Santa Catarina (UFSC), Florianópolis/SC, Brazil, julio.c.m.souza@ufsc.br*
[4]*Department of Biomaterials and Biomimetics, New York University College of Dentistry, New York University, New York, USA, yz21@nyu.edu*

This study evaluated the biaxial flexural stresses in graded zirconia-feldspathic porcelain composites. A finite element method and an analytical model were used to simulate the piston-on-ring test and to predict the biaxial stress distributions across the thickness of discs. An axisymmetric model and a flexure formula of Hsueh et al. were used in the FEM and analytical analysis, respectively. Continuous and stepwise transitions (using a power function) from the bottom zirconia layer to the top porcelain layer were studied. The highest tensile stresses were registered for porcelain rich interlayers ($p=0.25$) whereas the zirconia rich ones ($p=8$) yield the lowest tensile stresses. In addition, the maximum stresses in a graded structure can be tailored by altering compositional gradients. A decrease in maximum stresses with increasing values of p (a scaling exponent in the power law function) was observed. Graded zirconia-feldspathic porcelain composites exhibited a more favourable stress distribution relative to conventional bilayered systems. This fact can significantly impact the clinical performance of zirconia-feldspathic porcelain prostheses, namely reducing the fracture incidence of zirconia and the chipping and delamination of porcelain.

Keywords: Biaxial flexural test, stress distribution, functionally graded ceramic, zirconia

Session: Porous and Ordered Structures

Session Chair: V. Sanin

Date: Monday, September 19th, 2016, Afternoon Session: 14:20-17:05
Room: S 135/ NW III

14:20 – 14:55	**Soft Porous Materials for Acoustics** A. Kovalenko, S. Raffy, T. Brunet, J. Leng and Olivier Mondain-Monval
14:55 – 15:20	**Fabrication and Characterization of Functionally Graded CNTs/PMMA Microcellular Foams with Designed Cell Structure** Ruizhi Zhang, Guoqiang Luo, Lianmeng Zhang, Chun Gu, Qiang Shen, Jian Zhang, Meijuan Li, Chuanbin Wang
15:20 – 15:45	**Multifunctional polymer composites and ordered nanostructures of photochromic molecular magnets: synthesis and properties** Nataliya A. Sanina
15:45 – 16:15	**Coffee break**
16:15 – 16:40	**Plastic wave propagation velocity in graded metallic foam materials** M. Borovinšek, F. Schleifer, Z. Ren
16:40 – 17:05	**Low Velocity Impact Performance of Honeycomb Sandwich Structures Reinforced by Functionally Graded Face Plates** Kemal Arslan, Recep Gunes, M. Kemal Apalak, J.N. Reddy

Soft Porous Materials for Acoustics

A. Kovalenko[a], S. Raffy [a, b], T. Brunet [c], J. Leng [b], and O. Mondain-Monval[a,*]

ᵃ University of Bordeaux, Centre de Recherche Paul Pascal CNRS, 33600 Pessac, France

ᵇ University of Bordeaux, Laboratory of the Future CNRS-Solvay, 33600 Pessac, France ᶜ University of Bordeaux, Institut de Mécanique et d'Ingénierie CNRS-INPB, 33400 Talence, France

* Corresponding author: mondain@crpp-bordeaux.cnrs.fr

Using an emulsion templating procedure coupled to microfluidics, we were able to build a new material, which exhibits extraordinary acoustic properties [1-3]. In particular, we show that the material presents a negative refractive index over a wide range of frequencies in the ultrasonic range. I will describe the fabrication of the material and the acoustic measurements that were performed on the samples. Potential applications of the obtained acoustic metamaterials will also be discussed.
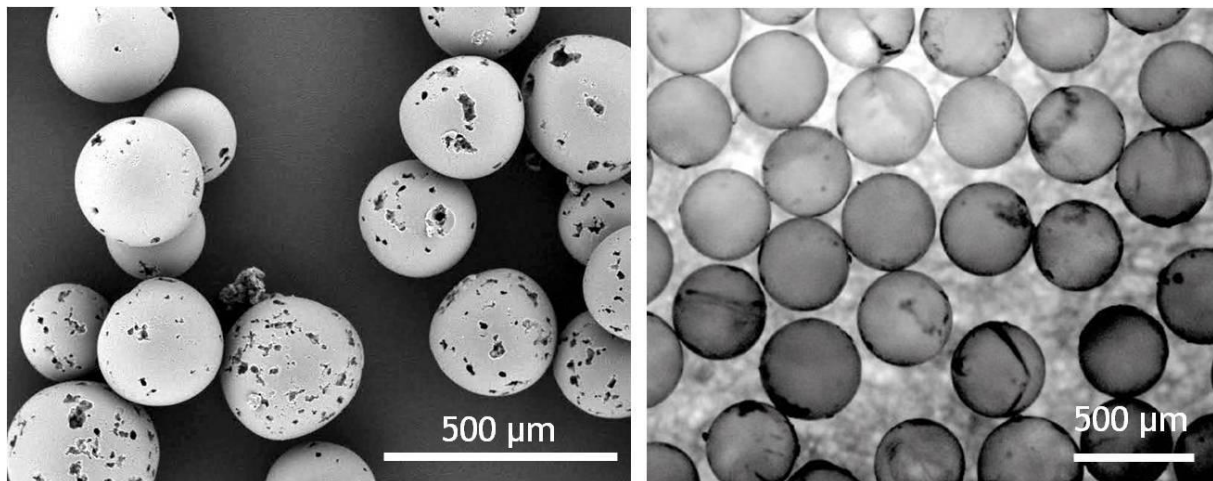
REFERENCES:

[1] T. Brunet, J. Leng and O. Mondain-Monval, *Science* **342**, 323 (2013)

[2] S. Raffy, B. Mascaro, T. Brunet, O. Mondain-Monval and J. Leng, *Adv. Mat*. 28, 1760-1764 (2016)

[3]   T. Brunet, A. Merlin, B. Mascaro, K. Zimny, J. Leng, O. Poncelet, C. Aristégui, and O. Mondain-Monval, *Nat. Mat.* **14**, 384–388(2015)

Fabrication and Characterization of Functionally Graded CNTs/ PMMA Microcellular Foams with Designed Cell Structure

Ruizhi Zhang, Guoqiang Luo, Lianmeng Zhang*, Chun Gu, Qiang Shen, Jian Zhang, Meijuan Li, Chuanbin Wang

State Key Laboratory of Advanced Technology for Materials Synthesis and Processing, Wuhan University of Technology, Wuhan 430070, China

corresponding author, Tel.: +86 186-2706-0013; fax: +86 27 87879468. Email address: luogq@whut.edu.cn

Light weight and high strength graded foams are of great significance to shock resistance in both civil and military fields. In this paper, a facile method was adopted to fabricate functionally graded CNTs/ PMMA microcellular foams with designed cell structure. The various gradient CNTs/ PMMA microcellular materials were hot pressured together, followed by batch foaming with supercritical carbon dioxide as blowing agent in a specialized constrain mold. Mechanical properties of different functionally graded CNTs/ PMMA microcellular foams and the bonding strength between adjacent layers in the functionally graded foams were investigated by the universal mechanical test machine. FESEM were used to visualize the foam morphology and bonding structure. The results show that the uniform microcellular foams exhibit narrow cell distribution and the functionally graded CNTs/ PMMA microcellular foams has a cell diameter ranging from 1μm to 40μm through designing. The strength between adjacent layers of functionally graded CNTs/ PMMA microcellular foams is higher than 10 MPa It is also found that the functionally graded foam is superior in the mechanical properties to the uniform one, and the structure could be optimized to achieve desirable mechanical properties.

Keywords: PMMA, Functionally Graded Foam, Morphology, Mechanical Properties, Bonding Strength

Multifunctional polymer composites and ordered nanostructures of photochromic molecular magnets: synthesis and properties

Nataliya A. Sanina[1]

[1]*Institute of Problems of Chemical Physics, Russian Academy of Sciences, Chernogolovka, 1, Acad. Semenov Av., Moscow region, 142432 Russian Federation, sanina@icp.ac.ru*

One of the key directions in nanotechnology is the organization of nano-objects in the system of interacting elements that are managed by external influences and is compatible with existing element base of electronic-optical devices. Design of the powder nanostructures widespread and brings the certain results, showing that the physical properties of organic and metal-organic materials essentially change as a result of nanostructuring. However actual application of nano-objects of the polyfunctional compounds is possible in case of their organization in an ordered structures. Complexes of 3d metals with photochromic organic cations have a number of advantages in comparison with known compounds displaying photocontrol magnetism: i) the possibility of a light reversible change magnetic moment at room temperature; ii) the change of the magnetic moment under the action of light by a large amount (50-100%); iii) to be convenient objects for nanostructuring and to create nanofilms. The latter can be considered as a technological project of nanochip creation with fotocontrol magnetic elements. In this work homogeneous polymeric composites [1] and ordered arrays of nanowires [2] of photochromic molecular magnets based on the 3d metal (tris)oxalates and photochromic spiropyrans were obtained for the first time. Their photochemical characteristics and magnetic properties were studied.

[1] Sanina N. A., Grachev et. al., Russ.Chem.Bull., 62,(2013) 2, 554-559.
[2] Sanina N.A., Morgunov R.B., Aldoshin S.M., Patent RF No. 2445256 (2012).

Keywords: polyfunctionsl molecular magnets, (tris)oxalates, salts of spiropyrans, nanostructures, X-Ray analysis, SQUID magnetometry.

Plastic wave propagation velocity in graded metallic foam materials

M. Borovinšek[1], F. Schleifer[2], Z. Ren[3]

[1]University of Maribor, Faculty of Mechanical Engineering, Slovenia,
matej.borovinsek@um.si
[2]Universität Bayreuth, f.schleifer@gmx.net
[3]University of Maribor, Faculty of Mechanical Engineering, Slovenia, zoran.ren@um.si

Plastic wave propagation in graded metallic foam materials under compression deformation at different strain rates was studied by means of computational simulations. A homogenized modelling approach was used, where properties of the homogenized material model were experimentally determined for density dependent material parameters of a porous AlSi7 metallic foam [1].

Parametric explicit finite element computer simulations at different loading speeds were carried out to determine the dependence of the plastic wave velocity in samples with different constant porosity from the loading speed. The results indicate that the resulting plastic wave velocity domain can be divided into three separate regions, namely quasi-static, intermediate and highly dynamic deformation behavior. Empirical relations for characteristic loading speeds in materials with different porosity were determined to differentiate between different deformation regions.

These findings were then applied to simulations of foam samples with spatially distributed (graded) porosity. Computationally determined plastic wave velocities in graded metallic foams were compared with the empirical model predictions, where a very good agreement of results was observed.

[1] Avalle M. et al., International Journal of Crashworthiness, 14:3 (2009), 269-285

Keywords: plastic wave propagation, graded metallic foam, computational simulations

Low Velocity Impact Performance of Honeycomb Sandwich Structures Reinforced by Functionally Graded Face Plates

Kemal Arslan[1*], Recep Gunes[2], M. Kemal Apalak[3], J.N. Reddy[4]

[1]Graduate School of Natural and Applied Sciences, Erciyes University, Turkey,
karslan@erciyes.edu.tr
[2]Department of Mechanical Engineering, Erciyes University, Turkey, recepg@erciyes.edu.tr
[3]Department of Mechanical Engineering, Erciyes University, Turkey,
apalakmk@erciyes.edu.tr
[4]Department of Mechanical Engineering, Texas A&M University, USA, jnreddy@tamu.edu

Sandwich structures are a special class of multilayered composite structures and extensively used in aerospace, marine and defense industries where dynamic effects are quite important with their high performance properties – lightweight, high flexural stiffness and high energy absorption capability. Honeycomb sandwich structures are one of the commonly used structure especially where energy is absorbed due to impact loadings. Functionally graded materials also exhibit a good impact performance combining the superior features of ceramic and metal.

Honeycomb sandwich structures reinforced by functionally graded (FG) face plates can be a good proposal for impact applications ranging from low to high velocity impacts. In the first section, low velocity impact performance and energy absorption capability of two different honeycomb sandwich structures are investigated comparatively using explicit finite element code, LS-DYNA®. In design of the sandwich structures, an aluminum honeycomb is used as core material and two different face plates, Al/SiC FG plates and pure Al plates, are used. The through thickness mechanical properties of the FG face plates are considered with respect to a power-law. Mori-Tanaka homogenization scheme is used for determining the locally effective mechanical properties of the FG face plates and TTO (Tamura-Tomota-Ozawa) model is implemented in finite element code in order to simulate the elastoplastic behavior of the FG face plates. In the second section, the influence of the material composition of the FG face plates, the geometrical variables of honeycomb core (cell size and core height) and impact energy on the energy absorption characteristics of the sandwich structure are investigated.

Keywords: Functionally graded materials, Honeycomb sandwich structures, Low velocity impact, Explicit finite element method.

Session: Manufacturing and Properties Assessment of Functionally Graded Materials and Structures II

Session Chair: Y. Watanabe

Date: Tuesday, September 20th, 2016, Morning Session: 11:05-12:45
Room: S 130/ NW III

11:05 – 11:30	**Stereolithographic Additive Manufacturing of Geometric Micro Patterns in Bulky Metal and Ceramic Components** Soshu Kirihra
11:30 – 11:55	**Challenge for Additive Manufacturing of Functionally Graded Materials Parts** Jean-Yves Hascoët, Matthieu Rauch
11:55 – 12:20	**Microstructure and Wear Property of Al-Al$_3$Ti FGMs Fabricated by Centrifugal Solid-Particle and *in-situ* Methods** Yoshimi Watanabe, Qi Zhou, Hisashi Sato
12:20 – 12:45	**Hierarchical Structured Intermetallic Alloys Produced by Centrifugal SHS-Casting Technology** V.N. Sanin, D.M. Ikornikov, D.E. Andreev, V.I. Yukhvid, E.A. Levashov, Zh.A. Sentyurina, A.A. Zaitsev, Yu.S. Pogozhev
12:45 – 13:45	**Lunch and Industrial Exhibition**

Stereolithographic Additive Manufacturing of Geometric Micro Patterns in Bulky Metal and Ceramic Components

Soshu Kirihra

Osaka University, kirihara@jwri.osaka-u.ac.jp

Metal and ceramic bulky components including dendritic networks were geometrically built by using stereolithographic additive manufacturing (AM). Geometric patterns with periodic, self-similar, graded and fluctuated arrangements were created by computer aided design, manufacture and evaluation (CAD/CAM/CAE) for effective modulations of energy and material flows through dielectric lattices in photonic crystals, porous electrodes in fuel cells and biological scaffolds in artificial bones. Two dimensional (2D) cross sectional patterns were created through photo polymerization by ultra violet laser drawing on spread resin paste including ceramic nanoparticles, and three dimensional (3D) composite models were sterically printed by layer lamination through chemical bonding. An automatic collimeter was equipped with the laser scanner to adjust beam diameter. Fine or coarse beams could realize high resolution or wide area drawings, respectively. As row material of the stereolithographic AM, fine metal and ceramic particles were dispersed in to photo sensitive liquid resins from 40 to 60 % in volume fraction. The resin paste was spread on a glass substrate at 10 μm in layer thickness by a mechanically moved knife edge. An ultraviolet laser beam of 355 nm in wavelength was adjusted from 10 to 300 μm in variable diameter and scanned on the pasted resin surface. Irradiation power was changed automatically from 10 to 200 mW for enough solidification depth for 2D layer bonding. The created 3D composite precursor was dewaxed and sintered in an air atmosphere to obtain full metal and ceramic components. Alumina and copper photonic crystals to control electromagnetic waves, yttria stabilized zirconia electrodes for solid oxide fuel cell, lithium intermetalics patterns for solid electrolytes and calcium phosphate and titanium alloy scaffolds for artificial bones were created successfully.

Challenge for Additive Manufacturing of Functionnally Graded Materials Parts

Pr. Jean-Yves Hascoët, Dr. Matthieu Rauch

Ecole Centrale de Nantes - France

jean-yves.hascoet@ec-nantes.fr; matthieu.rauch@ec-nantes.fr

Functionally Graded Materials (FGM) parts are heterogeneous objects with material composition and microstructure that change gradually into the parts. The distinctive feature of FGM structure gives the possibility of selecting the distribution of mechanical, physical, chemical properties to meet the functional requirements. Additive manufacturing processes, in particular Direct Energy Deposition (DED) processes are well dedicated to manufacture complex FGM parts. Customized homogeneous parts are manufactured from digital data, but the manufacturing of heterogeneous parts is limited to samples: most of the FGM parts are not functional, with simple morphology and simple material distribution and functional AM parts are very often made with one material. To move from these samples to functional parts a methodology with a global approach is necessary. The presentation focuses on various challenges covered by this approach to move from the concept imagined by a designer to the manufacturing of the part.

The first aspect focuses on the numerical definition of the part in the CAD/CAM/process data chain. Most of the current CAD description formats do not support multimaterial attributes for a single part. It is consequently hardly possible to define accurately material distributions and properties by using FEM simulations or topological optimizations algorithms. In contrast, high level CAD/CAM/CNC approaches such as STEP-NC can be highly valuable to overtake these limitations. Their interest is the first issue discussed in the presentation.

The second issue focuses on DED process modelling to determine the appropriate parameterization and manufacturing strategy. It is essential to identify the actual behavior of the process implemented, for example, the evolutions of the material compositions changes when switching from one ratio to another. The resulting model is a key element to prepare the manufacturing strategy. Indeed, for FGM parts the control of the material composition at any point of the part is as important as the part geometry. In addition, this process model can be useful to perform DFAM operations on the part to manufacture.

The last focus of this presentation concerns DED process toolpaths generation for FGM parts. By using the process model developed, the evaluation of manufacturing strategies and a process control to reduce the difference between the desired material distribution and the material distribution in the manufactured part is enabled. New kind of path strategies can be proposed and tested off line on a process simulator. As a result, complex parts can be produced with the desired geometries and the desired material distributions.

Keywords: Functionally Graded Materials (FGM) parts, additive manufacturing, process modelling, process optimization, tool paths.

Microstructure and Wear Property of Al-Al$_3$Ti FGMs Fabricated by Centrifugal Solid-Particle and *in-situ* Methods

Yoshimi Watanabe[1], Qi Zhou[2], Hisashi Sato[3]

[1]*Nagoya Institute of Technology, yoshimi@nitech.ac.jp*
[2]*Nagoya Institute of Technology, damonzqzq@yahoo.co.jp*
[3]*Nagoya Institute of Technology, sato.hisashi@nitech.ac.jp*

Fabrication of FGMs by centrifugal method can be classified into two categories by the relationship between the process temperature and the liquidus temperature of the master alloy [1]. One is the centrifugal solid-particle method if the process temperature is lower than the melting point of the master alloy. The other one is the centrifugal *in-situ* method if the process temperature is higher than the melting point of it. In previous study [2], it has been found that microstructure of Al-Al$_3$Ti FGMs fabricated by the centrifugal solid-particle method cast at 800°C was different from that by centrifugal *in-situ* method cast at 1600°C. However, the microstructures of Al-Al$_3$Ti FGMs fabricated by the centrifugal *in-situ* method cast at a temperature around the liquidus temperature (1100°C for Al -11vol% Al$_3$Ti alloy) is not studied. In this study, the microstructures of Al-Al$_3$Ti FGMs fabricated at 1000°C (centrifugal solid-particle method) and 1200°C (centrifugal *in-situ* method) were investigated. In addition, wear properties of the fabricated Al-Al$_3$Ti FGMs were also studied.

[1] Y. Watanabe, I. S. Kim and Y. Fukui, Metals and Materials International, 11 (2005), 391-399.
[2] S. H. El-Hadad, H. Sato, P. D. Sequeira, Y. Watanabe and Y. Oya-Seimiya, Materials Science Forum, 631632 (2010), 373-378.

Keywords: centrifugal force, cast, microstructure, hardness, wear

Hierarchical Structured Intermetallic Alloys Produced by Centrifugal SHS - Casting Technology

V.N. Sanin[1], D.M. Ikornikov[1], D.E. Andreev[1], V.I. Yukhvid[1],
E.A. Levashov[2], Zh.A. Sentyurina[2], A.A. Zaitsev[2], Yu.S. Pogozhev[2]

[1]*Institute of Structural Macrokinetics and Materials Science, Russian Academy of Sciences, Chernogolovka, Moscow, 142432 Russia. Email: svn@ism.ac.ru*
[2]*National University of Science and Technology MISiS, Leninskii pr. 4, Moscow, 119049 Russia*

A cost-effective SHS process (combustion synthesis) for fabricating cast intermetallic Ni-AlCr-Co-Hf alloy as an electrode material for centrifugal sputtering of powders for additive technology was demonstrated on the first part of work. The SHS reactions yielding the cast intermetallic alloy [1] can be represented by the following scheme: $(MeO)_1 + (MeO)_2 + (MeO)_3 + (MeO)_i + Al + (FA) \square [Cast Alloy] + Al_2O_3 + Q$, where $(MeO) - NiO, Cr_2O_3, Co_3O_4$, etc.; Al-metal reducer, FA is an functional additive facilitating phase segregation, and Q - the heat evolution. SHS-casting parameters has been optimized in wide range of centrifugal acceleration a = 10–400 g. Optimization criteria were (a) to improve the phase separation, (b) to remove gaseous byproducts, (c) to diminish the grain size of the final product, and (d) to make intermetallic product more uniform. Cr-based nano- and micro- sized precipitations controlled mechanical behavior of high strength NiAl alloy were investigated by SEM, TEM, indentation methods. Electrodes and powders based on NiAl were produced and studied.

The second part was devoted to searching the reactive systems and process parameters that would be favorable for: (i) SHS surfacing of the cast alloys onto Fe and Ti substrates, (ii) formation of graded structure cast alloys through the centrifugal assistant infiltration of the melt in-situ SHS [2]. The optimal experimental parameters were verified experimentally. The phase composition and microstructure of synthesized FGMs were investigated. Graded materials obtained are promising candidates for implementation in marine and aerospace engineering, gas/oil transportation, structural engineering materials, etc.

[1] V. N. Sanin and others. *Russian Journal of Non-Ferrous Metals*, Vol. 55, No. 6 (2014), pp. 613-619.
[2] V.N. Sanin and others. *International Journal of SHS*. Vol. 11, Number 1 (2002), pp. 31-44.

Session: Testing of Functionally Graded Structures and Materials
Session Chair: C. Körner

Date: Tuesday, September 20th, 2016, Morning Session: 11:05-12:45
Room: S 135/ NW III

11:05 – 11:30	**Microstructural Characterization of Mg/Al Diffusion Bonded Joint Using Al-Ni Interlayer** Jian Zhang, Guoqiang Luo, Qiang Shen, Lianmeng Zhang
11:30 – 11:55	**Hot corrosion behavior of 8Y-ZrO_2/$ZrSiO_4$ ceramic sealed by Laser-assisted Microwave Plasma Processing** Christian Richter, Monika Willert-Porada
11:55 – 12:20	**Measurement of Young's Modulus at Elevated Temperatures of Thermal Barrier Coating by Bending Resonance Method** Satoru Takahashi, Kazuki Ookubo, Hiroyuki Waki, Masahiko Kato, Syusui Ogawa, Fumio Ono
12:20 – 12:45	**Development of measurement system of thermoelectric properties of thin films in the thickness direction** Yoshikazu Shinohara, Hiroshi Kawakami, Yukihiro Isoda
12:45 – 13:45	**Lunch and Industrial Exhibition**

Microstructural Characterization of the Mg/Al Diffusion Bonded Joint Using Al-Ni Interlayer

Jian Zhang[1,a] [*], Guoqiang Luo[1,b], Ruxia Liu[1,c], Mei Rao[1], Qiang Shen[1], Lianmeng Zhang[1]

[1]*State Key Lab of Advanced Technology for Materials Synthesis and Processing, Wuhan University of Technology, Wuhan 430070, China*
E-mail: [a]isaiah178@hotmail.com, [b]luogq@whut.edu.cn, [c]mignonliu1@163.com

Dissimilar welding of Mg and Al would achieve weight reduction and high efficiency of production by substitution of Mg and Al for steels. In this investigation, a vacuum hot-pressed diffusion method was used to prepare an Mg/Al layer composite using an Al thin film and Ni foil interlayers. The interfaces microstructure and shear strength of the joints were investigated by means of SEM, XRD and universal machine. The results showed that the joints were bonded well and the Mg-Al intermetallic compounds were impeded. Al thin film and Ni foil successfully strengthened the weak interface of Mg/Al welding joint. With the increasing of the holding time, the shear strength of the joints increases firstly and then decreases. The fracture took place somewhere at the interface of the Al-Ni.

Keywords: Mg/Al; diffusion bonding; holding time; shear strength

Hot corrosion behavior of 8Y-ZrO$_2$/ZrSiO$_4$ ceramic sealed by Laserassisted Microwave Plasma Processing

Christian Richter [1], Monika Willert-Porada[2]

[1] Christian.Richter@uni-bayreuth.de
[2]Monika.Willert-Porada@uni-bayreuth.de

Due to the low thermal conductivity and enhanced thermal shock resistance, ZrO$_2$-ZrSiO$_4$/NiCr functionally graded materials are promising candidates for thermal barrier application. In comparison to direct coating of TBC on metal substrates, e.g. by plasma spraying, a compositional gradient reduce thermal stresses, which are caused by CTE mismatch at the interface. Nevertheless, for usage in gas turbines, to improve combustion efficiency, the fulfillment of adequate corrosion resistance is necessary.

In this study, the ceramic phase of such a metal-ceramic FGM, sintered porous 8Y-ZrO$_2$ ceramic and composite ceramics consisting of 8Y-ZrO$_2$ and ZrSiO$_4$, were selected as a model system and were surface sealed by a new process, called Laser Assisted Microwave Plasma Processing (LAMPP). Hot corrosion tests with molten V$_2$O$_5$, Vanadium Pentoxide, which are used to characterize hot-corrosion resistance of Thermal Barrier Coatings, were employed to proof the quality of surface sealing. The reactions taking place upon LAMPP and formation of a compositional and porosity gradient due to melting and rapid solidification of the ceramic phases are discussed.

Keywords: hot corrosion, Laser-Microwave process, thermal barrier,

Measurement of Young's Modulus at Elevated Temperatures of Thermal Barrier Coating by Bending Resonance Method

Satoru Takahashi[1], Kazuki Ookubo[2], Hiroyuki Waki[3], Masahiko Kato[4], Syusui Ogawa[5], Fumio Ono[6]

[1]Tokyo Metropolitan University, takahashi-satoru@tmu.ac.jp
[2]Tokyo Metropolitan University, ookubo-kazuki@ed.tmu.ac.jp
[3]Iwate University, waki@iwate-u.ac.jp
[4]Hiroshima University, mkato@hiroshima-u.ac.jp
[5]Japan Fine Ceramics Center, syusui@jfcc.or.jp
[6]Osaka Science & Technology Center, f.ono@ostec.or.jp

Thermal barrier coatings (TBCs) are the indispensable technology for hot-section components of an advanced industrial gas turbine. A TBC consists of a metallic bond-coat (BC) and a ceramic top-coat (TC) on a superalloy substrate. The reliable values of various properties on the coatings have been required to design the superior TBC. Especially, the Young's moduli of the BC and the TC are important mechanical properties to evaluate mechanical and thermal stresses. Waki et al. derived a closed-form solution for the Young's modulus of the TC layer using the equation of motion for the bending vibration of a composite beam and experimentally confirmed the effectiveness of this method at room temperature [1]. In this study, the Young's modulus at elevated temperatures of TBC was measured using the developed resonance method.

Several kinds of TBC specimens were produced by plasma sprayings. The schematic illustration of the resonance device is shown in Fig.1. A TBC specimen was suspended using alumina fibers in an electric furnace. The resonance frequency was measured at from room temperature to 900 ℃ and the Young's modulus was determined using the developed resonance method. It was found that the reliable Young's moduli of the TC and the BC can be obtained even at elevated temperatures.
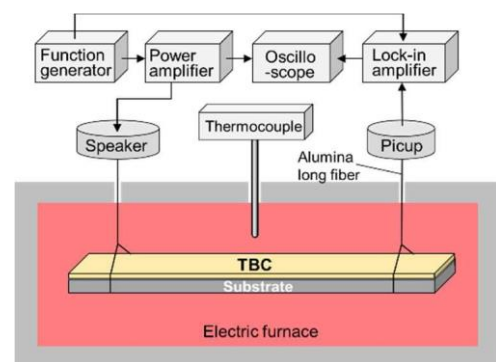
Resonance

[1] H. Waki, K. Takizawa, M. Kato, S. Takahashi, *J. Therm. Spray Technol*., 25(4) (2016), 685-693

Keywords: Thermal Barrier Coating (TBC), Young's Modulus, Resonance, Composite Beam, Thermal Spray

Development of measurement system of thermoelectric properties of thin films in the thickness direction

Yoshikazu SHINOHARA[1*], Hiroshi KAWAKAMI[2], Yukihiro ISODA[1]

[1]National Institute for Materials Science (NIMS), Japan
[2]New Energy and Industrial Technology Development Organization (NEDO), Japan
[*]E-mail address: SHINOHARA.Yoshikazu@nims.go.jp

Thermoelectric materials can generate electrical power directly from heat without any vibration. That is why thermoelectric power generation is promising as an isolated compact power source such as automobile generators, solar heat generator. We have already clarified that the segmented thermoelectric legs of generators, which is based on a FGM concept, are effective to improve the generated power using bulk Pb-Te materials. Recently thin film thermoelectric generators are paid more attention to as energy harvesting applications. However, how to measure the thermoelectric properties of thin films in the thickness direction quantitatively is not determined. In the present study, some electrode structures were tried for in the thickness direction and the measurement system has been developed.

[1] Y.Shinohara, Y.Imai, Y.Isoda, I.A.Nishida, H.T.Kaibe, I.Shiota, Proc. International Conference on thermoelectrics (1997), pp.386-389

Keywords: measurement, thermoelectric properties, thin film

Session: Functionally Graded Amorphous and Semi-Crystalline Materials

Session Chair: A. R. Boccaccini

Date: Tuesday, September 20th, 2016, Afternoon Session: 14:35-16:25

Room: S 130/ NW III

14:35 – 15:10	**Gradient-Index Micro-Optics by Ion Exchange in Glass and its Applications to Optical Metrology and Biophotonic Imaging** Bernhard Messerschmidt, Sandra Gerlach
15:10 – 15:35	**Confocal chromatic sensor systems based on gradient index optics** Alexander Streicher
15:35 – 16:00	**Compositionally graded glass by microwave field assisted ion exchange** T. Gerdes, A. Schmid-Rodenkirchen, H.S. Park, B. Scharfe, M. Willert-Porada
16:00 – 16:25	**Glassceramics with graded photocatalytic activity** D. Leykam, A.Rosin, T. Gerdes, M. Willert-Porada
16:25 – 16:45	**Coffee break and Poster presentations**

Gradient-Index Micro-Optics by Ion Exchange in Glass and its Applications to Optical Metrology and Biophotonic Imaging

Sandra Gerlach[1], Bernhard Messerschmidt[1]

[1]*GRINTECH GmbH, gerlach@grintech.de*

Gradient-index micro-optics in glass with planar optical surfaces enables the miniaturization and integration of optical systems with a complex function. The lens performance of GRIN lenses is achieved by specific refractive index profiles in glass rods and slabs, which are produced by Silver, Sodium and Lithium ion exchange in appropriate glasses. Curved surfaces of conventional lenses are replaced by plane surfaces of GRIN lenses, which makes the fabrication of individual lenses with diameters down to 200 µm and less possible. The talk will introduce gradient index optics and its optical design aspects and presents the potentials and current limitations of the ion exchange technology in glass, as well as applications in optical sensing and biophotonic imaging.

Keywords: GRIN lens, ion exchange, micro-optics

Confocal chromatic sensor systems based on gradient-index optics

Alexander Streicher[1]

[1]Micro-Epsilon Messtechnik GmbH & Co. KG, Ortenburg, Germany,
alexander.streicher@micro-epsilon.de

Micro-Epsilon is known for high precision measurement technology and solutions. The sensor specialist has continuously set milestones especially in the confocal chromatic measurement technology for years.

Sensor systems based on the confocal chromatic measurement principle provide extremely high accuracy as well as axial and radial resolution using true non-contact technology. Due to these advantages, confocal chromatic sensors are frequently used in challenging applications in the manufacturing industry, quality control and for research purposes. The multi-lens optical pen which disperses the polychromatic light of the controller into a focused, monochromatic light by controlled chromatic aberration is a key element of the measurement system. In addition to the high precision standard sensors made of discrete optical elements, we also use gradient-index technology for confocal probes.

Gradient-index (GRIN) lenses enable to miniaturize the size of the multi-lens system to extremely small sensor probes with a diameter of 3.3 mm. Due to the small dimension of the GRIN probe, new applications such as inline inspection of small boreholes or movement and distance measurement in small cavities, especially in vacuum chambers can be solved.

Keywords: confocal chromatic, Gradient-index lens, distance measurement, borehole inspection, Micro-Epsilon

Compositionally graded glass by microwave field assisted ion exchange

T. Gerdes[1,2], A. Schmidt-Rodenkirchen[1], H.S. Park[2], B. Scharfe[3], M. Willert-Porada[1,2]

[1]InVerTec eV, Bayreuth, Germany
[2]Chair of Materials Processing, University of Bayreuth, Bayreuth, Germany
[3]Technologie-Anwenderzentrum Spiegelau, Spiegelau, Germany

Distribution of electrical field gradients developing upon microwave heating glass parts immersed in an alkaline salt melt is analyzed by simulation. It is assumed that such gradients influence the process of ion exchange between the molten salt and the silicate glass immersed in it. It is shown that strong E-field gradients exist between the melt and the solid glass which could enhance ion transport due to an electro-migration effect superimposing the concentration gradient. In addition, interaction of the solid glass with microwave radiation could facilitate stress relaxation in the glass, which upon thermally induced ion exchange is retarding diffusion of alkali ions.

A special microwave applicator has been developed which enables equilibration of inhomogeneous electromagnetic field distribution by mechanical movement of the samples subjected to ion exchange in order to analyze the overall effect of electromagnetic filed influence on ion exchange phenoemena.

Keywords: Compositional gradient in glass Field asisted ion exchange

Glass ceramics with graded photocatalytic activity

D. Leykam[1*], A. Rosin[1], T. Gerdes[1], M. Willert-Porada[1]

[1]*Chair of Materials Processing, University of Bayreuth, Germany, *daniel.leykam@uni-bayreuth.de*

Photocatalytic treatment of waste water suffers from adequate exposition of the photocatalyst to both (sun) light and the aqueous phase. A common approach is a coating of photo-catalytic active particles like titania on carrier materials to enable a durable catalytic activity.

However the interaction of the coating with the wastewater leads to gradual abrasion of the photocatalyst and a limited life time. A solution to overcome this drawback is a titania based glass ceramic where the photo active phase is dispersed in the volume of the carrier material.

Glasses in the system SiO_2-TiO_2-B_2O_3-MgO-CaO-Na_2O-Al_2O_3 with varying amounts of Na_2O, Al_2O_3, B_2O_3, and TiO_2 were investigated and amorphous phases with a TiO_2 amount of up to 28 wt.-% were produced. The glass was transferred to a glass ceramic via a two-step heat treatment, resulting in crystalline titania phases dispersed in an amorphous matrix. By hydrochloric acid leaching a porous glass ceramic with a specific surface of around 200m²/g was obtained.

The photocatalytic activity of those porous structures are increased 80 times compared to the dense material. The optical bandgaps of the titania is between 3.0 and 3.17 eV.

Within the paper the preparation process as well as the photocatalytic activity measured via degradation of methylene blue will be discussed.

Keywords: Photo catalysis, glass ceramics, water purification

Session: Modelling of Functionally Graded Materials and Structures II

Session Chair: C. Santangelo

Date: Tuesday, September 20th, 2016, Afternoon Session: 14:35-16:25
Room: S 135/ NW III

14:35-15:10	**FGM Thermal Barrier Coatings Under Hot Burner Testing** Michael Gasik, Akira Kawasaki
15:10-15:35	**Stress wave propagation in a functionally graded cylinder** M. Kemal Apalak, Mehmet Dorduncu
15:35-16:00	**Nonlinear Dynamic of Imperfect FGM Shallow Shell with Time Dependent Parameters in Temperature Field** Fatieieva Yu
16:00-16:25	**Elastoplastic analysis of axially loaded FGM box section column** S. Burzyński, J. Chróścielewski, K. Daszkiewicz, W. Witkowski
16:25-16:45	**Coffee break and Poster presentations**

FGM THERMAL BARRIER COATINGS UNDER HOT BURNER TESTING

Michael Gasik[1], Akira Kawasaki[2]

[1] Aalto University Foundation, Finland; michael.gasik@aalto.fi
[2] Tohoku University, Graduate School of Engineering, Japan;
kawasaki@material.tohoku.ac.jp

For thermal barrier coatings (TBC) thermal-mechanical fatigue due to temperature cycling is one of the critical parameters; which determines their lifetime. For improved TBC designs and increasing performance demands it becomes more important to critically evaluate the performance of different TBC under accelerating tests. A method known as "hot burner test" (JIS H7851) is being used to compare different types of coatings [1]. When FGM TBC is applied, its better thermal and mechanical performances might not be evident form the tests parameters, unless latter are optimized to reflect the proper operational conditions [2]. In this work extended FEM analysis of the heat flux, temperature, stresses and strains inside FGM coating has been performed. FGM TBC with different gradation profiles were compared with homogeneous (duplex) coating. With a multi-objective optimization method, the optimal gradation profile was found. The opportunities of the extrapolation of the test results onto real applications for FGM TBC are discussed.

[1] Gasik M., Kawasaki A., Kang Y.S. Mater. Sci. Forum, 492-493 (2005), 9-14. [2] Gasik M., Kawasaki A. Mater. Sci. Forum, 631-632 (2010), 79-84.

Keywords: thermal barriercoatings; thermal cycle; stress; testing; modelling

Stress wave propagation in a functionally graded cylinder

M. Kemal Apalak[1], Mehmet Dorduncu[2]

[1]*Department of Mechanical Engineering, Erciyes University, Kayseri 38039, Turkey, apalakmk@erciyes.edu.tr*
[2]*Department of Aerospace and Mechanical Engineering, The University of Arizona, Tucson, AZ 85721, USA, dorduncu@email.arizona.edu*

This study covers a simple analysis for wave propagation in a functionally graded circular cylinder subjected to an impulsive loading. The cylinder material composition was assumed to vary through the thickness direction with a power-law distribution in terms of volume fractions of the constituents: metal (Ni) and ceramic (Al2O3). The Mori-Tanaka homogenization scheme was implemented to the estimation of the through-thickness material properties of the functionally graded circular cylinder. The governing equations of the wave propagation in the functionally graded circular cylinder were simply discretized by using the finite difference method. von Neumann stability approach was applied for the stability of the numerical solution. The results show that the material composition variation had evident effects on wave propagation through the functionally graded circular cylinder. In particular, the spatial derivatives of the mechanical properties of the local material composition were included in the governing equations of motion and their effects on the wave propagation were analyzed. The amplitudes of the temporal variations of the displacement and stress components exhibited differences in case the spatial coordinates are considered.

Keywords: Functionally graded materials; stress wave propagation; finite difference method

Nonlinear Dynamic of Imperfect FGM Shallow Shell with Time Dependent Parameters in Temperature Field

Fatieieva Yu

Department of Applied Mathematics and Mechanics, Zaporizhzhe National University
Zhukovskogo str., 66, Zaporizhzhe, 69063, Ukraine, fateevajulia@gmail.com

Thin walled structures made of functionally graded materials (FGM) with metal inner surface and ceramic in outer surface are widely used, for example, in modern air-space systems, engeenering applications, medicine and others. Nonlinear vibration of imperfect thin shallow shell made of functionally graded materials (FGM) under external forces and temperature loading are investigated. The shell material consists of two layers - metal and ceramic. The properties of structure are changing in the thickness direction according to the power low distribution in terms of volume fraction of material and initial conditions. The non-linear strain-displacement relationships based upon the von Karman theory for moderately large normal deflections. The problem leads to necessity integration of nonlinear non-homogeneous singular differential equation with variable in time parameters. Three steps hybrid asymptotic approach, which consist of perturbation (for nonlinear problem), phase integral and Galerkin methods are used to find an approximate analytical solution of the problem. Comparison of approximate analytical solution and direct numerical integration of initial equation of the problem for some structure characteristics and asymptotic parameters values are given. For some parameters of structure an analytical solutions are in a good enough correlations with direct numerical solutions of initial singular nonlinear differential equations with variable coefficients. In some cases one-term WKB-approximation gives good results for the practical purpose.

[1]   Dao Huy Bich; Yu Do Long: Nonlinear Dynamical Analysis of Imperfect Functionally Graded Materials Shallow Shells. *Vietnam Journal og Mechanics*, *VAST*, 32, 1 (2010), 1-14.
[2]   Vu Thi Thuy Anh; Nguyen Dinh Duc: Nonlinear Axisymmetric Response of Thin FGM Shallow Spherical Shells with Ceramic-Metal-Ceramic Layers under External Pressure and Temperature. *VNU Journal of Mathematics – physics*, 29, 2 (2013), 1-15.

Keywords: Functionally graded material, Imperfect shellow shell, Approximate analytical solution, Time dependent thickness.

Elastoplastic analysis of axially loaded FGM box section column

S. Burzyński[1], J. Chróścielewski[2], K. Daszkiewicz[3], W. Witkowski[4]

Gdańsk University of Technology, Department of Mechanics of Materials, 80-233 Gdańsk, G. Narutowicza 11/12, Poland, [1]staburzy@pg.gda.pl, [2]jchrost@pg.gda.pl, [3]kardaszk@pg.gda.pl, [4]wojwit@pg.gda.pl

The purpose of the research is determination of nonlinear response and load capacity of axially loaded box section column made of functionally graded material (FGM). The elastoplastic constitutive equations were formulated in the framework of 6-parameter shell theory. The application of this theory to shell problems with orthogonal intersections gives accurate results. The ceramic-metallic TiB/Ti FGM section with material parameters from work [1] was used in computations. We assumed the elastoplastic material model for titanium and elastic model for ceramic constituent. The influence of FGM parameters, micropolar material constants and method of through the thickness integration of the constitutive equations was investigated. For instance, the influence of the power law exponent k on nonlinear equilibrium curves is presented in figure. The results from author's FEM code were compared with results from Abaqus code. We demonstrated that stability of postbuckling equilibrium path depends on value of the power law exponent. Moreover, calculation of critical buckling force and postbuckling path allow for safe design of FGM structures.
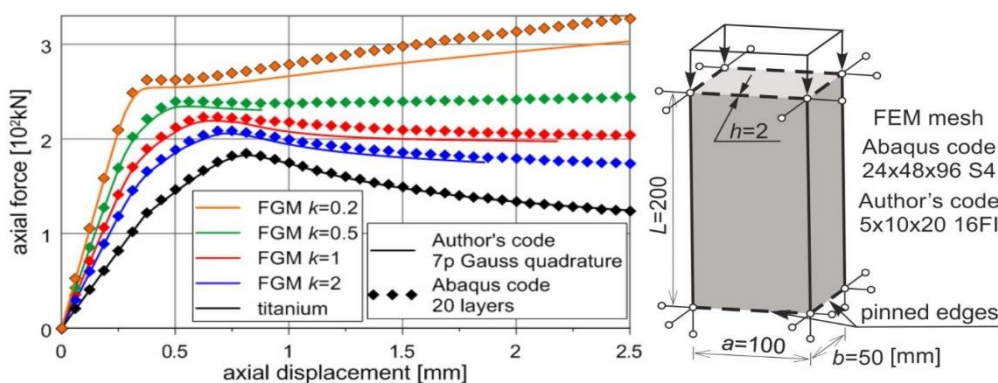
[1] Jin ZH, Paulino GH, Dodds RH, Cohesive fracture modeling of elastic–plastic crack growth in functionally graded materials, Engineering Fracture Mechanics 70 (2003) 1885–1912.

Keywords: FGM, elastoplastic analysis, box section, postbuckling,

ISFGMs 2016

Session: Manufacturing and Properties Assessment of Functionally Graded Materials and Structures III

Session Chair: L.A. Rocha

Date: Wednesday, September 21st, 2016, Morning Session: 10:15-12:20
Room: S 130/ NW III

10:15 – 10:40	**Research on FGM for Nuclear Applications** Chang-Chun GE, Xiaona Ren, Qing-Zhi YAN, Ying-Chun ZHANG, Zhang-Jian ZHOU, Min XIA
10:40 – 11:05	**Experimental Investigation of Microstructural and Micromechanical Properties of Fe/B$_4$C-Fe/B Functionally Graded Materials** Mustafa Hamamci, Fehmi Nair, A. Alper Cerit
11:05 – 11:30	**Friction and Wear Characteristics of MoS$_2$/Cu-Sn Composite Film** Hitoshi Kohri, Takayoshi Yagasaki
11:30 – 11:55	**Functionally Graded Cu ZnS Phosphor and its Applications** Jehong Park, Seungchan Cho, Akira Kawasaki, Kwangjae Park, Kwonhoo Kim, Hansang Kwon
11:55 – 12:20	**Electrospark Deposited FGMs Coatings with Enhanced Characteristics** E. Levashov, E. Zamulaeva, N. Litovchenko, A. Potanin, D. Shtansky
12:20 – 13:30	**Lunch**

Research on FGM for Nuclear Applications

Chang-Chun GE, Xiaona REN, Qing-Zhi YAN, Ying-Chun ZHANG, Zhang-Jian ZHOU, Min XIA

Institute of Nuclear Materials (INM)

University of Science and Technology Beijing (USTB), Beijing, China

This presentation highlights the research on bulk and coating FGM, both for nuclear fusion reactors and advanced fission reactors in INM, USTB.

Three kinds of bulk FGM, including W/Cu, B4C/Cu and SiC/Cu with discontinuous composition distribution have been developed and fabricated with self-innovative technology named sintering through direct electric current under ultra-high pressure. While W/Cu FGM with continuous graded composition distribution can also be made with molten Cu infiltration through sintered gradient porous skeleton.

Four kinds of coating technology for making coating composites including coating FGMs are developing in INM, USTB: (1) plasma spraying with spherical powders for making continuous B4C /Cu coating FGMs and W/Cu coating FGMs; (2) Cold spraying for making W-based graded coatings on Cu substrates; (3) Chemical vapor deposition of W-coatings on Cu substrates with $W(CO)_6$ as precursor; (4) Na_2WO_4–WO_3 molten salt electro-deposition on complex shapes of different matrix including Cu(CuCrZr, Al_2O_3-DSCu), Low activation steels, V alloys, graphite has been developed. Uniform diffusion W graded coatings with high thickness, strong interface strength, low oxygen content on different matrix have been successfully obtained.

Experimental Investigation of Microstructural and Micromechanical Properties of Fe/B$_4$C-Fe/B Functionally Graded Materials

Mustafa Hamamci[1], Fehmi Nair[2], A. Alper Cerit[3]

[1,2]Composite Research Laboratory, Department of Mechanical Engineering, Erciyes University, Kayseri, Turkey

[3]Department of Industrial Design Engineering, Erciyes University, Kayseri, Turkey
[1]mhamamci@erciyes.edu.tr , [2]fnair@erciyes.edu.tr, [3]acerit@erciyes.edu.tr

In the present work, microstructure and micromechanical properties of the functionally graded Fe/B$_4$C-Fe/B materials (FGMs), fabricated by powder metallurgy, were investigated experimentally. Samples were manufactured at different number of layers (10 and 20) which graded from ceramic dense layer, volume fraction of $V_{c\ max}$ as 0,7 and 0,9 to pure iron layer with a constant compositional gradient (n=1) and uniaxially compacted at 450°C under 600 MPa pressure in a cylindrical hot work tool steel die. In order to better understand the relationship between processing, structure and mechanical properties of the samples, pressureless sintering was conducted at 1000 and 1150°C for 60, 90 and 120 minutes under argon atmosphere. Microstructural evaluations were done by optical microscopy, scanning electron microscopy (SEM) and energy dispersive X-ray (EDX) analysis. Microhardness measurements were done with a Vickers indenter under 100 gr load to get information of their mechanical behaviours. The relative density and porosity of samples were determined by Archimedes principle. The correlation between microstructure and mechanical properties was examined. Each layer demonstrated good adhesion without seperation or serious microcracks.

As a result of interaction between the Fe matrix and B$_4$C-B particules, FeB and Fe$_2$B secondary phases were observed and related peaks were increased at increasing volume fractions of ceramics and sintering time. Porosity decreased with increasing the sintering time. It was found that the hardness of Fe/B$_4$C and Fe/B samples strongly depend on their structural composition and sintering parameters. When the B$_4$C-B ratio, towards ceramic dense layer and sintering time increased, the hardness of samples also increased. The transition of hardness from metal dense layer to ceramic was found smoother when the number of layers increases.

Keywords: Functionally graded materials, Powder metallurgy, Boronizing, Secondary intermetallic phases, FeB-Fe$_2$B.

Friction and Wear Characteristics of MoS$_2$/Cu-Sn Composite Film

Hitoshi Kohri[1], Takayoshi Yagasaki[2]

[1]*School of Advanced Engineering, Kogakuin University, kohri@cc.kogakuin.ac.jp*
[2]*School of Advanced Engineering, Kogakuin University, yagasaki@cc.kogakuin.ac.jp*

It is difficult to use an ordinary bearing in a vacuum and/or at a high temperature, because of evaporation or deterioration of the lubricant oil. A solid lubricant like as MoS$_2$ is promising in such condition. Recently, a thin solid lubricant film is often applied on a hard material by PVD or CVD. The thin film is, however, easily removed when the load or friction speed is too high. On the other hand, when the lubricant is dispersed in the surface layer of bearing, it is expected that the solid lubricant exists by abrasion on the surface of the bearing. The aim of this report is to examine friction and wear behavior of the MoS$_2$/Cu-Sn composite film.   The lubricant particles dispersed Sn layer was formed on the Cu substrate by electroless deposition. Then the plated sample was heat treated at various temperature due to become bronze. Friction properties of composites were determined by using a ball-on-disk type testing machine. The test was performed in a vacuum without oil at the room temperature.

The coefficients of dynamical friction of the composite films were decreased by the lubricant than the one of Cu. The effect of the lubricant was much remarkable in vacuum. From the results of 0.076 ms^{-1} in the sliding speed, the coefficient of dynamical friction of as deposited sample, which is MoS$_2$/Sn, was lower than the one of heat treated sample, which is MoS$_2$/bronze. On the contrary, for the results of 0.12 ms^{-1} in the sliding speed, the coefficient of dynamical friction of heat treated sample was lower than the one of as deposited sample. The wear rates of the composites were much less than one of Cu in a vacuum. The wear rate of heat treated sample was 2.5% less than the one of as deposited sample in both test condition.

Keywords: Friction, Wear, Solid lubricant, Electroless deposition, Composites

Functionally Graded Cu-ZnS Phosphor and its Applications

Jehong Park[1], Seungchan Cho[2], Akira Kawasaki[3], Kwangjae Park[4], Kwonhoo Kim[4], Hansang Kwon[1,4]

[1]Next-Generation Materials Co., Ltd.(NGM),ngm01@ngm.re.kr
[2]Korea Institute of Materials Science,sccho@kims.re.kr
[3]Tohoku University,kawasaki@material.tohoku.ac.jp
[4]Pukyong National University,kwon13@pknu.ac.kr

We describe a functionally graded metal-phosphor adapting the concept of the functionally graded materials (FGMs); copper (Cu) is selected as a metal and Cu- and Cl-doped ZnS (ZnS:Cu,Cl) is selected as a phosphor and FG [Cu]-[ZnS:Cu,Cl] is fabricated by a simple powder process through spark plasma sintering (SPS). The FG [Cu]-[ZnS:Cu,Cl] reveals a dual-structured functional material composed of dense Cu and porous ZnS:Cu,Cl, which is completely combined through six graded mediating layers. FG [Cu]-[ZnS:Cu,Cl] also exhibits diode characteristics and photo reactivity for 365 nm -UV light. Our FG metal-phosphor concept can pave the way to simplified manufacturing of low-cost and can be applied to various electronic devices.
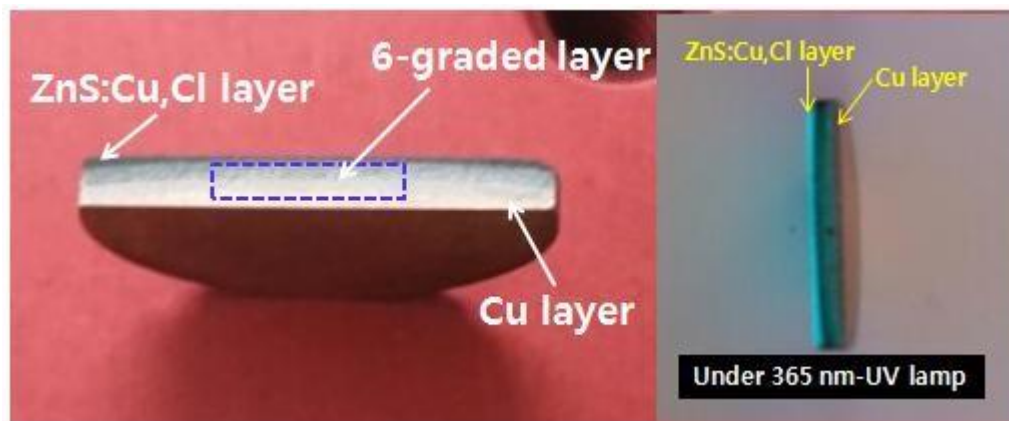
Keywords: Functionally Graded Materials (FGMs); Metal; Phosphor; Spark Plasma Sintering (SPS)

Electrospark Deposited FGMs Coatings with Enhanced Characteristics

E. Levashov, E. Zamulaeva, N. Litovchenko, A. Potanin, D. Shtansky

National University of Science and Technology "MISiS", Leninsky prospect 4, *Moscow119049, Russia, Email: levashov@shs.misis.ru*

Pulsed electrospark deposition (PED) is widely used for surface treatment. Special features of PED (short heat-up pulses 10^{-6}-10^{-3} s and high rates of warm-up and cool-down) require the optimization of deposition conditions (pulse duration, current, frequency, media) to provide alloying and/or chemical reactions as well as to avoid overheating and thermal decomposition of deposited material. Two examples are considered: tribological coatings on the base of MAX-phase Cr_2AlC; Ag- doped TiC-Ti bioactive coatings with antibacterial effect. The results obtained show that TiC layer is formed during the initial stage of PED due to interaction Cr_2AlC electrode (anode) and Ti substrate (cathode). At high-energy PED in Ar, the TiC layer quickly developed and acted as cathode with erosion-resistant higher than anode, therefore Cr_2AlC with lamellar structure became a main phase. In case of low-energy PED there are two ways to obtain coating with MAX phase: annealing at 700^0C or preliminary PED with graphite electrode. Electrodes with TiC, Ti_3PO_x, CaO, CoTiP, TiCo, Ag_7Ca_2 produced by combustion synthesis were used to obtain coating based on TiC, TiCo, and Ti - solid solution with Ca, P, O, Ag. Bioactivity was evaluated in vitro using simulated body fluid (SBF) and compared with that of bioactive glass Biogran.

Keywords: electrospark deposition, coating, tribology, bioactivity

ISFGMˢ 2016

Session: Structure Dominated Biomaterials II
Session Chair: G. Lang

Date: Wednesday, September 21st, 2016, Morning Session: 10:15-12:20
Room: S 135/ NW III

10:15 – 10:40	**Recombinant spider silk proteins as bioinks** Elise DeSimone, Kristin Schacht, Jürgen Groll, Thomas Scheibel
10:40 – 11:05	**Collagen-based gradient materials for tendon replacement** Christian Haynl, Thomas Scheibel
11:05 – 11:30	**Mechanical Testing of Engineered Spider Silk Filaments Provides Insights into Molecular Features on a Meso-Scale** Gregor Lang, Benedikt R. Neugirg, Daniel Kluge, Andreas Fery, Thomas Scheibel
11:30 – 11:55	**Study on the functionally graded characteristics of biofilms** Makoto Miyaoka, Kouichi Nakano, Toshinari Maeda
11:55 – 12:20	**Decomposition and Recovery Technology of Multi-Function Type Print Circuit Board with Substrate a Biodegradable Resin** Arashi Ohmukai, Takayoshi Yagasaki, Hitoshi Kohri, Ichiro Takano
12:20-13:30	**Lunch**

Recombinant spider silk proteins as bioinks

Elise DeSimone[1], Kristin Schacht[1], Jürgen Groll[2], Thomas Scheibel[1]

[1]Lehrstuhl Biomaterialien, Universität Bayreuth, thomas.scheibel@bm.uni-bayreuth.de
[2]Lehrstuhl für Funktionswerkstoffe der Medizin und der Zahnheilkunde, Universitätsklinikum Würzburg, juergen.groll@fmz.uni-wuerzburg.de

3D bioprinting has recently gained popularity as a fabrication technique to overcome common disadvantages of traditional tissue engineering (e.g. poor control over placement of scaffold's components). However, the number of process compatible materials is limited, due to stringent requirements placed on these materials. These so-called 'bioinks', therefore, are the current focus of research and development in this field. Recently, recombinant spider silk based proteins were used successfully in a 3D bioprinting process [1]. It was therefore the objective of this work to further characterize the recombinant spider silk-based bioinks, expand the possible variations of the bioinks, and establish the printing parameters for these bioinks.

[1] Schacht et al, Angew. Chem. Int. Ed., Vol. 54 (2015), 2816 –2820

Keywords: 3D bioprinting, bioinks, recombinant spider silk protein

Collagen-Based Gradient Materials For Tendon Replacement

Christian Haynl[1], Thomas Scheibel[2]

[1]*Lehrstuhl Biomaterialien, Fakultät für Ingenieurwissenschaften, Universität Bayreuth, Universitätsstraße 30, 95440 Bayreuth, Germany, christian.haynl@bm.uni-bayreuth.de*

[2]*Lehrstuhl Biomaterialien, Fakultät für Ingenieurwissenschaften, Universität Bayreuth, Universitätsstraße 30, 95440 Bayreuth, Germany, thomas.scheibel@bm.uni-bayreuth.de*

Tendons are collagen-based tissues, which transfer forces from muscle to bone. Due to their fundamental role in work movements, tendons are often affected by injuries. However, tendon repair is still poorly conceived and current tendon replacement materials from synthetic sources show insufficient biocompatibility. On the other side, reconstituted natural materials generally lack mechanical stability, which appears mostly at the interfaces between implant and tissue. For this reason, collagenous materials exhibiting a longitudinal gradient of their mechanical properties in order to connect soft muscle and stiff bone are of high scientific interest.

gradient material

hard   soft

[1] K. U. Claussen, R. Giesa, T. Scheibel, H. W. Schmidt, *Macromol Rapid Comm (***2012***)*, *33*, 206-211.

Keywords: gradient material, tendon replacement, biomaterial, collagen

Mechanical Testing of Engineered Spider Silk Filaments Provides Insights into Molecular Features on a Meso-Scale

Gregor Lang,[1,2†] Benedikt R. Neugirg,[3†] Daniel Kluge,[3] Andreas Fery[4*],
Thomas Scheibel[1*]

[1]*Department of Biomaterials, University of Bayreuth, Bayreuth 95440, Germany*
[2]*Professorship for Biopolymer Processing, University of Bayreuth, Bayreuth 95447, Germany*
[3]*Department of Physical Chemistry II, University of Bayreuth, Bayreuth 95440, Germany*
[4]*Chair for Physical Chemistry of Polymeric Materials, Technical University Dresden,
Dresden 01069, Germany*

Spider dragline silk shows the highest toughness in comparison to all other natural or man-made fibers. Despite a broad experimental foundation concerning the macroscopic silk thread properties as well as a simulationbased molecular understanding, the impact of the mesoscale building blocks, namely nano-/submicron-sized filaments, on the mechanical properties of the threads remains the missing link. Here, we illustrate the function of these meso-scaled building blocks using electrospun
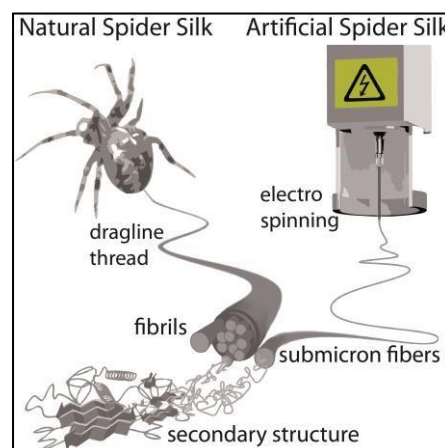
fibers made of a recombinant spider silk protein and show the impact of β-sheet formation and fiber hydration on their mechanical performance. Specifically elucidating the interplay between β-sheet-cross-linking and structural water effecting the fiber's extensibility, the results bridge the gap between the molecular and the macroscopic view on the mechanics of spider silk. Finally, the set-up enables a precise control of mechanical properties and morphology of man-made spider silk mimics, a pre-requisite for future applications of the precious biopolymer fibers [1].

[1] Aldo Leal-Egana, Gregor Lang, Carolin Mauerer, Jasmin Wickinghoff, Michael Weber, Stefan Geimer and Thomas Scheibel, Advanced Biomaterials, 14, No. 3 (2012), B67-B75

Study on the functionally graded characteristics of biofilms

Makoto Miyaoka[1], Kouichi Nakano[2], Toshinari Maeda[3]

[1]*Graduate School of life Science and Systems Engineering, Kyushu Institute of Technology,*
miyaoka-makoto@edu.life.kyutech.ac.jp
[2]*Graduate School of life Science and Systems Engineering, Kyushu Institute of Technology,*
nakano@life.kyutech.ac.jp
[3]*Graduate School of life Science and Systems Engineering, Kyushu Institute of Technology,*
toshi.maeda@life.kyutech.ac.jp

As regarding graded function on biomaterials, for example, we can find it in the graded distribution of fibrovascular bundle or lacuna on the cross-sectional surface of bamboo or seashell. These three dimensional structure is evaluated as the ideal buckling resistance structure for realizing high strength and weight saving.

On the other hand, biofilms are used for activated-sludge process in wastewater treatment and producing useful materials in lactic fermentation. It has been observed that the biofilm on the root surface of plants dissolves phosphorus.[1]

From the above, we think that biofilms have functionally graded characteristics even though there are few reports about it.

So, we investigated the functionally graded characteristics of some biofilms so as to control and utilize biofilms for the industrial use in the future.

[1] Yamaga, F. et al.: Environ. Sci. Technol, 44, (2010), 6470.

Keywords: biofilm, biomaterials, functionally graded characteristics

Decomposition and Recovery Technology of Multi-function Type Print Circuit Board with Substrate a Biodegradable Resin

Arashi Ohmukai[1], Takayoshi Yagasaki[2], Hitoshi Kohri[3], Ichiro Takano[4]

[1] *Graduate school, Kogakuin University, bm15005@ns.kogakuin.ac.jp*
[2] *School of Advanced Engineering, Kogakuin University, yagasaki@cc.kogakuin.ac.jp*
[3] *School of Advanced Engineering, Kogakuin University, kohri@cc.kogakuin.ac.jp*
[4] *Faculty of Engineering, Kogakuin University, ct97912@ns.kogakuin.ac.jp*

In recent years, resins (plastics) have been used in large quantities as substrate materials for making printed circuit boards. Problems associated with the disposal of these resin materials—including the exhaustion of landfill areas and generation of toxic gases during disassembly—have long been pointed out. Accordingly, there is much interest from the standpoint of environmental protection in the potential of biodegradable resins that are broken down to water and carbon dioxide by microorganisms as replacements for conventional resins. However, because the dissolution behavior of biodegradable resins in different environments is still poorly understood, methods for collecting and breaking down biodegradable resins have not yet been established.

In this study, polylactic acid (PLA) as a biodegradable resin with high potential for use as a general-purpose material was selected, and carefully examined the decomposition characteristics of PLA, modified at the microstructural level to multi-functionalize it with respect to the end goal of use in printed circuit boards. It was found that the decomposition characteristics of the resin essentially did not change, even when the resin was modified at the microstructural level to improve various functions. It was also found that the rate of decomposition significantly varied depending on the liquid medium used during decomposition (i.e., the decomposition solution). These results demonstrate that microstructural modification and choice of decomposition solution can either promote or inhibit decomposition.

Keywords: Biodegradation, Polylactide acid, Print Circuit Board, Proteinase K

Session: Manufacturing and Properties Assessment of Functionally Graded Materials and Structures IV

Session Chair: B. Henriques

Date: Wednesday, September 21ˢᵗ, 2016, Afternoon Session: 13:30-15:00

Room: S 130/ NW III

13:30 – 14:05 **(H36)**	**Electromagnetic induced segregation of aluminum alloy cast parts** Bernard Nacke
14:10 – 14:35	**Synthesis and Mechanical Properties of Graded TC4 Titanium Alloy via Plasma Activated Sintering** Yi Sun, Guoqiang Luo, Chuandong Wu, Jianian Hu, Jian Zhang, Meijuan Li, Qiang Shen, Lianmeng Zhang, Rhuizi Zhang
14:35 – 15:00	**Innovative Preparation of Nano-sized WC/W2C/W Functionally Graded Material (FGM)** Xiaona Ren, Min Xia, Qingzhi Yan, Changchun Ge
15:00 – 16:00	**Panel discussion and closing ceremony**

Electromagnetic induced segregation of aluminum alloy cast parts

Bernard Nacke

Institute of Electrotechnology, Leibniz Universität Hannover
nacke@etp.uni-hannover.de

The Electromagnetic Induced Segregation (EIS) of cast parts is an innovative technology for diecasting of aluminum alloys. Due to the different action of electromagnetic forces to high and low conductive materials electromagnetic fields can be used for separation of the different materials during the liquid phase before solidification [1]. This principle has been applied during casting of aluminum/silicon alloys cast parts in order to produce a primary silicon concentration gradient during casting. The paper shows the principle of the electromagnetic induced segregation effect, the design of a suitable inductor system for casting of engine blocks using numerical simulation, principle experiments in a pilot casting installation and the realization of the process in an industrial casting production machine. Finally four inductor systems were produced and installed in an industrial casting machine for 8-cylinder engine blocks [2]. Four cylinder bores of the engine block were casted using electromagnetic induced segregation and the other four bores were casted conventionally without electromagnetic treatment. Standard running tests of the casted engine have confirmed a comparable wear resistance compared to conventionally produced engine blocks, but with high advantages due to the fact of graded structures in the engine blocks.

Keywords: functional graded materials, electromagnetic separation, aluminum casting

Synthesis and Mechanical Properties of Graded TC4 Titanium Alloy via Plasma Activated Sintering

Yi Sun, Guoqiang Luo, Chuandong Wu, Jian Zhang,
Qiang Shen, Lianmeng Zhang*

State Key Laboratory of Advanced Technology for Materials Synthesis and Processing, Wuhan University of Technology, Wuhan 430070, China
corresponding author, Tel.: +86 27 87879468; fax: +86 27 87879468.E-mail address: luogq@whut.edu.cn

In the present study, graded TC4 titanium alloy with a gradient variation of grain size and shape was successfully synthesized using cryomilling and plasma activated sintering. The microstructures were characterized by OM, SEM and TEM, while the phase compositions were investigated by XRD. To provide insight into the mechanical behavior of the graded TC4 titanium alloy, we measure the compressive strength and micro-hardness on the ambient temperature. Our results show that the graded TC4 titanium alloy has a dense structure with a relative density of 98.32%. The intimate combination between different layers can be observed. The grain sizes show a gradient variation. The phase compositions of each layer change along with the grain sizes. The graded sample exhibits notable mechanical properties, the Vickers micro-hardness, the yield strength and the compression fracture strength of the as-prepared sample reaches 470.9HV, 1229.2MPa, and 2090.3MPa, respectively. The crack initial in fine grain zone, and then grows along grain boundaries.

Keywords: TC4 Titanium Alloy; graded material; cryomilling; plasma activated sintering; mechanical properties

Innovative Preparation of Nano-sized WC/W$_2$C/W Functionally Graded Material (FGM)

Xiaona Ren[1], Min Xia[1]*, Qingzhi Yan[1], Changchun Ge[1]*

[1]Institute of Nuclear Energy and New Energy System Materials, School of MaterialsSciences and Engineering, University of Science and Technology Beijing (USTB), Beijing100083, China.

Corresponding author: Tel: +86-01062334951; E-mail: xmdsg@ustb.edu.cn (Min XIA),

ccge@mater.ustb.edu.cn (Chang-Chun GE)

Functionally gradient material (FGM) is considered as a kind of non-uniform composite functional materials, which is composition-graded or/and structure-graded. Here we first proposed an innovative technology for preparing a kind of nano-sized FGMs, namely WC/W$_2$C/W graded nanorods with diameters of 50nm and less, which consist of WC, W$_2$C and W from the outside to its core. Ammonium metatungstate was encapsulated into the hollow core of nanostructured carbon with hollow macroporous core/mesoporous shell, then it was reduced in H$_2$ and converted to tungsten nanowire. Through heat treatment at 1400ºC, tungsten in the tube reacted with the carbon shell. Similar to carburization, the outer sphere of nanorod received more carbon and WC formed. And deeper along the radical direction, carbon became less, therefore W$_2$C formed. While tungsten in the core could not react with carbon. Hence the WC/W$_2$C/W graded nanorods formed. Results revealed that this graded nanorods possess excellent peroxide-like activity.

ISFGM^s 2016

Session: Performance Verification of Functionally Graded Materials and Structures

Session Chair: M. K. Apalak

Date: Wednesday, September 21st, 2016, Afternoon Session: 14:10-15:00

Room: S 135/ NW III

14:10 – 14:35	**Effect of Number of Layers on the Ballistics Performance of Functionally Graded Sandwich Plates** M. Aydin, M. K. Apalak, Z. G. Apalak
14:35 – 15:00	**High pressure injection valve with magnetic gradient** Stefan Oetinger, R. Moos, M. Willert-Porada
15:00 – 16:00	**Panel discussion and closing ceremony**

Effect of Number of Layers on the Ballistics Performance of Functionally Graded Sandwich Plates

M. Aydin[1], M. K. Apalak[2], Z. G. Apalak[3]

[1]*Department of Aeronautical Engineering, Erciyes University, Kayseri 38030, Turkey,*
aydin@erciyes.edu.tr
[2]*Department of Mechanical Engineering, Erciyes University, Kayseri 38030, Turkey,*
apalakmk@erciyes.edu.tr
[3]*Department of Mechanical Engineering, Erciyes University, Kayseri 38030, Turkey,*
apalakz@erciyes.edu.tr

Further developments in the design of weapons based on kinetic or chemical energy have mandated the new evolved light and high performance armors. A new idea of material design has concentrated on mechanically functional materials. FGMs are composed of at least two constituents and have continuous composition variation along one or more directions. In general, the most common constituents are ceramic and metal materials whose combinations of their superior properties, such as the toughness, heat resistivity, hardness, can be quite suitable for overcoming the hard, high temperature service environments. FGMs have been applied successfully in specific areas such as space, nuclear, and automotive industries and become an indisputable candidate for defense industries due to their good strength against structural and thermal loadings as well as their advantages in ballistic applications. Therefore, the mechanical responses under ballistic loadings and the material characterization of the functionally graded materials have become a broad research field in last decade.

In this study the damage and deformation mechanisms of functionally graded sandwich plates (FGSPs) which have different layer thickness have been investigated and their performances were compared to each other under ballistics impact loadings. The functionally graded sandwich plate is composed of a mixture of ceramic (SiC) and metal (Al) phases, at a ratio of which is determined by a power-law distribution of the volume fraction. In order to investigate the ballistic performance of FGSPs, a gas gun test system and 0.3 caliber fragment simulating projectiles (FSP) were used. Functionally graded sandwich plates were manufactured by means of the powder stacking-hot pressing method, their ballistic tests were performed and it was concluded that number of layers of FGSPs affected the ballistic performance considerably.

Keywords: Functionally graded materials (FGMs), Ballistic performance, Sandwich plates

High Pressure Injection Valve With Magnetic Gradient

Dr.-Ing. Stefan Oetinger

Robert Bosch GmbH, Bamberg, stefan.oetinger@de.bosch.com

Function optimized gasoline injection valves are able to decrease the consumption of a gasoline engine and increase its power. Therefore a magnetic separation is introduced into a magnetic circuit of an electromagnetic valve, which means a paramagnetic zone with a magnetic saturation of nearly 0 T within a soft magnetic jacket. This can be realized by a local induction heat treatment process of a soft magnetic jacket.

The short-time induction austenitization of the three stainless steels X30 CrMoN 15-1, X50 CrNiAl 17-2 and X90 CrMoV 18 were investigated. The result is a partially magnetic to non-magnetic material state of mixed austenitic and martensitic microstructure.

Process parameters (900…1225 °C, 0,1…10 s) were investigated in order to create the desired local magnetic separation. The resulting local functionally graded properties were characterized by microstructure, hardness and magnetic properties (saturation, coercitivity).

The characteristic of the magnetic separation, which is based on a local change in microstructure, is a heat affected zone with gradient magnetic and mechanical properties between the non-affected initial material of the soft magnetic jacket and the non-magnetic center. It was recognized, that the heat affected zone consists of a partially magnetic, a hardened and a tempered zone.
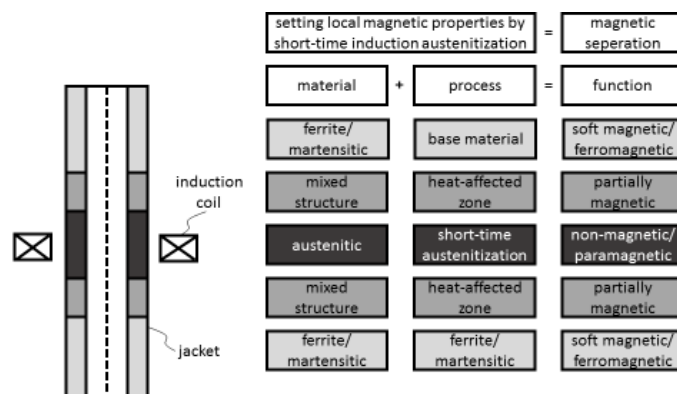
Keywords: stainless steel, magnetic properties, magnetic separation, short-time austenitization, induction heating

Paper

Functionally graded WC-Co cemented carbides: The state of the art

I. Konyashin[1,2], S. Hlawatschek[1], B. Ries[1], E. Levashov[2], A. Zaitsev[2]

[1]*Element Six GmbH, Burghaun, Germany. Email: igor.konyashin@e6.com*
[2]*National University of Science and technology MISiS, Moscow, Russia. Email:*
levashov@shs.misis.ru

Abstract

The fabrication of cemented carbides with functionally graded composition, microstructure and properties has been an issue of great interest in the cemented carbide industry for a long time. The history of the development and fabrication of functionally graded cemented carbides is outlined. Different technologies employed for the manufacture of functionally graded WC-Co cemented carbides are reviewed. Various types of functionally graded WC-Co materials designed for specific applications and fabricated by tailored sintering techniques are described. The functionally graded cemented carbides are characterized by a unique combination of various properties including exceptionally high hardness and fracture toughness, which cannot be achieved in bulk WC-Co materials. Carbide articles are described in which functional gradients of hardness, cobalt content and WC grain size have been obtained as a result of creating Co drifts and regulating the WC grain growth by controlling the carbon content of the surface layer. Modern trends in the research and development of novel functionally graded WC-Co cemented carbides are outlined.

Keywords: cemented carbides, sintering, hardness, fracture toughness

1. Introduction

The fabrication of cemented carbides with functionally graded composition, microstructure and properties has been an issue of great interest in the cemented carbide industry for a long time. In the most cases, the hardness and consequently wear-resistance of WC-Co cemented carbides can be improved only at the expense of fracture toughness. Conventional cemented carbides obtained by varying the WC mean grain size and Co content lie within a narrow band on the curve: Palmquist toughness – hardness [1]. The major challenge of research in the cemented carbide field is to "escape" from this band, in other words, to simultaneously improve both hardness and fracture toughness of cemented carbides, which can be achieved by the fabrication of functionally graded cemented carbides.

2. First industrial functionally graded cemented carbides

The first industrial functionally graded cemented carbide was the Sandvik DP60 grade, or the so-called "dual properties - DP" cemented carbide. This grade is employed for rock drilling and mineral cutting and comprises a core with the η-phase [2]. Functionally graded cemented carbides similar to the Sadnvik DP60 grade were produced and examined also in refs. [3, 4]. The functionally graded cemented carbides of the DP-type are produced in a two stage process comprising: (1) Fabrication of fully sintered carbide articles deficient with respect to carbon and therefore containing the η-phase, and (2) Carburization of the articles in a carburizing atmosphere at temperatures above 1300°C in the presence of liquid phase. As a result of this fabrication process, carbon diffuses

from the surface toward the core leading to the carburization of the η-phase and its disappearance in the near-surface layer, which causes a Co drift from the surface toward the interface with the η-phase-containing core region. As a result, a graded structure generally comprising the three following constituent parts forms: (1) a near-surface layer of nearly 1 to 2 mm characterized by a significantly lower Co content and higher hardness than on average; (2) a layer adjacent to the near-surface layer comprising no η-phase and having a noticeably higher Co content and lower hardness than on average; and (3) a core comprising the η-phase. The functionally graded cemented carbides of the DP-type can be employed in mining due to the presence of the near-surface layer with high hardness, however, they have a limited applicability because of the brittle core comprising the η-phase.

3. Modern trends in the research and development of functionally graded WC-Co cemented carbides

The fabrication of functionally graded cemented carbides not comprising the brittle η-phase has been the issue of great interest in the carbide industry for a long time. If one can produce cemented carbides with a near-surface region with a significantly lower Co content than the average Co content, this region would have a high hardness leading to its better wear-resistance. It is also expected that this near-surface region would be characterized by high residual compression stresses resulting in its higher fracture toughness. This occurs as a result of very different shrinkage rates in two parts of a carbide article with various Co contents during liquid-phase sintering, as the shrinkage factor of the part with a higher Co content is significantly greater than that of the part with a lower Co content.

The two following major approaches to the fabrication of functionally graded cemented carbides not containing the η-phase are described in the literature.

The first approach is based on selective introducing WC grain growth inhibitors (mainly Cr and V) into the cemented carbide near-surface layer as a result of applying the grain growth inhibitors or their precursors to the surface of green articles (see e.g. ref. [5]). As a result of this technology, the near-surface region comprising much Cr or V becomes significantly finer than the core after liquid-phase sintering resulting in its high hardness and wear-resistance. Nevertheless, there are significant difficulties related to applying the grain growth inhibitors or their precursors to the surface of carbide articles of complicated shape in the green state, as they are very fragile.

The second approach is based on obtaining a Co drift in carbide articles, which are inhomogeneous with respect to their WC mean grain size and/or carbon content in the green state. In general, the following two major phenomena can be used for fabricating functionally graded WC-Co materials in this case: (1) If there are two adjacent layers of WC-Co with various carbon contents in the green state, cobalt drifts from the layer with the higher carbon content into the layer with the lower carbon content during liquid phase sintering; (2) If there are two adjacent layers of WC-Co with various WC mean grain sizes in the green state, cobalt drifts from the layer with coarser microstructure into the layer with finer microstructure during liquid phase sintering as a result of different capillary forces. These phenomena were described in detail in numerous publications with respect to bi-layer cemented carbides pressed and sintered from various WC-Co graded powders, see e.g. [6, 7]. It can be expected that, if one can regulate the WC mean grain size and/or carbon content in the carbide near-surface layer and core in the green state, it would be possible to create and control the Co drift during the final liquid-phase sintering thus obtaining functionally graded cemented carbides.

A new technology for the fabrication of WC-Co articles with a low cobalt content and consequently high hardness of the near-surface layer and not comprising the η-phase was described by Guo et al. and Fang et al. [8, 9]. According to this technology, WC-Co articles with original low carbon contents are subjected to carburization at a temperature, at which solid tungsten carbide, liquid cobalt and solid Co coexist. In spite of the fact that there is neither η-phase nor free carbon in the functionally graded cemented carbides obtained in such a way, the technology mentioned above allows the formation of only very thin hard near-surface layers having a thickness of roughly 0.1 mm. It appears that such thin hard layers should have a limited application in mining and construction, as the wear of carbide inserts in these applications is typically of the order of 1 mm or more.

Another new technology for the fabrication of functionally graded cemented carbides comprising neither η-phase nor free carbon was developed by Konyashin et al., [10, 11]. It is based on the following steps: (1) making WC-Co grade powders with a low carbon content but not corresponding to the η-phase formation and pressing green articles, (2) tailored pre-sintering of the green articles to obtain a certain gas permeability of their near-surface layer in the green state, (3) selective carburization of this near-surface layer up to a certain depth in the solid state,

and (4) final liquid-phase sintering of the articles to obtain a Co drift in the liquid phase from the surface towards the core and their full densification. As a result of this technology, it is possible to vary the thickness of the layer with the low Co content and consequently high hardness in a range of nearly 1 mm to several millimeters. This allows one to produce carbide articles for various applications with tailored near-surface layers characterized by high combinations of hardness and fracture toughness. The near-surface layer is characterized by high residual compression stresses in both the WC phase and Co phase, resulting in its high fracture toughness. This leads to an exceptionally high combination of hardness and fracture toughness of the near-surface layer providing evidence that it is possible to "escape" from the curve relating the fracture toughness and hardness for conventional WC-Co materials due to obtaining the functionally graded WC-Co cemented carbides with the hard and tough near-surface layer.

4. Conclusions

Functionally graded cemented carbides can be designed for specific applications by use of tailored sintering techniques. They are characterized by a unique combination of various properties, which cannot be achieved in bulk cemented carbides. Therefore, functionally graded cemented carbides being presently employed in some fields are expected to substitute conventional cemented carbides in numerous applications in near future.

Acknowledgements

References

[1] Roebuck B., Gee M.G., Morrell R. In: Kneringer G, Rödhammer P, Wildner H (Eds.) Proceedings of the 15th International Plansee Seminar, 2001, vol.4, 245-266.

[2] Aronsson B., Hartzell T., Aakerman J. Structure and properties of dual carbide for rock drilling. In Proceedings of Adv. Hard Mater. Prod. Conf, 1988), 19/1 – 19/6.

[3] Zhang L, Wang Y., Yu X., Chen S, Xiong X. Int. J. Refract. Met. Hard Mater, 26 (2008)295–300.

[4] Liu Y., Wang H,m Long Z, Liaw P., Yamg J, Baiyun H, Mater. Sci. Eng., A 426(2006)346-354.

[5] Greenfield M. S., Edward V.C, US patent 4,859,543, 1989.

[6] Liu Y., Wang H., Yang J., Huang B., Long Z, J. Mater. Sci., 39(2004)4397-4399.

[7] Eso O. Fang P, Fang Z., Int J Refract Met Hard Mater, 25(2007)286-293.

[8] Fang Z, Fan P, Guo J, US Patent Application US2010/0101368A1, 2010.

[9] Guo J, Wang F, Advanced in Powder Metallurgy & Particulate Materials, Washington, USA: Metal Powder Industries Federation, 2010, 8/29-8/39.

[10] Konyashin I, Hlawatschek S, Ries B., Lachmann F., Sologubenko A., Weirich T., Int. J. Refract. Met. Hard Mater, 28(2010)228–237.

[11] Konyashin I, Hlawatschek S, Ries B, Lachmann F., PCT Patent Application WO2010/097784, 2010.

Fabrication of Mg-Cu Graded-Density Impactors from Powder Processing for Accurately Controlled Complex Loading Paths

Guoqiang Luo[1,a], Jiayu He[1,b], Lianmeng Zhang[1,c] *, Xiaozhuang Zhou[1], Jian Zhang[1], Qiang Shen[1], Meijuan Li[1], Chuanbin Wang[1]

[1]*State Key Laboratory of Advanced Technology for Materials Synthesis and Processing, Wuhan University of Technology, Wuhan 430070, China*
E-mail: [a]luogq@whut.edu.cn, [b]wuthejiayu@163.com, [c]lmzhang@whut.edu.cn

Abstract

Compositionally graded Mg-Cu structures were fabricated by powder processing and hot-press sintering. Layers of pressed metal powders were stacked in sequence according to designed density-thickness curves to attain desired thermodynamic loading paths. Powder processing was simple to operate and allowed excellent control of the composition and thickness. The samples were highly densified (≥98.7%). There are no intermetallic compounds or magnesium oxides. Mg and Cu phases were dispersed homogeneously and well compacted. There are no obvious pores or voids between layers. A 14 layer graded-density impactor was prepared successfully. The thickness of each layer deviated little from the designed values, with errors of 0.06-1.13%.

Keywords: Powder processing; Graded-density impactors; Mg-Cu

1. Introduction

Investigating the properties of materials at extreme conditions (e.g., megabar pressures or thousands of Kelvin) is of great interest in many fields such as biology, condensed-matter physics, and planetary science [1]. Experiments in extreme conditions can be classified into three categories: quasi-static measurements using diamond-anvil cells [2], shock compression [3], and quasi-isentropic compression [4]. However, these methods are limited in practical applications by their characteristic thermodynamic paths and loading rates. Therefore, novel loading techniques must be developed to bridge the gap between the differing strain rates currently used and to tailor their thermodynamic paths to access states beyond the principal Hugoniot and isentrope.

Recently, researchers have been increasingly interested in complex compression during experiments that use light-gas guns [5-8]. In order to simulate the conditions that materials experience during dynamic high pressure experiments precisely, Nguyen et al. [9, 10] developed an experimental approach that used graded-density impactors (GDIs) to engender complex loading paths. By using an impactor with a layered structure, one can easily design a desired applied-pressure profile combining shock loading, quasi-isentropic compression, controlled release, and constant pressure [5]. Layered impactors can be fabricated using a number of techniques, such as diffusion bonding [5-8], bonded multi-plate [11], hot-pressing [5-7], and tape-casting [9]. Powder processing techniques have been widely used to fabricate GDIs; for example, Luo et al. [12] fabricated Mg-W impactors in this way. Powder processing can produce GDIs with continuously variable density and impedance based on the chosen composition; additionally, the technique is simple and can control the density-thickness profile of the impactors during fabrication accurately.

In the present work, the powder processing technique is demonstrated to be an effective route to accurately fabricate the GDIs. A series of characterization methods were used to demonstrate the GDIs have been fabricated accurately.

2.   Materials and Testing Methods

Mg powder (Alfa Aesar; 375 mesh average particle size, >99% purity) and Cu powder (Alfa Aesar; 20 μm average particle size, >99.9% purity) were used in our experiments. After Mg and Cu powder qualities which were calculated by the rules of mixtures were weighed, they were blended into uniform powder mixtures, which then were laminated into green samples after being layered accurately. The GDIs were formed by stacking different green samples according to the designed curve. The graded green samples were sintered using hot-pressing. The sintering of GDI samples followed the same process as sintering Mg-Cu monolithic pellets. Samples were put into molds and subsequently vacuum hot-press sintered at 783 K under a pressure of 100 MPa with a soaking time of 2 h.

The relative density was measured by Archimedes' method, phase composition was measured by X-ray diffraction (XRD; Ultima III; Rigaku, Tokyo, Japan), and microstructure was evaluated by Field-emission scanning electron microscopy (FESEM, Quanta-250).

3.   Results and Discussion

Figure 1 shows the measured, calculated densities, and relative densities of the Mg-Cu monolithic pellets of various compositions. As shown in the Figure 1, the measured densities agree well with the calculated, indicating that these composites are highly densified. The lowest relative density exceeds 98.7%.

Figure 2 shows SEM images of the fracture surfaces from single-composition pellets with (a) 80% Cu, (b) 50% Cu, and (c) 20% Cu. As shown in the Figure 2, the fractures emanated from uniaxial tension experiments. The composites exhibit typical intergranular fracture, indicating that the Mg and Cu phases were well compacted. No obvious pores were found in these micrographs, and thus we deduce that the composites are highly densified, which is consistent with the results of relative density.

Mg and Cu are known to have two intermetallic phases $MgCu_2$ and Mg_2Cu. Reported density for Mg_2Cu (3.18g/cm3) and MgCu2 (8.55 g/cm3) deviate from the density predicted by the rules of mixtures [13]. The differing densities change the designed density-thickness curves. In addition, these compounds are brittle, making complex loading with a GDI difficult. Figure 3 shows XRD patterns of Mg-Cu monolithic pellets with different compositions from 100% Mg to 100% Cu. As shown in the Figure 3, these patterns are dominated by Mg and Cu peaks with no obvious peaks from intermetallic compounds. Previous work has also shown that Mg is prone to be oxidized [9], and then Mg-Cu composites are difficult to be densified in the presence of MgO. However, no obvious MgO peaks are found in Figure 3, which is attributed to our sintering process in vacuum.
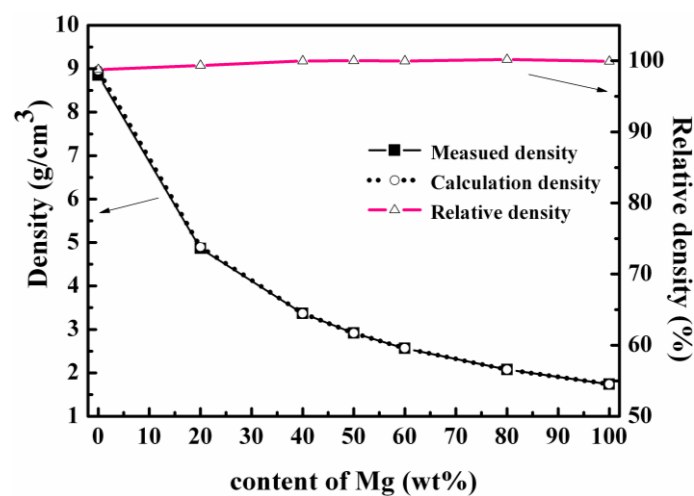
Figure 1: The measured, calculated density and relative density curves of Mg-Cu composites with different compositions
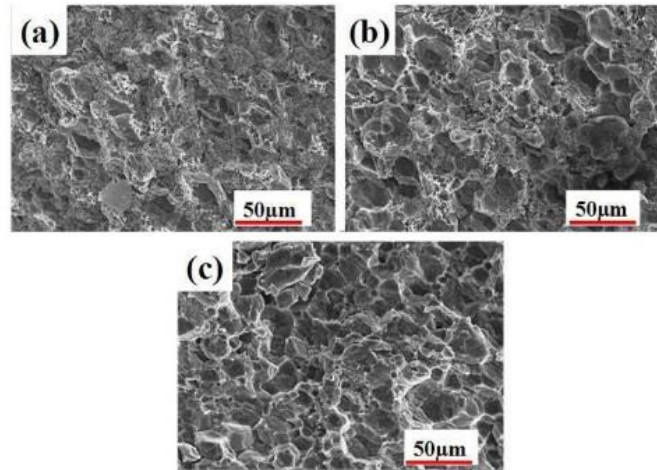
Figure 2: SEM images of the fracture surfaces from single composition pellets: (a) 80% Cu, (b) 50% Cu, and (c) 20% Cu
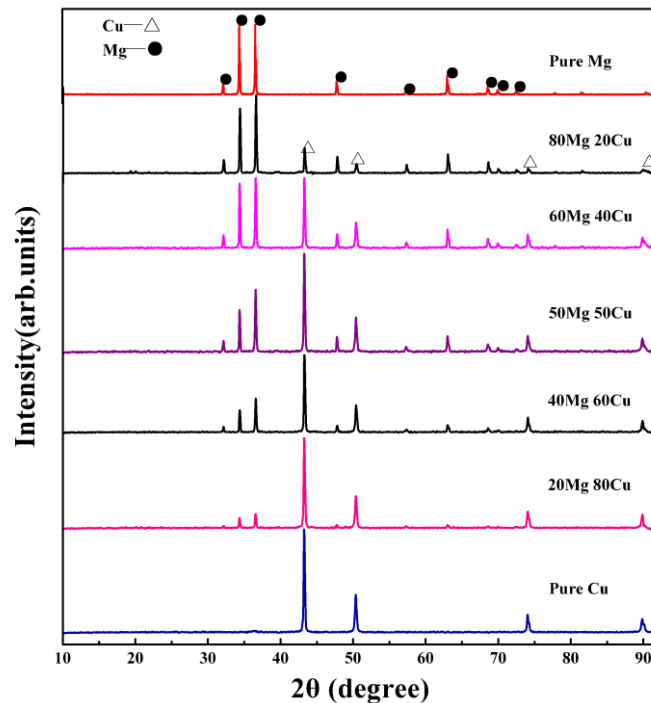
Figure 3: XRD patterns of Mg-Cu monolithic pellets with different compositions

Figure 4 shows the measured and designed density-thickness curves of a 14-layer GDI chosen from a series of samples randomly. As shown in the Figure 4, the first layer is pure Cu, the second layer is pure Mg, and the remaining layers are mixtures graded from 0% Cu to 90% Cu. The measures used to calculate the thickness and density of each layer was reported by Luo et al. [12]. The two curves agree well with each other. Compared with the total designed thickness of 2.4 mm, the total measured thickness is 2.397 mm, with an error of 0.125%. The range of thickness errors for the individual layers is 0.06-1.13%. These are very small errors, indicating that powder processing allows us to control the layer thickness accurately. In comparison, tape casting produces layers with thickness errors of 1.5-2.5% [9]. Based on these results, it can be concluded that the precision of thickness control by powder processing is comparable with reports.

Figure 5 shows the microstructure of the sample described in Figure 4. Mg and Cu phases are distributed uniformly and well compacted in all layers. As shown in the Figure 5, No obvious pores or gaps between the layers are found.
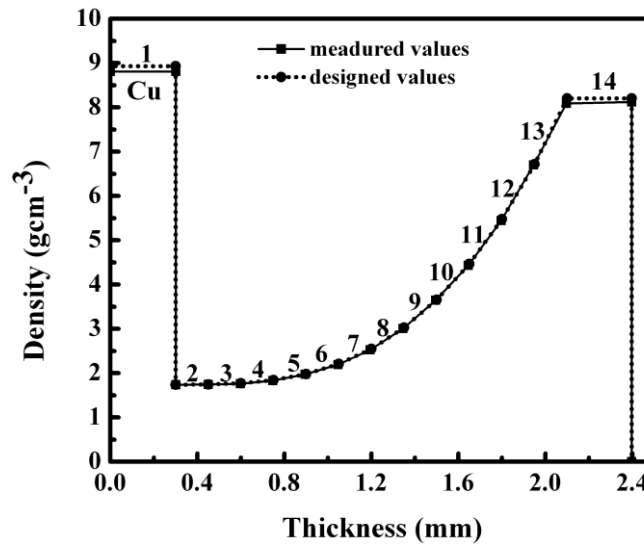
Figure 4: The measured and designed density-thickness curves of a 14-layer GDI
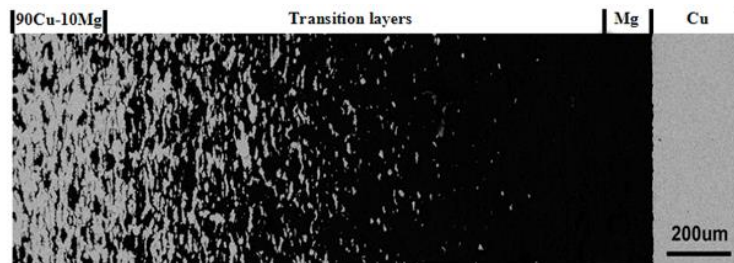
Figure 5: SEM image of a polished cross-section of the 14-layer Mg-Cu GDI

4. Conclusions

Mg-Cu GDI samples have fabricated accurately by powder processing and performing hot-press sintering. The conclusions are as follows:

1. The measured densities of the Mg-Cu monolithic pellets of various compositions agree well with the calculated. These composites are highly densified, and exhibit typical intergranular fracture. The lowest relative density exceeds 98.7%.
2. The XRD patterns of Mg-Cu monolithic pellets are dominated by Mg and Cu peaks with no obvious peaks from intermetallic compounds.
3. The measured density-thickness profile of 14-layer GDI agrees well with the designed. The errors of individual layers' thickness are only 0.06-1.13%.

Acknowledgements

References

[1] A.C. Mitchell, W.J. Nellis, *J. Appl. Phys*. **52** (1981), 3363–74.

[2] M. Eremets, High Pressure Experimental Methods, Oxford Uni-versity Press, Oxford, UK, 1996, 3–4.

[3] Y.B. Zel'dovich, Y.P. Raizer, Physics of Shock Waves and High-Temperature Hydrodynamic Phenomena, Academic Press, New York, USA, 1967.

[4] C.A. Hall, *Phys. Plasmas*. **7** (2000), 2069–75.

[5] J.H. Nguyen, D. Orlikowski, F.H. Streitz, J.A. Moriarty, N.C. Holmes, *AIP Conf. Proc*. **706** (2004), 1225–30.

[6] Q. Shen, C.B. Wang, L.M. Zhang, J.S. Hua, H. Tan, F.Q. Jing, *Key Eng. Mater*. **249** (2003), 287–290.

[7] H. Xiong, L. Zhang, L. Chen, R. Yuan, T. Hirai, *Mater. Trans. A*. **31**A (2000), 2369–73.

[8] W. J. Nellis, S.T. Weir, A.C. Mitchell, *Phys. Rev. B*. **59** (1999), 3434–49.

[9] J.H. Nguyen, D. Orlikowski, F.H. Streitz, J.A. Moriarty, N.C. Holmes, J. *Appl. Phys*. **100** (2006), 0235–42.

[10] J.H. Nguyen, D. Orlikowski, F.H. Streitz, N.C. Holmes, J. A. Moriarty, *AIP Conf. Proc*. **706** (2004), 1225–30.

[11] J.H. Nguyen, D. Orlikowski, F.H. Streitz, J.A. Moriarty, N.C. Holmes, *J. Appl. Phys*. **100** (2006), 1–4.

[12] G.Q. Luo, J.S. Bai, H. Tan, Q. Shen, J.B. Hua, L.M. Zhang, *Metall. Mater. Trans*. A. **41** (2010), 2389–95.

[13]. $MgCu_2$: JCPDF #013-0504, Mg_2Cu: JCPDF #001-1226

Stress and Vibration analysis of the FG plate with in-plane material properties variation

Maedeh Amirpour[1], Simon Bickerton[1], Raj Das[1], Brian Mace[2]

[1] *Center of Advanced Composite Materials (CACM), Department of Mechanical Engineering, University of Auckland, New Zealand maedeh.amirpourmolla@auckland.ac.nz*
[2] *Department of Mechanical Engineering, University of Auckland, New Zealand*

Abstract

This paper presents the bending and free vibration solution of functionally graded (FG) plates with variation of material properties through their length using higher order shear deformation theory (HSDT). The present theory accounts for both the shear deformation and thickness stretching effect by a sinusoidal variation of the displacement field across the thickness. The problem is then modelled using the finite element method (FEM) using graded solid element. This element has the spatially graded property distribution (at different Gauss points), which is implemented by the user subroutines UMAT and USDFLD for bending and vibration analysis, respectively. It can be concluded that the present exact formulation is not only accurate, but also simple in predicting the bending and vibration of the FG plates.

Also, the good agreement found between the exact solution and the numerical simulation demonstrates the effectiveness of graded solid element in the modelling of the FG plate. Moreover, the combination of the derived analytical and numerical results will enable us to understand the behavior of new materials with controlled macro properties through the specific direction with potential relevance to biomedical and aerospace sectors.

Keywords: FG plates, In-plane properties variation, Stress, Vibration

1. Introduction

One of the most important consequences in fully understanding the mechanical behavior of natural materials, e.g. bones and sea shells, is the inspiration of a new class of advanced materials. Functionally Graded Materials (FGMs) are advanced engineered materials whereby material composition and properties vary spatially in macroscopic length scales, which are created by specialized manufacturing processes [1]. Nowadays, FGMs are alternative materials widely used in biomechanical, aerospace, civil, automotive and other applications. Moreover, FGMs are gaining attention for biomedical applications, especially for implants. Implants can be made of FGMs with spatial property variation to create an optimized mechanical behavior and achieve biocompatibility improvement [2]. The static solutions for FG plates have been mainly based on classical plate theory (CPT), which is valid for thin plates, as it does not consider shear deformation. This may lead to inaccurate results for thick plates, which is thicker than 1/20 of its larger span [3]. The First-order shear deformation theories (FSDT) consider the transverse shear deformation effects. However, a shear correction factor is needed to satisfy the zero transverse shear stress boundary conditions at the top and bottom of the plate [4]. For eluding the use of shear correction factors, several HSDT have been proposed. In addition, all two-dimensional plate theories ignore the thickness stretching effect. Indeed, a constant transverse displacement through the thickness was considered. This assumption is not appropriate for thick FG plates. The importance of the thickness stretching effect in a thick FG plate has been identified in [5]. So this effect should be taken into
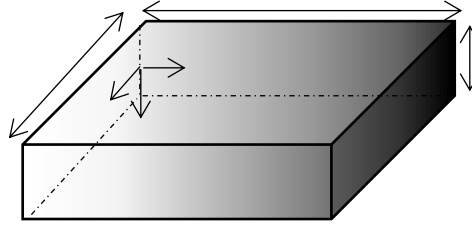
Figure 1: Schematic representation of the geometry (left) and distribution of volume fraction along x direction of the FG plate (right)

consideration. In most of the applications reported in the literature the variation of material properties is through the thickness only. However, no attention has been paid on considering the distribution of volume fraction through the length, resulting in the variation of stiffness along it. The objective of this paper is to propose a new closed form approach and numerical methodology for bending and free vibration analysis of simply supported thick rectangular FG plates with in-plane material properties variation based on HSDT.

2. Analytical Solution

A rectangular FG plate of uniform thickness h, length a and width b is shown in Figure 1, with origin z = 0 coinciding with the mid-surface of the plate.

The material is assumed to be elastic and inhomogeneous, and the material stiffness vary continuously through the length of the plate and obey a simple power-law distribution of volume fraction of constituents as given by:

$$V_i(x) = \left(\frac{x}{a}\right)^n \tag{1}$$

where n is a parameter that governs the material variation profile through the length. The displacement field of the present theory which was recently developed by Blabed et al. [5] is adopted based on the following assumptions: (1) the transverse displacements are divided into bending, shear and stretching components; and (2) the shear components of the in-plane displacements produce the sinusoidal variations of shear strains. Based on these assumptions, the following displacement field relations can be obtained:

$$u(x, y, z) = u_0(x, y) - z \frac{\partial w_b(x, y)}{\partial x} - \xi(z)\vartheta_1$$

$$v(x, y, z) = v_0(x, y) - z \frac{\partial w_b(x, y)}{\partial y} - \xi(z)\vartheta_2$$

$$w(x, y, z) = w_b(x, y) + w_s(x, y) + \varsigma(z)\varphi(x, y) \tag{2}$$

The governing equations of the present theory are derived from the static version of the Principle of Virtual Displacements (PVD), which is called the Hamilton's principle. The internal virtual work is initially formulated as follows:

$$\int_0^T (\delta U + \delta V - \delta K)dt = 0 \tag{3}$$

After some mathematical solution and substitution the expression for stress and strain into equations (3), the following governing equations of the FG plate with the variation of material property through the length are obtained as follows:

$$\delta u_0 : d_1 N_x + d_2 N_{xy} = I_0 \ddot{u}_0 - I_1 d_1 \ddot{w}_b - J_1 d_1 \ddot{w}_s \tag{4a}$$

$$\delta v_0 : d_2 N_y + d_1 N_{xy} = I_0 \ddot{v}_0 - I_1 d_2 \ddot{w}_b - J_1 d_2 \ddot{w}_s \tag{4b}$$

$$\delta w_b : d_{11} M_x^b + d_{22} M_y^b + 2 d_{12} M_{xy}^b + q =$$
$$I_0 (\ddot{w}_b + \ddot{w}_s) + I_1 (d_1 \ddot{u}_0 + d_2 \ddot{v}_0) - I_2 (d_{11} \ddot{w}_b + d_{22} \ddot{w}_b) - J_2 (d_{11} \ddot{w}_s + d_{22} \ddot{w}_s) + J_1^s \ddot{\varphi} \tag{4c}$$

$$\delta w_s : d_{11} M_x^s + d_{22} M_y^s + 2 d_{12} M_{xy}^s + d_1 S_{xz}^s + d_2 S_{yz}^s + q =$$
$$I_0 (\ddot{w}_b + \ddot{w}_s) + J_1 (d_1 \ddot{u}_0 + d_2 \ddot{v}_0) - J_2 (d_{11} \ddot{w}_b + d_{22} \ddot{w}_b) - K_2 (d_{11} \ddot{w}_s + d_{22} \ddot{w}_s) + J_1^s \ddot{\varphi} \tag{4d}$$

$$\delta \varphi : d_1 S_{xz}^s + d_2 S_{yz}^s + q \varsigma(z) - N_z = J_1^s (\ddot{w}_b + \ddot{w}_s) + K_2^s \ddot{\varphi} \tag{4e}$$

The required mentioned displacement fields which satisfy the boundary conditions of simply supported boundary conditions are assumed as follows:

$$\begin{Bmatrix} u_0 \\ v_0 \\ w_b \\ w_s \\ \varphi \end{Bmatrix} = \sum_{m=1}^{\infty} \sum_{n=1}^{\infty} \begin{Bmatrix} U_{mn} e^{iwt} \cos \lambda_m x \sin \mu_n y \\ V_{mn} e^{iwt} \sin \lambda_m x \cos \mu_n y \\ W_{bmn} e^{iwt} \sin \lambda_m x \sin \mu_n y \\ W_{smn} e^{iwt} \sin \lambda_m x \sin \mu_n y \\ \varphi_{mn} e^{iwt} \sin \lambda_m x \sin \mu_n y \end{Bmatrix} \tag{5}$$

3. Finite Element Modelling

For verification of analytical modelling, the numerical simulation of the same FG plate was carried out using the Finite Element Method in this section. The linear hexahedral (C3D8R) graded elements were used in the finite element program ABAQUS to implement an effective continuous variation of material elastic properties. This type of element is implemented by means of direct sampling properties at the integration (Gauss) points of the element. The user subroutine UMAT and USDFLD function coded with FORTRAN was used for modelling of the FG plate with graded solid elements in the ABAQUS FE software. The Young's modulus (material stiffness) and density of the FG plate as a material property was defined as a function of length for each integration point throughout the length (x) of the specimen.

4. Results and Discussions

A thick rectangular FG plate with a=b=5h and n=3 is used as an example of bending problem. Figure compares the analytical and numerical solutions of the deflection of the FG plate along the length. It is found that the analytically derived mid-surface, out-of-plane displacement of the FG plate exhibits close agreement with those values obtained from the FEM predicted solutions with a maximum relative error smaller than 8%. It is noteworthy that the maximum deflection does not occur in the middle of the plate. While for homogenous and FG plates with thickness-wise variation, the maximum deflection occur in the middle of the plates.
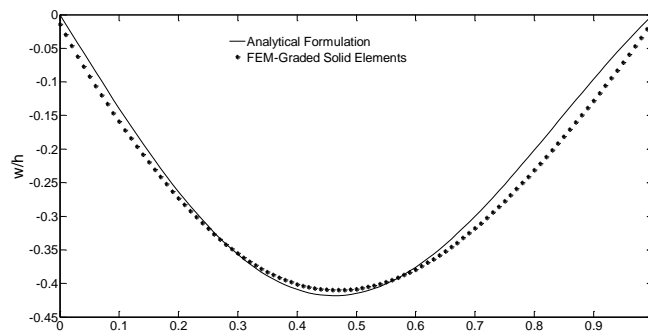
Figure 2: Deflection of the FG plate with variation of the material stiffness through the length

Table 1:

τ=h/a	Method	Mode (SSSS)				
		f_1	f_2	f_3	f_4	f_5
	Analytical	156.34	390.60	390.62	624.55	780.30
0.02	FEM	156.48	390.63	392.14	624.43	778.72
	Error (%)	0.077	0.007	0.387	0.019	0.203
	Analytical	530.06	1313.89	1313.97	2084.74	2591.64
0.07	FEM	529.51	1299.46	1305.11	2009.91	2508.61
	Error (%)	0.104	1.110	0.679	3.723	3.310

In Table 1, based on the present exact analytical solutions and graded FEM, the first five non-dimensional natural frequencies λ have been obtained for FG plates when power law index n=3. An excellent agreement is observed between the present exact HSDT and proposed graded FEM. It can be seen that frequencies rise with an increase in thickness of plate. This phenomena originates from the increasing the rigidity of plate.

5. Conclusions

In this study, the closed- from solution based on the sinusoidal higher shear deformation theory for bending and free vibration analysis of rectangular FG plates with power-law distribution of volume fraction through the length is presented. The results predicted by the proposed theory are in very good agreement with FE simulations. The FE solution is obtained using solid elements with spatially graded property distribution. The research will be beneficial for real life applications of FG plates with in-plane variation of material stiffness in engineering structures such as wing components, prosthesis, scaffold for biomedical applications

Acknowledgements

References

[1] Chakraborty, A. and S. Rahman, Stochastic multiscale models for fracture analysis of functionally graded materials. Engineering Fracture Mechanics, 2008. 75(8): p. 2062-2086.
[2] Mehrali, M., et al., Dental implants from functionally graded materials. J Biomed Mater Res A, 2013. 101(10): p. 3046-57.
[3] Chi, S.-H. and Y.-L. Chung, Mechanical behavior of functionally graded material plates under transverse load—Part I: Analysis. International Journal of Solids and Structures, 2006. 43(13): p. 3657-3674.
[4] Reissner, E., Reflection on the theory of elastic plates. . ASME J Appl Mech, 1945. 38: p. 1453-1464.
[5] Belabed, Z., M.S.A. Houari, A. Tounsi, S.R. Mahmoud and O. Anwar Bég, An efficient and simple higher order shear and normal deformation theory for functionally graded material (FGM) plates. Composites Part B: Engineering, 2014. 60: p. 274-283.

Investigation on the Ballistic Limit of Functionally Graded Plates

Recep Gunes[1], Mevlut Hakan[2], M. Kemal Apalak[3], J.N. Reddy[4]

[1] Department of Mechanical Engineering, Erciyes University, Kayseri 38039,
recepg@erciyes.edu.tr
[2] Department of Mechanical Engineering, Erciyes University, Kayseri 38039,
mevluthakan@erciyes.edu.tr
[3] Department of Mechanical Engineering, Erciyes University, Kayseri 38039,
apalakmk@erciyes.edu.tr
[4] Department of Mechanical Engineering, Texas A&M University, College Station,
TX 77843-3123, USA,
jnreddy@tamu.edu

Abstract

Armor technologies are continuously improving against projectile threats which increasing ravage and destruction area. The use of composite materials as the armor structures provides high resistance against projectile, as well as facilitate the mobility by reducing the weight of structure. Besides, it is very important to design of composite armors both to disrupt the projectile tip geometry and to protect the structural integrity in ballistic applications. In this respect, functionally graded materials consisting of ceramic and metal are extremely suitable for ballistic applications due to their nature. Namely, the ceramic constituent provides high ballistic resistance against projectile while the metal constituent supplies the structural integrity of the FGM armor.

The aim of this study is to investigate the effect of through-thickness material properties of the FG plates and impact angle of the projectile on the ballistic limits of FGM armor system. Mori-Tanaka homogenization scheme is used as the micro-mechanical model to determine the through-thickness material properties in the graded region. Three-dimensional explicit finite element simulations are carried out for the FGM armor impacted at 0º, 15º, 30º, 45º and 60º obliquity by a 0.30 caliber Fragment Simulating Projectile (FSP). The ballistic limit, absorbed energy by the FGM armor, and the critical impact angle of the projectile are quantified.

Keywords: Functionally graded materials, Oblique impact, Ballistic limit, Explicit finite element method.

1. Introduction

The design of protective materials as armor has become a very important case against developing weapons technology. The two most important features expected from an armor system is low weight and high impact resistance. Armor structures should have low weight to provide the mobility of staff or vehicle as well as stop the threats which may come from outside [1]. Functionally graded plates, composed of Aluminum and Silicon Carbide, have extremely lightweight as well as exhibits high resistance against mechanical impact loading.

Although functionally graded materials are new and developing technologies, they have a wide range of critical applications such as aerospace, nuclear, defense and automotive industry. Ever since the emergence of the idea of functionally graded materials, many scientific researches and studies have been performed [2-5]. Thermal barrier, corrosion and wear, automotive, energy, opto-electronics, aerospace and even used in the medical field, functionally graded materials is used in ballistic applications that required high mechanical strength. Therefore, it
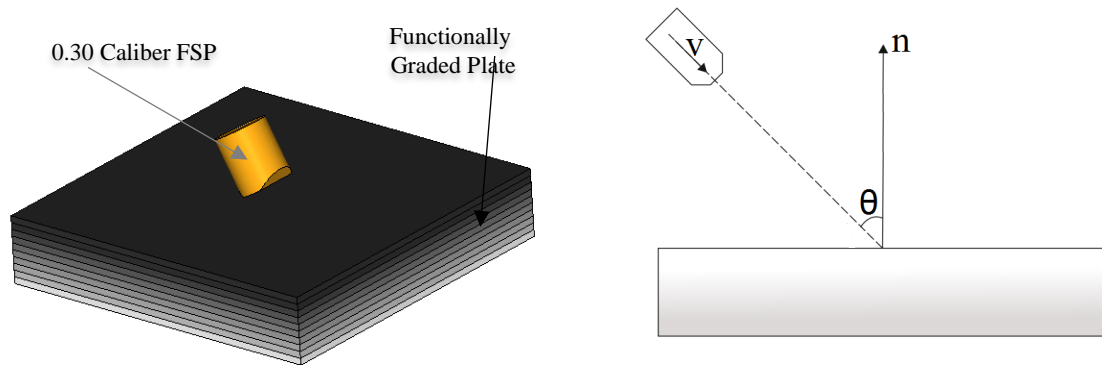
Figure 1: Functionally graded plate and 0.30 caliber FSP, the angle with the normal and impact point.

is important to determine the ballistic performance of functionally graded materials. This study investigates the effect of through-thickness material properties of the FG plates and impact angle of the projectile on the ballistic limits of FGM armor.

2. Theoretical Model

In order to determine the ballistic limits of functionally graded plates subjected to ballistic impact at several angles with a steel projectile, a series of numerical analyses were performed using nonlinear explicit finite element code ANSYS LS-DYNA [6]. The functionally graded plates were modeled in three different through-thickness material composition variations (n = 0.1, 1.0, and 10.0) to determine the material properties on the ballistic limit of FG plates. The locally effective material properties of the FG plates can be determined linearly or nonlinearly through-thickness variation of ceramic constituent using the Mori-Tanaka homogenization scheme [4,7]. The bottom layer of the plate is elasto-plastic pure metal (Al6061) and the top layer of the plate contains 70% linear-elastic ceramic (SiC) and 30% elasto-plastic metal (Al6061) constituents. The elasto-plastic behavior of a metal/ceramic FG plate was modelled using the TTO (Tamura-Tomota-Ozawa) model [4,8]. Thus, the failure strains in all layers were determined using TTO model in order to predict the damages each layer through the thickness of FG plates under ballistic impact. Functionally graded plate was considered 50 mm ×50 mm square and 10 mm in thickness. Ballistic impact analysis was carried out with 0.30 caliber Fragment Simulating Projectile (FSP) defined by STANAG-2920 [9] and MIL-DTL-46593B (MR) [10] (Fig.1). Plastic kinematic material model is used for projectile [11]. The mechanical properties of constituents of FG plate, and projectile are presented in Table 1. The FG plate and projectile were meshed with SOLID164 elements. The FG plate was modeled using 10 layers through the thickness and it was divided into 30 elements through the plate thickness, and each layer had 3 elements through thickness. The FG plate is fully clamped along its lateral surfaces.

Contact modeling is critical for predicting the ballistic response of armor structures. In this study, an ERODING_SINGLE_SURFACE contact was defined in order to take into account self-contacting interfaces during the projectile impact process. An ERODING_SURFACE_TO_SURFACE contact definition was defined between the projectile and the FG plate.

Table 1. Material properties of the constituents of FG plate and (FSP) projectile

Materials	Young's modulus (GPa)	Poissons's ratio	Density (kg/m^3)	Yield stress (MPa)	Tangent modulus (MPa)	Failure strain
Al 6061	67	0.33	2702	95	-	0.74
SiC	302	0.17	3100	-	-	0.01
AISI 4340H	200	0.29	7850	970	470	0.77

3. Results

The effect of the compositional gradient exponent "n" and impact angle of the projectile on the ballistic performance of FG plates were investigated for metal-rich (n = 0.1), linear (n=1.0) and ceramic-rich (10.0). The fragment simulating projectile (FSP), defined by STANAG-2920 and MIL-DTL-46593B (MR), was used to determine the V_{50} and the ballistic limit. Lambert-Jonas equation defined as

$$V_R = A \cdot (V_I^p - V_{50}^p)^{1/p} \tag{1}$$

where V_R is residual velocity, V_I is impact velocity and V_{50} is the ballistic limit velocity. A and p are empirical parameters depending on material. According to Lambert-Jonas equation, when the residual velocity is zero, impact velocity becomes equal to the ballistic limit velocity. A series of ballistic analysis were performed to determine the residual velocity is zero for all compositional gradient exponents (n = 0.1, 1.0, and 10.0) of the FG plates. Variations of residual velocity of the projectile as a function of the impact velocity for the metal-rich (n=0.1), linear (n=1.0) and ceramic-rich (n=10.0) material compositions of the FG plates subjected to projectile impact with a 0 degree angle were presented in Figure 2.

The FG plate with n=10.0 exhibits the highest ballistic limit, which is estimated to be 660 m/s. For the n=1.0, FG plate have a ballistic limit of 575 m/s, and the metal-rich (n=0.1) FG plate results in a ballistic limit value of 420 m/s. The residual velocities increase with increasing impact velocities for material composition values of 0.1, 1.0 and 10.0. Figure 3 shows that the residual velocities versus impact angle of projectile for metal-rich (n = 0.1), linear (n = 1.0) and ceramic-rich (n = 10.0) Al/SiC FG plates subjected to FSP having impact velocity of 750 m/s. For this velocity, the perforation limit angles are 55°, 39° and 25° for the FG plate with n=0.1, 1.0 and 10.0, respectively. The stiffness of the FG plate increases with increasing through-thickness ceramic phase, hence, this situation causes decreased perforation limit angle of the FG plate in according to the TTO model.
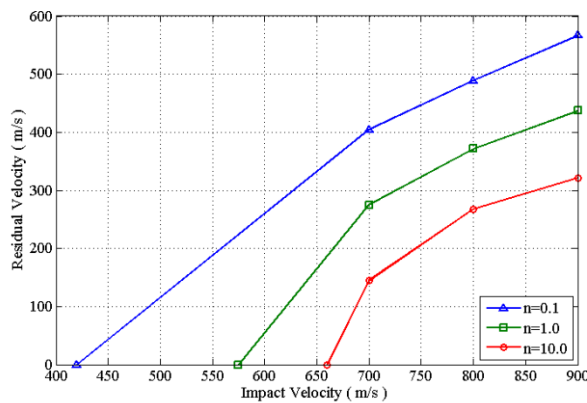
Figure 2: Residual velocity versus impact velocity of projectile for a) metal-rich (n = 0.1), b) linear (n = 1.0) and c) ceramic-rich (n = 10.0) Al/SiC FG plate (θ=0°).
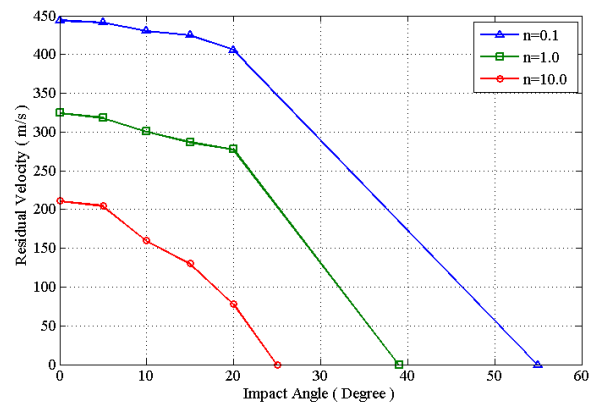
Figure 3: Residual velocity versus impact angle of projectile for a) metal-rich (n = 0.1), b) linear (n = 1.0) and c) ceramic-rich (n = 10.0) Al/SiC FG plate (v=750 m/s).

Figure 4 shows penetrated or perforated metal-rich (n = 0.1), linear (n = 1.0) and ceramic-rich (n = 10.0) Al/SiC FG plates impacted at 0º, 15º, 30º, 45º and 60º obliquity by a 0.30 caliber Fragment Simulating Projectile (FSP) which has impact velocity of 750 m/s at the time of 0.5 ms. The perforation time or penetration distance of the FG plate decreased with increasing through-thickness ceramic phase which causes high ballistic resistance. In addition, the ballistic effect of the FSP on the FG plate decreased with increasing impact angle of the FSP.
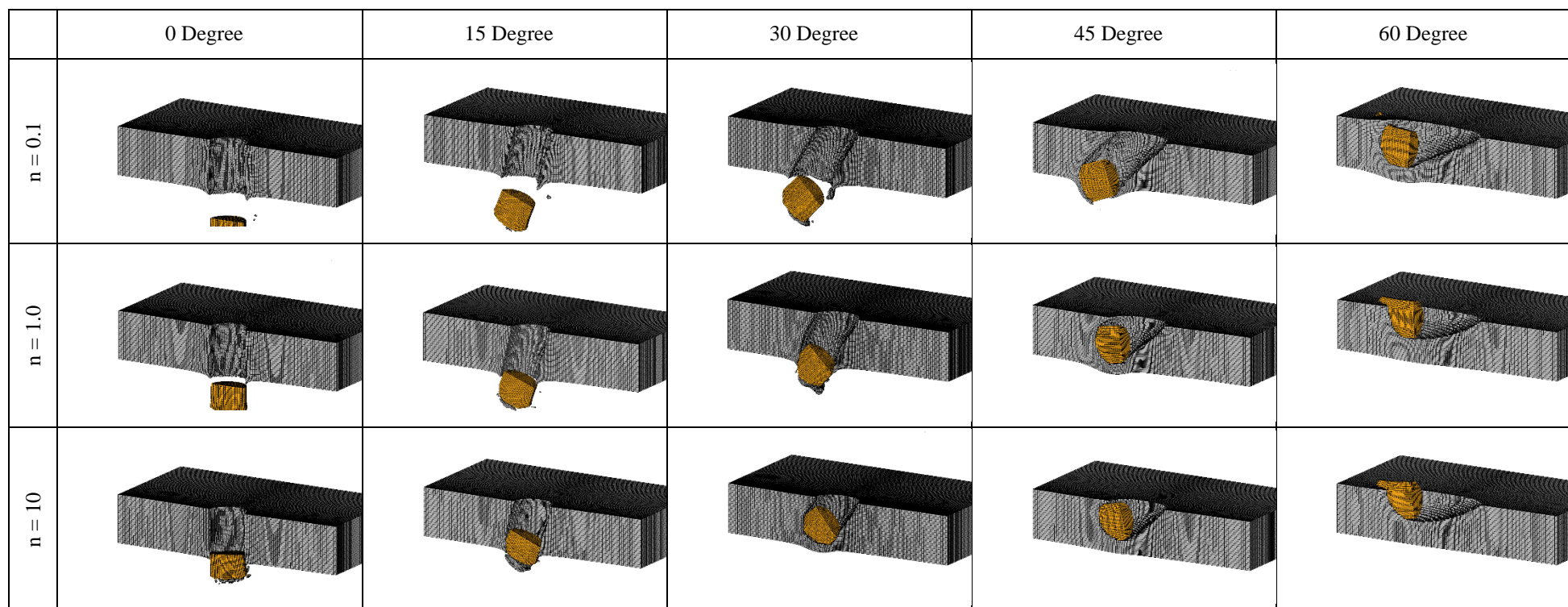
Figure 4: Penetrated or perforated metal-rich (n = 0.1), linear (n = 1.0) and ceramic-rich (n = 10.0) Al/SiC FG plates impacted at 0º, 15º, 30º, 45º and 60º obliquity by a 0.30 caliber Fragment Simulating Projectile (FSP) (v=750 m/s, time=0.5 ms.).

4. Conclusions

In this study, the effect of material composition and impact angle of the FSP on the ballistic response of the FG plates were investigated numerically. Three types of material composition (n = 0.1, 1.0, and 10.0) for the FG plate were considered during ballistic impact analyses. In order to determine the ballistic limit velocities and perforation limit angles of FG plates, a series of ballistic simulations were performed by a 0.30 caliber Fragment Simulating Projectile (FSP) using non-linear explicit finite element code ANSYS LS-DYNA®. Numerical results showed that increasing compositional gradient exponent caused an increase in ballistic limit velocity, while a decrease in perforation limit angle of the FG plate. This is because increasing the compositional gradient exponent causes more rigid FG circular plate against to ballistic impact. The perforation and penetration results showed that both through-thickness material composition and impact angle are very effective parameters on the ballistic response of the FG plates. The desirable ballistic response of the FG plate can be obtained by a proper selection of material composition depending on the impact angle of projectile.

Acknowledgements

References

[1] J.A. Zukas, High Velocity Impact Dynamics, John Wiley & Sons Inc., USA, 1990.
[2] N.A. Apetre, B.V. Sankar, D.R. Ambur, Low-velocity impact response of sandwich beams with functionally graded core, International Journal of Solids and Structures, 43 (2006), 2479-2496.
[3] E. Etemadi,A.A. Khatibi, M. Takaffoli, 3D finite element simulation of sandwich panels with a functionally graded core subjected to low velocity impact, Composite Structures, 89 (2009), 28-34.
[4] R. Gunes, M. Aydin, M.K. Apalak, J.N. Reddy, Experimental and numerical investigations of low velocity impact on functionally graded circular plates, Composites: Part B, 59 (2014), 21-32.
[5] N. Gupta, B.Basu, V.V. Bhanu Prasad, M. Vemuri, Ballistic Studies on TiB_2-Ti Functionally Graded Armor Ceramics, Defence Science Journal, 62(2012),382-389.
[6] ANSYS LS-DYNA®. The general purpose finite element software. Houston, Texas: Swanson Analysis Systems, Inc.
[7] T. Mori, K. Tanaka, Average stress in matrix and average elastic energy of materials with misfitting inclusions, Acta Metallurgica, 21 (1973), 571-574.
[8] I. Tamura, Y. Tomota, H. Ozawa, Strength and ductility of Fe-Ni-C alloys composed of austenite and martensite with various strength, In: Proceedings of the Third Conference on Strength of Metals and Alloys, 1 (1973) 611-615.
[9] NATO STANAG 2920: 2003. Ballistic test method for personal armour materials and combat clothing.
[10] MIL-DTL-46593 B (MR) w/AMENDMENT 1: 2008. Projectile, calibers .22, .30, .50, and 20 mm fragment-simulating.
[11] N.V. Nechitalio and R.C. Batra, Penetration of steel plates by long ceramic rods. Metalurgical and Materials Applications of Shock-Wave and High-Strain-Rate Phenomena, 64 (1995) 543-550.

Geometrically Nonlinear Free Vibration of Clamped-Clamped Functionally Graded Beam With an Edge Crack

CHAJDI Mohcine[1], MERRIMI El Bekkaye[1], EL BIKRI Khalid[1]

[1]*Mohammed V University in Rabat.ENSET - Rabat, LaMIPI. Rabat, Morocco*
chajdimohcine@gmail.com, e.merrimi@um5s.net.ma, k.elbikri@um5s.net.ma

Abstract

The free vibration of a functionally graded beam is investigated within the framework of Euler-Bernoulli beam theory and Von Karman geometric nonlinearity using the semi-analytical method. It is assumed that material properties follow power law distributions through thickness direction. It is assumed that the beam is fully clamped at its ends. A homogenization procedure is developed and used to reduce the problem under consideration to that of an equivalent isotropic homogeneous cracked beam. Upon assuming harmonic motion, the discretized expressions for the total strain and kinetic energies of the beam are then derived, and by applying Hamilton's principle, the problem is reduced to a system of coupled nonlinear algebraic equations. Direct iterative method is employed for solving the eigenvalue equation, in order to show the effect of the crack depth and the influences of the volume fraction on the dynamic response.

Keywords: *vibration, functionally graded material, beam, crack.*

1. Introduction

Functionally graded materials (FGMs) have huge immense attention from research and engineering communities due to their outstanding properties such as they improved inter laminar stress reduction, high resistance to temperature gradients, high wear resistance, etc. However, it is well known that crack in a structural element caused by fatigue or stress concentration affects its stiffness, damping properties and certainly changes its vibration characteristics [1]. Further, the increasing use of FGM beams as structural components in various fields has necessitated the study of their dynamic behavior. In recent years, the large amplitude vibration and nonlinear analysis of FGM structures have attracted increasing research efforts. The investigations concerning the effect of crack defects on the dynamic behavior of FGM structures haven also received increasing attention recently [2]. Kitipornchai S. et al [3] studied the nonlinear free vibration of edge-cracked FGM beams based on Timoshenko beam theory and Von Karman nonlinearity. Ke et al. [4] considered the free vibration and elastic/post buckling of cracked Timoshenko FGM beam by using Ritz method. Yang and Chen [5] discussed analytically the influence of open edge cracks on the vibration and buckling of Euler-Bernoulli FGM beams with different boundary conditions. In the present paper, the problem of geometrically nonlinear free vibrations of clamped-clamped FGM beam containing an open crack in the center is investigated using Hamilton's principle and spectral analysis. Based on the classical theory of beams developed by Euler-Bernoulli and Von Karman assumptions [6], a homogenization procedure, previously proposed in [7] in the case of laminated composed beams, is used which reduces the problem studied to that of isotropic homogeneous cracked beams. Iterative solutions are presented to calculate the fundamental non linear parameters. This work is restricted to the fundamental mode in order to concentrate on the study of the influence of the crack and the fraction volume on the non-linear dynamic response.
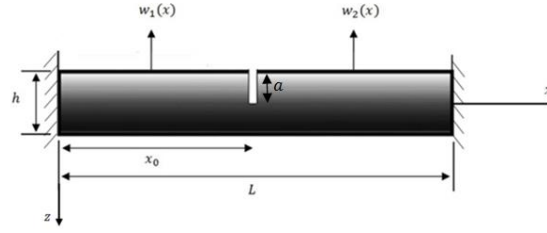
Figure 1: Geometrical modelling of the FGM beam with crack.

2. Theory and formulation for the free vibration

2.1 Material properties

Fig. 1 shows an FGM beam of length L and thickness h, containing an edge crack of depth a located at a distance x_0 from the left end. Its Young's modulus $E(z)$ and mass density $\rho(z)$ are functionally graded in the thickness direction.

According to the rule of mixture (power-law distribution), the effective material properties P, can be expressed as:

$$P(z) = (P_c - P_m)\left(\frac{z}{h} + \frac{1}{2}\right)^k + P_m \tag{1}$$

Where the subscripts m and c denote the metallic and ceramic constituents, respectively. And k is a non-negative parameter (power-law exponent) which dictates the material variation profile through the thickness of the beam.

2.2. Nonlinear free vibration analysis

The Von Karman type nonlinear strain displacement relations are given by:

$$\varepsilon_x^a = \frac{\partial u}{\partial x} + \frac{1}{2}\left(\frac{\partial W}{\partial x}\right)^2 , k_x = \frac{\partial^2 W}{\partial x^2} \tag{2,3}$$

The elastic deformation energy V_T total Euler-Bernoulli beam is given by:

$$V_T = \frac{1}{2}\int_0^l N_x \varepsilon_x^a + M_{fy} k_x dx \tag{4}$$

Where N_x is the axial resultant force and M_{fy} is the bending moment, are linked to ε_x^a and k_x respectively:

$$N_x = \int_s E(z)\varepsilon_x^a dS = bA_{11}\varepsilon_x^a + bB_{11}k_x \tag{5}$$

$$M_{fy} = \int_s zE(z)\varepsilon_x^a dS = bB_{11}\varepsilon_x^a + bD_{11}k_x \tag{6}$$

Where A_{11}, B_{11} and D_{11} are the extension-extension, bending-extension, bending-bending coupling coefficients respectively.

Using the axial static equilibrium equation for the beam, once the axial inertia and damping terms are neglected, and applying the conditions irremovable ends, the potential energy V_T only written in terms of transverse displacement Was follows:

$$V_T = \frac{(ES)_{eff}}{8l}\left(\int_0^l \left(\frac{\partial W}{\partial x}\right)^2 dx\right)^2 + \frac{(EI)_{eff}}{2}\int_0^l \left(\frac{\partial^2 W}{\partial x^2}\right)^2 dx \tag{7}$$

Such as:

$$(ES)_{eff} = bA_{11}, \qquad (EI)_{eff} = b\left(D_{11} - \frac{B_{11}{}^2}{A_{11}}\right) \qquad (8,9)$$

Then the expression of the energy of deformation due to the crack and the kinetic energy neglecting the axial and rotational inertia can be written as:

$$V_c = \frac{(EI_{eff})^2}{2K_f}\left(\frac{\partial^2 W}{\partial x^2}\right)^2\bigg|_{x=x_0}, \qquad T = \frac{(\rho S)_{eff}}{2}\int_0^l \left(\frac{\partial W}{\partial t}\right)^2 dx \qquad (10,11)$$

To obtain non-dimensional parameter, to find equations that do not depend on the size or characteristics of the beam, one puts:

$$x^* = \frac{x}{L}, \qquad W_i^* = \frac{W_i(x)}{H} \qquad (12,13)$$

Applying Hamilton's principle and expanding the displacement W in the form of a finite series, the following set of nonlinear amplitude equations is obtained:

$$2a_i K_{ir}^* + 3a_i a_j a_k B_{ijkr}^* - 2\omega^{*2} a_i M_{ir}^* = 0 \qquad (14)$$

Where K_{ir}^*, B_{ijkr}^* and M_{ir}^* m stand for the non-dimensional classical rigidity tensor, the nonlinear rigidity tensor and the mass tensor, respectively, which are defined as:

$$K_{ij}^* = \int_0^l \frac{\partial^2 W_i^*(x)}{\partial x^{*2}}\frac{\partial^2 W_j^*(x)}{\partial x^{*2}}dx^* + \beta \frac{\partial^2 W_i^*(x)}{\partial x^{*2}}\bigg|_{x_0^*}\frac{\partial^2 W_j^*(x)}{\partial x^{*2}}\bigg|_{x_0^*} \qquad (15)$$

$$B_{ijkl}^* = \alpha\left(\int_0^l \frac{\partial w_i^*(x)}{\partial x^*}\frac{\partial w_i^*(x)}{\partial x^*}dx^*\right)\left(\int_0^l \frac{\partial w_k^*(x)}{\partial x^*}\frac{\partial w_l^*(x)}{\partial x^*}dx^*\right) \qquad (16)$$

$$M_{ij}^* = \int_0^l w_i^*(x)w_j^*(x)\, dx^* \qquad (17)$$

With $\alpha = \frac{h^2}{48}\frac{(ES)_{eff}}{(EI)_{eff}}$ for FGM beam with a rectangular section,

and $\beta = \frac{(EI)_{eff}}{K_f L}$ $\qquad (18,19)$

3. Numerical results and discussions

In the problem considered herein, the top surface of the FGM is ceramic rich (Ec=350GPa, ρc=3800 Kg/m3), whereas the bottom surface of the FGM is metal rich (Em=210GPa, ρm=7850 Kg/m3).

In table 1, the first nonlinear frequency ratios ω_{nl}^*/ω_l^*, calculated in the present work, is compared with the results obtained in [6]. It is noted that the solutions given in [6] overestimate the frequencies of the fully clamped FGM beam, especially for high values of dimensionless amplitude.

Table 1: Comparisons of first non-linear mode shape of a C–C cracked beam with k=0, and isotropic homogeneous C-C beams for a/h = 0.1

W_{max}^*	ω_{nl}^*/ω_l	
	Present	[6]
0.079575821	1.00113980	1.00053987
0.47617067	1.03995969	1.03942916
0.94572196	1.14878218	1.14844776
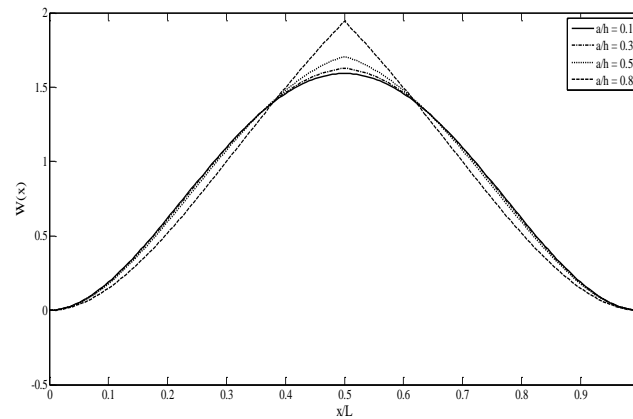
Figure 2: First non-linear mode shape of a beam with a crack of various depths

It can be shown from Fig. 2, that from the crack of 0.5mm depth we notice on the graphs that there is a discontinuity at the center of the beam, this may mean that local flexibility and increases the stiffness of the material decreases.

4. Conclusion

In this work the geometrically non-linear free vibrations of a clamped–clamped FGM beam with an edge crack is studied using a theoretical model developed previously in [6] for thin elastic structures, The model, based on Hamilton's principle and spectral analysis, reduces the non-linear free vibration problem to a set of non-linear algebraic equations and the homogenization procedure is used which reduces the problem studied to that of isotropic homogeneous cracked beams. Numerical data corresponding to various values of the crack depths up to about once the beam thickness are given. The results show that the crack causes, as expected, a decrease in the natural frequencies of flexural vibrations of the beam. The intensity of these changes increases non-linearly with the increase of the relative depth of the crack. The natural modes are also affected by the presence of the crack.

References

[1] Dimarogonas, A.D., 1996a. Vibration of cracked structures: a state of the art review. Eng. Fract. Mech. 55, 831-857.

[2] Aydin, K., Free Vibration of Functionally Graded Beams with Arbitrary Number of Surface Cracks, European Journal of Mechanics / A Solids (2013), doi: 10.1016/ j.euromechsol.2013.05.002.

[3] S. Kitipornchai, L.L. Ke, J. YangandY. Xiang, Nonlinear vibration of edge cracked functionally graded Timoshenko beams, Journal of Sound and Vibration ,Volume 324, Issues 3–5, 24 July 2009, Pages 962–982.

[4] Ke, L., Yang, J. & Kitipornchai, S. Meccanica (2010) 45: 743. Doi: 10.1007/s11012-009-9276-1.

[5] J.Yang,Y.Chen, Free vibration and buckling analyses of functionally graded beams with edge cracks, Composite Structure 83 (2008) 48–60.

[6] K. El Bikri, R. Benamar, M.M. Bennouna, Geometrically non-linear free vibrations of clamped-clamped beams with an edge crack, Composite Structure 84 (7)(2006)485–502.

[7] K. El Bikri, E. B. Merrimi, R. Benamar, "Geometrically Nonlinear Free Vibrations of Laminated Composite Beams: An Effective Formulation", Applied Mechanics and Materials, Vols. 105-107, pp. 1681-1684, 2012

FEM and analytical analysis of the bending stress distribution in graded zirconia-based dental ceramics

Bruno Henriques[1], Douglas Fabris[1], Julio C.M. Souza[3], Joana Mesquita-Guimarães[1], Yu Zhang[4], Marcio C. Fredel[1], Filipe Silva[2]

[1]*Ceramic and Composite Materials Research Group (CERMAT), Federal University of Santa Catarina (UFSC), Florianópolis/SC, Brazil*
[2]*CMEMS-UMinho, University of Minho, Campus de Azurém, Guimarães, Portugal*
[3]*CEPID, Department of Dentistry (DODT), Universidade Federal de Santa Catarina (UFSC), Florianópolis/SC, Brazil*
[4]*Department of Biomaterials and Biomimetics, New York University College of Dentistry, New York University, New York, USA*

Abstract

This study evaluated the biaxial flexural stresses in graded zirconia-feldspathic porcelain composites. A finite element method and an analytical model were used to simulate the piston-on-ring test and to predict the biaxial stress distributions across the thickness of discs. An axisymmetric model and a flexure formula of Hsueh et al. were used in the FEM and analytical analysis, respectively. Continuous and stepwise transitions (using a power function) from the bottom zirconia layer to the top porcelain layer were studied. The highest tensile stresses were registered for porcelain rich interlayers (p=0.25) whereas the zirconia rich ones (p=8) yield the lowest tensile stresses. In addition, the maximum stresses in a graded structure can be tailored by altering compositional gradients. A decrease in maximum stresses with increasing values of p (a scaling exponent in the power law function) was observed. Graded zirconia-feldspathic porcelain composites exhibited a more favourable stress distribution relative to conventional bilayered systems. This fact can significantly impact the clinical performance of zirconia-feldspathic porcelain prostheses, namely reducing the fracture incidence of zirconia and the chipping and delamination of porcelain.

Keywords: Biaxial flexural test, stress distribution, functionally graded ceramic, zirconia

1. Introduction

Dental restorations have two main requirements: adequate strength and good aesthetic. Porcelain is widely used as dental material due to its aesthetic and color that matches the remaining natural teeth. However, it has low strength and toughness; thus, it is unable to withstand high tensile stresses [1]. Therefore, a stronger material must be used to support the porcelain veneer, increasing the overall strength of the restoration [2]. Zirconia have been used as framework material in dental restorations due to its excellent mechanical properties, good aesthetic and biocompability [2,3]. In the processing of all-ceramic restorations, porcelain is fired onto the zirconia framework at high temperatures, creating thermal residual stresses upon cooling to room temperature that arise mainly due to different CTEs (Coefficient of Thermal Expansion) between the framework and the veneering porcelain [4,5]. At the same time, the mismatch of elastic properties between the two material favour the formation of deleterious stress fields at the interface when the restoration is subjected to occlusion loading, which can lead to crack formation, porcelain chipping and ultimately catastrophic failure of the prosthesis [5,6]. A solution to this problem, related to the mismatch between mechanical and thermal properties of the different materials, is using a composite intermediate layer with intermediate properties between the framework and the veneering that will reduce the

mismatches in materials properties. This solution, so-called Functionally Graded Material (FGM), consist in a gradual change in the volume fraction between two phases [7], allowing a smooth transition in the materials properties, decreasing their mismatch.

Uniaxial bending tests (e.g. three or four points bending tests) and biaxial bending tests (e.g. ball-on-three-balls and piston-on-ring tests) are the standard methods to evaluate the flexural strength of ceramics. One problem with uniaxial bending test is the sensitivity to flaws along the sample edges, resulting in large variations in the strength data recorded [8]. However, in a biaxial test, the maximum stresses are located near the centre of the sample, and edge failures are usually eliminated, resulting in a more accurate estimate of strength [9]. Besides, restorative materials are usually subjected to a multiaxial loading in clinical situations, thus the biaxial data are more useful for the component design [10]. For these reasons, biaxial bending tests are the standard method for dental materials evaluation. In a biaxial test, the sample, generally a disc, is supported on its lower face by rigid spheres or a ring, while a load is applied on the centre of its upper face.

The objective of this study is to evaluate the mechanical behavior of a compositionally graded zirconia-porcelain disc and compare it with the classic situation, where there is a sharp interface between the two materials. Finite elements method (FEM) was used to simulate the stress state in a "piston-on-ring" biaxial test. Several different gradations profile were simulated to evaluate their influence in the stress state. The simulated results were compared with an analytical solution proposed by Hsueh et al [10,11].

2. Methods

The discs were 2 mm thick and had radius 7 mm. The loading piston has radius 0.075 mm and the ring had 6 mm. The force applied by the piston was considered 1000 N. For the analysis of the classic situation, a disc with two layers was considered. The top layer is made of feldspathic porcelain and the bottom one is made of zirconia (Y-TZP), with 1 mm each. For the graded discs, a stepwise gradation was considered. The disc contain seven layers, each one made of constant composition. The top and the bottom layers were still porcelain and zirconia, respectively, and had a constant thickness (0.2 mm). The five intermediate layers were made of a zirconia and porcelain mixture (volume fracture of porcelain of 0.1, 0.3, 0.5, 0.7 and 0.9, from the bottom to top layer, respectively) and have varying thickness. To calculate the thickness of each intermediate layer, first a continuous change in the volume fraction of porcelain was considered, represented by a power law function (eq. 1), where the volume fraction is a function of the axial position (y), the thickness of the graded region (t) and a parameter p:

$$f_{porc} = \left(\frac{y}{t}\right)^p \tag{1}$$

For different values of p, the concentration of zirconia and porcelain along the thickness changes as shown in Fig.1(a). To calculate the thickness of each layer, first the values of y/t for a given value of p were calculated for the corresponding values of volume fraction of porcelain of 0.0, 0.2, 0.4, 0.8 and 1.0. These values were used to calculate the thickness of each layer as shown in Fig. 1(b).
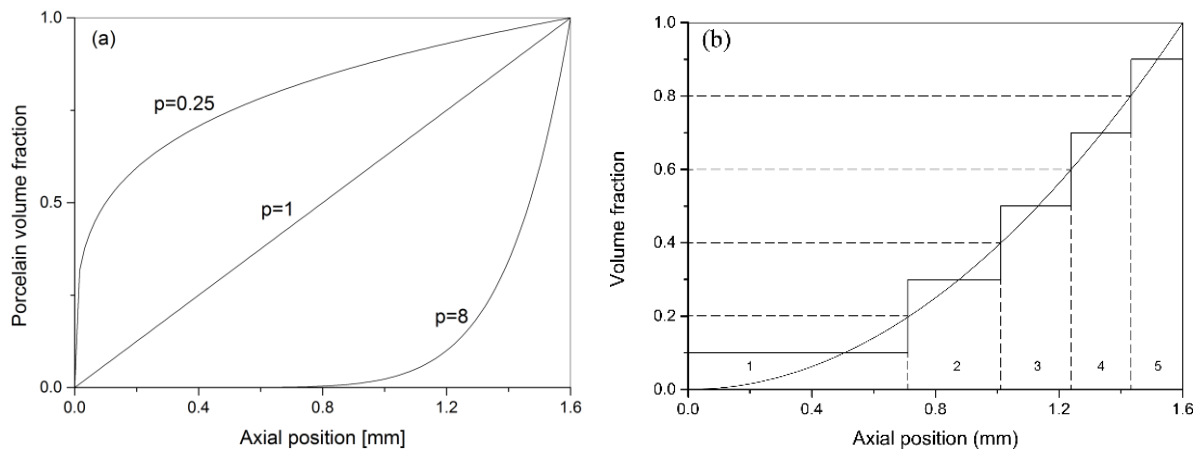
Figure 1 – (a) Variation in the volume fraction of porcelain along thickness for different values of *p* and (b) procedure to calculate the layers thickness of the graded region.

The properties of each layer were calculated by the law of mixtures. The properties of the base materials (zirconia and porcelain) were obtained from the study of Zhang et al. [12].

Finite element method was used to simulate the stress distribution on the 'piston-on-ring' test. A two dimensional axisymmetric model was used to simplify the calculations. The simulations were conducted using the commercial software COMSOL. All layers are considered to remain bonded. The supporting ring is fully constrained, and the loading piston cannot move in the horizontal axis. The force is considered constant in the contact area between the piston and the disc. An extremely fine mesh with free triangular elements was used to ensure the accuracy of the results. The elements were refined even more near the region where the stress was the largest, i.e. the region near the z-axis, which is the centre of the disc. In this study, the friction between the disc and the supporting ring was ignored. The analysis was focused on the central axis of the disc, where the stress is maximum. As previously discussed, the results were compared with an analytical model.

3.   Results and discussion

Figure 2(a) shows the stress distribution along the thickness in the center of the disc. The maximum stress is 627 MPa and it is located at the bottom of the disc. For the graded disc, conditions for p=0.25, 0.5, 1, 2, 4 and 8 were simulated and calculated analytically. Figure 2(b) shows the simulated and analytical stress distribution for the FGM discs. The highest and lowest values, taken from the simulated model, were registered for p=0.25 and p=8, with 681 MPa and 530 MPa, respectively. The simulated results agree well with the analytical model, with a maximum deviation of 5% between them observed for p=8, where the maximum deviation between the results is registered. The exception is the region under compression, near the loading piston. This is because the analytical model does not include the contact stress under the piston in the calculations.

The results showed that the huge stress mismatch at the interface of bilayered discs is replaced by a smooth profile in stress distribution of graded discs. The stress mismatch between layers need to be controlled because it can lead to delamination at the interfaces if the bonding is not strong after multilayer fabrication [13]. Besides, the gradation of properties decreased the maximum stress at the bottom of the disc. For the graded discs, discs with higher content of zirconia (higher p values) in the graded region showed smaller maximum stress than the ones with smaller values of p. The maximum tensile stress in the disc is increased by 28% when the content of the graded region switches from zirconia rich (p=8) to porcelain rich (p=0.25).

4.   Conclusion

The results of a simulated piston-on-ring test for a bilayered disc with sharp interface and a graded disc were compared. The graded disc has a lower maximum stress value in the centre than the bilayered disc. The stress discontinuities are also significantly smaller in the graded disc. Increasing the porcelain content in the graded region, decreased the maximum stress at the bottom of the discs. The simulation using finite element method agrees well with the model proposed by Hsueh et al.
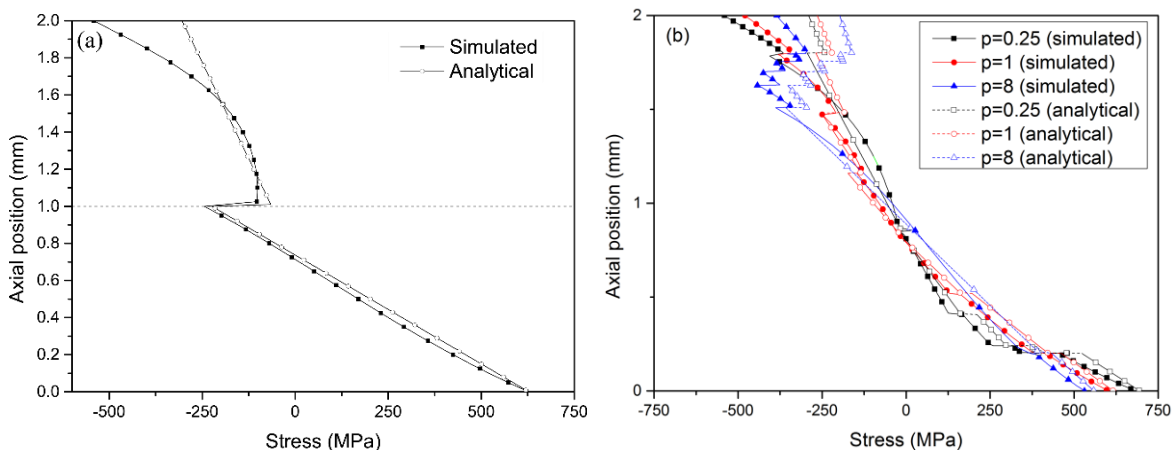
Figure 2 – Stress distribution throughout the disc thickness for a biaxial test considering (a) the traditional situation and (b) the FGM.

References

[1] Fischer J, Stawarczyk B, Hämmerle CHF. J Dent, 36(2008), 316–21.
[2] Zarone F, Russo S, Sorrentino R. Dent Mater, 27(2011), 83–96.
[3] Denry I, Kelly JR. Dent Mater, 24(2008), 299–307.
[4] Baldassarri M, Stappert CFJ, Wolff MS, Thompson VP, Zhang Y. Dent Mater, 28(2012), 873–9.
[5] Choi JE, Waddell JN, Swain M V. Dent Mater, 27(2011), 1111–8.
[6] Swain M V. Acta Biomater, 5(2009), 1668–77.
[7] A. Kawasaki, R. Watanabe, Ceram. Int., 23(1997) 73–83.
[8] Wagner W., Chu T. J Prosthet Dent, 76(1996), 140–4.
[9] Thompson GA. Dent Mater, 20(2004), 51–62.
[10] Hsueh C-H, Luttrell CR, Becher PF. Dent Mater 22(2006), 460–9.
[11] Hsueh CH, Luttrell CR, Becher PF. Int J Solids Struct, 43(2006), 6014–25.
[12] Z. Zhang, S. Zhou, Q. Li, W. Li, M. V. Swain. Dent. Mater, 28 (2012), e6-e14.
[13] Fabris, D., Souza, J. C., Silva, F. S., Fredel, M., Mesquita-Guimarães, J., Zhang, Y., & Henriques, B. Ceramics International, 42(9) (2016), 11025-11031.

Fabrication and Characterization of Functionally Graded CNTs/PMMA Microcellular Foams with Designed Cell Structure

Lianmeng Zhang[1,a], Ruizhi Zhang[1,b], Guoqiang Luo[1,c] *, Chun Gu[1], Qiang Shen[1], Meijuan Li[1], Chuanbin Wang[1], Jian Zhang[1], Yuanlu Xiong[2].

[1]*State Key Lab of Advanced Technology for Materials Synthesis and Processing, Wuhan University of Technology, Wuhan 430070, China*
[2]*International School of Materials Science and Engineering, Wuhan University of Technology, Wuhan 430070, China*
E-mail: [a]*lmzhang@whut.edu.cn,*[b]*zhangrz1991@gmail.com,*[c]*luogq@whut.edu.cn*

Abstract

Light weight and high strength graded foams are of great significance to shock resistance in both civil and military fields. In this paper, a facile method was adopted to fabricate functionally graded CNTs/PMMA microcellular foams with designed cell structure. Various gradient CNTs/PMMA microcellular materials were hot pressured together, followed by batch foaming with supercritical carbon dioxide as blowing agent in a specialized constraint mold. Mechanical properties of different functionally graded CNTs/ PMMA microcellular foams and the bonding strength between adjacent layers in the functionally graded foams were investigated by the universal mechanical test machine. FESEM were used to visualize the foam morphology and bonding structure. The results show that the graded CNTs/ PMMA microcellular foams exhibit wider cell distribution than uniform microcellular foams. It is also found that the functionally graded foam is superior in the mechanical properties to the uniform one, and the structure could be optimized to achieve desirable mechanical properties.

Keywords: PMMA, Functionally Graded Foam, Morphology, Mechanical Properties

Paper withdrawn

Plastic Wave Propagation Velocity in Graded Metallic Foam Materials

M. Borovinšek[1], F. Schleifer[2], Z. Ren[3]

[1]University of Maribor, Faculty of Mechanical Engineering, Slovenia,
matej.borovinsek@um.si
[2]Universität Bayreuth, f.schleifer@gmx.net
[3]University of Maribor, Faculty of Mechanical Engineering, Slovenia, zoran.ren@um.si

Abstract

Plastic wave propagation in metallic foam materials under compression deformation at different strain rates was studied by means of computational simulations. A homogenized modelling approach was used, where properties of the homogenized material model were experimentally determined for density dependent material parameters of a porous AlSi7 metallic foam [1].

Parametric explicit finite element computer simulations at different compressive loading speeds and foam densities were carried out to determine the relationship between the loading speed, density and plastic wave speed. Simulation results showed that plastic wave speed is constant at chosen constant loading speed and constant foam density. The simulation results were used to derive an empirical relation for the corresponding plastic wave speed. These findings were then applied to simulations of foam samples with spatially distributed (graded) porosity. Computationally determined plastic wave speeds in graded metallic foams were compared with the empirical model predictions, where a very good agreement of results was observed.

Keywords: metallic foam, graded porosity, plastic wave propagation, dynamic analysis, computational simulations

1. Introduction

The metallic foam materials became first popular in the 1960's and since then a variety of production methods and applications have been developed. Since the 1990's the demand for metallic foams is increasing mostly because of the material's superior performance in terms of their weight-specific stiffness and energy absorption. However, a reliable characterization of their material parameters is required for their broad industrial use.

The metallic foams have a specific stress-strain relationship under uniaxial compressive loading that shows a distinct plateau region due to progressive plastic buckling deformation of the cell walls and trusses. At higher strains the material eventually densifies, resulting in a sudden increase of stress [2]. This behavior was first described with a stress-strain function by Rusch [3, 4, 5].

Avalle et al [1] have conducted experiments of aluminum foams with different densities between 0.27 and 0.68 g/cm3 to determine parameters for the Crushable Foam material model, available in the finite element software Abaqus. They were able to reproduce the results of their experiments with the finite element simulations.

Crushable foam plasticity model is intended for the analysis of crushable foams that are typically used as energy absorption structures. It is able to model the enhanced ability of a foam material to deform in compression due to cell wall buckling processes. The model applies a yield surface in the shape of the ellipsoid which evolves with plastic strain but retains its shape [6].
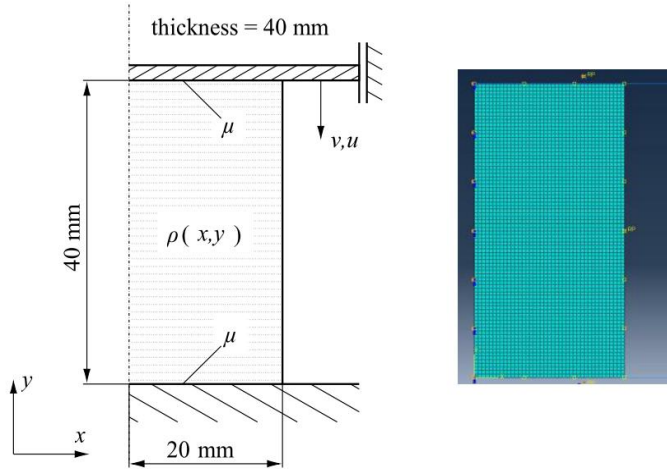
Figure 1: Two dimensional finite element model used for simulations (left) and meshed finite element model (right). Symmetric boundary conditions are applied to the middle axis and loading is applied via two rigid plates.

2. The finite element model

Dynamic simulations of metallic foam samples under compressive loading were carried out using the finite element system Abaqus. A cubical foam sample with a size of 40 x 40 x 40 mm was used, which corresponds to specimens tested by Avalle at al. [1]. A simplification from a three dimensional model to a two dimensional plain strain symmetric model was assumed. The model is shown in Figure 1. The boundary conditions were applied via two rigid plates at the top and bottom of sample with fixed rotational degrees of freedom. The bottom plate was fixed in space while the top plate moved with a prescribed constant velocity v towards the bottom plate. Simulations ended when a prescribed displacement u was reached.

The influence of geometrical simplification (3D to 2D) was examined beforehand by comparing the results obtained by the 3D models solved with an explicit solver and 2D models solved with an implicit solver, which showed comparable load dependent behavior over several orders of magnitude.

The finite element mesh of the model consists of 3200 uniform four node bilinear generalized plane strain quadrilateral elements. The finite element mesh was chosen so that its resolution precisely mapped all applied density distribution fields.

3. The material model

The crushable foam material model was used to model the metallic foam behavior. The foam material parameters were taken from Avalle et al. [1]. The graded density of foam sample was achieved by prescribed functional dependence of all material parameters from the density field variable.

3.1 Density distribution

The sample density distribution was symmetric in respect to the symmetric axis of the model. A constant, linear and parabolic density fields were investigated in this study. The density was varied in dependence from x direction (Figure 1). Non-constant density field was computed by the following equation:

$$\rho(x) = \rho_0 \cdot \left(1 + \beta \cdot \left(\frac{x}{l}\right)^n\right) \tag{1}$$

where ρ_0 represents the initial density, parameter β defines the maximum relative density variation, l is the length of the specimen and n is used to define a linear ($n = 1$) or parabolic ($n = 2$) density field. The density function was normalized to an average density of 0.6 g/cm^3 in this study to achieve equal mass samples.
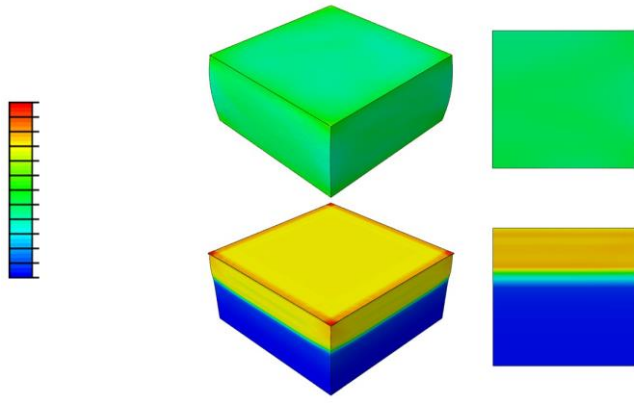
Figure 2: True strain plotted onto the deformed three dimensional and two dimensional models loaded with the speeds of $v = 20$ m/s (top) and 200 m/s (bottom).

4. Results and discussion

The first simulations were used to validate the used computational models by reproducing the experiments and simulations of static uniaxial compression and hydro-compression tests of Avalle et al. in a satisfactory manner.

4.1 Constant density field

Figure 2 shows the computed true strain in loading direction for the loading speeds of $v = 20$ m/s and 200 m/s plotted onto the deformed specimens at engineering strain of $\varepsilon_{eng} = 0.5$ for three and two dimensional models. Material density is 0.80 g/cm^3. The deformation and strain distributions are similar for both models (2D and 3D). In uniaxial loading ε_{yy} is the only non-zero component of the strain tensor and will henceforth be referred to as the strain ε.

It was found that at comparably low loading speeds the specimen deforms uniformly. The stresses and strains are almost constant throughout the volume as quasi static assumptions would predict. This behavior is shown in Figure 2 for a loading speed of 20 m/s. Small deformations can be observed perpendicular to the loading direction due to the Poisson's ratio effect. Yielding starts almost instantaneously as it is typical for ductile metallic foams [2]. The determined true strain values are therefore treated as equal to plastic strain values.

For higher loading speeds the behavior changes. The deformation is not uniform anymore due to inertia effects. As the influence of the inertia effects rises, evenly distributed deformation is replaced by a state in which the region in contact with the loading plate deforms while the deformation of the rest of the specimen is governed by propagation of elastic and plastic waves. Figure 2 shows that there is a distinct border between plastically deformed (green) and undeformed material (blue). Such behavior was previously experimentally determined Tanaka et al. [7].

Performing parametric simulations with varying loading speeds and different constant material densities showed that the speed of the plastic wave front c_{pl} is constant through time and its dependence on the loading speed v and the foam density ρ can be determined by the following equation:

$$c_{pl}(\rho) = \frac{\alpha_A}{v} \cdot \rho + v + \alpha_B \cdot \rho \tag{2}$$

α_A and α_B are the constants obtained by regression analysis and are equal to 6051.246 m^{5}s^{-2}t^{-1} and 66.373 m$^{2.5}$s^{-1}t$^{-0.5}$, respectively.
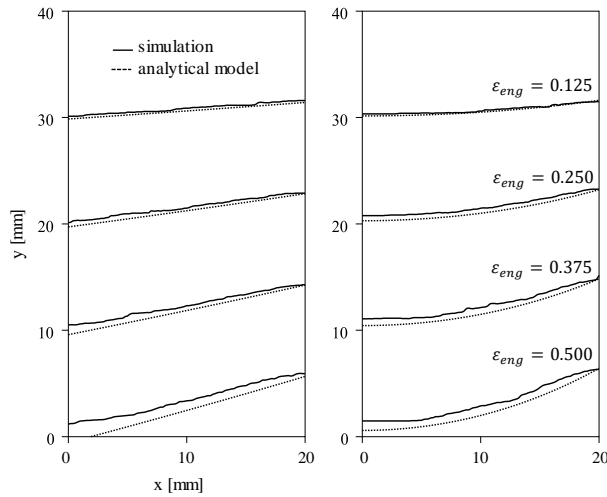
Figure 3: Propagation of the deformation front through the material of non-constant density for a linear (left) and a parabolic density field (right) determined with the simulation and analytical model

4.2   Non-constant density fields

Figure 3 shows the propagation of the plastic deformation front through samples with non-constant density at different engineering strains for a linear (left) and a parabolic density distributions (right) along the *x* axis. The mean density of the material is 0.6 g/cm³, β is -0.4 and +0.4 for the loading speed equals to 100 m/s. The solid lines show the obtained simulation results while the dotted lines show predictions made with the analytical model (2).

To compare the results of the simulations ($\bar{c}_{pl}$) and the results of the analytical model ($\bar{c}_{pl,am}$) the plastic wave speed was determined in dependence of the *x*-coordinate (hence in dependence of the density) from the *y* position of the front and the corresponding time. Then the average $\overline{err}$ and maximal err_{max} relative deviation of the analytical model was determined. Comparison of the results is given in Table 1. The average speeds of the plastic wave fronts are around 182 m/s. The deviations are in general larger by the linear density distribution at the sample center where the largest deviation equals to 4.53 %.

5.   Conclusions

Dynamic simulations of metallic foam samples in compression over a large range of loading speeds were conducted to investigate the speed variation of the plastic wave front.
For high loading speeds it was found that the material deforms at the impact region while the rest of the material deforms through propagation of elastic and plastic deformation fronts. Both fronts propagate through the material at speeds dependent of the density. An analytical model was derived to describe the dependence of the speed of plastic front propagation on the loading speed v and the foam density ρ for analyzed foams.
To test the analytical model simulations with non-constant density distributions were conducted. Comparison of the results shows a good agreement between the simulations and the analytical model with a maximal relative deviation of 4.53 %.

Table 1: The resulting average plastic wave speeds determined by the simulations $\bar{c}_{pl}$, determined by the analytical model $\bar{c}_{pl,am}$ and the average $\overline{err}$ and maximal err_{max} relative deviation of the analytical model from the simulations

Density field type	β	$\bar{c}_{pl}$	$\bar{c}_{pl,am}$	$\overline{err}$	err_{max}
	[/]	[m/s]	[m/s]	[%]	[%]
Linear	-0.4	183.23	187.61	2.39	4.25
Linear	+0.4	181.82	187.73	3.25	4.53
Parabolic	-0.4	183.84	187.65	2.07	2.64

References

[1] M. Avalle, D. Lehmhus, L. Peroni, H. Pleteit, P. Schmiechen, G. Belingardi, M. Busse, International Journal of Crashworthiness, 14 (2009), 269–285

[2] L. J. Gibson, M. F. Ashby, Cellular Solids: Structure and Properties, Cambridge University Press, 1997

[3] K. C. Rusch, Journal of Applied Polymer Science 13 (1969), 2297–2311

[4] K. C. Rusch, Journal of Applied Polymer Science 14 (1970), 1433–1447

[5] K. C. Rusch, Journal of Applied Polymer Science 14 (1970), 1263–1276

[6] V. S. Deshpande, N. A. Fleck, Journal of the Mechanics and Physics of Solids, 48 (2000), 1253–1283

[7] S. Tanaka, K. Hokamoto, S. Irie, T. Okano, Z. Ren, M. Vesenjak, S. Itoh, Measurment 44 (2011), 2185–2189

Low Velocity Impact Performance of Honeycomb Sandwich Structures Reinforced by Functionally Graded Face Plates

Kemal Arslan[1*], Recep Gunes[2], M. Kemal Apalak[3], J.N. Reddy[4]

[1]*Graduate School of Natural and Applied Sciences, Erciyes University, Turkey, karslan@erciyes.edu.tr*
[2]*Department of Mechanical Engineering, Erciyes University, Turkey, recepg@erciyes.edu.tr*
[3]*Department of Mechanical Engineering, Erciyes University, Turkey, apalakmk@erciyes.edu.tr*
[4]*Department of Mechanical Engineering, Texas A&M University, USA, jnreddy@tamu.edu*

Abstract

Honeycomb sandwich structures reinforced by functionally graded (FG) face plates can be a good proposal for impact applications ranging from low to high velocity impact loads. Low velocity impact performance and energy absorption capability of honeycomb sandwich structures reinforced by FG face plates were investigated using explicit finite element code, LS-DYNA®. In design of the sandwich structures, an aluminum honeycomb core and Al/SiC FG face plates were used. The through thickness mechanical properties of the face plates were considered with respect to a power-law. Mori-Tanaka homogenization scheme was used for determining the locally effective mechanical properties of functionally graded region and TTO (Tamura-Tomota-Ozawa) model was implemented in finite element code in order to simulate the elastoplastic behavior of the face plates. The influence of material composition of the face plates, impact energy and core height of the honeycomb on the energy absorption characteristics of the sandwich structures were investigated. The core height was not an influential parameter whilst the material composition was a considerable parameter on the low velocity impact response of the sandwich structures.

Keywords: Functionally graded materials, Honeycomb sandwich structures, Low velocity impact, Explicit finite element method.

1. Introduction

Sandwich structures are special class of multilayered composite structures and extensively used in aerospace, marine and defense industries with their high performance properties – lightweight, high flexural stiffness and high energy absorption capability. Honeycomb sandwich structures are commonly used in impact applications by reason of their high energy absorption capacity. Functionally graded materials (FGMs) consisting of ceramic and metal constituents have become a good choice for impulsively loaded conditions with their superior features. The ceramic constituent provides high stiffness and impact resistance while the metal constituent provides toughness and structural integrity.

Honeycomb sandwich structures including different type of face plates and core materials subjected to low velocity impact loads are well-known research topic for energy absorption applications [1,2]. FGMs have also increasingly become a popular research area for impact applications. In literature, it was obtained that functionally graded structures exhibit a better performance compared with homogeneous structures under impact loads in terms of damage and deformation [3,4]. In present study, low velocity impact performance of honeycomb sandwich

Table 1. Material properties of the constituents of face plates and honeycomb core.

Materials	Young's modulus (GPa)	Poisson's ratio	Density (kg/m^3)	Yield stress (MPa)	Tangent modulus (MPa)	Failure strain
Al 6061	67	0.33	2702	95	-	0.85
SiC	302	0.17	3100	-	-	0.01
Al 5052-H39	70	0.33	2680	265	700	0.67

structures reinforced by FG face plates was investigated in terms of material composition of the face plates, impact energy and core height of the honeycomb.

2.   Finite Element Model

Low velocity impact performance and energy absorption capability of honeycomb sandwich structures reinforced by FG face plates were investigated using explicit finite element code, LS-DYNA® [5]. Al6061 and SiC constituents were used in design of the face plates and Al5052-H39 aluminum honeycomb was used as core material. The material properties of the constituents of face plates and honeycomb core were listed in Table 1. Three different material compositions, metal-rich (n = 0.1), linear (n = 1.0) and ceramic-rich (n = 10.0), were used for the face plates. The locally effective material properties of functionally graded region were determined using Mori-Tanaka homogenization scheme [6] and TTO (Tamura-Tomota-Ozawa) model [7] was used in order to define elastoplastic material behavior of the face plates. TTO model was implemented by Gunes et al. [8] for Al/SiC FG circular plates and it was obtained that TTO model was more successful by varying the material composition from ceramic-rich to metal-rich in accordance with the experimental and numerical results. In this numerical study, the same constituents were used for the FG face plates. The bottom layer of the face plates was pure metal and the top layer of the face plates possessed 30%Al-70%SiC volume fractions of the constituents. The stress-strain curves of the face plates obtained from TTO model for metal-rich (n = 0.1), linear (n = 1.0) and ceramic-rich (n = 10.0) compositions were shown in Fig. 1.

The aluminum honeycomb core which has a cell size of 6.35 mm, core height of 15 mm and cell wall thickness of 0.0762 mm and Al/SiC FG face plates with 5 mm thickness and 10 layers through thickness were used for approximately 100x100 mm sandwich structure construction. The sandwich structures were subjected to hemispherical rigid impactor with 20 mm diameter. The face plates and rigid impactor were modelled with 8-node solid elements and the honeycomb core was modelled with 4-node shell elements. The elastoplastic material behavior of the face plates and honeycomb core were defined with piecewise linear plasticity and plastic kinematic material models, respectively. The impactor was modelled with rigid material model. The finite element model of the sandwich structure and impactor was given in Fig. 2.

Contact modelling is a critical step for impact simulations. An automatic single surface contact algorithm was defined in order to consider self-contacting surfaces. An automatic surface to surface contact algorithm was defined between impactor and sandwich structures. The contacts between face plates and honeycomb core were assumed to be perfecly bonded and a tied nodes to surface contact algorithm was defined.

The ceramic-rich surfaces of the face plates were positioned as the first impact surfaces and in the same direction. The bottom surface of the sandwich structures was constrained with 15 mm portion from each side in impact direction and all edges of the sandwich structures were constrained in their normal directions.

(a) $n = 0.1$ (b) $n = 1.0$ (c) $n = 10.0$
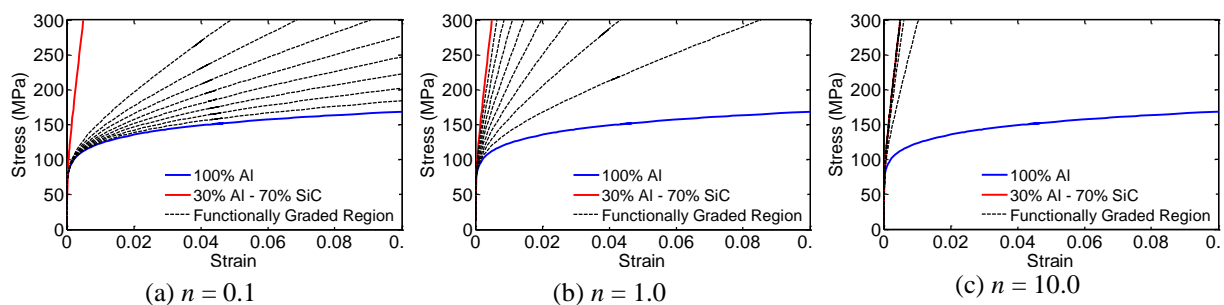
Fig. 1. Stress-strain curves obtained from TTO model for (a) metal-rich, (b) linear and (c) ceramic-rich compositions.
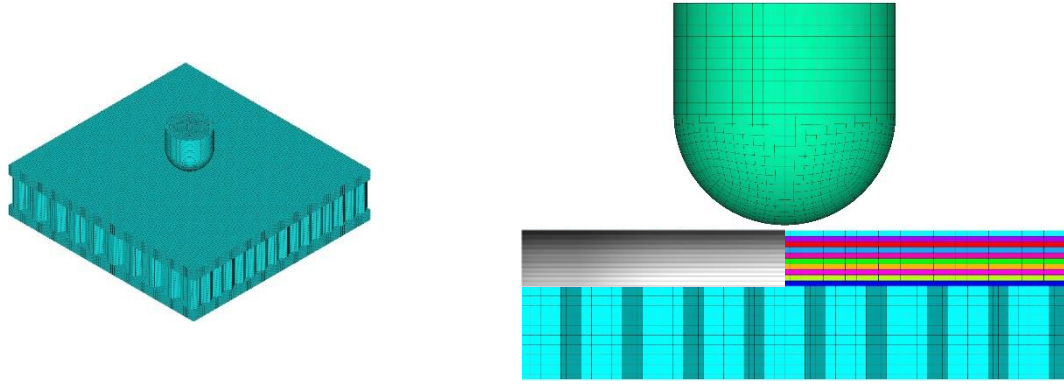
Fig. 2. Finite element model of the sandwich structure and impactor

(a) $E = 100$ J   (b) $E = 150$ J   (c) $E = 200$ J
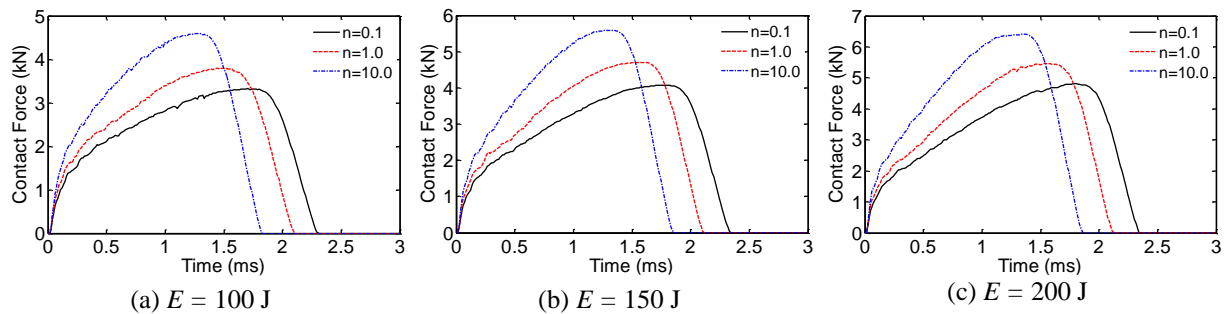
Fig. 3. The influence of the material composition and impact energy on the contact force histories of the sandwich structures.

(a) $n = 0.1$ (b) $n = 1.0$ (c) $n = 10.0$
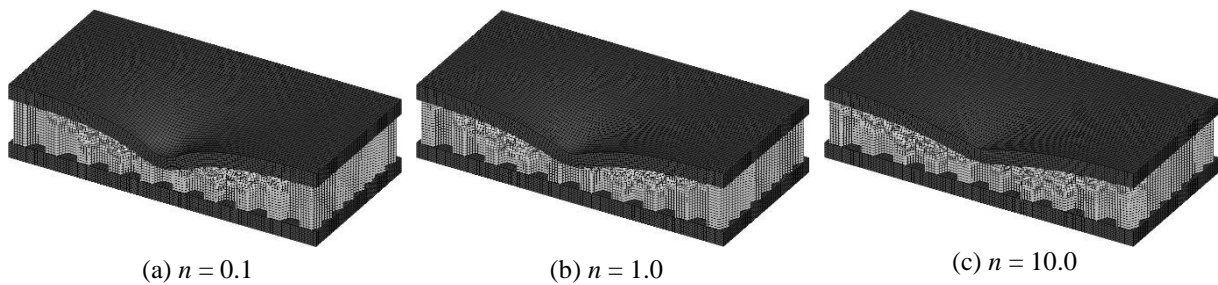
Fig. 4. The influence of the material composition on the plastic deformation of the sandwich structures for 150 J impact energy.

3. Results

The influence of the material composition of the face plates, impact energy and core height of the honeycomb on the low velocity impact performance of the honeycomb sandwich structures reinforced by FG face plates were investigated for metal-rich, linear and ceramic-rich compositions.

a. *The influence of the material composition and impact energy*

The influence of the material composition and impact energy on the contact force histories of the sandwich structures was shown in Fig. 3. The peak contact force increased and contact duration decreased by varying the material composition from metal-rich to ceramic-rich (increasing the ceramic fraction of the face plates) by reason of increasing the stiffness and strength of the face plates. The contact force histories exhibited the same variation in terms of the material composition and the peak contact force increased with increasing the impact energy. The peak contact forces from metal-rich to ceramic-rich composition were 3.32, 3.80 and 4.60 kN for 100 J; 4.07, 4.71 and 5.59 kN for 150 J and 4.81, 5.47 and 6.41 kN for 200 J, respectively.

The influence of the material composition on the plastic deformation of the sandwich structures was given in Fig. 4 for 150 J impact energy. The central plastic deflections of the sandwich structures for the material composition from metal-rich to ceramic-rich composition were 7.95, 7.08 and 5.75 mm. The plastic deformation and central

(a) $E = 100$ J   (b) $E = 150$ J   (c) $E = 200$ J
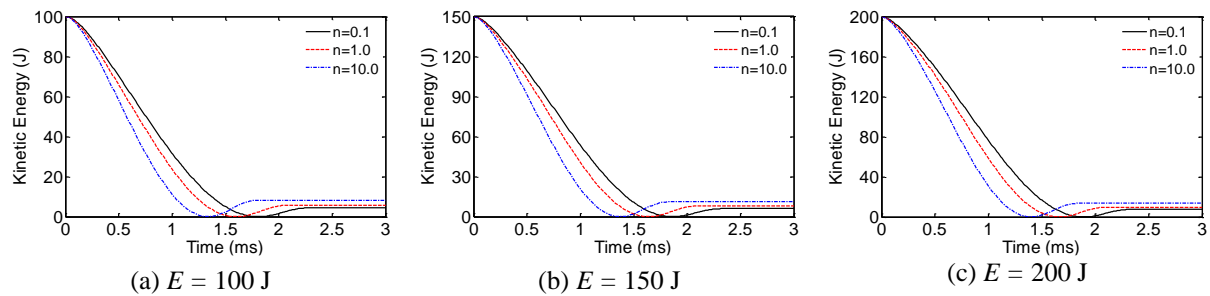
Fig. 5. The influence of the material composition and impact energy on the kinetic energy histories of the sandwich structures.

(a)   (b)
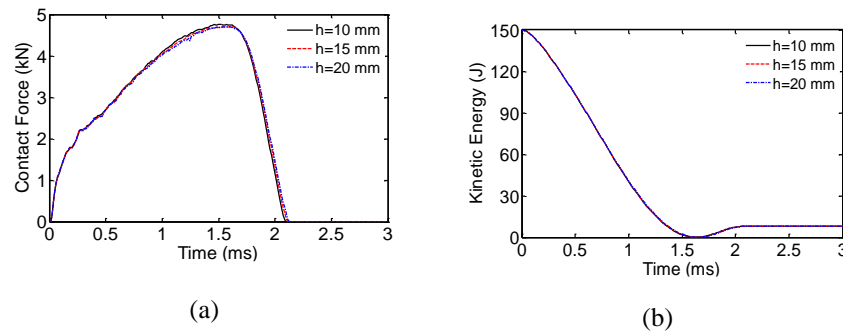
Fig. 6. The influence of the core height on the contact force and kinetic energy histories of the sandwich structure for linear composed face plates and 150 J impact energy.

deflection of the top face plate decreased with increasing ceramic fraction in the face plates by reason of increasing the impact resistance of the face plates. The buckling deformations occurred in the honeycomb core were different depending on the ductility of the face plates. The buckling deformation concentrated in the contact region for the sandwich structure with metal-rich face plates. For linear and ceramic-rich compositions, the buckling deformation propagated to boundary of the sandwich structures because impact effect did not propagated expeditiously to the substrates depending on the stiffness of the face plates and the buckling deformation increased by reason of increasing the compressive forces on the honeycomb core from the top face plate.

The influence of the material composition and impact energy on the kinetic energy histories of the sandwich structures was shown in Fig. 5. The energy absorption capacity of the sandwich structure decreased by varying the material composition from metal-rich to ceramic-rich by reason of decreasing the plastic deformation in the sandwich structures. The energy absorption ratios from metal-rich to ceramic-rich composition were 95.6%, 94.3% and 91.7% for 100 J; 96.0%, 94.7% and 92.5% for 150 J and 96.2%, 95.1% and 93.2% for 200 J.

b. *The influence of the core height*

The influence of the core height on the low velocity impact performance of the honeycomb sandwich structure with linear composed face plates was investigated for 10, 15 and 20 mm core heights and 150 J impact energy. The influence of the core height on the contact force and kinetic energy histories of the sandwich structure was shown in Fig. 6. The peak contact forces and energy absorption capacity of the sandwich structure remained approximately at the same level. The core height was not an influential parameter on the low velocity impact performance of the sandwich structure.

4. Conclusion

Low velocity impact performance of the honeycomb sandwich structures reinforced by FG face plates was investigated numerically. The peak contact force increased and contact duration decreased with increasing the ceramic fraction of the face plates. The central plastic deflections of the sandwich structures decreased with increasing ceramic fraction in the face plates by reason of increasing the impact resistance of the face plates. The buckling deformations occurred in the honeycomb core was different depending on the ductility of the face plates. The energy absorption capacity decreased with increasing ceramic fraction in the face plates by reason of

decreasing the plastic deformation in the face plates. The core height was not an influential parameter whereas the material composition was a significant parameter on the low velocity impact response of the sandwich structures.

References

[1] I. Ivañez, S. Sanchez-Saez, Numerical modelling of the low-velocity impact response of composite sandwich beams with honeycomb core, Composites Structures, 106 (2013), 716-726.

[2] D. Zhang, D. Jiang, Q. Fei, S. Wu, Experimental and numerical investigation on indentation and energy absorption of a honeycomb sandwich panel under low-velocity impact, Finite Elements in Analysis and Design, 117-118 (2016), 21-30.

[3] N.A. Apetre, B.V. Sankar, D.R. Ambur, Low-velocity impact response of sandwich beams with functionally graded core, International Journal of Solids and Structures, 43 (2006), 2479-2476.

[4] E. Etemadi, A.A. Khatibi, M. Takaffoli, 3D finite element simulation of sandwich panels with a functionally graded core subjected to low velocity impact, Composite Structures, 89 (2009), 28-34.

[5] Livermore Software Technology Corporation (LSTC), LS-DYNA® Keyword User's Manual, Version 971, 2009.

[6] T. Mori, K. Tanaka, Average stress in matrix and average elastic energy of materials with misfitting inclusions, Acta Metallurgica, 21(1973), 571-574.

[7] I. Tamura, Y. Tomota, M. Ozawa, Strength and ductility of Fe-Ni-C alloys composed of austenite and martensite with various strength, In: Proceedings of the Third Conference on Strength of Metals and Alloys, Cambridge, 1973, 611-615.

[8] R. Gunes, M. Aydin, M.K. Apalak, J.N. Reddy, Experimental and numerical investigations of low velocity impact on functionally graded circular plates, Composites: Part B, 59 (2014), 21-32.

Challenge for Additive Manufacturing of Functionnally Graded Materials Parts

Pr. Jean-Yves Hascoët – Dr. Matthieu Rauch

Ecole Centrale de Nantes - France
jean-yves.hascoet@ec-nantes.fr; matthieu.rauch@ec-nantes.fr

Keywords: Functionally Graded Materials (FGM) parts, additive manufacturing, process modelling, process optimization, tool paths.

Functionally Graded Materials (FGM) parts are heterogeneous objects with material composition and microstructure that change gradually into the parts. The distinctive feature of FGM structure gives the possibility of selecting the distribution of mechanical, physical, chemical properties to meet the functional requirements. Additive manufacturing processes, in particular Direct Energy Deposition (DED) processes are well dedicated to manufacture complex FGM parts. Customized homogeneous parts are manufactured from digital data, but the manufacturing of heterogeneous parts is limited to samples: most of the FGM parts are not functional, with simple morphology and simple material distribution and functional AM parts are very often made with one material. To move from these samples to functional parts a methodology with a global approach is necessary. The presentation focuses on various challenges covered by this approach to move from the concept imagined by a designer to the manufacturing of the part.

Figure 1: Geometrical complexity vs. material composition complexity for FGM parts
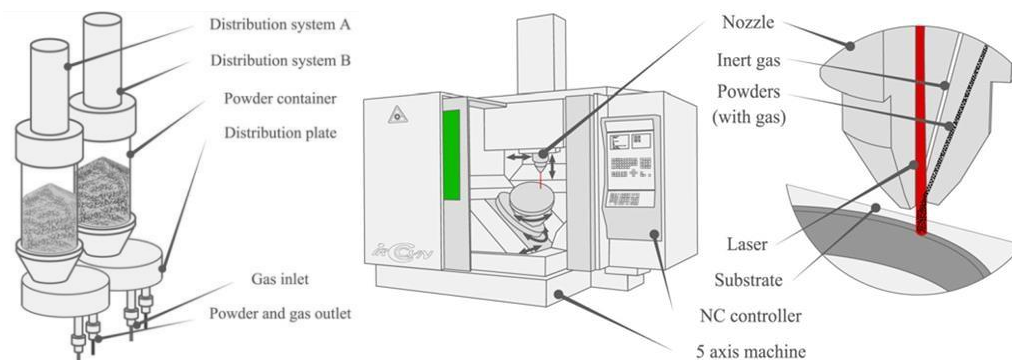
Figure 2: DED Additive Manufacturing equipment to manufacture FGM parts at ECN

The first aspect focuses on the numerical definition of the part in the CAD/CAM/process data chain. Most of the current CAD description formats do not support multimaterial attributes for a single part. It is consequently hardly possible to define accurately material distributions and properties by using FEM simulations or topological optimizations algorithms. In contrast, high level CAD/CAM/CNC approaches such as STEP-NC can be highly valuable to overtake these limitations. Their interest is the first issue discussed in the presentation.
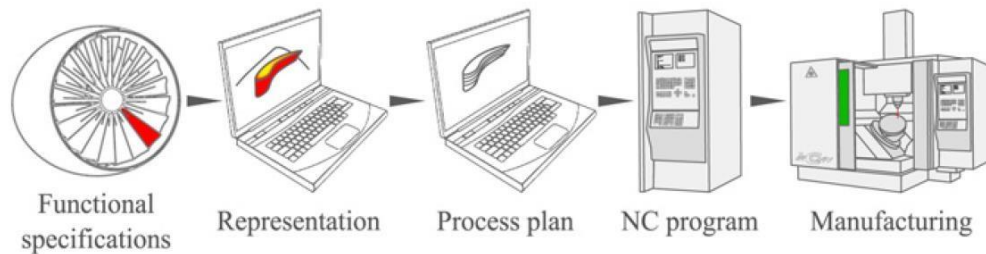
Figure 3: Usual Additive Manufacturing process data chain

The second issue focuses on DED process modelling to determine the appropriate parameterization and manufacturing strategy. It is essential to identify the actual behavior of the process implemented, for example, the evolutions of the material compositions changes when switching from one ratio to another. The resulting model is a key element to prepare the manufacturing strategy. Indeed, for FGM parts the control of the material composition at any point of the part is as important as the part geometry. In addition, this process model can be useful to perform DFAM operations on the part to manufacture.
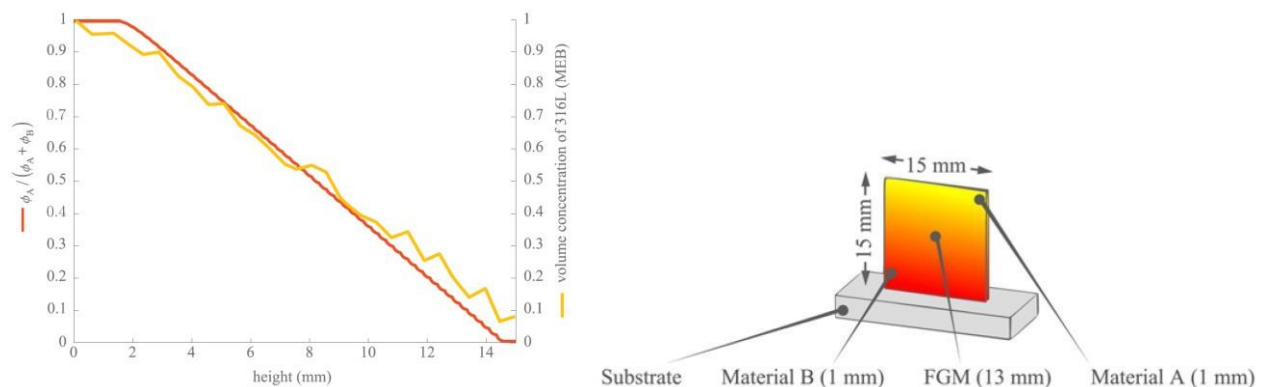
Figure 4: Simulation and measure of the material function during the process

The last focus of this presentation concerns DED process toolpaths generation for FGM parts. By using the process model developed, the evaluation of manufacturing strategies and a process control to reduce the difference between the desired material distribution and the material distribution in the manufactured part is enabled. New kind of path strategies can be proposed and tested off line on a process simulator. As a result, complex parts can be produced with the desired geometries and the desired material distributions.
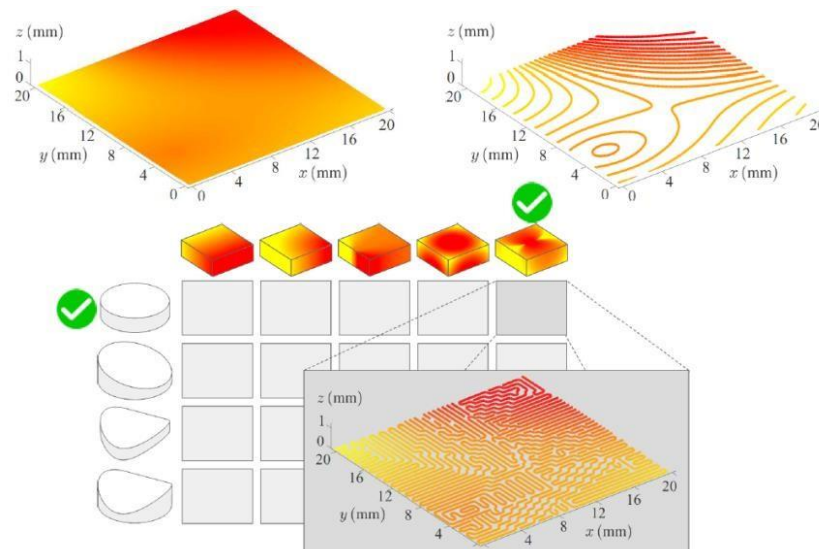
Figure 5: Manufacturing tool paths automatic generation to meet the material function requirements

References

S. Choi, H. Cheung, A topological hierarchy-based approach to layered manufacturing of functionally graded multi-material objects, Computers in Industry 60 (2009) 349–363

P. Mognol, P. Muller, J. Hascoeˈt, A novel approach to produce functionally graded materials for additive manufacturing, in: Proceedings of the Conference on Advanced Research in Virtual and Rapid Prototyping, Leiria, Portugal, 2011, pp. 473–478.

P. Muller, P. Mognol, J. Hascoet, Modeling and control of a direct laser powder deposition process for Functionally Graded Materials (FGM) parts manufacturing, Journal of Materials Processing Technology 213 (2013) 685–92.

Niino, M., Suzuki, A., Hirai, T., Watanabe, R., Hirano, T., Kuroishi, N., 1987, Method of producing a functionally gradient material. Ausz.Eur. Patentanmeld. I3, 1555

X. Qian, D. Dutta, Design of heterogeneous turbine blade, Computer-Aided Design, 35 (2003), pp. 319–329

S. Ocylok, A. Weisheit, I. Kelbassa, Functionally graded multi-layers by laser cladding for increased wear and corrosion protection,Physics Procedia, 5 (2010), pp. 359–367

Um, J., Rauch M., Hascoët J.Y. and Ian Stroud, I. 2016. STEP-NC Compliant Process Planning of Additive Manufacturing: Remanufacturing. The International Journal of Advanced Manufacturing Technology, May, 1‑16.

Microstructure and Wear Property of Al-Al$_3$Ti FGMs Fabricated by Centrifugal Solid-Particle and *in-situ* Methods

Yoshimi Watanabe[1], Qi Zhou[1], Hisashi Sato[1]

[1]Nagoya Institute of Technology, yoshimi@nitech.ac.jp
[2]Nagoya Institute of Technology, damonzqzq@yahoo.co.jp
[3]Nagoya Institute of Technology, sato.hisashi@nitech.ac.jp

Abstract

Fabrication method of functionally graded materials (FGMs) by centrifugal casting can be classified into two categories on the basis of the relationship between the process temperature and the liquidus temperature of a master alloy. They are the centrifugal solid-particle method and the centrifugal *in-situ* method, which could be carried out at process temperatures lower and higher than the liquidus temperature of the master alloy, respectively. In this study, Al-Al$_3$Ti FGMs were fabricated at 1200°C from Al-5 mass%Ti master alloy, where liquidus temperature of the Al-5 mass%Ti alloy is about 1040°C. Microstructure and wear property of the fabricated Al-Al$_3$Ti FGMs were studied.

Keywords: Centrifugal casting, Al$_3$Ti, platelet, orientation, wear

1. Introduction

Centrifugal casting is a pressure casting, in which the force of gravity is enhanced by spinning the mold. It is possible to create a compositional gradient due to the difference in material density [1]. Fabrication of functionally graded materials (FGMs) by centrifugal casting can be classified into two categories by the relationship between the process temperature and the liquidus temperature of the master alloy [2]. One is the centrifugal solid-particle method if the process temperature is lower than the melting point of the master alloy. The other one is the centrifugal in-situ method if the process temperature is higher than the melting point of it. In previous study [3], it has been found that microstructure of Al-Al$_3$Ti FGMs fabricated by the centrifugal solid-particle method cast at 800 °C was different from that by centrifugal in-situ method cast at 1600 °C. However, the microstructures of Al-Al$_3$Ti FGMs fabricated by the centrifugal in-situ method cast at a temperature around the liquidus temperature (about 1040 °C for Al-5 mass%Ti alloy) is not studied. In this study, the microstructures of Al-Al$_3$Ti FGMs fabricated at 1200 °C were investigated. In addition, wear properties of the fabricated Al-Al$_3$Ti FGMs were also studied.

2. Experimental methods

An Al-5 mass% Ti commercial alloy ingot with 11 vol% Al3Ti platelets was used as the initial material. The ingot was heated up to 1200 °C, a temperature just above the liquidus line, ensuring the complete melting of all phases before processing (centrifugal in-situ method). The melt was directly poured into a spinning mold through an inlet, for which the applied centrifugal forces were 300 and 600 G. Temperature of mold pre-heating furnace is set tobe 478 °C or 300 °C or room temperature (R. T.). During melt pouring, however, the temperature of the molten metal drops to a certain degree, which results in the crystallization of the primary Al$_3$Ti crystal phase in the melt before application of centrifugal force (centrifugal solid-particle method). Notation of samples XX°C-YYG indicates the temperature of mold pre-heating furnace and applied centrifugal force, respectively.

The wear tests were carried out by ball-on-block type wear machine under reciprocal movement, where the counter ball was bearing steel (JIS: SUJ2) with 5mm in diameter. Initial load, sliding time and average sliding speed of wear tests were 9.8 N, 5400 s and 30 m/s, respectively. To study the anisotropy of wear resistance in the FGMs, wear tests were carried out in three directions.

3. Results and discussion

Microstructures and histograms of volume fractions of the Al$_3$Ti platelets in 478°C-300G specimen, 300°C-300G specimen, R.T.-300G specimen and 300°C-600G specimen are shown in Figs. 1 (a), (b), (c) and (d), respectively [4]. There are two types of particles namely, platelet shaped particles and small particles. It is seen from this figure, compositional gradients are observed for all specimens. Comparison between 300°C-300G and 300°C-600G specimens, it is seen that a steeper compositional gradient formed in larger-G-number specimens. Note that negative gradients are found in the outer regions of the ring for 300°C-300G and R.T.-300G specimens. These findings indicate that mold temperature plays an important role in the solidification behavior in centrifugal casting. It must be noted here that a large number of platelets are arranged with their platelet planes nearly normal to the centrifugal force direction, which is in agreement with previous studies on the centrifugal solid-particle method [5]. Therefore, the anisotropy of wear resistance should be appeared. By comparing the microstructures of 300°C-300G and 300°C-600G specimens, a larger orientation effect is found for the larger-G-number specimen. Moreover, smaller orientation effects are found at larger-normalized-thickness regions. In our previous study [5], it was found that the larger orientation effects is found at outer regions of the ring in the Al-Al$_3$Ti FGMs fabricated by the centrifugal solid-particle method.
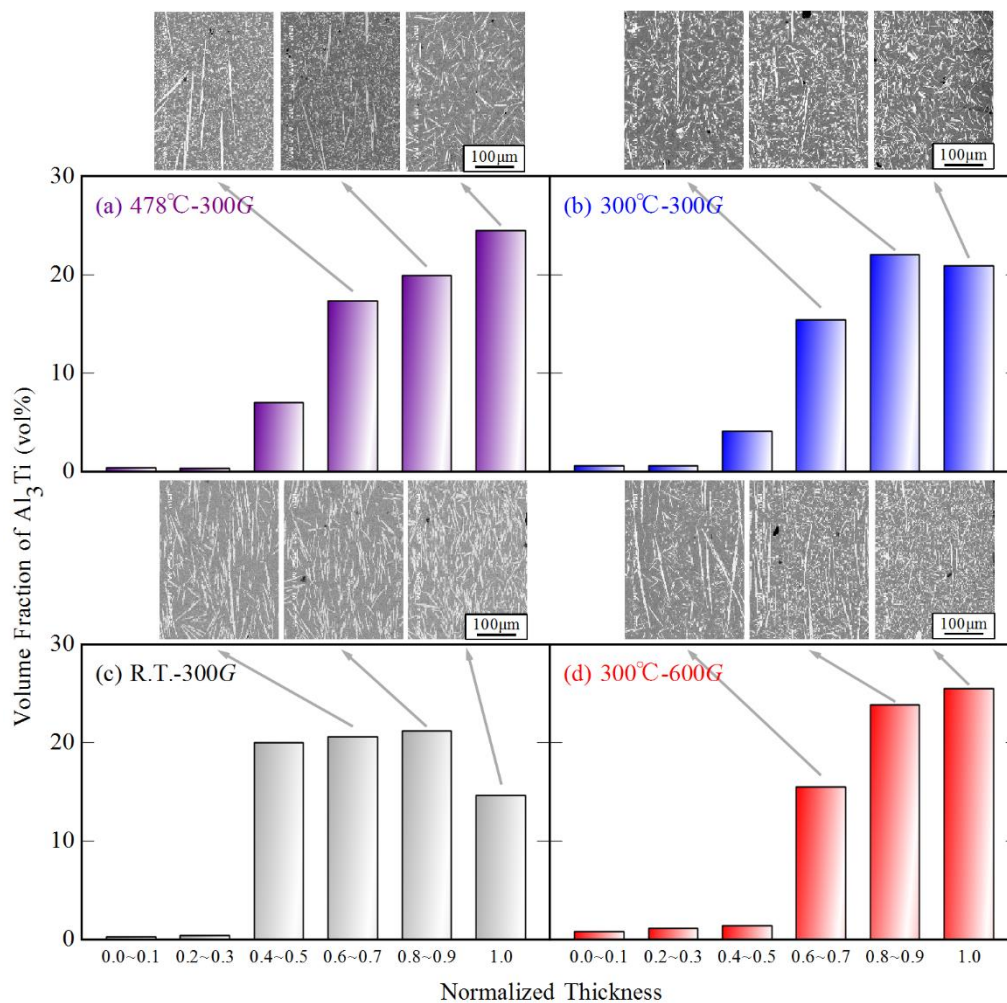
Figure 1: Typical microstructures observed at normalized thickness of 0.6, 0.8 and 1.0 regions and histograms of volume fractions of the Al$_3$Ti platelets in the specimens [4]. Vertical direction in these photos is centrifugal direction. (a) 478ºC-300G, (b) 300ºC-300G, (c) R.T.-300G and (d) 300ºC-600G specimens.
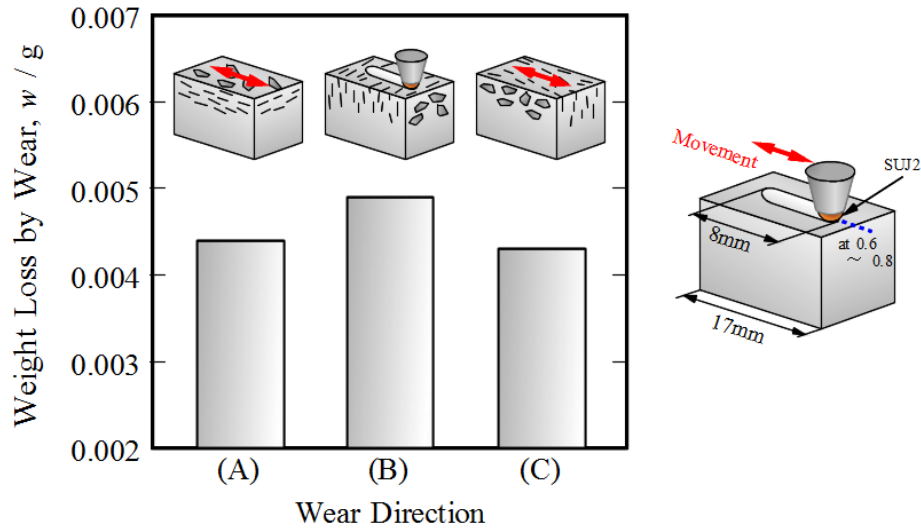
Figure 2: The effects of wear direction on the weight loss by wear. There is notable difference in the weight loss by wear among the three tested wear directions.
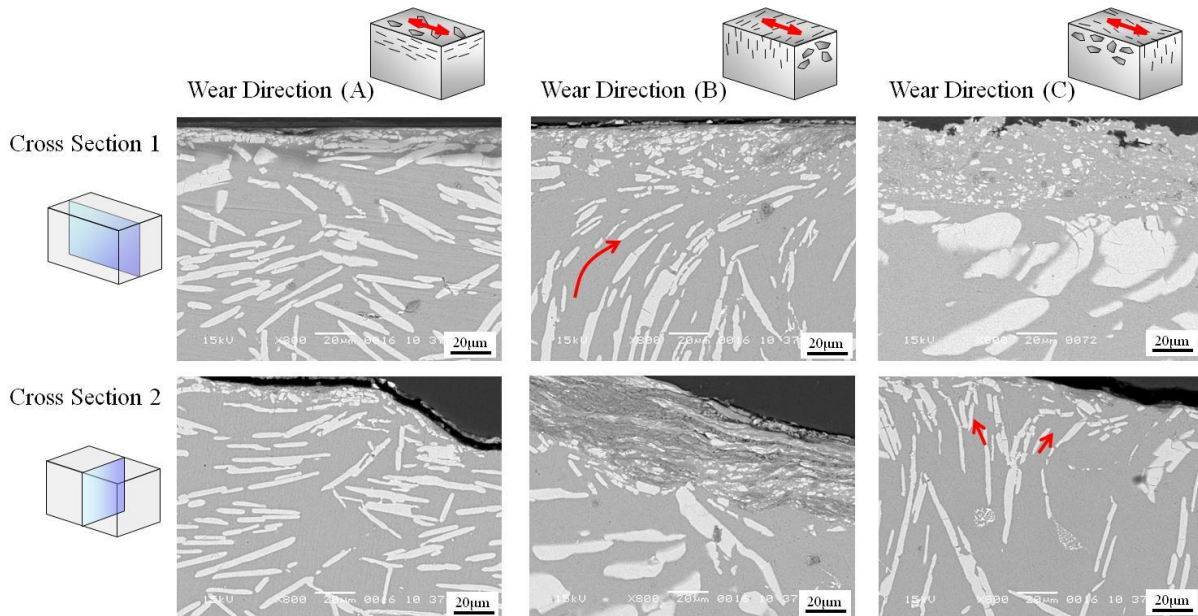
Figure 3: The cross-sections parallel (upper figures) and perpendicular (lower figures) to the sliding direction of worn specimens. These photos are backscatter compositional images.

These findings indicate unexpected orientation effects in the FGMs fabricated by the centrifugal in-situ method. By comparing among 478°C-300G specimen, 300°C-300G specimen and R.T.-300G specimen, smaller orientation effects are found for the FGMs fabricated at a lower temperature of the mold preheating furnace. Again, mold temperature plays an important role in the solidification behavior in centrifugal casting [4].

Three kinds of wear specimens were prepared taking into account the morphology of the Al_3Ti platelets in 478°C-300G specimen. In case of the wear direction (A), the worn plane nearly coincides with the Al_3Ti platelet planes. On the other hand, the worn planes coincided with the platelets' two edge planes, and the wear directions are along the thickness direction and the longitudinal direction of the Al_3Ti platelets for wear directions (B) and (C), respectively. Figure 3 shows the weight loss by the wear test under the applied load of 9.8N. There is a notable difference in the weight loss by wear among the three tested wear directions. Namely, wear direction (B) shows the lowest wear resistance among the three wear directions, while wear directions (A) and (C) show similar and relatively better wear resistance. Similar results are found in the block-on-ring type wear tests for the Al-Al_3Ti FGMs fabricated by the centrifugal solid-particle method [6].

In order to investigate the microstructural features near the worn surface, cross-sections of the specimens parallel and perpendicular to the sliding direction were observed. The results are shown in Fig. 3. Damaged layers containing broken Al_3Ti platelets are found in all figures. Especially, in the case of direction (B), the wear tests led to fracture and bending of the Al_3Ti platelets along the wear test direction. Since it is known that Al_3Ti is brittle in nature, the Al_3Ti platelets for direction (B) break easily during the wear test, whereas the platelets for directions (A) and (C) are more difficult to break. Thus, direction (B) shows a lower wear resistance, while directions (A) and (C) show better wear resistance.

4. Conclusions

In this study, the microstructures of Al-Al_3Ti FGMs fabricated at 1200°C from a master alloy of an Al-5 mass% Ti ingot containing 11 vol% Al_3Ti platelets in the Al matrix are investigated. Compositional gradient and orientation effects are found in the Al-Al_3Ti FGMs. It is found that the mold temperature plays an important role in the solidification behavior by the centrifugal casting. Anisotropic wear resistance is found to be dependent on the direction of the test wear relative to the Al_3Ti platelet orientation. Specimen tested along the Al_3Ti platelets thickness direction shows the smallest wear resistance among the three orientations due to the ease with which the Al_3Ti platelets broke.

References

[1] Y. Watanabe and H. Sato: Review Fabrication of Functionally Graded Materials under a Centrifugal Force, in "Nanocomposites with Unique Properties and Applications in Medicine and Industry", edited by J. Cuppoletti, InTech, (2011), pp. 133-150.
[2] Y. Watanabe, I. S. Kim and Y. Fukui, Metals and Materials International, 11 (2005), 391-399.
[3] S. H. El-Hadad, H. Sato, P. D. Sequeira, Y. Watanabe and Y. Oya-Seimiya, Materials Science Forum, 631-632 (2010), 373-378.
[4] Y. Watanabe, Qi Zhou, H. Sato, T. Fuji and T. Inamura: Japanese Journal of Applied Physics, 56, (2017), accepted for publication.
[5] Y. Watanabe, P. D. Sequeira, H. Sato, T. Inamura and H. Hosoda: Japanese Journal of Applied Physics, 55, (2016), 01AG03 (7 pages).
[6] Y. Watanabe, N. Yamanaka and Y. Fukui: Metallurgical and Materials Transactions A, 30 (1999), 3253-3261.

Microstructural Characterization of the Mg/Al Diffusion Bonded Joint Using Al-Ni Interlayer

Jian Zhang[1,a] *, Guoqiang Luo[1,b], Ruxia Liu[1,c], Mei Rao[1], Qiang Shen[1], Lianmeng Zhang[1]

[1]*State Key Lab of Advanced Technology for Materials Synthesis and Processing, Wuhan University of Technology, Wuhan 430070, China*
E-mail: [a]isaiah178@hotmail.com, [b]luogq@whut.edu.cn, [c]mignonliu1@163.com

Abstract

Dissimilar welding of Mg and Al would achieve weight reduction and high efficiency of production by substitution of Mg and Al for steels. In this investigation, a vacuum hot-pressed diffusion method was used to prepare an Mg/Al layer composite using an Al thin film and Ni foil interlayers. The interfaces microstructure and shear strength of the joints were investigated by means of SEM, XRD and universal machine. The results showed that the joints were bonded well and the Mg-Al intermetallic compounds were impeded. Al thin film and Ni foil successfully strengthened the weak interface of Mg/Al welding joint. With the increasing of the holding time, the shear strength of the joints increases firstly and then decreases. The fracture took place somewhere at the interface of the Al-Ni.

Keywords: Mg/Al; diffusion bonding; holding time; shear strength

Paper withdrawn

Hot Corrosion Behavior of 8Y-ZrO$_2$/ZrSiO$_4$ Ceramic Sealed by Laser-assisted Microwave Plasma Processing

Christian Richter [1], Monika Willert-Porada[2]

[1] *University of Bayreuth, Christian.Richter@uni-bayreuth.de*
[2] *University of Bayreuth, Monika.Willert-Porada@uni-bayreuth.de*

Abstract

Sintered porous 8Y-ZrO$_2$ ceramic and composite ceramics consisting of 8Y-ZrO$_2$ and ZrSiO$_4$ were surface sealed by a new process, called Laser Assisted Microwave Plasma Processing (LAMPP). Hot corrosion tests with molten V$_2$O$_5$, Vanadium Pentoxide, which are used to characterize hot-corrosion resistance of Thermal Barrier Coatings, were employed to proof the quality of surface sealing. The penetration depth of the molten salt was investigated at exposure times of 4 hours as a function of ceramic composition and LAMPP processing parameters. Upon reaction with V$_2$O$_5$ the stabilizing oxide Y$_2$O$_3$ is extracted from the Y-stabilized zirconia, leading to severe crack formation due to transition to monoclinic ZrO$_2$. LAMPP sealed zirconia barrier coatings showed a better resistance to hot corrosion as compared to 8Y-ZrO$_2$/ZrSiO$_4$ ceramics. The reactions taking place upon LAMPP and formation of a compositional and porosity gradient due to melting and rapid solidification of the ceramic phases are discussed. Application of such coatings as Environmental Barrier Coating for Thermal Barrier Coatings is addressed.

Keywords: LAMPP, Hot Corrosion, TBC, zirconia

1. Introduction

Extended usage of Y-ZrO$_2$ based ceramic coatings is practiced for thermal barrier applications since the mid-80ties and state-of-the-art gas-turbine engines require high temperature thermal barrier coating (TBC) for improved efficiency and performance. [1] These protective coatings require a low thermal conductivity along with high erosion and chemical corrosion resistance. In essence, these coatings enhance turbine efficiency and reduce emissions by increasing the in service temperature. [2] Moreover, they enhance life-time by protecting the turbine from molten contaminants such as calcium-magnesium-alumina-silicates (CMAS) or molten salts. For thermal protection, (e.g., of Ni-Based super alloys) TBC's have been amply studied in the last decade. [3–5] State of the art TBC's for aircraft turbines are built up by a metallic bond coat, usually MCrAlY (M: Ni, Co or NiCo) layers followed by a 7 wt% Y$_2$O$_3$ doped ZrO$_2$ top coat, deposited either by electron beam physical vapor deposition (EB-PVD) or by atmospheric plasma spraying (APS). [6] For both processes, the resulting microstructure provides a bond coat oxidation and, for a certain application period, a spalling and delamination of the top coat. [7] Another essential requirement is that the material must resist high stress upon thermal cycling caused by the mismatch in coefficient of thermal expansion (CTE) between alloy, bond coat, and top coat.

Recently, increased importance of energy efficiency for combustion engines, like turbines, poses new challenges to the thermal and hot gas as well as ash corrosion resistance of such coating. While for low thermal conductivity at high-temperature porous structures are beneficial, their resistance to combustion fumes, particle erosion and hot corrosion is low. Industrial gas turbines can be operated with low-quality fuels. These fuels contain certain amount of elemental impurities such as vanadium or phosphorus. During combustion, these fuels create ash deposits inter alia composed of vanadium pentoxide, V$_2$O$_5$, with a low melting point of 690°C. [8–10] Thus, at typical gas turbine

operating temperatures the vanadic ash deposits are molten or gaseous, and thereby accelerate the surface corrosion rate of TBCs. The material degradation in TBC systems by hot corrosion is mainly caused by the reaction of molten deposits with yttria stabilizer. This chemical attack of YSZ coatings result in reaction products like YVO_4 and therefore initiates phase transformation of cubic or tetragonal zirconia (c and $t-ZrO_2$) to monoclinic zirconia ($m-ZrO_2$) which comes along with volume expansion. [11]

Ideally, a well understood material, like APS sprayed or EB-PVD deposited Zirconia coatings would be further developed to achieve an improved lifetime in turbines. Unfortunately, the zirconia based ceramics themselves are sensitive to hot ash corrosion and are responsible for a high oxygen diffusivity which limits the lifetime of the TBC system due to thermally grown oxide delamination. As a solution to overcome these problems while increasing the combustion temperature for improved efficiency application of so called environmental barrier coating is being intensively investigated, with the aim to develop new TBC materials and replace Y-Zirconia. [12–14] However, despite extended research a convincing solution has not been found so far. We therefore concentrate in our work on the development of new processing methods which enable densification of porous zirconia based TBC to enhance corrosion stability but preserve the overall porosity required to keep the thermal conductivity low and the thermal shock resistance high. The ideal microstructure of such coating would exhibit a continuous porosity gradient extending over coating thickness, starting with a dense Zirconia at the surface and ending with a porous material towards the metal side of a TBC system. Previous work at our chair showed that ZrO_2–$ZrSiO_4$/NiCr functionally graded materials (FGM) have the potential for high-temperature application because of the spatially control of material composition as well as material properties and structure and a low volume fraction of zircon ($ZrSiO_4$) benefit mechanical properties of the ceramic composite. [15–18] Therefore, the ceramic model systems in the present study are 8 mol% Y_2O_3-stabilised zirconia ($8Y-ZrO_2$) and $ZrSiO_4$ as an additive. The idea is to achieve a dense corrosion resistance sealing of the surface by Laser Assisted Microwave Plasma Processing (LAMPP). The main principle of LAMPP is to scan microwave induced spatial plasma with a laser source over the surface sample. [19] All experiments were performed in a lab-scale single mode microwave cavity with a CO_2 laser and a magnetron source at 2,45 GHz frequency. This paper addresses the hot corrosion behavior in presence of molten V_2O_5 with respect to microscopic observation and phase analysis. The hot corrosion behavior experiments are carried out at 1000 °C for 4-hour treatments.

2. Experimental

2.1 Sample preparation and LAMPP Surface sealing

Ceramic powders were mixed into water based slurries and poured into a preform. Debinding and pressure-less sintering was performed using a Al_2O_3 tube furnace (Thermal Technology, USA) in Ar/H_2 atmosphere (gas flow rate 25 l h^{-1}). The samples were heated to 1300 °C, at 2 K min^{-1}, followed by 1 h dwell time and then cooled down at 2 K min^{-1} to room temperature. Surface-sealing is performed by LAMPP. Two coherent radiation sources enable plasma ignition: a CO_2 laser (10.6 µm wavelength; 3.8 ± 0.4 mm Beam size; < 4 mrad beam divergence; 100 W cw- output power; TEM$_{00}$ mode; DeMaria EletroOptics Systems, Inc.); and a ripple magnetron (2.45 GHz $\pm$ 10 MHz frequency; 2 kW power out; Muegge Germany). To enable preheating of the ceramic, the sintered specimen is laid down on a SiC susceptor inside the alumina cavity and microwave power is applied. Above 700 °C, the laser is turned on to ignite a surface near plasma and to scan the plasma over the surface. Laser is controlled by WeldMark 3.0 Software (Raylase Germany).

2.2 Hot Corrosion Testing

Hot corrosion testing was carried out by deposition of pressed V_2O_5-pallet (diameter: 5 mm; weight: 5 mg) on top of the samples. Afterwards the samples were heated up to 1000 °C with a muffle-furnace (Nabertherm Germany) at ambient atmosphere for 4 hours' dwell time. After dwell time, the samples were allowed to cool to room temperature inside the furnace and then were put out for characterization methods.

2.3 Characterization

Cross-section microstructure were investigated using scanning electron microscopy (JSM-840A, Jeol, Japan). Element distributions were determined by using energy dispersive X-ray analysis (EDX, Oxford Instruments, UK). The crystalline phases are determined by XRD measurements with Cu-Kα radiation k = 0.154178 nm (Phillips PW 1140/90, Netherlands). Micro-hardness profiles were determined with a Vickers indenter (MHT-10, Anton Paar, Germany) with a load of 0.2 N from the cross section surface towards center of the sample.

3. Results and discussion

3.1 Characterization prior to hot corrosion testing

Cross-section of the sintered $8Y$-ZrO_2 is shown in Figure 1 (a) and (b). The porosity is homogenously dispersed within the sample with no accumulation. Due to the starting powder $8Y$-ZrO_2 ($d_{50} = 0.54\ \mu m$) with a low sintering activity at 1300 °C only a slightly grain growth is observed within the thermally etched microstructure. The grain sizes are in the range of 0.5 µm to 1.5 µm. Cross section microstructure of the LAMPP sealed $8Y$-ZrO_2 is shown in Figure 2. No cracks or voids are observed, neither within the sealed zone, nor at the transition zone. The achieved thickness of the sealed layer is approximately 200 µm and at the head of the LAMPP zone, a little spalling was observed. The transition zone revealed a slightly pore accumulation. The thermally etched microstructure reveals a grain size gradient, starting with grains smaller than 5 µm at the transition zone, coming up to grains > 60 µm. As compared to the as-sintered state the pores are not exclusively enriched at the grain boundaries, but rather within the grains.

Figure 1 (c) and (d) presents the cross-section morphology of sintered $8Y$-$ZrO_2/ZrSiO_4$. The $ZrSiO_4$ particles correspond to the dark grey spots, marked with red arrows. The zircon-distribution appears homogenous, without any agglomerated or sediment areas. The thermally etched microstructure shows a grain size > 1 µm. This implies a slightly grain growth during sintering. After LAMPP surface sealing the microstructure changes from the top region to the bottom region in the sealed zone, as it is seen from Figure 3. It appears with a wavelike structure, originating from the line spacing (750 µm) of the laser path during LAMPP. Within the laser paths the average thickness of the sealed layer is 800 µm, whereas between the laser paths only 500 µm. The transition zone shows a striking pore seam with an additional porosity gradient. Starting from the substrate with pore sizes smaller than 10 µm, the sizes increase towards LAMPP zone to approximately 50 µm in diameter. Within the LAMPP zone, there are only a few randomly distributed small pores. In principle, the LAMPP zone appears in a dense state with two different microstructures: a recurrent sequence of non-orientated dendrite structure with a circular expansion of about 40 µm diameter. Furthermore, spherical grains, approximately smaller than 5 µm right beside the dendrites. Meanwhile, the region nearby the transition zone shows a coarsened equiaxed grain structure Furthermore, this region appears with a gradient in grain size.
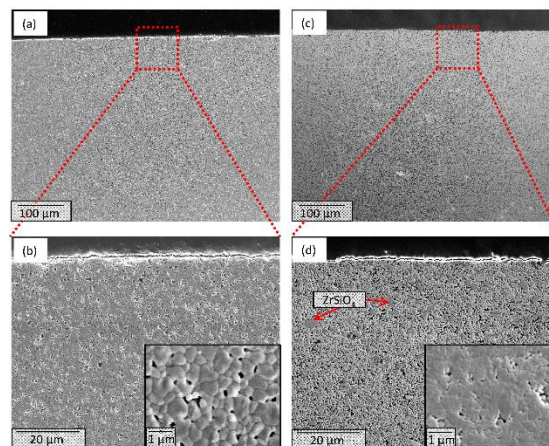
Figure 1: Cross-section microstructure and thermally etched microstructure (high magnification image): (a) and (b): Sintered $8Y$-ZrO_2; (c) and (d): Sintered $8Y$-$ZrO_2/ZrSiO_4$
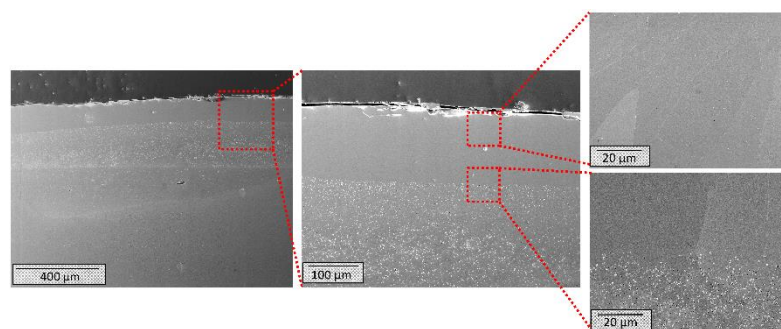
Figure 2: *Cross-section microstructure of LAMPP 8Y-ZrO₂*
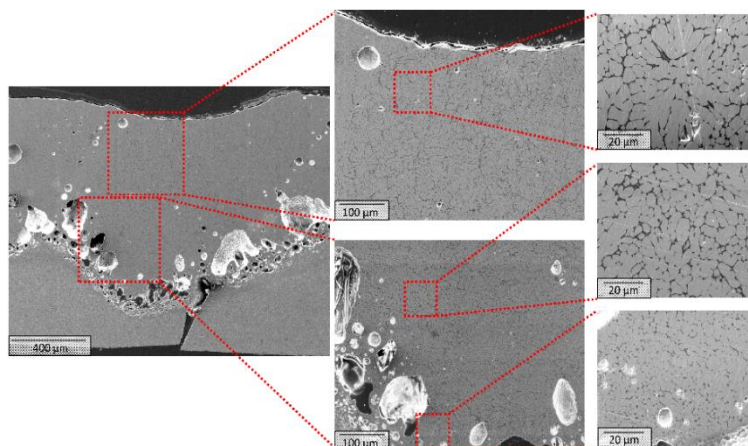
Figure 3: Cross-section microstructure of the LAMPP-sealed 8Y-ZrO$_2$/ZrSiO$_4$
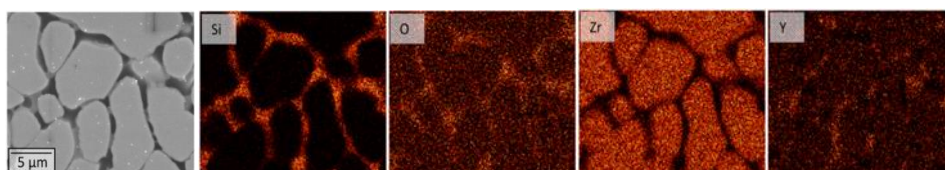
Figure 4: Elemental mapping of a typical cross section within the LAMPP-sealed zone of 8Y-ZrO$_2$/ZrSiO$_4$

In consideration of the EDX mapping, see Figure 4, the zirconia particles are embedded in a silicon-rich phase. Furthermore, the oxygen signal is significant within the same areas as the silicon signal. Thus, it can be deduced that these areas consist of SiO$_2$. Additionally, a third phase between the zirconia grains is observed, identified by medium grey appearance within the SEM image of Figure 4. The mapping revealed an enrichment of yttrium, but the amount of silicon signal is weak within this third phase.

The XRD measurement of the 8Y-ZrO$_2$/ZrSiO$_4$, see Figure 5, reveals that in case of the sintered sample the peaks of the zirconia-phase are solely the cubic phase. After LAMPP the ZrSiO$_4$ peaks disappear and nearly all the former cubic ZrO$_2$ can be assigned to the tetragonal phase. To substantiate this assumption, Rietveld refinement was performed. The fit data, with GOF of 2.55 and R$_{exp}$ of 9.38, results in 94.9% tetragonal and 5.1% cubic phase portions. Microscopic observations and XRD analysis showed that the ZrSiO$_4$-phase disappears after LAMPP. This phenomenon is related to the huge thermal energy intake during LAMPP, leading to decomposition of the ZrSiO$_4$ particles. The decomposition reaction of zircon as follows (at temperatures higher than 1600 °C):

$$ZrSiO_4 \rightarrow ZrO_2 + SiO_2 \tag{1}$$

Dissociation of zircon is based on formation of a siliceous melt: SiO$_2$ within the zircon dissolves and ZrO$_2$ grains precipitate as a dendritic structure. During cooling, two phases coexist: the liquid phase SiO$_2$ and particulate solid ZrO$_2$ phase. After sealing, the zirconia solidifies, but SiO$_2$ is still in molten state and therefore builds up a matrix between zirconia grains. Due to the reaction (1) there is an excess of non-stabilized ZrO$_2$ within the ceramic phase. This excess is thermodynamically unbalanced because of the high yttria content in the nearby surrounding consisting of 8 mol% yttria-stabilized zirconia. The high process temperature provides sufficient energy for huge diffusion rate of the involved species where the total zirconia content increased but yttria content is still at 8 mol%. This newly formed alloy therefore consists of a lower relative yttria stabilizing content and therefore the dominant crystallographic phase should be tetragonal. XRD analysis underpinned this assumption, because mainly t-ZrO$_2$ was found. Even though the LAMPP treated surface shows a nearly pore-free surface, a large number of pores were concentrated at the boundary between the laser treated zone and the untreated bulk. These pore accumulations may act as stress concentrators and may reduce the thermal cycling resistance and finally could lead to spalling of the sealed surface. On the other hand, porosity enhances heat isolation. Therefore, the observed porosity formation
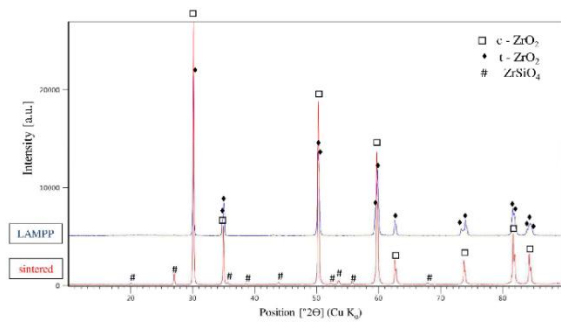
Figure 5: 8Y-ZrO₂/ZrSiO₄: XRD diffraction pattern of the solely sintered (lower pattern) and additional LAMPP sealed sample (upper pattern).
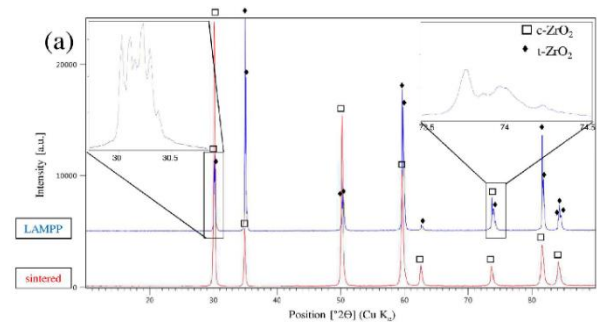
Figure 6: 8Y-ZrO₂: XRD diffraction pattern of the solely sintered (lower pattern) and additional LAMPP sealed sample (upper pattern).

at the boundary is governing the mechanical integrity
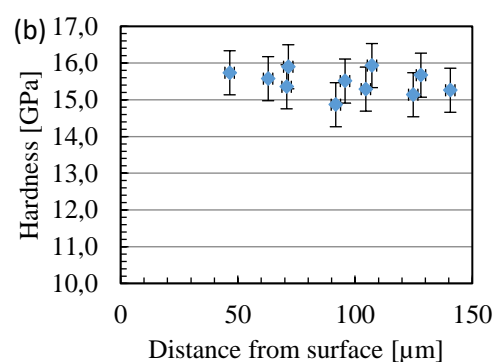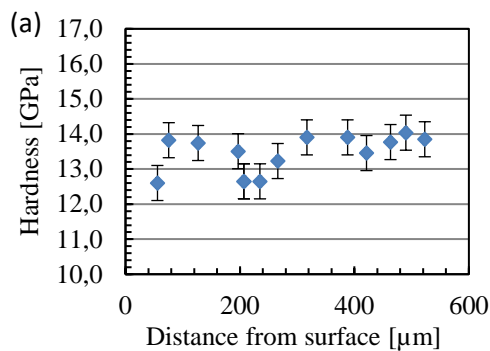
Figure 7: Diagrams show the micro hardness within the LAMPP zone: (a) LAMPP 8Y-ZrO₂/ZrSiO₄; (b) LAMPP 8YZrO₂

of the ceramic body. There are two different mechanism leading to the porosity formation at the boundary: motion of bubbles in the molten pool based on thermocapillary forces (Marangoni-effect); and pore coalescence due to bubble motion. Both mechanism result in fewer but larger pores.

XRD analysis of 8Y-ZrO₂ samples, see Figure 6, indicates that the sintered sample consists only of the cubic zirconia. After LAMPP sealing the dominant crystallographic phase is tetragonal zirconia with a small amount of cubic zirconia. The insets of the {100} und {400} Peaks, at 30 °2Θ and 74 °2Θ, respectively, were selected in order to illustrate the multiple peak splitting. Typically phase identification of heat treated Y-ZrO₂ is performed at the {400} peak, because the cubic and tetragonal peaks do not overlap within this section. Additionally, the Rietveld refinement addresses the combination of the different phases. Based on the refinement, the phase portions are 96.5% cubic and 3.5% tetragonal zirconia, respectively. Monoclinic as well as other phases related to precipitated yttrium-phases could not be detected.

Vickers micro-hardness was determined on the cross section of the sealed samples, starting within the LAMPP zone until the porous zone was reached. Indentation was performed 50 µm away from the sample surface, to prevent breakout during testing. For the sealed 8Y-ZrO₂/ZrSiO₄ the hardness values vary between 12.6 to 14.0 GPa whereas the sealed zone of the 8Y-ZrO₂ shows a higher hardness between 14.9 to 15.9 GPa, see Figure 7. A clear tendency related to a hardness gradient from the head towards porous substrate is not clearly observable. The lower average hardness value of the LAMPP 8Y-ZrO₂/ZrSiO₄ sample is due to the glassy silicon-rich phase. This amorphous phase lowers the hardness

3.2 Hot Corrosion behavior

EDX analysis was performed based on the detection of the element vanadium. In case of no vanadium signal detected, it can be assumed that at this depth the vanadium ingress ends. Fewer pores are detected within the reaction zone of the sintered samples, relating to the martensitic transformation of zirconia along with volume expansion. The total vanadium detection depth for the Sintered 8Y-ZrO₂/ZrSiO₄ is about 107 µm. It can be traced that the porosity of the sintered samples enables pathway for the molten V₂O₅. Pitted spots an pitted structure on
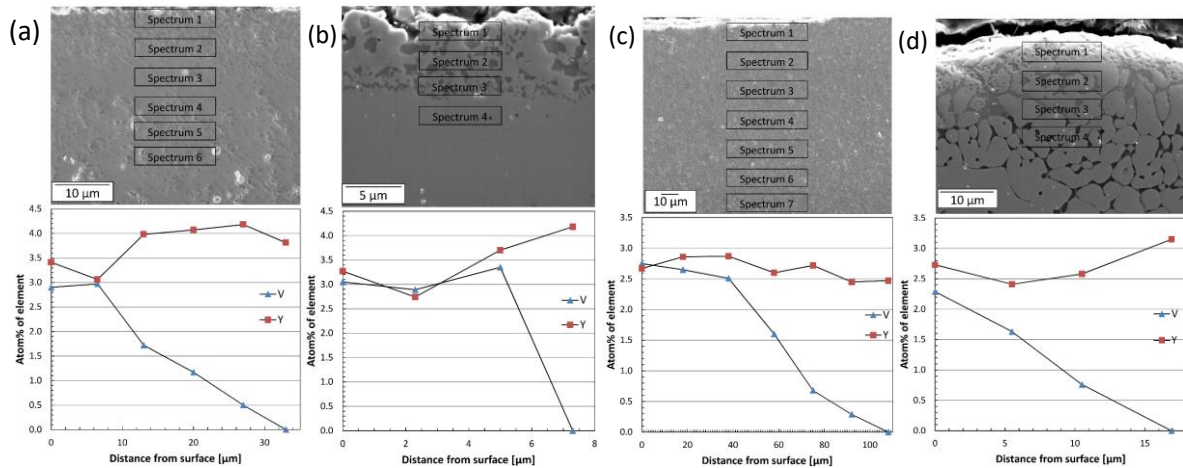
Figure 8: C*ross-section microstructure after isothermal hot corrosion testing for 4 h: (a) Sintered 8Y-ZrO₂, (b) LAMPP 8Y-ZrO₂ (c) Sintered 8Y-ZrO₂/ZrSiO₄, (d) LAMPP 8Y-ZrO₂/ZrSiO₄*

the surface near region of LAMPP 8Y-ZrO_2/$ZrSiO_4$ in Figure 8 (d) show reaction products from vanadium ingress. It can be seen that the vanadium ingress path is mainly along the SiO-matrix between the zirconia grains. Altough the surface of LAMPP 8Y-ZrO_2 appears with pitted an crumbled surface, the vanadium ingress respectively the vanadium detection depth is lowest, as it is seen from the EDX measurement of Figure 8. The maximum detection limit of vanadium is many times lower with LAMPP sealing. Furthermore, there is a significant difference between the samples with and without $ZrSiO_4$. The sealed 8Y-ZrO_2 represents the benchmark with a detection depth of 7 µm ± 2 µm, see Table 1.

The XRD pattern of the Sintered 8Y-ZrO_2 sample after the hot corrosion test is shown in Figure 9(a). Before hot corrosion testing, the predominant phase was solely c-ZrO_2. However, after corrosion testing, only a small amount of c-ZrO_2 could be measured. Furthermore, it was found that after the hot corrosion testing the diffraction peaks of m-ZrO_2 dominate along with YVO_4. Therefore, in the surface near region nearly all the stabilizing yttrium from the cubic zirconia phase reacted with the vanadium, which initiates the monoclinic transition within the zirconia phase. In contrast, XRD analysis of the LAMPP 8Y-ZrO_2 exhibit that the intensity of cubic and tetragonal phase is more pronounced, as well as the YVO_4 peaks. However, the monoclinic phase portion is decreased. In case of the Sintered 8Y-ZrO_2/$ZrSiO_4$ after the hot corrosion testing, see Figure 10, the dominant phases are m-ZrO_2, YVO_4 and $ZrSiO_4$ with small amount of tetragonal zirconia. The phase fraction of tetragonal zirconia within the LAMPP 8Y-ZrO_2/$ZrSiO_4$ is much more pronounced compared to the sintered state with less amount of m-ZrO_2. Furthermore, only small amount of YVO_4 is seen.

The principal driving force for the degradation of TBC's by hot corrosion is the chemical reaction between stabilizing oxides and molten vanadate-deposits. The corrosion products YVO_4 and m-ZrO_2 after the hot corrosion testing with V_2O_5 revealed the high solubility of yttria in presence of molten vanadium. At high temperatures, vanadium leeches the stabilizing element yttria from the stabilized zirconia forming YVO_4: Possible reaction that can take place upon temperatures above the melting point from V_2O_5 of 690 °C, is:

$$Y_2O_3 \ (s) \ (in \ YSZ) + V_2O_5 \ (l) \ \rightarrow 2YVO_4 \ (s) + m\text{-}ZrO_2 \ (s) \tag{2}$$
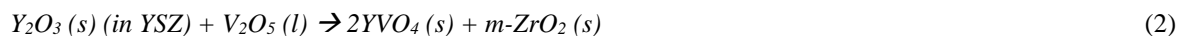
This depletion of yttria within zirconia leads to depletion and subsequently transformation from cubic/tetragonal to monoclitic-ZrO_2 phase. This transformation is accompanied by a volume expansion of about 3-5%. The formation of this depletion zone is governed primarily by the dissolution and reaction of the V_2O_5 with the surface layer of the YSZ and is observed at all investigated samples. The reaction mechanism between V_2O_5 and yttria stabilized ZrO_2 are a Lewis acid–base concept.[20, 21] Therefore, metal oxides with the highest basicity will react with the V_2O_5, which has a huge acidity. It can be assumed, that the molten vanadium oxide attacks only the yttria, because the acidity of yttria is low relative to the ZrO_2 while only minimally attack of the more acidic ZrO_2 occurs.

Table 1: Vanadium detection depth of the samples after hot corrosion testing with molten V_2O_5.

Material comp.	8Y-ZrO_2	8Y-ZrO_2/$ZrSiO_4$
without LAMPP	33 µm ± 3 µm	107 µm ± 3 µm
with LAMPP	7 µm ± 2 µm	17 µm ± 2 µm
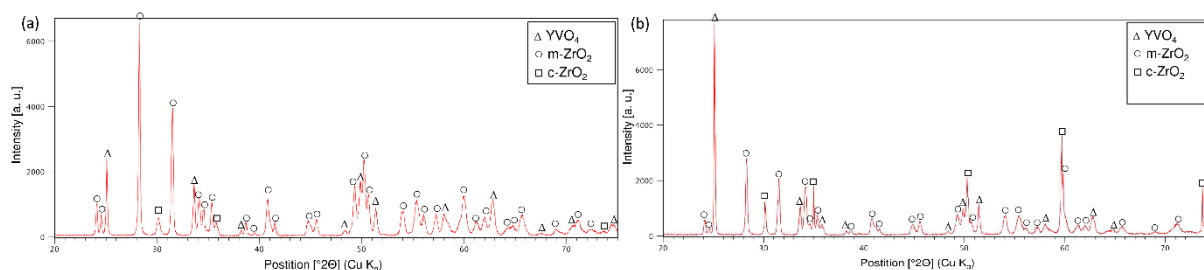
Figure 9: Phase analysis after 4 h hot corrosion testing: (a) Sintered 8Y-ZrO$_2$, (b) LAMPP 8Y-ZrO$_2$
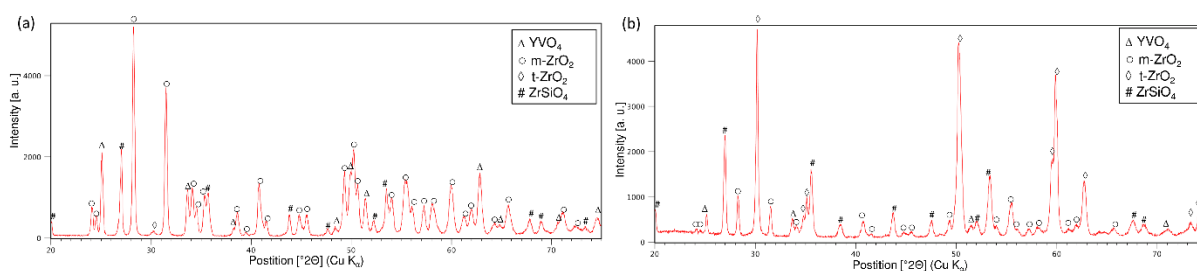
Figure 10: Phase analysis after 4 h hot corrosion testing: (a) Sintered 8Y-ZrO$_2$/ZrSiO$_4$, (b) LAMPP 8Y-ZrO$_2$/ZrSiO$_4$.

The appearance of ZrSiO$_4$-phase within the XRD measurement of LAMPP 8Y-ZrO$_2$/ZrSiO$_4$ after hot corrosion testing is atributed to the lowered recombination temperature of ZrSiO$_4$ in presence of vanadate: monoclinic zirconium dioxide and silicon dioxide were found to react to form zirconium silicate in the presence of vanadium pentoxide at temperatures between 800 °C and 1000 °C. [22, 23] With increasing amount of V$_2$O$_5$ the recombination temperature decreases significantly.

4. Conclusion

LAMPP-sealing can retard the penetration of V$_2$O$_5$ and therefore suppress the reaction between Y$_2$O$_3$ and V$_2$O$_5$. The enhanced durability against molten vanadate leads to enhanced lifetime of the material. Thus, it can be said that the reaction of the vanadium with the sintered samples is higher than the sealed samples due to the higher surface roughness and porosity in the surface.

(1) LAMPP-sealing provides dense surface layers without crack formation. Two different morphologies were distinguished in cross-sectional views prior to hot corrosion testing: (a) Equiaxed zone with grain gradient at 8Y-ZrO$_2$. (b) dendritic structure with amorphous silicon-rich surrounding at 8Y-ZrO$_2$/ZrSiO$_4$.

(2) Both material systems showed that hot corrosion testing led to the formation of YVO$_4$ due to the reaction of the V$_2$O$_5$ melt with the stabilizer Y$_2$O$_3$.

(3) Thus, a sealed ceramic top-layer, facilitated by LAMPP, enables reduction of vanadium ingress.

References

[1] Carlos G. Levi, John W. Hutchinson, Marie-Helene Vidal-Setif, Curtis A. Johnson, *MRS Bulletin* **2012** *(37)*, 932.

[2] A. Keyvani, M. Saremi, M. Heydarzadeh Sohi, Z. Valefi, *Journal of Alloys and Compounds* **2012**, *541*, 488.

[3]   D. R. Clarke, C. G. Levi, *Annual Review of Materials Research* **2003**, *33 (1)*, 383.

[4]   A. G. Evans et al., *Progress in Materials Science* **2001**, *46 (5)*, 505.

[5]   Stiger, M. J., Yanar N.M., Topping M.G., Pettit F.S., Meier G.H., *Materials Research and Advanced Techniques/Zeitschrift fuer Metallkunde*, *1999 (90)*, 255.

[6]   C. G. Levi, *Current Opinion in Solid State and Materials Science* **2004**, *8 (1)*, 77.

[7]   A. Karlsson, J. Hutchinson, A. Evans, *Materials Science and Engineering: A* **2003**, *351 (1-2)*, 244.

[8]   X. H. Zhong et al., *Journal of the European Ceramic Society* **2010**, *30 (6)*, 1401.

[9]   Z. Chen, J. Mabon, J.-G. Wen, R. Trice, *Journal of the European Ceramic Society* **2009**, *29 (9)*, 1647.

[10]   H. Dong et al., *Journal of the European Ceramic Society* **2014**, *34 (15)*, 3917.

[11]   Hamilton, J. C. and Nagelberg, A. S, *Journal of the American Ceramic Society* **1984**, *67 (10)*, 686.

[12]   Z. Negahdari, M. Willert-Porada, F. Scherm, *Materials Science Forum* **2009**, *631-632*, 97.

[13]   F. Stolzenburg et al., *Acta Materialia* **2016**, *105*, 189.

[14]   K. Wang et al., *Journal of the European Ceramic Society* **2014**, *34 (15)*, 3597.

[15]   R. Borchert, *Verfahrensentwicklung zur Herstellung metallisch-keramischer Gradientenwerkstoffe durch Mikrowellensintern*, 1st ed., Cuvillier, Göttingen **1998**.

[16]   K. Wu, S. Scheler, H.-S. Park, M. Willert-Porada, *Journal of the European Ceramic Society* **2013**, *33 (6)*, 1111.

[17]   K. Wu, A. Rosin, H. Park, M. Willert-Porada, *Journal of Physics: Conference Series* **2013**, *419*, 12013.

[18]   K. Wu, *Process development for ZrO2-ZrSiO4/NiCr functionally graded materials*, Berichte aus der Materialwissenschaft, Shaker, Aachen **2013**.

[19]   M. Willert-Porada, R. Borchert, *Materials Science Forum* **1999**, *308-311*, 422.

[20]   R. L. Jones, Williams C. E., Jones S. R., *Journal of The Electrochemical Society* **1986**, *133 (1)*, 227.

[21]   D. B. Belykh et al., *Glass Physics and Chemistry* **2002**, *28 (1)*, 36.

[22]   C. Valentín, M. C. Muñoz, J. Alarcón, *Journal of Sol-Gel Science and Technology* **1999**, *15 (3)*, 221.

[23]   G. Monros, J. Carda, P. Escribano, J. Alarcon, *Journal of Materials Science Letters* **1990**, *9 (2)*, 184.

Measurement of Young's Modulus at Elevated Temperatures of Thermal Barrier Coating by Bending Resonance Method

Satoru Takahashi[1], Kazuki Ookubo[2], Hiroyuki Waki[3], Masahiko Kato[4], Syusui Ogawa[5], Fumio Ono[6]

[1]Tokyo Metropolitan University, takahashi-satoru@tmu.ac.jp [2]Tokyo Metropolitan University, ookubo-kazuki@ed.tmu.ac.jp [3]Iwate University, waki@iwate-u.ac.jp [4]Hiroshima University, mkato@hiroshima-u.ac.jp [5]Japan Fine Ceramics Center, syusui@jfcc.or.jp [6]Osaka Science & Technology Center, f.ono@ostec.or.jp

Abstract

The Young's modulus of individual layer in thermal barrier coatings (TBCs) consisting of metallic bond-coats (BCs) and ceramic top-coats (TCs) was measured at a range from room temperature up to 1000 ℃ by the bending resonance method. Several kinds of TBC specimens were prepared by plasma sprayings. The resonance frequencies of the specimens were measured and the Young's moduli were determined using the bending resonance method of a multilayered specimen developed in the previous study. It was found that the reliable Young's moduli of the TC and the BC can be obtained at elevated temperatures as well as room temperature.

Keywords: Thermal Barrier Coating, Young's Modulus, Bending Resonances, Plasma Spraying

1. Introduction

Thermal barrier coatings (TBCs) are highly advanced material systems, generally applied to surfaces of hot-section components of power-generation gas turbines and aero-engines. A TBC consists of a metallic bond-coat (BC) and a ceramic top-coat (TC) on a superalloy substrate. Various properties of the TBC have been required for designing the TBC with the high durability. Especially, the Young's modulus is one of the important mechanical properties to evaluate mechanical and thermal stresses. For determining the Young's modulus of TBC at room temperature, the four point bending test was developed [1] and has been established as ISO 19477:2016[2]. As the next step, Waki et al. derived a closed-form solution for the Young's modulus of the TC layer using the equation of motion for the bending vibration of a composite beam and experimentally confirmed the effectiveness of this method at room temperature [3]. In the present study, the Young's modulus of TBC at elevated temperatures was measured using the developed resonance method.

2. Method for Determining Young's Modulus of TBC Specimen using Bending Resonance

Using the first bending resonance of a multilayered specimen comprising a substrate, a BC and a TC, the Young's modulus of a TC can be obtained according to Eq. (1)-(6) [3]. Here, E, h, b, L and ρ are the Young's modulus, thickness, width, length and density, respectively. The subscripts "c", "b" and "s" represent the TC, the BC, and the substrate, respectively. The Young's modulus of the TC can be obtained from the resonance frequency f of the TBC specimen, if the dimensions and mass of the specimen and the Young's moduli of all the other layers are known. Similarly, the Young's modulus of the BC is also determined using a BC specimen comprising a BC and a substrate.

$$E_c = \left(-B + \sqrt{B^2 - 4AC}\right)/2A \qquad (1)$$

$$A = \beta^2 h_c^4 \qquad (2)$$

$$B = 2h_c \left[\begin{array}{c} \beta^4[E_b h_b(2h_c^2 + 3h_c h_b + 2h_b^2) + E_s h_s\{2h_c^2 + 3h_c h_s + 6h_b^2 + 6h_b(h_c + h_s) + 2h_s^2\}] \\ -24\pi^2 f^2 m L^3/b \end{array} \right] \quad (3)$$

$$C = \beta^4\{E_b^2 h_b^4 + 2E_b E_s h_b h_s(2h_b^2 + 3h_b h_s + 2h_s^2) + E_s^2 h_s^4\} - 48\pi^2 f^2 m L^3(E_b h_b + E_s h_s)/b \quad (4)$$

$$m = bL(h_c \rho_c + h_b \rho_b + h_s \rho_s) \quad (5)$$

$$\beta = 4.730 \quad (6)$$

3. Experimental Procedures

3.1. Preparation of Specimens

The Ni-base superalloy Hastelloy X was selected as the substrate alloy. Beam type specimens, 100 mm in length, 10 mm in width and 2.05 mm in thickness, were machined from the substrate alloy. One side surface was blasted and subsequently coated with CoNiCrAlY-BC by atmospheric plasma spraying (APS). Then, three types of $ZrO_2 7\sim 8Y_2O_3$ (YSZ) powders for TC were selected and were deposited by APS. The coating processing and the nominal thickness of each coating are summarized in Table 1. Figure 1 shows the typical cross-sectional microstructures as observed by back scattered electron imaging for three types of TBC specimens. The TC (D) is relatively densified compared with the TC (N) which was made with the popular YSZ powder as the TC. The TC(P), in contrast, has many globular micropores. Some specimens were subjected to heat treatment in vacuum at 1000 ℃ for 2 h. The thickness of individual layer for the calculating the Young's modulus was measured on the cross-sectional microstructure. Furthermore, the porosity of the TC was also evaluated using an image analysis.

3.2. Measurement of Young's Modulus of TBC by Bending Resonance Method

A schematic illustration of the apparatus is shown in Fig.2. This method measures the bending frequency of the specimen by exciting it at continuously variable frequency. The apparatus consists of the driving circuit and the detecting circuit. A TBC specimen was suspended by alumina fibers in an electric furnace. Mechanical excitation of the specimen was provided through the speaker. The AE sensor was used to detect the mechanical vibration and to convert it into an electrical signal.

Table 1 Coating processing and nominal thickness of individural coating in various specimens

Code	Substrate	Bond-coat (BC)	Top-coat (TC)
Sub specimen	Hastelloy X	No	No
BC specimen	Hastelloy X	CoNiCrAlY / 0.3	No
TBC (N) specimen	Hastelloy X	CoNiCrAlY / 0.15	TC (N) / ZrO_2-8Y_2O_3 (Oerlikon Metco 204NS) / 0.30, 0.50, 0.70
TBC (D) specimen	Hastelloy X	CoNiCrAlY / 0.15	TC (D) / ZrO_2-7Y_2O_3 (Showa Denko K-89) / 0.50
TBC (P) specimen	Hastelloy X	CoNiCrAlY / 0.15	TC (P) / ZrO_2-8Y_2O_3 (Oerlikon Metco 204NS-G + Polyester) / 0.50
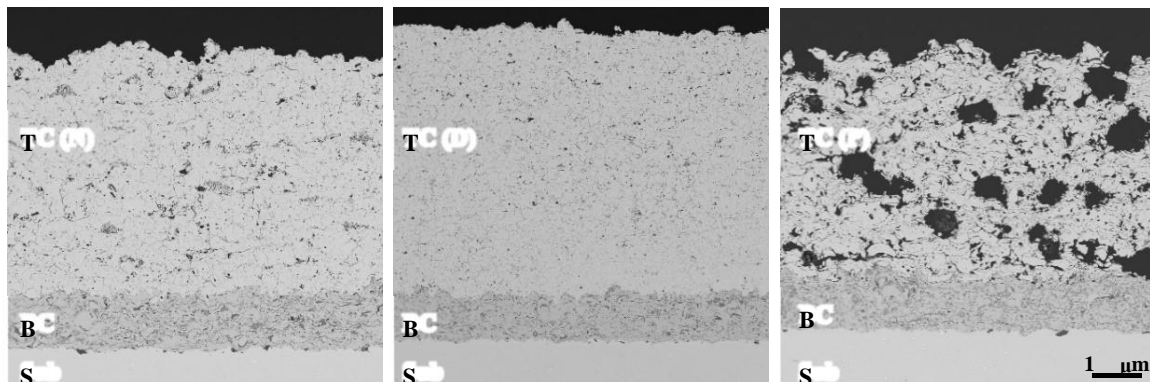
Figure 1: Typical cross-sectional microstructures of three kinds of TBCs.
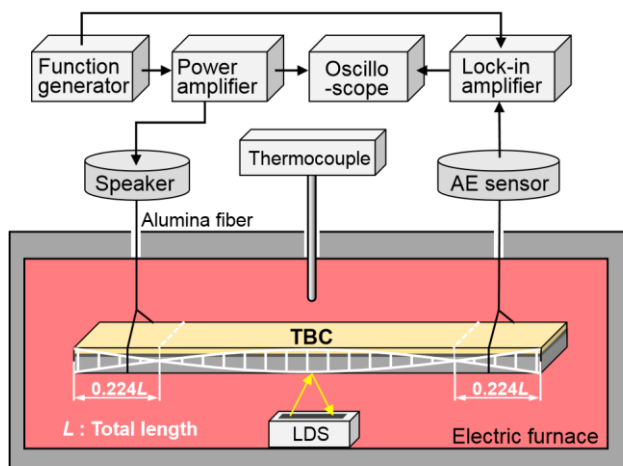
Figure 2: Schematic illustration of the apparatus.
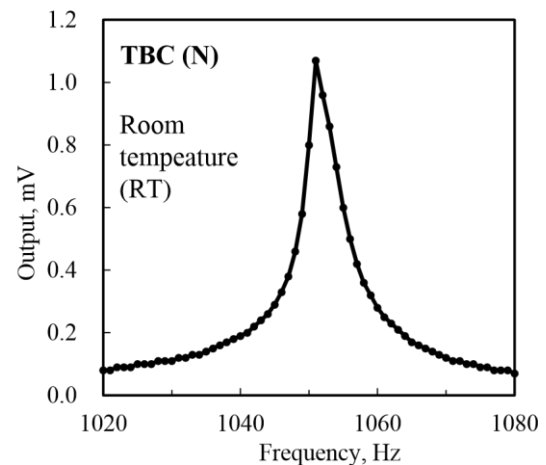
Figure 3: Example of peak response.

The peak response of the signal at room temperature was investigated. The out-of-plane displacements of the specimen at the peak response was measured by a laser displacement sensor (LDS) to confirm the first bending mode and the resonance frequency was determined. Then, the specimen was heated from RT to 1000 ℃ at 5 ℃/min and the resonance frequency was measured continuously.

4. Results and Discussion

Figure 3 shows a typical peak response of the output signal for the TBC(N) specimen at room temperature. A clear peak was observed at 1050Hz in frequency. The amplitude of the specimen vibrating at this frequency are shown in Fig. 4. The amplitudes at distance of 0.224 of the total length from each end, corresponding to the vibration nodes, were smaller than that of other positions. Since this distribution of the amplitude demonstrates the first bending mode, this frequency was determined as the bending resonance frequency of the specimen. Figure 5 shows the Young's moduli of the as-sprayed TCs with the different microstructure at room temperature. The Young's modulus of the TC(D), which was relatively densified, was higher, while the TC(P) with the porous microstructure exhibited the lower Young's modulus. The Young's modulus of the TC was found to depend on its porosity.

The Young's moduli of the BCs and the substrates at elevated temperatures are shown in Fig.6 (a). The Young's modulus of the heat-treated (HT) substrate was as almost same as that of the as-received substrate. On the other hand, the Young's modulus of the BC depended strongly on the heat treatment. The Young's modulus of the heattreated BC decreased gradually with increasing the temperature, although the as-sprayed BC exhibited the unstable behavior. This is attributed to the homogenization of microstructure of the BC due to the heat treatment

As a typical example of the Young's modulus of the TC at elevated temperatures, Fig. 6 (b) shows the Young's moduli of the TC (N) obtained from TBC (N) specimens. Regardless of the thickness of the TC, almost the same results were obtained by this method. The Young's modulus decreased at range from RT to 400 ℃ and then tended to increase slightly from 400 ℃ to 1000 ℃. These results were identical to that measured by other research institute (JFCC) and the reproducibility of the data was confirmed. Namely, it was found that the reliable Young's moduli of the TC and the BC by the bending resonance method can be obtained at elevated temperatures as well as room temperature. This method is expected to apply to TBCs consisting of TCs with a columnar structures made by such EB-PVD and suspension plasma spraying (SPS) processing.
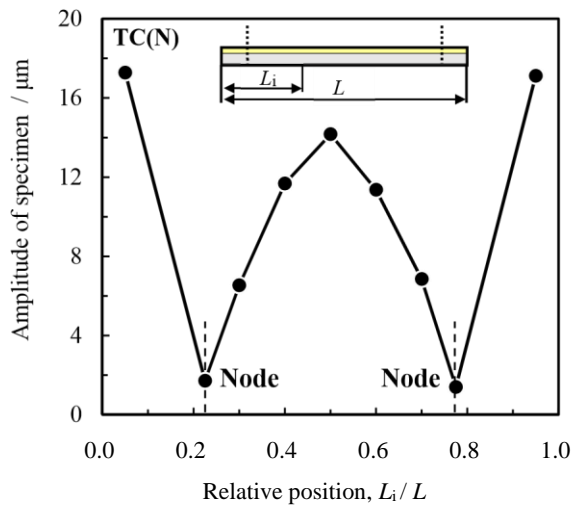
Figure 4: Distribution of amplitude for specimen.
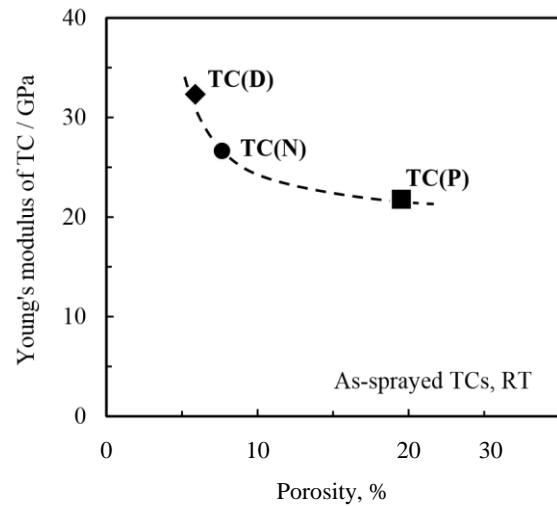
Figure 5: Young's modulus of various TCs.
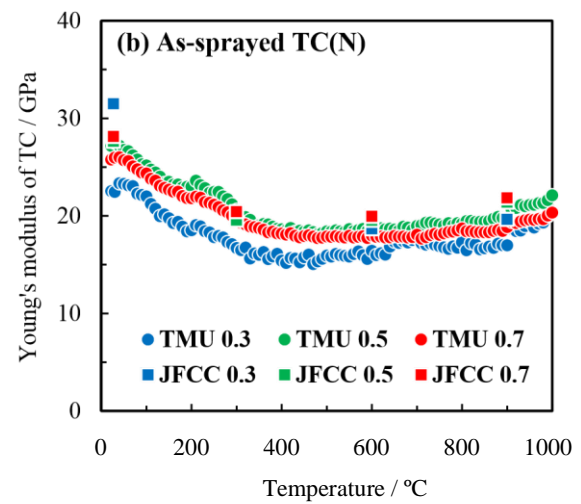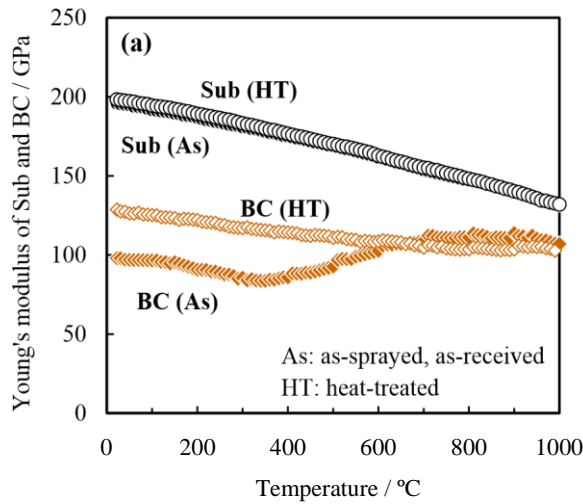
Figure 6: Young's moduli of the substrate, the BC and the TC at elevated temperatures.

4. Conclusion

The Young's moduli of the BC and the TC were determined using the bending resonance method of a multilayered specimen. This method can be obtained the reliable Young's modulus of the TBC at elevated temperatures as well as room temperature.

Acknowledgements

References

H. Waki, A. Oikawa, M. Kato, S. Takahashi, Y. Kojima, F. Ono, *J. Therm. Spray Technol*., **23** (8) (2014), 1291-1301.

[1] ISO 19477:2016 Metallic and other inorganic coatings – Measurement of Young's modulus of thermal barrier coatings by beam bending.

[2] H. Waki, K. Takizawa, M. Kato, S. Takahashi, *J. Therm. Spray Technol*., **25** (4) (2016), 684-692.

Development of measurement system of thermoelectric properties
of thin films in the thickness direction

Yoshikazu SHINOHARA[1], Hiroshi KAWAKAMI[2], Yukihiro ISODA[3]

[1]National Institute for Materials Science, Japan, SHINOHARA.Yoshikazu@nims.go.jp
[2]New Energy and Industrial Technology Development Organization, Japan,
kawakamihrs@nedo.go.jp
[3]National Institute for Materials Science, Japan, ISODA.Yukihiro@nims.go.jp

Abstract

Thermoelectric materials can generate electrical power directly from heat without any vibration. That is why thermoelectric power generation is promising as an isolated compact power source such as automobile generators, solar heat generator. We have already clarified that the generated power can be improved by applying the segmented structure based on FGMs concept to thermoelectric legs of power generators. Recently thin film thermoelectric generators are paid more attention to as energy harvesting applications. Quantitative evaluation methods of thermoelectric properties of thin films in the thickness direction has not been established. In the present study, the electrode structure for the measurement in the thickness direction has been prepared for and the measurement apparatus has been developed.

Keywords: measurement, thermoelectric properties, thin film

1. Introduction

Paris Agreement was concluded among 196 participant countries at COP (Conference of the Parties) 21 in Paris on 12th Dec, 2015 to stop the global warming [1]. Effective use of energy generated from fossil fuels such as oil, coal and natural gas is an important route to reduce GHG. One third of the primary input energy in Japan is used effectively, while the remaining two thirds is exhausted as waste heat [2]. Thermoelectric materials, which convert heat to electricity directly, can generate power from heat. The characteristics of thermoelectric power genetration are as follows;

1) Compact energy conversion system
2) Silent system without any moving parts
3) Almost maintenance free operation

According to these, thermoelectric power generation is a useful technique to use waste heat spread widely in our lives effectively. Isolated compact power sources such as automobile generators, boiler heat generators, solar heat generators and wearable power supplies are promising as its applications. Its disadvantage is low power in comparison with other power generation such as binary power, solar power, vibration power, Starling engine power and so on. We have already clarified that the generated power can be improved by applying the segmented structure, which is based on FGMs concept, to thermoelectric legs of power generators [3].

Recently power generators using thermoelectric thin films are paid more attention to as energy harvesting applications. Some industrial sensors and home temperature sensing systems using waste heat have been already applied and wearable health managers using body heat are being developed [4]. For the purpose of promotion of thin film power generator, the quantitative evaluation methods of thermoelectric properties of thin films in the thickness direction should be established, but not yet. In the present study, the electrode structure was specially

designed for the measurement in the thickness direction and the measurement apparatus of thermoelectric properties of Seebeck coefficient and electrical conductivity has been developed.

2. Experimental procedure

2.1 Specimens

We prepared for five kinds of materials as the specimens; Si wafer, Pt plate, polyaniline pellets, poly(3-alkylthiophene) films and BiTe nanowire array. The Si wafer and Pt plate were a standard to clarify the error level of the developed apparatuses. The polyaniline pellets were used for selection of an electrode material. The poly(3-alkylthiophene) films and BiTe nanowire array were used for actual exercises of the developed apparatuses.

2.2 Measurement apparatus in the planar direction

Prior to development of the apparatus for measurement in the thickness direction, we constructed the apparatus in the planar direction to get basic information on electrode material, thermocouples, paste material and small heater to give a temperature difference to specimens. Four-probe method was applied to measurement of electrical conductivity. The Pt plate was used as a standard for error level check.

2.3 Measurement apparatus in the thickness direction

On the basis of the information accumulated in *2.2.*, the apparatus for measurement in the thickness direction was constructed. Specially prepared sample stages were designed and prepared for both the measurements of Seebeck coefficient and electrical conductivity. Two-probe method was applied to measurement of electrical conductivity. The Si wafer was used as a standard for error level check.

3. Results and Discussions

3.1 Measurement apparatus in the planar direction

The electrode materials of In, Cu and Au were tested on contact resistance with polyaniline pellets. Cu and In indicated high contact resistance due to low conatct and large difference in work function, respectively. Au was selected as an electrode material. K-type, T-type and R-type thermocouples were tested on thermo-electromotive force, thermal conductivity and flexibility. R-type thermocouples were selected from low thermal conductivity and high flexibility for the planar measurement. Paste materials of Ag, Au and Pt were tested on electrical conductivity and work function. Au was selected from high electrical conductivity. Peltier modules were selected as small heaters to give a temperature difference to specimens, from low electric field around the heater.

The developed apparatus in the planar direction is shown in Figure 1. The Peltier module is sandwiched by Al blocks to give a temperature difference to the specimen. The cast film of poly(3-alkylthiophene) on a quarts substrate is set on them. The error level of measured data of electrical conductivity and Seebeck coefficient is less than 1%.
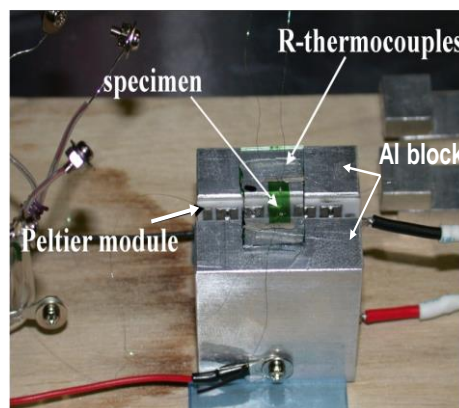
Figure 1: Developed measurement apparatus in the planar direction. A specimen is a film of Poly(alkylthiophene) film on a quarts substrate.
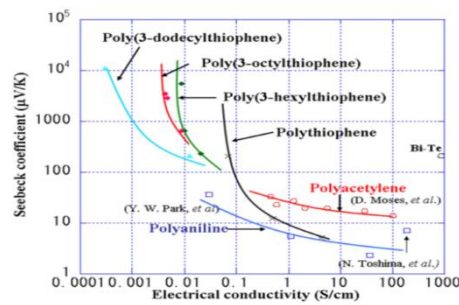
Figure 2: The relationships between electrical conductivity and Seebeck coefficient of poly(3-alkylthiophenes)
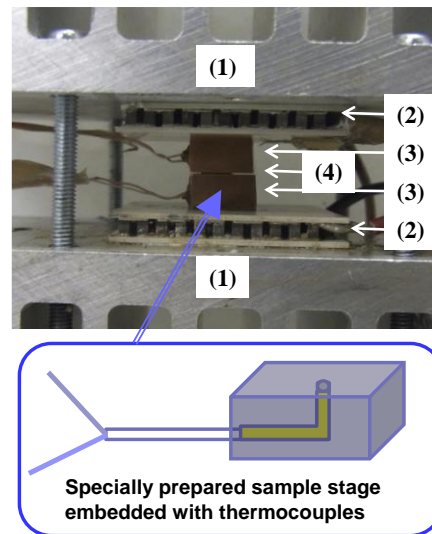
Figure 3: Developed measurement apparatus in the thickness direction. (1) Heat sink, (2) Peltier module, (3) sample stage and (4) specimen

The measured thermoelectric properties at room temperature of electrical conductivity and Seebeck coefficient of poly(3-alkylthiophenes) are shown in Figure 2 [5]. The data in the region of low electrical conductivity of less than 0.01S/cm and high Seebeck coefficient of more than 1000µV/K were successfully obtained. When the electrical conductivity is compared among poly(3-alkylthiophenes) for the same Seebeck coefficient of 1000µV/K, the electrical conductivity increases with a decreasing side chain size of poly(3-alkylthiophenes). This is due to an increasing density of polythiophene main chains in the films with an decreasing side chain size.

3.2   Measurement apparatus in the thickness direction

The developed apparatus in the thickness direction for Seebeck coefficient measurement is shown in Figure 3. The specimen is sandwiched by specially prepared Cu sample stages embedded with thermocouples. T-type thermocouples were selected from flexibility and good contact with Cu sample stage. For electrical conductivity measurement, two Cu electrodes are added between a Cu sample stage and Peltier module. The error level of measured data of electrical conductivity and Seebeck coefficient is less than 3%.

This apparatus was applied to measurement of thermoelectric properties of the BiTe nanowire array showed in Figure 4. The nanowire array was synthesized by electrodeposition process using Al_2O_3 template of 50µm thickness with penetrated holes of 200nm diameter. The measured values of electrical conductivity and Seebeck coefficient at room temperature of the BiTe nanowire array is summarized at Table 1.
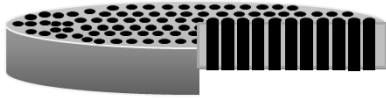
Figure 4: The schematic view of BiTe nanowire array synthesized by electrodepostion process using Al_2O_3 template

Table 1: Measured values of electrical conductivity and Seebeck coefficent of BiTe nanowire array and estimated values of nanowires

	σ/ Scm^{-1}	S / μVK^{-1}	PF / μWm^{-1}K^{-2}
nanowire-array	535※1	-50	134
nanowire	1338※2	-50	335

※1Contact resistance: 5.16×10^{-3} Ωcm^{-2}
※2Density of nano wires: 40% from SEM photograph

The electrical conductivity of 535S/cm was obtained by correcting the raw value by contact resistance between the nanowire array and sample stage. The area fraction of nanowires in the cross-sectional area of the nanowire array is 40%. By assuming the density of nanowires is equal to the area fraction, the electrical conductivity of only nanowire in the Al_2O_3 template was 1340S/cm. The nanowires of 200nm diameter reveal the relatively high electrical conductivity than the common BiTe legs applied to the practical modules. The quantitative values of nanowires was firstly reported at the international conference on thermoelectrics [6].

4. Conclusions

The specially designed electrode structure has been newly prepared for and the measurement apparatus of thermoelectric properties of Seebeck coefficient and electrical conductivity in the thickness direction has been successfully developed for thin thermoelectric materials of less than 100□m thickness. The error level of measured data was less than 3%. The disadvantage of thermoelectric power generation is low power in comparison with other power generation such as binary power, solar power, vibration power, Starling engine power and so on. We have already clarified that the generated power can be improved by applying the segmented structure based on FGMs concept using thick materials. We are going to the research on the segmented thermoelectric films with multilayer structures by applying the present developed apparatus.

Acknowledgements

References

[1] http://www.env.go.jp/earth/cop/cop21/
[2] National Institute for Materials Science, NIMS Report on thermoelectrics, Ibaraki, (2014)
[3] Y. Shinohara, Y. Imai, Y. Isoda, I. A. Nishida, H. T. Kaibe and I. Shiota, Proc. International Conference on Thermoelectrics, (1997), pp.386-389
[4] http://micropelt.com/index.php
[5] Y.Shinohara, K.Ohara, Y.Imai, Y.Isoda, H.Nakanishi, Proc. 23rd International Conference on Thermoelectrics, (2004), CDROM
[6] European Conference on Thermoelectrics, Madrid, Spain, (2014)

Gradient-Index Micro-Optics by Ion Exchange in Glass and its Applications to Optical Metrology and Biophotonic Imaging

Sandra Gerlach[1], Bernhard Messerschmidt[1]

[1]GRINTECH GmbH, Schillerstrasse 1, D – 07745 Jena
gerlach@grintech.de

Abstract

Gradient-index (GRIN) micro-optics in glass with planar optical surfaces enables the miniaturization and integration of optical systems with a complex function. The lens performance of GRIN lenses is achieved by specific refractive index profiles in glass rods and slabs, which are produced by Silver, Sodium and Lithium ion exchange in appropriate glasses. Curved surfaces of conventional lenses are replaced by plane surfaces of GRIN lenses, which make the fabrication of individual lenses with diameters down to 200 µm and less possible.

The talk will introduce gradient index optics and its optical design aspects and presents the potentials and current limitations of the ion exchange technology in glass, as well as applications in optical sensing and biophotonic imaging.

Keywords: GRIN lens, ion exchange, micro-optics

1. Introduction

GRIN micro lenses with almost parabolic radial or lateral index profiles represent an interesting alternative to conventional homogeneous glass lenses since the lens performance depends on a continuous change of the refractive index within the lens material. Instead of surfaces of complicated shape, plane-optical surfaces are used. The light rays are continuously bent within the lens until, finally, they are focussed on a spot. Miniaturized lenses are fabricated of 3 mm down to 0.2 mm in diameter. The simple geometry allows the cost-effective production in larger volumes and simplifies the assembly of rather complex systems essentially, including optical fibres, prisms and beam splitters, because these plane-optical components can be attached directly to the GRIN lenses. Varying the lens length implies an enormous flexibility at hand to fit the lens parameters as, e.g., the focal length and working distance to a specific requirement. Preferred ranges of application are the optical telecom components, laser diode-to-fibre couplers, miniaturized endoscopes, and a variety of optical sensors. New emerging fields are endomicroscopic probes with high resolution requirements and miniaturized heads for optical coherence tomography (OCT).

2. Optical design aspects

In contrast to conventional refractive optics where light is refracted at the abrupt transition from one homogeneous medium to a second one, the direction of the propagating light changes continuously in gradient index (GRIN) media, depending on the distribution of the refractive index n(x, y, z). The propagation in terms of geometrical optics is governed by the rules of Fermat's principle.

A radial, almost parabolic refractive index profile realizes a continuous cosine ray trace within a GRIN focussing lens, with a period or pitch length P (Figure 1).
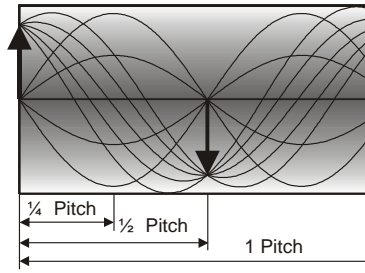
Figure 1: Ray traces within a GRIN focussing lens of different pitch lengths.
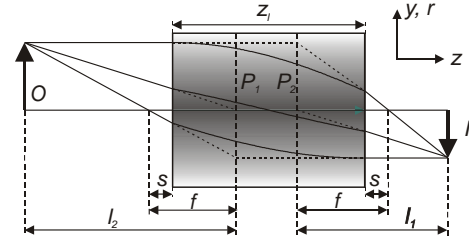
Figure 2: Image formation by a GRIN focussing lens.
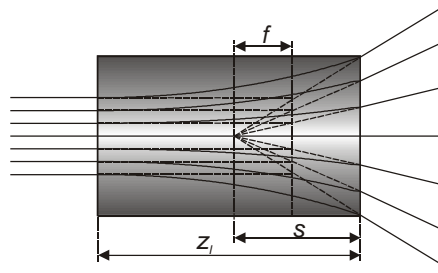
Figure 3: Ray traces in a GRIN diverging lens.

The geometrical gradient constant g of the radial index profile *(1)* characterizes the steepness of the index gradient and determines the focal length f and the working distance s of the lens, with the lens length z_l,

$$f = \frac{1}{n_0 g \sin(gz_l)}, \quad s = \frac{1}{n_0 g \tan(gz_l)} \quad . \tag{1}$$

Figure 2 illustrates the ray trace of a GRIN system using these parameters.

The maximum acceptance angle of a GRIN collimation lens or the maximum viewing angle of a GRIN objective lens, respectively, ϑ is determined by the numerical aperture NA. As in fibre optics, it is derived from the maximum index change of the GRIN profile,

$$\sin(\vartheta) = NA = \sqrt{n_0^2 - n_R^2} = n_0 \sqrt{1 - \text{sech}^2(gd/2)} \tag{2}$$

n_R is the refractive index at the margin of the profile, and *d* is the diameter of the lens.

Diverging lenses with plane optical surfaces are obtained by parabolic-shaped refractive index profiles *(3)*, with the minimum of the index n_0 at the centre of the profile.

A characteristic ray trace through a diverging lens is shown in Figure 3. The comparably short focal lengths of the lenses *f* are also determined by the lens length z_l,

$$f = -\frac{1}{n_0 g \sinh(gz_l)}, \quad s = -\frac{1}{n_0 g \tanh(gz_l)} \tag{3}$$

However, a periodic path of the rays is not obtained in this case. Those lenses are applied to the production of micro-optical telescopes and scanners.

For most customized applications it is necessary to introduce the required index profile into model functions which deviate from ideal and analytical examples. Normally, a polynomial expression is used introducing an appropriate number of design parameters. Numerical ray tracing is then performed to determine optimum index profile parameters for a specific configuration, considering also the technological feasibility. A more detailed introduction in the fundamentals of gradient index optics is given in [1, 2].
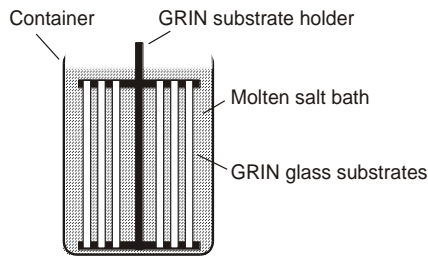
Figure 4: Ion exchange scheme for borosilicate glass rods and slabs in salt melts.
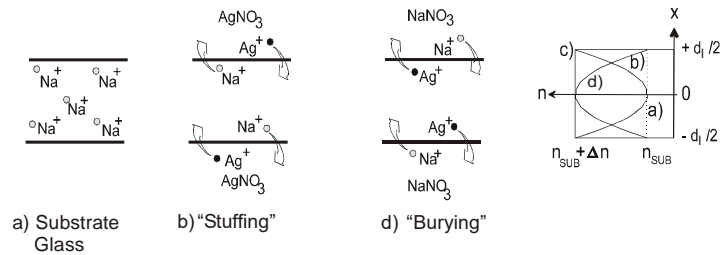
Figure 5: Silver-sodium ion exchange for producing high NA radial and one dimensional GRIN lenses.

3. Fabrication Techniques

Gradient index materials for visible light and near infra-red applications are usually based on transparent silicate glasses and sometimes on organic polymer materials. The refractive index can be changed by locally varying the chemical composition and structure and related optical and mechanical properties.

Although several techniques as, i.e., the Sol-Gel [3] and the Chemical Vapor Deposition (CVD) processes are described in the literature, the ion exchange or diffusion technology in glasses and plastics are of most practical importance for the production of gradient index lenses [4] and are described in more detail.

3.1 Ion exchange and diffusion processes in glass

For producing radial and lateral gradients in small diameters between 0.1 and 3.0 mm, the ion exchange of monovalent cations between salt melts and initially homogenous borosilicate glass rods or slabs is used [5] at elevated temperatures below or in the range of the transition temperature of the glass. Here, the network of the glass formers is still rigid, but monovalent ions have some mobility and the salts are liquid (Figure 4).
The fabrication time depends on the kinematic properties of the ion exchange, which is described as a interdiffusion process of the ions A and B in the glass and the salt melt,

$$A^+_{Glass} + B^+_{Salt} \leftrightarrow A^+_{Salt} + B^+_{Glass}$$
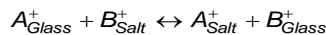
It is modelled by Fick's diffusion equation,

$$\frac{\partial c_A(\vec{r},t)}{\partial t} = \nabla\big(D(c_A,T)\,\nabla c_A(\vec{r},t)\big)$$

where c_A is the normalized concentration of cation A, and D is the diffusion coefficient. It generally depends on the concentration, the temperature T and relevant properties of the glass composition.

High-NA lenses with radial gradients are obtained by large index changes of > 0.1. This kind of GRIN lenses are generated by thallium / sodium – potassium ion exchange or by the silver – sodium one [5]. In contrast to silver, thallium is a very toxic material. Silver is almost non-toxic. Still, glasses with a high content of silver tend to reduce to metallic silver at typical melting temperatures above 1000 °C. Consequently, the silver colloids cause a dark colour of the glass. Hence, a two-step process is used for the production of focusing silver containing GRIN lenses [5]. The first step ("stuffing") is to receive a nearly uniform refractive index increase Δ*n* (Figure 5). In a second "burying" step, silver ions in the glass are partially removed and replaced by index-lowering sodium ions.

Many applications require longer ray periods P connected with lower numerical apertures and minimized chromatic aberrations. Preferably, the lithium-sodium ion exchange in alumo-borosilicate glasses is used to produce these types of radial GRIN lenses with smaller index changes Δn [6, 7].

4. Applications

A one-dimensional or cylindrical GRIN lens with plane surfaces is obtained by a parabolic-like one-dimensional index distribution, which is oriented perpendicular to and not varying along the optical axis (Figure 6). It is successfully produced by the ion exchange in glass plates and applied to the fast axis collimation of laser diode bars, or to the anamorphic shaping of elliptically diverging and often astigmatic beams of laser diodes into circular focussed beams which are necessary for the efficient coupling into fibres, or for the pumping solid state lasers [8].
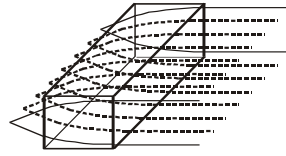
Figure 6: Cylindrical GRIN lens with a one-dimensional lateral index profile.
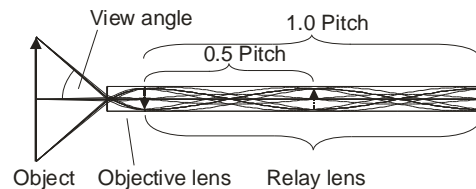
Figure 7: GRIN endoscope without eyepiece function.

In the field of conventional endoscopy, where an object in a hardly accessible hollow space needs to be imaged with a large viewing angle through a small opening, the GRIN lens technology is of important interest when the diameter of the optics has to be smaller than 2.0 mm, especially below 1.0 mm, as conventional lenses are difficult to manufacture and to assemble to long imaging systems. The complete imaging system of an endoscope can be built up with only two GRIN lenses, an objective lens of high numerical aperture (NA > 0.5), which generates a demagnified intermediate image of the object with a large viewing angle, and a relay lens of low numerical aperture (NA approx. 0.1), which relays the intermediate image of the objective to the outside of the body (Figure 7).

Several ray periods or pitches of the GRIN relay with additional intermediate images may be necessary to generate the required length of the endoscope. It is also possible to integrate the eyepiece or ocular function within the same relay lens [7] to avoid additional optical elements. These GRIN systems do not imply any internal Fresnel reflection losses because of the absence of internal optical surfaces inside the imaging tube. The aberrations have been analysed in comparison with those of conventional optical systems in endoscopes, and the possibilities of preventing and correcting the aberrations have been studied in detail [7]. Flexible endoscopes use coherent imaging fibre bundles for the image transmission over tens of centimetres. If the diameter of the optical channel is less than 1.0 mm, GRIN objective lenses, which can be attached directly to the fibre bundle, are preferably used as they yield a good image quality [9].

References

[1] K. Iga, Y. Kokubun, and M. Gikawa, "Fundamentals of Microoptics", Academic Press, New York, 1984.
[2] C. Gomez-Reino, M. V. Perez, C. Bao, "Gradient-Index Optics", Springer, Berlin, 2002.
[3] K. Shingyouchi and S. Konishi, Appl. Opt. **29**, 4061-4063 (1990).
[4] R. H. Doremus, Ion Exchange in Glasses in *Ion Exchange*, J. Marinski, Ed. (Marcel Decker, New York, 1966).
[5] B. Messerschmidt, T. Possner, and R. Goering, Appl. Opt. 34, 7825-7830 (1995).
[6] N. Haun, D. S. Kindred, and D. T. Moore, Appl. Opt. **29**, 4056-4060 (1990).
[7] L. G. Atkinson, D. T. Moore, and N. J. Sullo, Appl. Opt. 21, 1004-1008 (1982).
[8] J. M. Stagaman, D. T. Moore Appl. Opt. **23**, 1730 (1984).
[9] B. Messerschmidt, T. Possner, and P. Schreiber, in *Diffractive Optics and Micro-Optics*, OSA Techn. Digest 303-305 (2000).

Compositionally graded glass by microwave field assisted ion exchange

T. Gerdes[1,2,] A. Schmidt-Rodenkirchen[2], H.S. Park[1], B. Scharfe[3], M. Willert-Porada[1,3]

[1]*InVerTec eV, Bayreuth, Germany*

[2]*Chair of Materials Processing, University of Bayreuth, Bayreuth, Germany*

[3]*Technologie-Anwenderzentrum Spiegelau, Spiegelau, Germany*

Abstract

Distribution of electrical field gradients developing upon microwave heating glass parts immersed in an alkaline salt melt is analyzed by simulation. It is assumed that such gradients influence the process of ion exchange between the molten salt and the silicate glass immersed in it. It is shown that strong E-field gradients exist between the melt and the solid glass which could enhance ion transport due to an electro-migration effect superimposing the concentration gradient. In addition, interaction of the solid glass with microwave radiation could facilitate stress relaxation in the glass, which upon thermally induced ion exchange is retarding diffusion of alkali ions.

A special microwave applicator has been developed which enables equilibration of inhomogeneous electromagnetic field distribution by mechanical movement of the samples subjected to ion exchange in order to analyze the overall effect of electromagnetic filed influence on ion exchange phenoemena.

1. Introduction

Ion exchange has traditionally been applied to strengthen glass by "chemical hardening", based on introduction of a well-defined compressive stress into surface near regions of a brittle glass [1,2]. The compressive stress is build up by replacement of small ions, e.g., Na+ from the glass network by larger ions, e.g., K+ from a salt melt in which the glass is immersed. The driving force for this exchange of ions is a concentration gradient between the molten salt and the glass immersed in it. Due to chemical strengthening extremely strong and flexible thin glass is obtained - currently such processed glass is used for displays in smart phones and other electronic applications.

The idea, to assist the ion exchange with the help of a DC-electric field gradient has been developed already 40 years ago, for preparation of glass membranes [3]. Later on this methodology was applied to prepare optical devices known as "gradient index lenses" [4]. Spatial control of a thermochemical treatment by "FASSIE", Field-Assisted Solid-State Ion-Exchange, is a modern variant of ion exchange, which is successfully applied for doping silicate glasses with transition metal- and rare-earth-ions to obtain functional photonic devices or other optical communication devices [5].

Use of AC-electric field assistance upon ion exchange has also been reported in literature [6,7], and it raised some questions about the underlying physical phenomena, because enhanced ion exchange rates were found as compared to conventional heat treatment at nominally same temperature but no quantitative analysis of possible driving force enhancement was provided so far.

The main problem in previous work was the lack of knowledge about the electromagnetic field distribution between the molten salt serving as reservoir for ions to be exchanged and the solid glass serving as sink for these ions.

In our work we have therefore concentrated on design and implementation of an apparatus which enables not only measurement of temperature but also analysis of electric field gradients developing upon melt-based ion exchange in silicate glass. The knowledge of electromagnetic field distribution is a prerequisite to analyze the rather complex transport paths upon an ion exchange process, which is driven by several gradients – thermal (T), chemical activity (μ) , electro-migration potential (□) in case of presence of an external electrical field, and reaction kinetics (v), as shown by the overall transport equation:

$$ s = J_u \cdot \nabla \frac{1}{T^e} - \sum_k J_k \cdot \nabla \left(\frac{\mu_k}{T} \right) + \frac{I \cdot \left(-\nabla \phi_{AC} \right)}{T} + \sum_j \frac{A_j \cdot \upsilon_j}{T} $$

The description of the underlying transport mechanisms is given in the table below:

Process	Force Fα	Flow (current) Jα
Heat conduction	$\nabla \frac{1}{T}$	Energy flow J$_u$
Diffusion	$-\nabla \frac{\mu_k}{T}$	Diffusion current J$_k$
Electrical conduction	$\frac{-\nabla \varphi_{AC}}{T} = \frac{E}{T}$	Ion or other charged or polarized particle current I$_k$
Chemical reactions	$\frac{A_j}{T}$	Velocity of reaction υ_j

For enhanced ion exchange electro-migration due to an electrical potential difference ϕ is of prominent interest. Therefore in the work presented here the electrical field gradients were analyzed by simulation of the microwave field distribution in the melt and in the solid glass samples immersed in the melt. Along with the ion exchange process schematically shown in Fig. 1, also a relaxation of the glass network could take place, which would counteract the build-up of a compressive stress. This effect has not been analyzed in the simulation presented here.

Close to the glass transition temperature the relaxation frequency of certain parts of the glass network can reach GHz-frequency, which in case of a superimposed microwave field can cause an exponential increase of the temperature in the glass and eventually lead to a "thermal runaway", as described in [7]. It is therefore crucial to control the temperature very carefully upon microwave assisted ion exchange in order to enable a correct interpretation of possible deviations from ion exchange profiles achieved upon conventional heating.
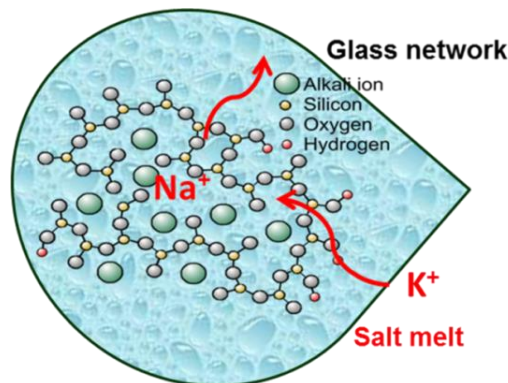
Fig. 1.   Schematic representation of the ion exchange process in a silicate glass; a Sodium-ion is replaced by an Potassium Ion.

The achievable depth profile of ion exchange is limited by mechanical stresses which build up due to ion exchange. Therefore the resulting compression stress, CS, namely the shape and depth of the CS-zone depend upon the time and temperature in a non-linear manner [8].

For microwave heating simulation the commercial software Quickwave 2013 was used. The dielectric properties of the solid glass and the alkaline-salt melts were selected according to the DC-ionic conductivity at the respective temperature. Such data are available in textbooks.

2. Experimental

All experiments were performed in air at ambient pressure. Temperature measurements were done by a pyrometer in both set-up variants: conventional heating and microwave heating. A potassium salt melt is used for ion exchange of soda-containing lime silicate glass. The microwave source has 2 kW power at 2.45 GHz.

3. Results and discussion

Quickwave 2013 uses the FDTD method. This program was used to develop the applicator as well as to simulate the electromagnetic field distribution upon ion exchange.

The mesh and the position of the glass samples in the applicator are shown in Fig.2. In the bottom part of Fig. 3 the electrical field distribution for two individual sample positions is shown, to visualize the importance of sample movement for equilibration of electrical field gradients.
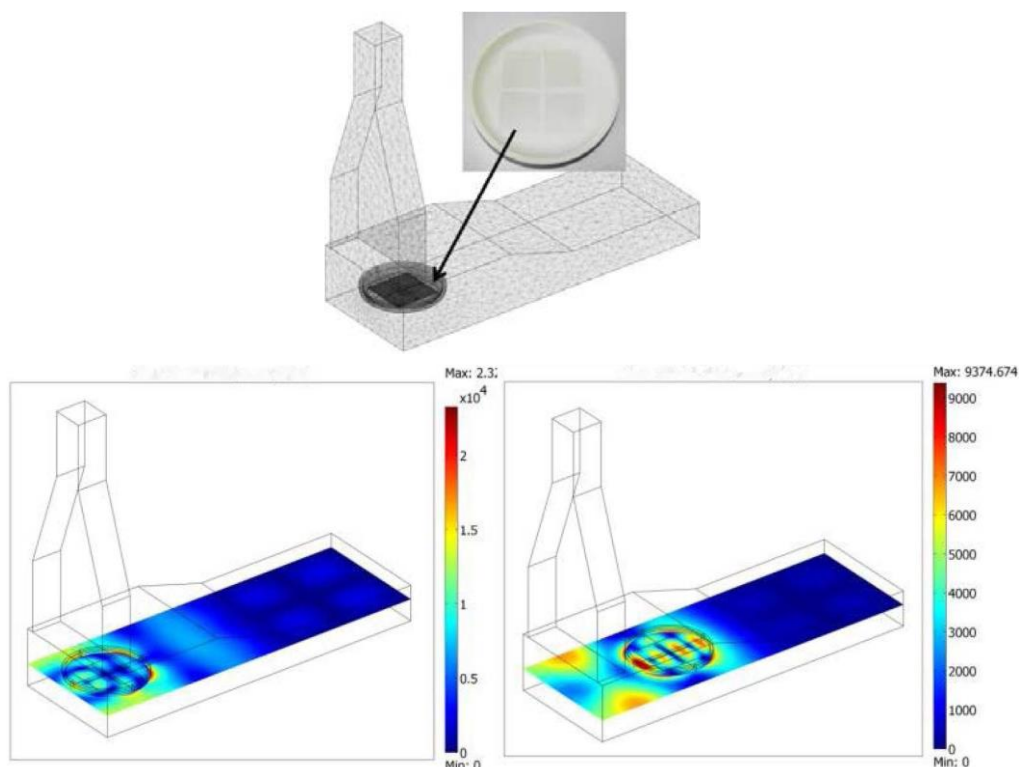
Fig. 2.   Mesh used for simulation (left); position of the dish containing the samples is shown and overall electrical field distribution for two different dish positions (right).
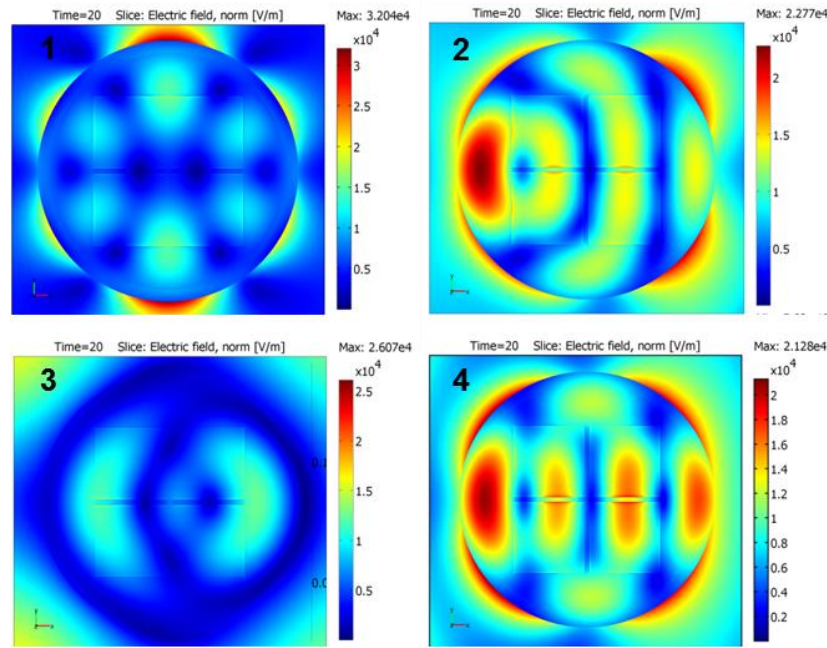
Fig. 3. Electric field distribution on glass plates (rectangular) immersed in a molten salt (circular) at 4 various positions in the cavity.

Even for thin glass plates the inhomogeneity of the vertical distribution of the electrical field has to be accounted for, as shown in Fig. 3. For analysis of potentially existing electrical field gradients relevant for electro-migration of ions a better resolution of the electrical field distribution is shown in Figure 3.

Because of the difference in dielectric properties between the molten salt and the solid glass – the difference in ionic conductivity is two orders of magnitude – pronounced E-field gradients develop at the interphase between molten salt and solid glass, as shown in Fig. 4. In addition, the field distribution is varying with position, as visible from the upper and the bottom part of Fig. 4.

From Fig. 4 it is clearly visible, that sufficient microwave field strength is present not only in the salt melt but also in the glass. Therefore with exception of chemical reactions all gradient forces shown in the fundamental transport equation are acting upon microwave assisted ion exchange.

For practical purposes equilibration of the electrical field gradient is required, to arrive at reproducible results of mechanical properties improvement resulting from ion exchange. Therefore a conveyor belt is used to move the dish containing a glass sample immersed in a molten salt bath periodically between the two positions shown in Fig. 2.
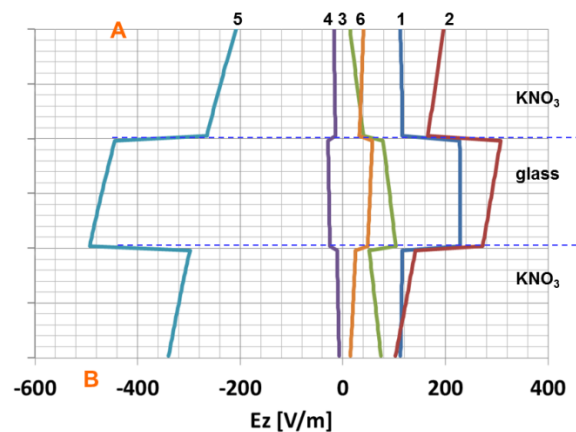
Fig. 4. Electric field gradients along the trace of line A - B (through the center of a glass sample).
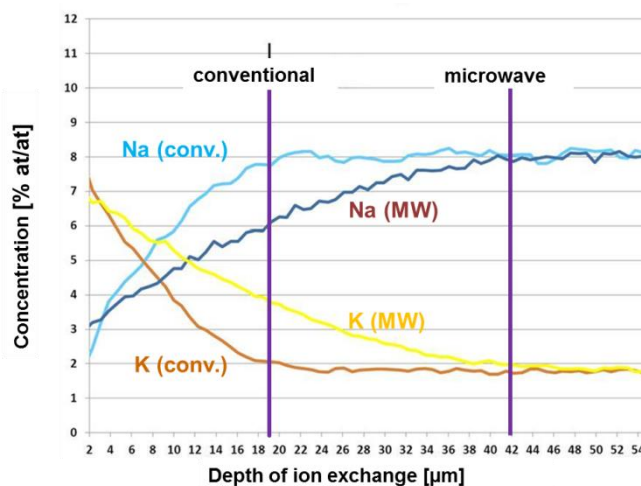
Fig. 5.   Measured concentration gradient and CS in ion exchanged glass upon conventional and microwave heating.

The E-field gradients developing at these positions are shown in Fig. 4. In the present stage of the study superposition of the electrical field with thermally induced convection of the molten salt as well as with a potential relaxation of the glass network could not be accounted for. But investigation of the depth of ion exchange revealed a significant difference between chemical hardening performed upon conventional heating as compared to chemical hardening assisted by microwave heating as shown in Fig. 5.

4.   Conclusion

For the first time the presence of electrical field gradients is shown by simulation upon microwave assisted ion exchange in glass immersed in a molten salt. The microwave processing applicator used for these experiments enables movement of the dish containing the melt and the solid sample with the help of a conveyor belt such as to equilibrate the steep electrical field gradient present at different position of the dish in the applicator. Even under such "average" electrical field conditions a significant difference of ion exchange depth is detected upon microwave assisted ion exchange as compared to conventional processing conditions.

Competing mechanisms govern the ion exchange process upon microwave heating. The clear difference in the build-up of a CS zone upon microwave heating as compared to conventional heating could be attributed to a persisting E-field gradient between the melt and the glass, which can facilitate electro-migration of ions.

Acknowledgement

References

[1] R. Gy, Ion exchange for glass strengthening, Materials Science and Engineering B 149, p.159–165 (2008)
[2] V.M. Sglavo, D.J. Green, Flaw-Insensitive Ion-Exchanged Glass: II, Production and Mechanical Performance, J. Am. Ceram. Soc., 84 [8], p. 1832–38 (2001)
[3] T.J. van Reenen, M. van Niekerk, W.J. de Wet, Investigations on the Ion-Exchange and Ionic Transport Properties of Glass Membranes in Molten Salts by an Electrolytic Transport Technique, The Journal of Physical Chemistry, Vol. 76, No. 18, 1971
[4] Jacques Albert and John W. Y. Lit, Full modeling of field-assisted ion exchange for graded index buried channel optical waveguides, Applied Optics, Vol. 29 [18], p. 2798-2804 (1990)
[5] K. Kamada, S. Yamashita, Y. Matsumoto, Electrochemical design of metal distribution in alkali silicate glass with ion-conducting microelectrodes, J. Mater. Chem., 2003 [13], p.1265–1268
[6] D. Atong, D.E. Clark, D.C. Folz, Surface modification of glasses using microwave energy. In Surface Active Processes in Materials; Ceramic Transactions, Vol. 101; American Ceramic Society: Westerville, OH, 2000, p. 75
[7] S. Schoemaker, M. Willert-Porada, Microwave behaviour of lead free and lead crystal glass dishes for food applications Eur. Journal of Glass Science and Technology Part A, Vol. 51, N°4, pp. 161-164 (2010)
[8] H. Kakiuchida, K. Saito, A.J. Ikushima, Dielectric relaxation in silica glass, J of Appl. Phys., Vol. 86 [12], p. 5983-5987 (1999)

FGM Thermal Barrier Coatings Optimization under Hot Burner Testing Conditions

Michael Gasik[1], Akira Kawasaki[2]

[1]*Aalto University Foundation, Espoo, Finland; michael.gasik@aalto.fi*
[2] *Tohoku University, Sendai, Japan; kawasaki@material.tohoku.ac.jp*

Abstract

For thermal barrier coatings (TBC) thermo-mechanical fatigue (TMF) is one of the critical parameters determining their lifetime. For increasing demands it is important to critically evaluate the performance of different TBC under accelerating tests. For the structure of the TBC based on FGM, the thermal and mechanical response might not be evident from the tests parameters, unless they are optimized to proper operational conditions. In this work modeling of heat flow and thermal stresses inside FGM coatings has been performed for the "hot burner test" (JIS H7851) method. With a multi-objective optimization method, the optimal gradation profile was found and the benefits of FGM have been shown. The opportunities of the extrapolation of the test results onto real applications for FGM TBC are discussed.

Keywords: thermal barrier coatings; thermal cycle; stress; testing; optimization'

1. Introduction

Thermal barrier coatings (TBC) are widely used to protect the hot parts of gas turbine systems from the heat and oxidized components of the combustion gases [1]. Typical TBC systems usually consist of yttria-stabilized $ZrO2$ (YSZ) layer for thermal insulation and MCrAlY type alloy as a bond coat (BC, M=Ni,Co), for oxidation resistance (duplex coatings). More additional layers can be used e.g. alumina or PtAl for better oxidation protection and suppression of elements diffusion [1,2]. Here "triplex" TBC is referring to the YSZ layer, alumina layer and the BC layer. Alumina layer acts as oxygen diffusion barrier and usually is being in situ generated by oxidation of aluminum-rich BC (is known as thermally grown oxide). The common problem of the TBC system is the failure of the layers due to thermal stresses and oxidation. At high temperatures, practically all elements are diffusing well, leading to a depletion of the layers and ceasing of the protection function [1,2]. The concept of functionally graded materials (FGM) has been introduced to TBC to solve these problems [1-3]. Coefficient of thermal expansion and elastic modulus in these FGM are designed to gradually change to decrease stresses [3]. FGM "triplex" TBC (double gradated YSZ-alumina and alumina-BC) system was designed using high-velocity oxygen flame (HVOF) process, demonstrated to have superior performance over similar TBC in "hot burner test" (standard JIS H7851) and under hot corrosion [3-5]. FEM analysis of the heat flux and temperature inside the 14 mm diameter test stainless steel jig has been performed in [4]. However, for better protection from oxidation, the introduction of O2 diffusion barrier layer such as Al2O3 is needed. This double gradation profile ("triplex FGM") was considered in the present work.

2. Modeling approach

The procedure of the hot burner test is described in JIS H7851 in [3,4]. Briefly, the coated head is subjected to alternating heat load from hydrogen-oxygen gas mixture flame with subsequently increased thermal flux ~0.2-0.6 MW/m^2. For new design several cases have been considered. First, the total thickness of TBC was fixed constant of 600 µm where the average thickness of YSZ-rich layer (material "A") and BC-rich layer (material "C") were

varied between 200-400 and 40-200 µm respectively. Thickness of alumina layer (material "B") is the difference from the total thickness of 600 µm. This design was also used for homogeneous TBC [6], with the same thicknesses of the layers, but with a sharp interface (no gradient transitions). Here we adopt a sigmoid function to approximate a smooth compositional gradation:

$$V_i(x) = \frac{1}{1 + \exp\left(-\frac{x - t_i}{t_i} w_i\right)} \qquad (1)$$

where $V_i(x)$ is the component volumetric concentration, x is thickness coordinate t_i is the average thickness of the layer i, and w_i is the spread (width) of the respective sigmoid peak. The advantage of sigmoid function (1) is that it always has its derivatives. When $w \to \infty$, the structure has homogeneous sharp layers. At the next simulation step, total thickness of FGM TBC was also varied H = 350-900 µm to check the effect of the thickness on temperature distribution and the stresses generated. Only two limiting cases are considered here: steady inward heat flux 0.85 MW/m² and cooling down to room temperature (zero heat flux). Both cases were applied as steady points, without considering heating or cooling rates [4]. Inelastic effects and initial stresses were not used and the solution was made analytically using micromechanical models [6,7] and linear plate theory for disk geometry, far from the edges, for 2D axial symmetry. For the purpose of establishing of integral parameters for comparison of many TBC cases, the integral thermal stresses (acting forces) ratio at maximal heat flux and an the room temperature, as well as their magnitude and expected TBC curvature ratios together with overall thermal resistance were chosen:

$$\text{Relative stresses ratio} \quad S = \frac{\int_0^H |\sigma_{FGM}(x, T(x))| dx}{\int_0^H |\sigma_{triplex}(x, T(x))| dx} \,,$$

$$\text{Relative stresses magnitude ratio} \quad MS = \frac{\int_0^H |\sigma_{FGM}(x, T(x)) - \sigma_{FGM}(x, RT))| dx}{\int_0^H |\sigma_{triplex}(x, T(x)) - \sigma_{triplex}(x, RT)| dx} \quad \text{Relative curvature} \quad C = \frac{k_{FGM}}{k_{triplex}} \,,$$

$$\text{Relative thermal resistance} \quad R_t = \frac{R_{FGM}}{R_{triplex}}, \quad R_i = \int_0^H \frac{dx}{\lambda_i(x, T_i(x))} \qquad (2)$$

where $T(x)$ is temperature inside TBC when heat flux is on (varies according to the profile, composition and thickness), RT is the room temperature (293 K), λ being the thermal conductivity of a specific TBC case. The choice of these parameters instead of traditional stresses distribution [6,8] was dictated by the need of a single parameter, which is capable of integration of information about the whole TBC across the whole thickness for a specific temperature distribution. It is known that stresses difference and their derivative differences are also important for materials performance besides the stresses magnitude [3,4]. The criteria above consider only absolute values of the stresses and their differences and thus might be overcautious in indication of optimal solution [4]. The objective of analysis of different FGM profiles is to compare S, MS and C (2) criteria (should be <1 unity if specific FGM design is better than a respective homogeneous coating). If the FGM phase areas spread or mean thickness changes, its effective thermal resistance also changes. The R_t value should be targeted to be ~1 to make a correct comparison of the coatings. If a composition or profile was found to result in lower thermal resistance (<95% of the triplex TBC), this combination was rejected. The optimization approach applied in this work was implemented in modeFrontier 4.4 (ESTECO, Italy) using Sobol generations of designs.

3. Test simulation results

The first design matrix results are shown in Fig. 1. Here all calculated combinations with different YSZ layer t_A and BC layer t_C thicknesses (varied spreads w_A and w_C) for H = 600 µm are shown. Objective criteria as relative thermal resistance (R_t, colour scale) and relative stress ratio (S, bubble size) are plotted vs. these two phases mean thicknesses. The spread and thickness of alumna-rich layer (B) is complementary to the total thickness and calculated automatically by subtraction of A- (YSZ) and C-rich (bond coat) layers. From Fig. 1 it is seen that too thin zirconia-rich layer in FGM (low A-layer thickness) leads to very low thermal resistances (blue colored bubbles). For a reasonable thermal resistance ($R_t \geq 1$ – green to red area), at least 250-300 µm YSZ layer is needed. Simple increase of thickness however leads to more stresses (larger bubbles) although there are also compositions with lower stresses due to different gradation.
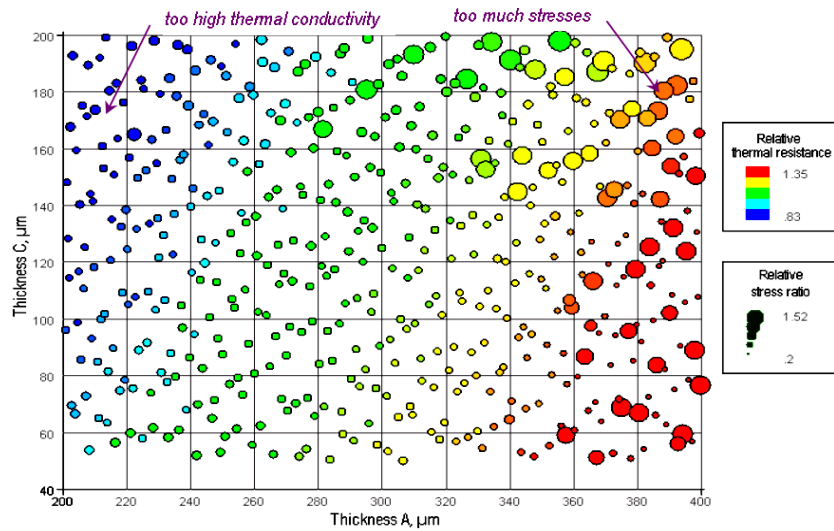
Figure 1: FGM TBC test matrix: R_t (colour) and S (size) criteria in the design field vs. mean thicknesses of YSZ (A) and bond coat (C) layers. Small red bubbles are the best potential solutions.
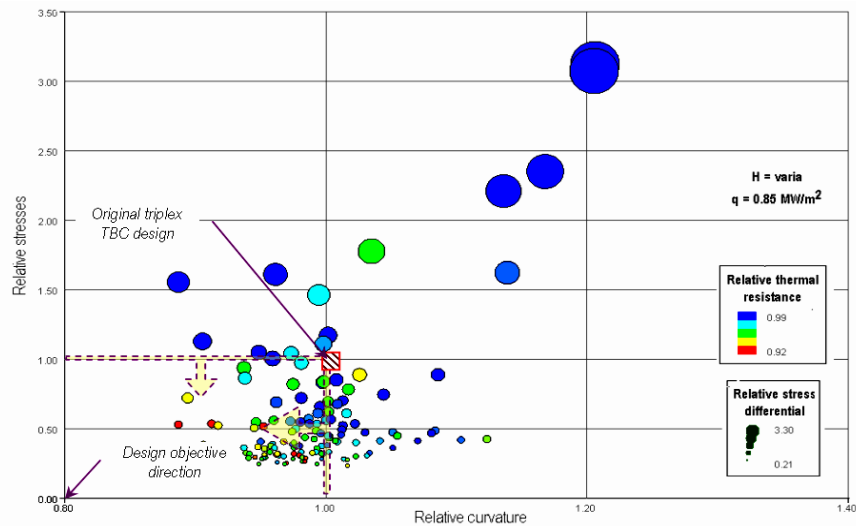
Figure 2: Comparison of feasible FGM TBC designs relatively to their homogeneous triplex compositions with varied total thickness *H* but fixed heat flux. The benefit of FGM is only when the design point is located in the area indicated by the arrows.

The upper right corner of Fig. 1 plot is the limit of a duplex TBC (no alumina layer).

Figure 2 shows the results similar to Fig. 1, but with a variation of the total thickness *H*. The domain indicated by the block arrows limits the area where FGM are beneficial vs. homogeneous ones. Smaller (less stress derivatives MS) and blue (the maximal thermal resistance R_t) dots should be selected, of which ones with the smallest thickness *H* and reasonable spreads w_A and w_C should be finally chosen. Exact values of such selected TBC designs can be obtained in a multi-variate analysis.

4. Discussion

In order to select the most "optimal" design, the point must be chosen which satisfy to all the conditions as $\{[S, MS, C] \rightarrow min \ \& \ [R_t \rightarrow \{max \ \& >0.95\}]\ \}$ over the whole designs of Fig. 1. The example of one of the possible solutions is shown in Fig. 3,a, vs. relative coordinate. Figure 3,b shows the difference between the calculated stress profiles for this FGM and for "zero" homogeneous TBC of the similar thicknesses. Sharp stress variations are effectively relaxed and the tensile stresses in alumina-rich layer are reduced several times. From the practical point of view, it is easier to select FGMs with lower spread values because manufacturing of too precise layers is
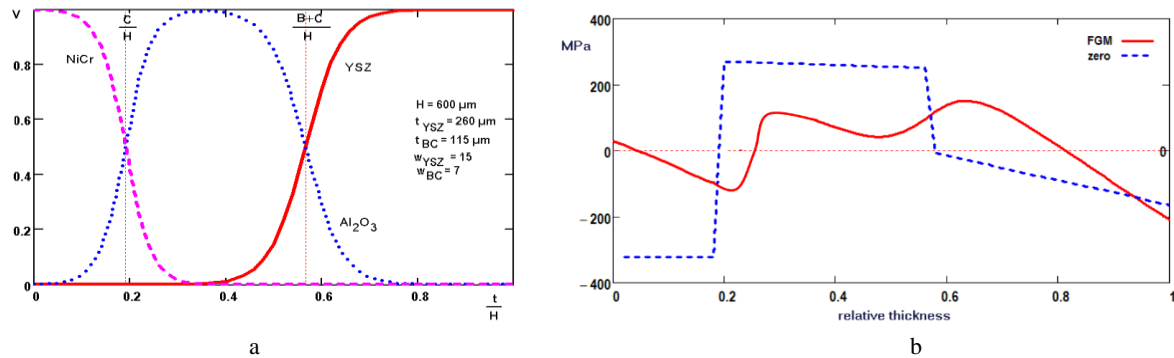
Figure 3: Optimized FGM design: (a) volume fraction of the phases vs. relative thickness and (b) calculated in-plane stresses in optimized FGM (solid red) and homogeneous triplex (dashed blue) TBC vs. relative thickness.

difficult. Also it would be interesting to decrease the total thickness H of TBC for lower costs and less mass of the turbine component.

This final selected optimized result in this work has lead to the following values: FGM TBC thickness H=590 µm, YSZ layer mean thickness 290 µm, bond coat layer mean thickness 130 µm, YSZ/alumina spread 9.5-10, alumina/BC spread 14.5 (results in alumina layer mean thickness of 170 µm). For a steady heat flux 0.85 MW/m^2 this provides all stresses relaxation by -25% at steady flow and by -45% during cooling with simultaneous stress differential reduction by 42% against homogeneous triplex TBC (Fig.3,b). This is accompanied by a trade-off of lower thermal resistance (0.96 vs. homogeneous TBC, i.e. about 4% lower with TBC cross-temperature drop of ~103 K). It is possible to get similar results with lower thickness (420-450 µm), but in that case a careful control of the profile is required.

It is also noteworthy this "optimal" FGM design has only been evaluated vs. its homogeneous counterpart (triplex TBC) of similar test parameters and materials (the same porosity level was assumed). Absolute values of stresses, curvatures, thermal performance values etc. should be compared to estimate FGM effect vs. initial TBC. Here initial stress distributions (depending on processing techniques) should be also included [4,9]. Use of developed hot burner test will allow a quickly assessment of the performance of FGM coatings which have been first manufactured closer to the selected "optimal" profiles.

5. Conclusions

In this work extended analysis of mechanical (thermal stresses, curvatures) and thermal (temperature distribution, thermal resistance) parameters has been carried out for FGM TBC with varied mean thicknesses and spreads of YSZ, alumina and BC layers. FGM TBC with different profiles were compared with homogeneous (triplex) coatings of different thicknesses. With a multi-objective optimisation method, the optimal profiles were found and main correlations between the TBC geometry and resulting factors like relative stresses and their differences have been evaluated. When the FGM TBC design target area is reached, it is possible to apply obtained values to conduct more extensive FEM evaluation of selected cases to assess their feasibility in 2D and 3D modelling cases. Here it is important that initial conditions are properly implemented into a model.

References

[1] Chan, K. S.; Cheruvu, N. S.; Leverant, G. R. J. Eng. Gas Turbines & Power (1998), 121, p. 609-14.
[2] Kawasaki, A.; Watanabe, R. Mater. Sci. Forum (1999), 308-311, p. 402-9.
[3] Gasik, M.; Kawasaki, A.; Kang, Y. S. Mater. Sci. Forum (2005), 492-493, p. 9-14.
[4] Gasik, M.; Kawasaki, A. Mater. Sci. Forum (2010), 631-632, p. 79-84.
[5] Nomura, N.; Gasik, M.; Kawasaki, A.; Watanabe, R. Ceramic Trans. (2001), 114, p. 223-9.
[6] Tsukamoto, H. Comp. Mater. Sci. (2010), 50, p. 429-36.
[7] Gasik, M. Comp. Mater. Sci. (1998), 13, p. 42-55.
[8] Ghafouri-Azar, R.; Mostaghimi, J.; Chandra, S. Comp. Mater. Sci. (2006), 35, p. 13-26.
[9] Itoh, Y.; Saitoh, M.; Tamura, M. J. Eng. Gas Turbines & Power (2000), 122, p. 43-9.

Stress Wave Propagation in a Functionally Graded Cylinder

M. Kemal Apalak[1], Mehmet Dorduncu[2]

[1]*Department of Mechanical Engineering, Erciyes University, Kayseri 38039, Turkey,*
apalakmk@erciyes.edu.tr
[2]*Department of Aerospace and Mechanical Engineering, The University of Arizona, Tucson,*
AZ 85721, USA, dorduncu@email.arizona.edu

Abstract

This study covers a simple analysis for wave propagation in a functionally graded circular cylinder subjected to an impulsive loading. The cylinder material composition was assumed to vary through the thickness direction with a power-law distribution in terms of volume fractions of the constituents: metal (Ni) and ceramic(Al_2O_3). Mori-Tanaka homogenization scheme was implemented for the estimation of the through-thickness material properties of functionally graded circular cylinder. The governing equations of the wave propagation through a functionally graded circular cylinder were simply discretized by using the finite difference method. von Neumann stability approach was applied for the stability of numerical solution. The results showed that the material composition variation had evident effects on the wave propagation through the functionally graded circular cylinder. In particular, the spatial derivatives of the mechanical properties of the local material composition were considered in the governing equations of motion and their effects on the wave propagation were analyzed. The amplitudes of the temporal variations of the displacement and stress components exhibited differences in case the spatial-material derivatives are considered.

Keywords: Functionally graded materials; stress wave propagation; finite difference method.

1. Introduction

The functionally graded materials have found many application areas [1]. The elastic wave propagation in functionally graded structures under impulsive loads has been investigated by applying analytical and numerical methods [2-9]. In this study an attempt was made to develop an improved two-dimensional model considering the spatial derivatives of material properties at a local point in an one-dimensional functionally graded cylinder in order to investigate the effects of these spatial-material derivatives. The motion equations in the improved model as well as the boundary conditions in terms of displacements and their coordinate derivatives were discretized using the finite difference equations, and the displacement components were calculated explicitly at internal points and implicitly at boundary points.

2. Basic Equations

2.1 Material Properties

We consider a functionally graded circular cylinder of a thickness *H* and a radius of *R*. The top surface of the cylinder is pure ceramic whereas the bottom surface is pure metal (Fig 1). The through-thickness material properties of the functionally graded circular cylinder were determined by the Mori-Tanaka homogenization scheme [10, 11].

According to Mori-Tanaka scheme, the sum of volume fractions of the all constituents is given as follows

$$V_c + V_m = 1 \tag{1}$$

where the subscripts m and c denote metal and ceramic phases, respectively. $V_c(z)$ and $V_m(z)$ indicate the volume fractions of ceramic and metal, respectively. The metal phase at any axial position z is expressed as

$$V_m(z) = \left(\frac{z}{h}\right)^n \tag{2}$$

where n is the compositional gradient exponent with a value between 0 and 10. The bulk modulus K, and shear modulus G of the functionally graded material can be written as

$$K(z) = K_m + \frac{V_c(K_c - K_m)}{1 + (1 - V_c)\frac{3(K_c - K_m)}{3K_m + 4G_m}} \quad \text{and} \quad G(z) = G_m + \frac{V_c(G_c - G_m)}{1 + (1 - V_c)\frac{G_c - G_m}{G_m + f_1}} \tag{3}$$

in which the variable f_1 is defined as

$$f_1 = \frac{G_m(9K_m + 8G_m)}{6(K_m + 2G_m)} \tag{4}$$

Based on the volume fractions of constituents, the modulus of elasticity and Poisson's ratio are defined as

$$E(z) = \frac{9KG}{3K + G} \text{ and } \nu(z) = \frac{3K - 2G}{2(3K + G)} \tag{5}$$

and the density ρ is given based on the linear rule of mixtures as

$$\rho(z) = V_m\rho_m + V_c\rho_c \tag{6}$$

$$\lambda = \frac{\nu E}{(1 + \nu)(1 - 2\nu)}, \qquad \mu = \frac{E}{2(1 + \nu)} \tag{7}$$

2.2 Equations of Motion

A cylindrical coordinate system (r, θ, z) is suitable to analyze the propagation of elastic waves in the FG cylinder. Due to axial symmetry, the deformations become symmetrical with respect to the z-axis, so that the angular displacement component θ vanishes [12]. Hence, for two dimensional cylindrical coordinates (r, z), the equations of motion in terms of stress components are given by

$$\rho\frac{\partial^2 u}{\partial t^2} = \frac{\partial \sigma_{rr}}{\partial r} + \frac{\partial \sigma_{rz}}{\partial z} + \frac{\sigma_{rr} - \sigma_{\theta\theta}}{r} \quad \text{and} \quad \rho\frac{\partial^2 w}{\partial t^2} = \frac{\partial \sigma_{rz}}{\partial r} + \frac{\partial \sigma_{zz}}{\partial z} + \frac{\sigma_{rz}}{r} \tag{8}$$

where $u = u(r, z)$ and $w = w(r, z)$ are the displacement components in radial and axial directions, respectively, t is time, and $\sigma_{rr}, \sigma_{rz}, \sigma_{\theta\theta}$ and σ_{zz} are stress components. The stress-displacement relationships can be expressed as

$$\sigma_{rr} = (\lambda + 2\mu)\frac{\partial u}{\partial r} + \lambda\left(\frac{\partial w}{\partial z} + \frac{u}{r}\right), \quad \sigma_{\theta\theta} = (\lambda + 2\mu)\frac{u}{r} + \lambda\left(\frac{\partial u}{\partial r} + \frac{\partial w}{\partial z}\right)$$
$$\sigma_{zz} = (\lambda + 2\mu)\frac{\partial w}{\partial z} + \lambda\left(\frac{\partial u}{\partial r} + \frac{u}{r}\right), \quad \sigma_{rz} = \mu\left(\frac{\partial u}{\partial z} + \frac{\partial w}{\partial r}\right) \tag{9}$$

The properties of an elastic medium are given by the two Lamé constants $\lambda = \lambda(z)$, $\mu = \mu(z)$ in Eqs (9). Substituting Eqs (9) into Eqs (8) yields

$$(\lambda + 2\mu)\left(\frac{\partial^2 u}{\partial r^2} + \frac{1}{r}\frac{\partial u}{\partial r} - \frac{1}{r^2}u\right) + (\lambda + \mu)\frac{\partial^2 w}{\partial r\partial z} + \mu\frac{\partial^2 u}{\partial z^2} + \frac{\partial \mu}{\partial z}\left(\frac{\partial u}{\partial z} + \frac{\partial w}{\partial r}\right) = \rho\frac{\partial^2 u}{\partial t^2}$$
$$(\lambda + 2\mu)\frac{\partial^2 w}{\partial z^2} + \mu\left(\frac{\partial^2 w}{\partial r^2} + \frac{1}{r}\frac{\partial w}{\partial r}\right) + (\lambda + \mu)\left(\frac{\partial^2 u}{\partial r\partial z} + \frac{1}{r}\frac{\partial u}{\partial z}\right) + \frac{\partial \lambda}{\partial z}\frac{\partial u}{\partial r} + \left(\frac{\partial \lambda}{\partial z} + 2\frac{\partial \mu}{\partial z}\right)\frac{\partial w}{\partial z} + \frac{\partial \lambda}{\partial z}\frac{u}{r} = \rho\frac{\partial^2 w}{\partial t^2} \tag{10}$$

2.3 Problem Description

A functionally graded circular cylinder is composed of Al_2O_3 and Ni through the region between the top ceramic (Al_2O_3) surface and the bottom metal (Ni) surface (Fig 1), and has a thickness $H = 10$ mm and a radius $R = 30$ mm. The through-thickness material properties are computed using the Mori-Tanaka homogenization scheme. The compositional gradient exponent n describes metal-rich, balanced and ceramic-rich composition variations for ($n = 0.1, 1.0$ and 10.0), respectievely.

The effects of the compositional gradient exponent and especially the spatial derivatives of local mechanical properties on the displacement and stress waves of functionally graded circular cylinder were investigated under an impulsive load (Fig 1) defined as

$$f(r,t) = -\psi(t)P\left(H(r) - H(r - r_p)\right) \tag{11}$$

where P is 690 MPa, $r_p = 5\ mm$, $\psi(r,t)$ and H denote load profile function and Heaviside step function, respectively.

2.4 Initial and Boundary Conditions

Initial conditions (at $t = 0$) are defined as

$$\frac{\partial u}{\partial t} = \frac{\partial w}{\partial t} = 0 \text{ and } u(r,z) = w(r,z) = 0 \tag{12}$$

The stress-free boundary conditions on lateral and bottom surfaces are

$$\sigma_{rz} = 0 \text{ and } \sigma_{zz} = f(r,t) \text{ along } z = 0$$
$$\sigma_{rz} = 0 \text{ and } \sigma_{zz} = 0 \text{ along } z = H \tag{13}$$
$$\sigma_{rz} = 0 \text{ and } \sigma_{rr} = 0 \text{ along } r = R$$

The axisymmetric boundary conditions are

$$\frac{\partial w}{\partial r} = 0 \text{ and } u = 0 \text{ along } r = 0. \tag{14}$$

2.5 Finite-Difference Discretization

The finite difference method has been employed successfully to approximate solutions for the wave equation [12-14]. In the finite difference scheme, a partial differential equation is discretized both in space and in time. A domain grid on the rz-plane is illustrated in Fig 2. The grid denotes the spatial discretization performed along the r- and z-axes with the grid sizes Δr and Δz. i and j are the set of indices in the r and z directions, respectively. nr and nz are the total numbers of mesh points in the r and z directions, respectively.

The centered-difference equations of the second-order derivatives of a displacement component, such as $\phi = \phi(r,z)$ at the nodal point (i,j) with respect to time t is given by

$$\left.\frac{\partial^2\phi}{\partial t^2}\right|_{i,j}^k = \frac{\phi_{i,j}^{k+1} - 2\phi_{i,j}^k + \phi_{i,j}^{k-1}}{(\Delta t)^2} \tag{15}$$

where Δt is the time step size, the superscript k refers to the time index ranging from 0 to nt, the total number of time steps. The finite difference equations of the first- and second-order derivatives of the displacement component $\phi = \phi(r,z)$ at the node (i, j) with respect to the spatial variables r and z given as follows:

$$\left.\frac{\partial\phi}{\partial r}\right|_{i,j}^k = \frac{\phi_{i+1,j}^k - \phi_{i-1,j}^k}{2\Delta r}, \quad \left.\frac{\partial\phi}{\partial z}\right|_{i,j}^k = \frac{\phi_{i,j+1}^k - \phi_{i,j-1}^k}{2\Delta z}$$

$$\left.\frac{\partial^2\phi}{\partial r^2}\right|_{i,j}^k = \frac{\phi_{i+1,j}^k - 2\phi_{i,j}^k + \phi_{i-1,j}^k}{(\Delta r)^2}, \qquad \left.\frac{\partial^2\phi}{\partial z^2}\right|_{i,j}^k = \frac{\phi_{i,j+1}^k - 2\phi_{i,j}^k + \phi_{i,j-1}^k}{(\Delta z)^2}, \tag{16}$$

$$\left.\frac{\partial^2\phi}{\partial r\partial z}\right|_{i,j}^k = \frac{\phi_{i+1,j+1}^k - \phi_{i+1,j-1}^k - \phi_{i-1,j+1}^k - \phi_{i-1,j-1}^k}{4\Delta r\Delta z}$$

Discretization for interior points can be achieved by considering $i = [2{:}nr - 1]$ and $j = [2{:}nz - 1]$ respectively, and substituting the finite differences into Eqs (15-16) into Eqs (10). Finally, we get

$$
\begin{aligned}
u_{i,j}^{k+1} = {} & 2u_{i,j}^k - u_{i,j}^{k-1} + c_l^2(\Delta t)^2\left(\frac{u_{i+1,j}^k - 2u_{i,j}^k + u_{i-1,j}^k}{(\Delta r)^2} + \frac{1}{r_{i,j}}\frac{u_{i+1,j}^k - u_{i-1,j}^k}{2\Delta r} - \frac{1}{r_{i,j}^2}u_{i,j}^k\right) \\
& + c_{ls}^2(\Delta t)^2\frac{w_{i+1,j+1}^k - w_{i+1,j-1}^k - w_{i-1,j+1}^k - w_{i-1,j-1}^k}{4\Delta r\Delta z} + c_s^2(\Delta t)^2\frac{u_{i,j+1}^k - 2u_{i,j}^k + u_{i,j-1}^k}{(\Delta z)^2} \\
& + \frac{(\Delta t)^2}{\rho_{i,j}}\frac{\mu_{i,j+1}^k - \mu_{i,j-1}^k}{2\Delta z}\left(\frac{u_{i,j+1}^k - u_{i,j-1}^k}{2\Delta z} + \frac{w_{i+1,j}^k - w_{i-1,j}^k}{2\Delta r}\right)
\end{aligned}
$$

$$
\begin{aligned}
w_{i,j}^{k+1} = {} & 2w_{i,j}^k - w_{i,j}^{k-1} + c_l^2(\Delta t)^2\frac{w_{i,j+1}^k - 2w_{i,j}^k + w_{i,j-1}^k}{(\Delta z)^2} + c_s^2(\Delta t)^2\left(\frac{w_{i+1,j}^k - 2w_{i,j}^k + w_{i-1,j}^k}{(\Delta r)^2} + \frac{1}{r_{i,j}}\frac{w_{i+1,j}^k - w_{i-1,j}^k}{2\Delta r}\right) + \\
& + c_{ls}^2(\Delta t)^2\left(\frac{u_{i+1,j+1}^k - u_{i+1,j-1}^k - u_{i-1,j+1}^k - u_{i-1,j-1}^k}{4\Delta r\Delta z} + \frac{1}{r_{i,j}}\frac{u_{i+1,j}^k - u_{i-1,j}^k}{2\Delta r}\right) + \frac{(\Delta t)^2}{\rho_{i,j}}\frac{\lambda_{i,j+1}^k - \lambda_{i,j-1}^k}{2\Delta z}\left(\frac{u_{i+1,j}^k - u_{i-1,j}^k}{2\Delta r}\right) + \\
& + \frac{(\Delta t)^2}{\rho_{i,j}}\frac{\mu_{i,j+1}^k - \mu_{i,j-1}^k}{2\Delta z}\left(\frac{w_{i+1,j}^k - w_{i-1,j}^k}{2\Delta r}\right) + \frac{(\Delta t)^2}{\rho_{i,j}}\left(\frac{\lambda_{i,j+1}^k - \lambda_{i,j-1}^k}{2\Delta z} + 2\frac{\mu_{i,j+1}^k - \mu_{i,j-1}^k}{2\Delta z}\right)\left(\frac{w_{i,j+1}^k - w_{i,j-1}^k}{2\Delta z}\right) + \\
& + \frac{(\Delta t)^2}{\rho_{i,j}}\frac{1}{r_{i,j}}u_{i,j}^k\frac{\lambda_{i,j+1}^k - \lambda_{i,j-1}^k}{2\Delta z}
\end{aligned}
\tag{17}
$$

where $c_l^2 = \frac{\lambda+2\mu}{\rho}$, $c_s^2 = \frac{\mu}{\rho}$ and $c_{ls}^2 = \frac{\lambda+\mu}{\rho}$, respectively. Using the foregoing discretizations the boundary conditions can be applied as follows: along the top AD edge on which the impulsive load is applied $i = [2:nr-1]$ and $j = 1$

$$\sigma_{zz} = f(r,t) \ at \ z = 0, \quad \frac{-3w_{i,j}^{k+1}+4w_{i,j+1}^{k+1}-w_{i,j+2}^{k+1}}{2\Delta z} + \bar{\lambda}_{i,j}\left(\frac{1}{r_{i,j}}u_{i,j}^{k+1} + \frac{u_{i+1,j}^{k+1}-u_{i-1,j}^{k+1}}{2\Delta r}\right) = \bar{f}(r_{i,j},t)$$

$$\sigma_{rz} = 0 \ at \ z = 0, \quad \frac{-3u_{i,j}^{k+1}+4u_{i,j+1}^{k+1}-u_{i,j+2}^{k+1}}{2\Delta z} + \frac{w_{i+1,j}^{k+1}-w_{i-1,j}^{k+1}}{2\Delta r} = 0$$

(18)

along the bottom edge BC with $i = [2:nr-1]$ and $j = H$

$$\sigma_{zz} = 0 \ at \ z = H, \quad \frac{3w_{i,j}^{k+1}-4w_{i,j-1}^{k+1}+w_{i,j-2}^{k+1}}{2\Delta z} + \bar{\lambda}_{i,j}\left(\frac{1}{r_{i,j}}u_{i,j}^{k+1} + \frac{u_{i+1,j}^{k+1}-u_{i-1,j}^{k+1}}{2\Delta r}\right) = 0$$

$$\sigma_{rz} = 0 \ at \ z = H, \quad \frac{3u_{i,j}^{k+1}-4u_{i,j-1}^{k+1}+u_{i,j-2}^{k+1}}{2\Delta z} + \frac{w_{i+1,j}^{k+1}-w_{i-1,j}^{k+1}}{2\Delta r} = 0$$

(19)

for the free-surface CD is discretized at $i = nr$ and $j = [2:nz-1]$

$$\sigma_{rr} = 0 \ at \ r = R, \quad \frac{u_{i+1,j}^{k+1}-u_{i-1,j}^{k+1}}{2\Delta r} + \bar{\lambda}_{i,j}\left(\frac{1}{r_{i,j}}u_{i,j}^{k+1} + \frac{w_{i,j+1}^{k+1}-w_{i,j-1}^{k+1}}{2\Delta z}\right) = 0$$

$$\sigma_{rz} = 0 \ at \ r = R, \quad \frac{u_{i,j+1}^{k+1}-u_{i,j-1}^{k+1}}{2\Delta z} + \frac{w_{i+1,j}^{k+1}-w_{i-1,j}^{k+1}}{2\Delta r} = 0$$

(20)

at corner D with $i = nr$ and $j = 1$

$$\sigma_{rr} = 0 \ at \ z = 0 \ and \ r = R, \quad \frac{u_{i+1,j}^{k+1}-u_{i-1,j}^{k+1}}{2\Delta r} + \bar{\lambda}_{i,j}\left(\frac{1}{r_{i,j}}u_{i,j}^{k+1} + \frac{-3w_{i,j}^{k+1}+4w_{i,j+1}^{k+1}-w_{i,j+2}^{k+1}}{2\Delta z}\right) = 0$$

$$\sigma_{rz} = 0 \ at \ z = 0 \ and \ r = R, \quad \frac{-3u_{i,j}^{k+1}+4u_{i,j+1}^{k+1}-u_{i,j+2}^{k+1}}{2\Delta z} + \frac{w_{i+1,j}^{k+1}-w_{i-1,j}^{k+1}}{2\Delta r} = 0$$

(21)

at corner C with $i = nr$ and $j = nz$

$$\sigma_{rr} = 0 \ at \ z = H \ and \ r = R, \quad \frac{u_{i+1,j}^{k+1}-u_{i-1,j}^{k+1}}{2\Delta r} + \bar{\lambda}_{i,j}\left(\frac{1}{r_{i,j}}u_{i,j}^{k+1} + \frac{3w_{i,j}^{k+1}-4w_{i,j-1}^{k+1}+w_{i,j-2}^{k+1}}{2\Delta z}\right) = 0$$

$$\sigma_{rz} = 0 \ at \ z = H \ and \ r = R, \quad \frac{3u_{i,j}^{k+1}-4u_{i,j-1}^{k+1}+u_{i,j-2}^{k+1}}{2\Delta z} + \frac{w_{i+1,j}^{k+1}-w_{i-1,j}^{k+1}}{2\Delta r} = 0$$

(22)

where $\bar{\lambda}_{i,j} = \left(\frac{\lambda}{\lambda+2\mu}\right)_{i,j}$ and $\bar{f}(r_{i,j},t) = \left(\frac{1}{\lambda+2\mu}\right)_{i,j} f(r_{i,j},t)$. The symmetry conditions along the symmetry axis AB at $i = 1$ and $j = [1:nz]$ are

$$u(r,z) = 0 \ at \ r = 0, \quad u_{i,j}^k = 0$$

$$\frac{\partial w}{\partial r} = 0 \ at \ r = 0, \quad \left.\frac{\partial w}{\partial r}\right|_{i,j}^{k+1} = \frac{-3w_{i,j}^{k+1}+4w_{i+1,j}^{k+1}-w_{i+2,j}^{k+1}}{2\Delta r} = 0$$

(23)

Since the finite difference scheme described above is an explicit scheme, the time step cannot be specified arbitrarily since too large a time step can lead to artificial blowup of the solution. To ensure the stability of solutions, the time step size Δt is determined using von Neumann stability criterion. The aforementioned criterion may be expressed in terms of time step and the spatial mesh sizes as [12-14]

$$t \le \Delta r\left(\frac{5}{4} + \left(\frac{c_s}{c_l}\frac{\Delta r}{\Delta z}\right)^2\right)^{-\frac{1}{2}} \ and \ \frac{\Delta t}{\Delta z} \le 1$$

(24)

3. Numerical Results

The axial and radial displacements were calculated explicitly at internal nodes and implicitly at nodes along the boundaries and axisymmetric axis of the cylinder by using difference equations. All displacement and stress components were calculated in Matlab software by developing a code [15]. The axial displacement and stress were more apparent. In order to show the effects of the gradient exponent n and the spatial-material derivatives the axial and radial variations of the axial displacement u_z and stress σ_{zz} were plotted at selected two points in the region where the impulsive waves were effective (Figs 3 and 4). The axial displacement u_z keeps wave form along the axial distance until the waves reach the bottom surface of the cylinder and then reflect (Fig 3a). As the material composition includes more ceramic constituent the axial displacement becomes higher and the waves travel faster whereas the wave forms remain similar. The improved model including the spatial-material derivatives predict higher displacement levels and similar wave forms. This effect becomes more apparent at further time steps. The radial variation of the axial displacement develops depending on the profile of the applied impulsive load until $t = 1 \ \mu s$ and then exhibit similar wave forms (Fig 3b). As the material composition becomes ceramic rich the waves travel faster and their amplitude reduce significantly after the impulsive load ends ($t = 1 \ \mu s$).
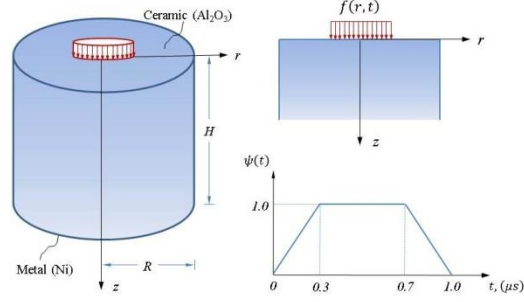
Figure 1: Functionally graded circular cylinder under an impulsive load.
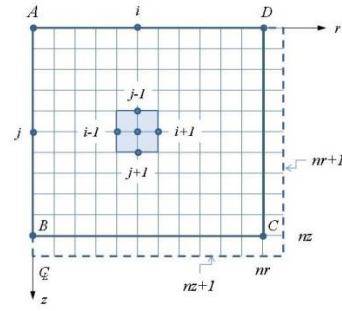
Figure 2. Finite difference stencil in (rz-plane).
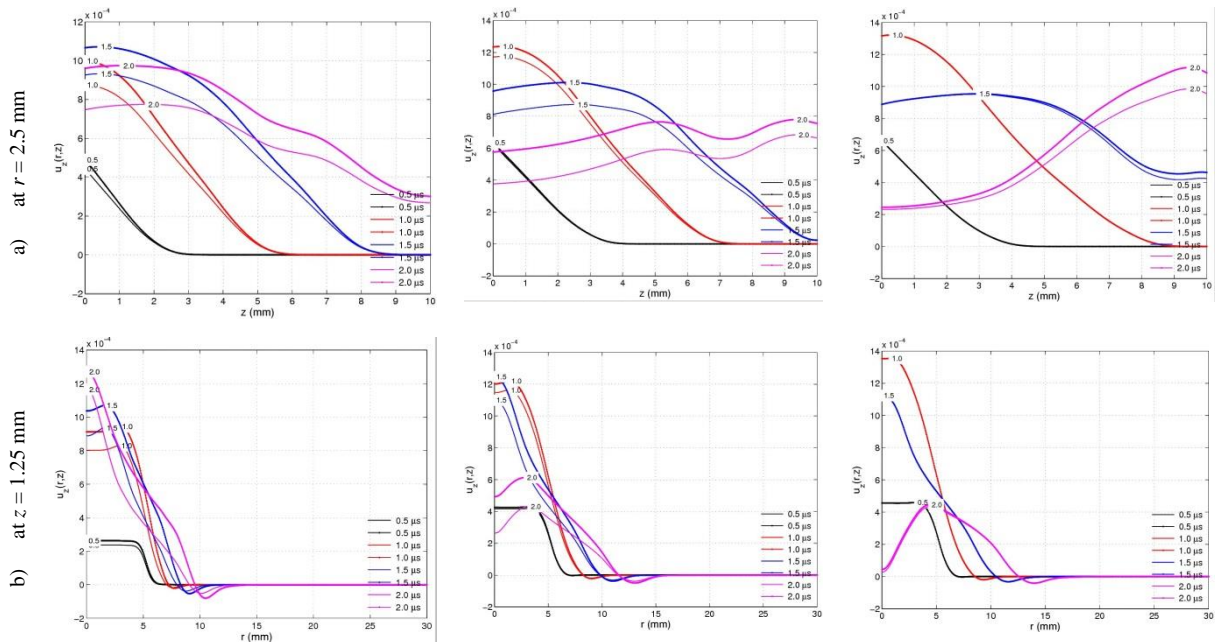
Figure 3. The effect of the compositional gradient (*n*) and the material derivation on a) the axial (at *r* = 2.5 mm) and b) the radial (at *z* = 1.25 mm) variations of the axial displacement $u_z(r, z)$ (mm) at different times between *t* = 0.5 and 2.0 μs.

The consideration of the spatial-material derivatives in the mathematical model results in only small changes in the displacement levels rather than the radial and axial variations.

The axial stress σ_{zz} exhibits similar wave forms in compression along the axial direction until the waves reach the bottom surface (Fig 4a). As the impulsive load ceases the amplitudes of compressive waves decrease and they travel in tension and compression after they reflected by the bottom surface. As the material composition becomes ceramic rich the axial stress waves reflect from the bottom surface in shorter time and become tensile from compressive. The consideration of the spatial material derivatives indicates small increases in the axial stress levels rather than the stress wave forms. The axial stress exhibits similar radial variations depending on the impulsive load variation until $t = 1\ \mu s$ (Fig 4b) and then the stress waves disappear. As the material composition becomes ceramic rich the axial stress levels increases slightly but the radial propagation speed of the stress waves remains almost same. The inclusion of the spatial material derivatives in the mathematical model predicts increases in the axial stress levels; however, the ceramic constituent is increased in the material composition these increases become negligible.

As a result the improved mathematical model on the stress wave propagation of a functionally graded cylinder subjected to an impulsive load showed that the consideration of the spatial-material derivatives gave higher displacement and stress levels whereas the displacement and stress variations along the radial and axial directions are not affected. As the material composition includes more ceramic the displacement and stress waves travel faster and especially the axial stress waves exhibit this effect apparently and they become tensile from compressive after they reflect from the bottom surface.
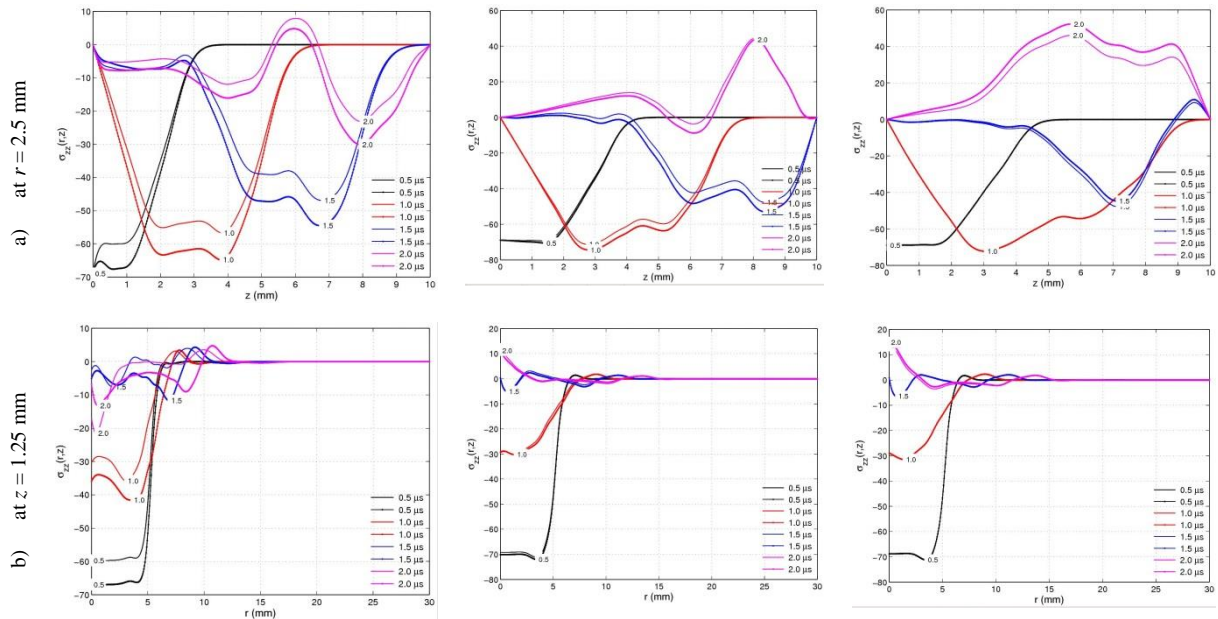
Figure 4. The effect of the compositional gradient (n) and the material derivation on a) the axial (at $r = 2.5$ mm) and b) the radial (at $z = 1.25$ mm) variations of the axial stress $\sigma_{zz}(r, z)$ (mm) at different times between $t = 0.5$ and 2.0 µs.

Acknowledgements

References

[1] Koizumi M. Composites Part B: Engineering 1997;7(28):1–4.

[2] Chiu T.C., Erdogan F. Journal of Sound and Vibration 1999;222(3):453–487.

[3] Han X., Lui G. R., Xi Z. C., Lam K. Y. International Journal of Solids and Structures 2000;38:3021–3037.

[4] Han X., Xu D., Liu G.R. Journal of Sound and Vibration 2001;251(5):783–805.

[5] Santare M.H., Thamburaj P., Gazonas G.A. International Journal of Solids and Structures 2003;40(21):5621–5634.

[6] Chakraborty A., Gopalakrishnan S. AIAA Journal 2006;44(7):1676–1685.

[7] Berezovski A., Engelbrecht J., Maugin G.A. World congress on ultrasonics 2003;507–509.

[8] Aksoy H.G., Senocak E. Finite Elements in Analysis and Design 2009;45:876–891.

[9] Cherukuri H.P., Shawki T.G. Acoustical Society of America 1996;100(4):2139–2155.

[10] Mori T., Tanaka K. Acta Metall 1973;21:571–574.

[11] Benveniste Y.. Mechanics of Materials 1987;6:147–157.

[12] Davis J.L. Mathematics of wave propagation. New Jersey: Princeton University Press, 2000.

[13] Alterman Z., Karal F.C. Bulletin of the Seismological Society of America 1968;5(1):367–398.

[14] H. Lan, Z. Zhang. Journal of Geophysics and Engineering 2011;8:275–286.

[15] Matlab ver R2006b, 1994-2012. The Language of Technical Computing. http://www.mathworks.com/.

Research on FGM for Nuclear Applications

Chang-Chun GE, Xiao-Na REN, Min XIA, Qing-Zhi YAN, Zhang-Jian ZHOU, Ying-Chun ZHANG,

Institute of Nuclear Materials (INM), University of Science and Technology Beijing (USTB), Beijing , China

Abstract

This presentation highlights the research on bulk and coating FGM, both for nuclear fusion reactors and advanced fission reactors in INM, USTB.Three kinds of bulk FGM, including W/Cu, B_4C/Cu and SiC/Cu with discontinuous composition distribution have been developed and fabricated with self-innovative technology named resistance sintering under ultra-high pressure consolidation (RSUHPC). While W/Cu FGM with continuous graded composition distribution can also be made with molten Cu infiltration through sintered gradient porous skeleton. Four kinds of coating technology for making coating composites including coating FGMs are developing in INM, USTB: (1) plasma spraying with spherical powders for making continuous B_4C/Cu coating FGMs and W/Cu coating FGMs; (2) Cold spraying for making W-based graded coatings on Cu substrates; (3) Chemical vapor deposition of W-coatings on Cu substrates with $W(CO)_6$ as precursor; (4) Na_2WO_4–WO_3 molten salt electro-deposition (MSED) on complex shapes of different matrix including Cu(CuCrZr, Al_2O_3-DSCu), Low activation steels, V alloys, graphite has been developed. Uniform diffusion W graded coatings with high thickness, strong interface strength, low oxygen content on different matrix have been successfully obtained.

Keywords: Nuclear materials, bulk FGM, coating FGM, RSUHP, MSED

1. Introduction

This presentation highlights the research on bulk and coating FGM, both for nuclear fusion reactors and advanced fission reactors in INM, USTB, putting emphasis on FGM for plasma facing components of fusion facilities. There are 2 kinds of plasma facing materials (PFM), which are used for divertor and first wall of fusion facilities and are the most important key materials for fusion reactors, suffering the most severe working conditions of the reactors. The fundamental design concept of modern magnetic confinement fusion facilities is based on the deuterium and tritium reaction: D+T→He+14MeV high energy neutrons +3.5MeV α particles, which together with the escaped particles from the plasma (D,T and impurities) and electro-magnetic radiation strongly impact on the divertor and first wall. They should have the following properties:

1. Resistance of the surface sputtering, blistering and erosion of the high energy particles , which severe contaminate to the plasma;

2. Resistance of high surface thermal impact, and resistance of the superhigh thermal load (ms order) during the plasma disruption events;

3. Resistance of neutron radiation damage, H, D, T brittleness and gas expansion;

4. Friendly adaptance with environment and low decay radiation products.

The surface covering layer of the PFM should be resistant to the high plasma erosion conditions and minimize its compositions contamination to the plasma. The structural materials under the surface covering layer should offer the mechanical support. Besides, PFM should have suitable working life under high neutron flux density, high thermal load and strong cooling environment.
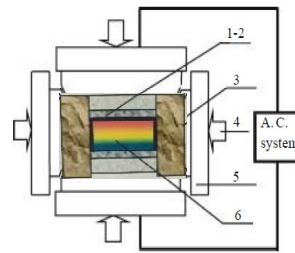
Figure 1: Schematic illustration of resistance sintering under ultra-high pressure consolidation setup. 1, 2-steel and graphite platelet; 3-pyrophyllite sleeve; 4-pressurized orientation; 5-anvil of WC hard alloy; 6-sintering compact.
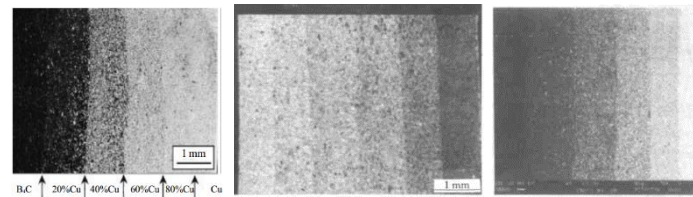
Figure 2 Back scattering image of 6-layered B_4C/Cu (a), W/Cu (b) and SiC/Cu graded composite (c)

2. Bulk FGM with self-innovative technologies

2.1 Resistance sintering under ultra-high pressure consolidation (RSUHPC)

Three kinds of bulk FGM including W/Cu, B_4C/Cu and SiC/Cu with discontinuous composition distribution have been developed and fabricated with self-innovative technology named RSUHPC. The volume fraction of W (or B_4C or SiC) of every layer was calculated by formula: $\Phi=(x/d)^P$. Where Φ is W(or B_4C or SiC) volume fraction of certain graded layer, x is location of the layer, d is thickness of the layer, and p is composition distribution exponent of W(or B_4C or SiC). When p value changes, the composition distribution profile of graded layers changes according to the p exponent. Taking W/Cu FGMs as example (as listed in table 1), when P=1, d=6, the composition distribution of a 6-layers FGM is listed in Table 1.

Specimens were prepared as follows: powders with compositons of each layer in Table 1 were mechanically alloyed in a ball mill with a rotation speed of 75 rpm. after dried, the mixed powders of each layer are sequentially put into mould, and then preliminary pressed (40MPa). Specimens, composed of green compact of W/Cu FGM, graphite platelet, and pyrophyllite sleeve, were put into press chamber, consolidated and electric resistance sintered under ultra-high pressure. Main processing parameters include pressure (7-8GPa), voltage (180-200V) and time (50s) . Fig.2 is BSI of 6-layers FGM of B4C/Cu, W/Cu, and SiC/Cu respectively. No damage occurred in W/Cu FGM after 140 times thermal impact of 100MW/m2.

While W/Cu FGM with continuous graded composition distribution was made with molten Cu infiltration through sintered gradient porous skeleton. No damage occurred after 1000times thermal impact of 100MW/m2.

2.2 Coating FGMs with self-innovative technologies

Four kinds of coating technology for making coating composites including coating FGMs are developing in INM, USTB.

2.2.1. Plasma spraying with spherical powders for making continuous B_4C/Cu and W/Cu coating FGM

Commercial B_4C powder (particle size 20μm) and Cu powder with <200 mesh were used. Dimensions of Cu substrates were $10x10x2mm^3$, $10x20x2mm^3$ and $\varphi15x2mm^3$. The plasma spraying parameters are in Table 2. The chemical sputtering yield of B_4C/Cu reduced to 17% of SMF800 graphite, while the thermal desorption of CH_4 reduced to 30-50% of SMF800 graphite. Both meet the demand of Southwest Nuclear Physics Institute.

Table 1: Composition distribution of a 6-layers FGM

Layer	0	1	2	3	4	5	6
W (vol%)	0	16.67	33.33	50	66.67	83.33	100
Cu (vol%)	100	83.33	66.67	50	33.33	16.67	0

Table 2: Parameters of the plasma spraying

Voltage （V）	Electric current （A）	Power (KW)	Main gas-Ar	Assist. gas -H_2	Powder feeding gas	Powder flow	Spray distance	Move speed
60	600	36	2880l/h	360l/h	Ar 180l/h	20g/min	10-12cm	20cm/s
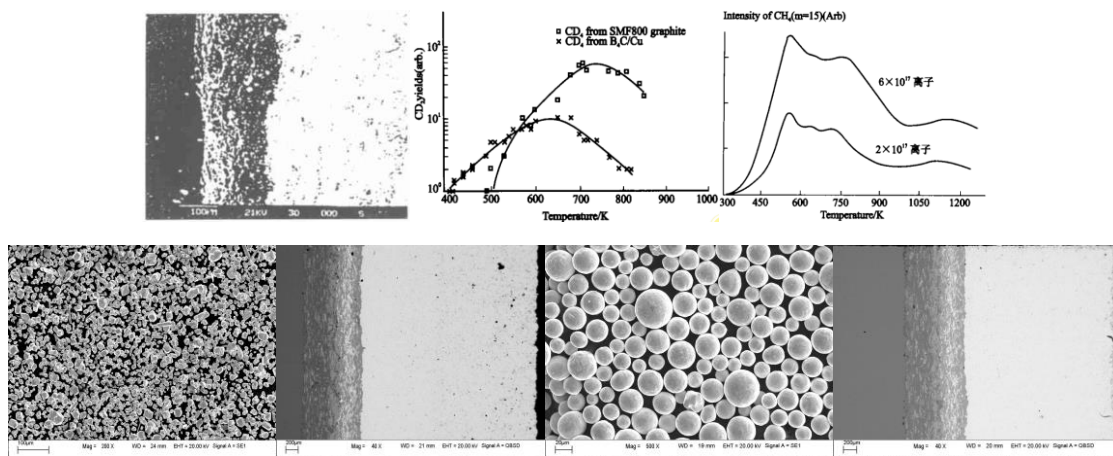
Figure 3: SEM image of the B_4C/Cu coating (a), Relation between temperature and CD_4 yields (b), Thermal desorption spectrums of B_4C coating (c), commercial W powder (d), cross-section of W/CuCrZr coating FGM using commercial W powder (e), spherical W powder (f), cross-section of W/CuCrZr coating FGM using spherical W powder (g)

2.2.2 Cold spraying W/Cu coating FGMs

Schematic diagram of cold spraying process is shown in Fig 4. In the process, the feedstock powder was preheated at 630°C to promote the plastic deformation of W particles before cold spraying. The preheated feedstock powder was cold-sprayed onto grit blasted (20 mesh grit) and acetone cleaned CuCrZr substrate (300 mmx200mmx30mm) at a stand-off distance of 15 mm. Air was used as both the accelerating gas at the pressure of 2.5 MPa, and as a carrier gas. Gun velocity was ~ 5 mm/s. Temperature and pressure were monitored by the computer. The commercial W (Xiamen Tungsten Co., Ltd.), Ni, Fe (Beijing Xing Rong Yuan Technology Co., Ltd.) powders with high purity were used (purity, W ≥ 99.95; Ni ≥ 99.65; Fe ≥ 99.73). The particle size of W, Ni, Fe is 3-10μ, 2-5μ, 2μ respectively. The W, Ni, Fe powders with different ratios were designed as 3 samples, sample "1" 75%W–17.5%Ni–7.5%Fe, sample "2" 93%W–4.9%Ni–2.1%Fe and sample "3" 93%W–4.9%Ni–2.1%Fe (2, surface) + 75%W–17.5%Ni–7.5%Fe (1, subsurface). Of particular mentioning, sample "3" was designed as graded layer, composition "1" was first deposited as subsurface and then composition "2" was prepared as top surface. Samples were mixed and then ball-milled in a stainless steel container with stainless steel balls (diameter 8 mm) at a ball-to-powder weight ratio of 3:1 for 12 h. Ball milled powders were then vacuum dried and sieved to achieve consistent powder feeding. Cold spray nozzle was set for ten passes for each coating.
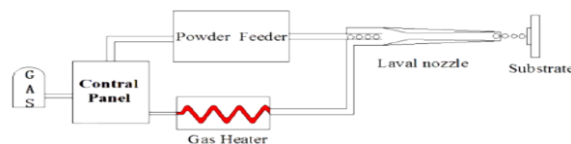
Figure 4: Schematic diagram of cold spraying process
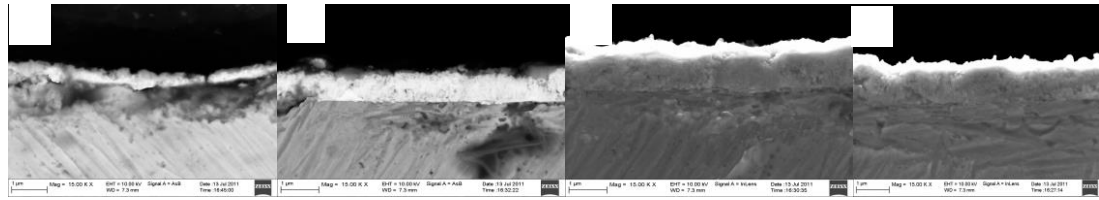
Figure 5: cross-section of the CVD W coating on CuCrZr at 270°C (a), 400°C(b), 500°C (c) and 600°C (d)
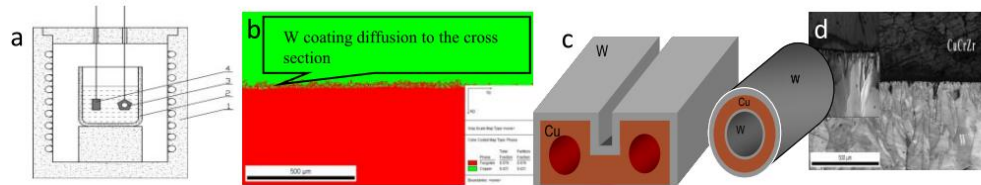
Figure 6 scheme of the molten salt electro-deposition of W coating FGMs (a), W diffusion into the substrate (b), scheme of the W/Cu FGM bulk (c), SEM image of cross-section of CuCrZr and W coating

Table 3: basic properties of the prepared coatings

Preparation method	Thickness(μm)	Hardness (HV)	Bonding strength (MPa)	Porosity (%)
PS (spherical W)	3800	340	7.07	1.56
CS (93%W)	544	468.8	>35.6	2.32
CS+CVD	1000	481.4	>34.96	2.44
MSED	1400.3	497	23.334	–

2.2.3. Chemical vapor deposition (CVD) of W coating on CuCrZr substrate with $W(CO)_6$ as precursor

CVD technology for preparing tungsten (W) coating is applied to surface engineering materials with advantages of simple operation, and the products are superior because of high purity, less porosity and strong adhesion to substrates. Gaseous WF_6 and WCl_6 are traditional precursors for preparing W coatings, which require high reduction temperature of >600°C and >1000°C, and both generate highly corrosive gas which damages equipments. C.C.GE first proposed to use $W(CO)_6$-CVD process to make PFM. The advantages of $W(CO)_6$ are as follows: low decomposition temperature at about 400°C, no corrosion problems for facilities, no reduction process. Tungsten coatings were deposited on copper substrates at 270°C, 400°C, 500°C and 600°C in hydrogen.

2.2.4 Molten salt electro-deposition of W coating FGM

Na_2WO_4-WO_3 molten salt electro-deposition on complex shapes of different matrix including Cu(CuCrZr, Al_2O_3-DSCu), Low activation steels, V alloys, graphite has been developed by Y.C. ZHANG. Uniform diffusion W graded coatings with high thickness, strong interface strength, low oxygen content on different matrix have been successfully obtained.

3. Conclusion

A series of plasma facing materials were prepared by independent innovative technologies, among the PFMs, except W/Cu have been reported before, the others have not been reported until our work has done. The prepared PFMs have broaden the application of FGMs to nuclear materials.

References

[1]   C.C. Ge, J.T.Li, Y.H. Ling, Journal of University of Science and Technology Beijing 10, 39 (2003).
[2]   J.T.Li, C.C. Ge, Y.H. Ling, Journal of University of Science and Technology Beijing 23, 257 (2001).
[3]   M. Xia, P. Huang, R.K. Chu, and C. C. Ge, Surface and Coatings Technology 291, 376-381 (2016).

Experimental Investigation of Microstructural and Micromechanical Properties of Fe/B$_4$C-Fe/B Functionally Graded Materials

Mustafa Hamamci[1], Fehmi Nair[2], Afşin Alper Cerit[3]

[1,2]*Composite Research Laboratory, Department of Mechanical Engineering, Erciyes University, Kayseri, Turkey*
[3]*Department of Industrial Design Engineering, Erciyes University, Kayseri, Turkey*
[1]*mhamamci@erciyes.edu.tr , [2]fnair@erciyes.edu.tr , [3]acerit@erciyes.edu.tr*

Abstract

In the present work, microstructure and micromechanical properties of the functionally graded Fe/B$_4$C-Fe/B materials (FGMs) were investigated experimentally. Samples were fabricated at different number of layers with a constant compositional gradient under hot pressing-powder metallurgy method. In order to better understand the relationship between processing, structure and mechanical properties of the samples, pressureless sintering was conducted at 1000°C for 30 and 60 minutes. Microstructural evaluations were done by optical microscopy, XRD and energy dispersive X-ray (EDX) analysis. Microhardness measurements were done with a Vickers indenter under 1 kg load to get information of their mechanical behaviours. The correlation between microstructure and mechanical properties was examined.

As a result of interaction between the Fe matrix and B$_4$C-B particles, FeB and Fe$_2$B secondary phases were observed. It was observed that hardness of Fe/B$_4$C and Fe/B samples strongly depend on their structural composition and sintering parameters. When the B$_4$C-B ratio, towards ceramic dense layer and sintering time increased, the hardness of samples increased to certain layer and then decreased. The transition of hardness from metal dense layer to ceramic was found smoother when the number of layers increases.

Keywords: Functionally graded materials, Powder metallurgy, Secondary intermetallic phases, FeB-Fe$_2$B.

1. Introduction

It is insufficient to provide new requirements emerged under the different conditions, although metal alloys or conventional composites show high performance. The formation of micro cracks caused by thermal stress leads to decrease of the service life, especially for gas turbine blades, power plants, internal combustion engines, aerospace and industrial applications which exposed to high temperatures and working in continuously repeated temperature conditions. Functionally Graded Materials (FGMs) formed by different types of graded materials, exhibits heterogeneous character with continuously changing properties and microstructure with a certain ratio and they are technically different from conventional composite materials. While the one side of the composite has high mechanical strength and toughness, the other side has high thermal and wear resistance. There are a wide range of fabrication processes for producing FGMs as basically vapour deposition, powder metallurgy, centrifugal and solid freeform fabrication method [1]. The common process for fabricating FGMs is powder metallurgy made below the melting tempereteres to obtain a rigid structure, based on the atomic diffusion and formation of micro welding between the particles contact with each other. This method also has some advantages as creation of microstructural bond, different mechanical and thermal properties forming a gradient in a material [2]. The bond formation between particles, secondary phases resulted after in situ reactions and pores in the structure affect the strength,

hardness, ductility, thermal conductitivity, heat transfer coefficient, wear resistant and other mechanical properties [3]. So it is inevitable to investigate the effects of production parameters (e.g. particle types, ratios and sintering parameters) on microstructural and mechanical properties of FGMs. It was observed that secondary iron-boride phases (FeB-Fe_2B) formed after B_4C/B particles dissolved in Fe matrix at 1000-1150°C [4]. The liquid phase, consisting by increasing the sintering tempereture (>1000°C), diffusion and sintering rate, causes the increase of boride phases compared to solid-phase sintering [5]. The formation of the iron borides primarily depends on the B_4C/B concentration and then on the sintering time-temperature, particle size, pores and other impurities in the structure. In general the FeB-Fe_2B ratio and hardness increases by increasing the B_4C/B ratio and sintering time [6]. In this context, the aim of this study is to fabricate functionally graded Fe/B_4C-Fe/B composites by powder metallurgy technique which have the ceramic density surface layer and metal density other surface layer, formed in the internal structure by gradually reduced ceramic ratio and increased metal concentrations for investigate the effect of ceramic based FeB-Fe_2B secondary phases will be formed after reactions of B_4C-B with Fe, investigating the microstructure and testing of the mechanical properties by measuring the hardness.

2. Experimental Procedure

a. Materials and sample production method

Fabrication of FGM samples were done by using 1-9 µm particle size of Fe powders for matrix, 12-40 µm B_4C and <40 µm B powders for reinforcements. It was found that Fe powder has high purity ratio with 99.8%, B_4C powder has 99.7% and B powder has 88% by the XRF chemical characterization and impurity analysis. 12% atomic carbon was found in the B powder. It was observed that iron particles have irregularly orbicular and flake geometry, B_4C and B powders consists of the mixture of irregular polygon, orbicular and rectangular particle geometries according to the SEM analysis. When the powder images were analyzed it was not observed significant flocculation or formation of aggregates. Properties of samples was determined by the simple power law with following equation which consist of pure metal at the bottom face to intensive ceramic face.

$$V_c + V_m = 1 \qquad\qquad V_m(z) = \left(1 - \frac{z}{h}\right)^n \qquad\qquad (1)$$

where V_c and V_m are the volume fraction of the ceramic and metal powders, $V_m(z)$ is the volume ratio of metal component in any distance of sample thickness along z-direction, h is the sample thickness and n is a parameter that controles the sample layers composition linearly or non-linearly through the thickness. Powder mixtures were determined by linear compositional gradient ($n=1$) and volume fraction of $V_{c\ max}$ as 0.9 and 0.7 with 10 and 20 layers to final sample thickness be 10 mm. Then powders were mixtured in different plastic containers for 1 hour at 100 rev/min in Turbula-T2F mixer. Each layer was sequentially pre-compacted under 240 Mpa and then all layers compacted under 700 Mpa pressure in a cylindrical hot work tool steel die with a diameter of 30 mm using a uniaxial hydraulic press. Pre-compacts were taken from die at room temperature afterwards heated in the die at 500°C for 30 minutes under constant pressure (700 Mpa). Sintering treatments were carried out in a high temperature tube furnace (Protherm-PTF18) at 1000°C for 30 and 60 minutes with 8°C/min heating rate under argon atmosphere and cooled to room temperature in the furnace. Microstructure and hardness properties were investigated after the classical metallographic sample preparation steps and cauterized with 5% Nital solution.

b. Microstructural evaluations

Microstructural evaluations were done by optical microscopy with 125-1250 times magnification. Ceramic intense 2-3 layer of samples was seperated when the pre-compacted sample taken from die. Seperations and cracks were observed in some regions between the high ceramic volume fraction layers both of the 10 and 20 layered samples. Figure 1 shows the Fe-B_4C/0.9/1/0.1/10 sample after pre-compacted and formation of crack between layers after sintering. It was clearly seen that the porosity was increased when the ceramic ratio increasing (Fig. 2-a). It was observed that B and B_4C particles were completely diffused in low ceramic density layers in spite of the partially diffused in high density layers into the Fe matrix after sintering. Therefore residual B_4C and B particles were found in ceramic dense layers (Fig. 3). This residual particles have caused to reduction of bonding strength, formation of pores between paticle and matrix interface, and seperation of layers. Sintering time has been effective in the size of diffusion area as increased with increasing the sintering time. But more residual particles were observed at low sintering time. The pores were formed over the certain rate of B_4C-B ratio in ceramic dense layers, instead of the diffusion areas. Peaks of the secondary boride phases (Fe_2B) were obrserved in XRD analysis and formation of this phase was increased by sintering time.
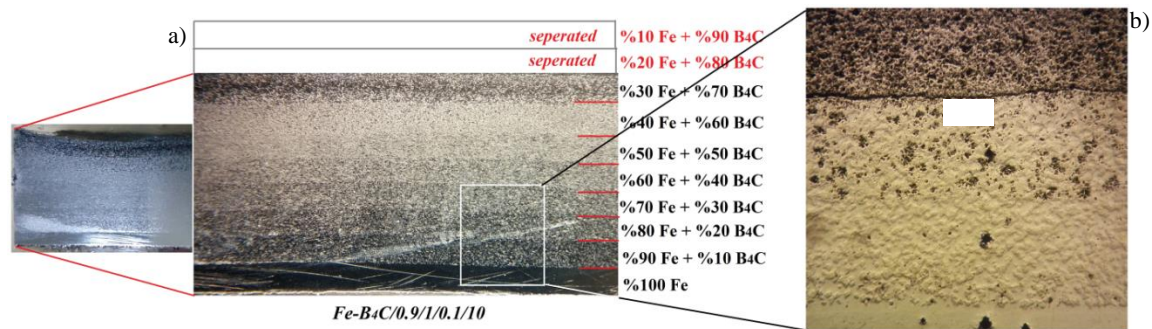
Figure 1: (a) Fe-B$_4$C/0.9/1/0.1/10 FGM sample after pre-compacted and volume fraction ratios of layers, (b) formation of crack between layers after sintering.
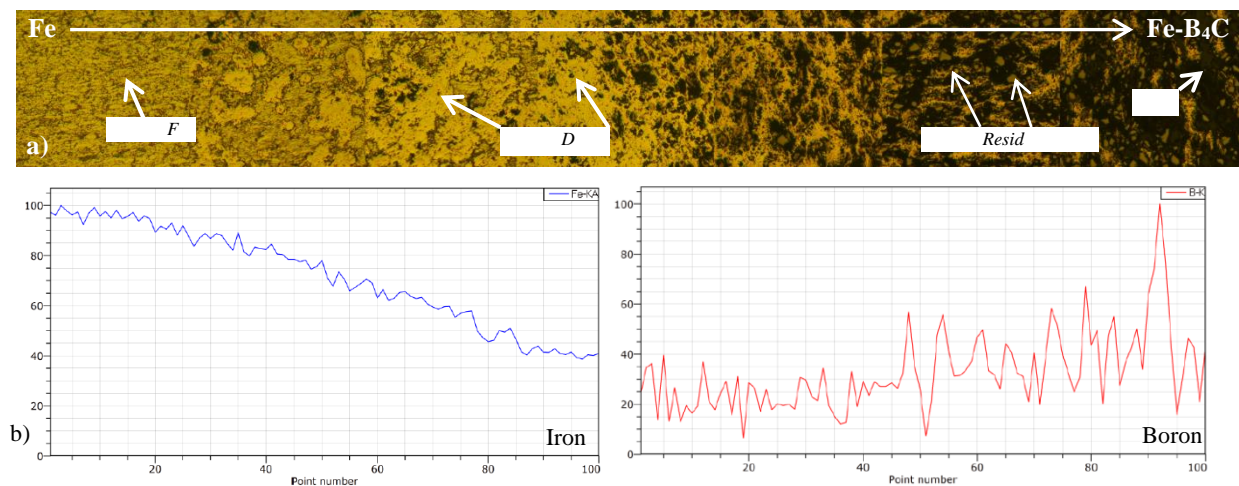
Figure 2: (a) Fe-B$_4$C/Vc:0.9/n:10 FGM microstructure after 1000°C, 60 minute sintering, (b) EDX analysis of FGM from pure Fe layer to ceramic dense layer towards the arrow line.
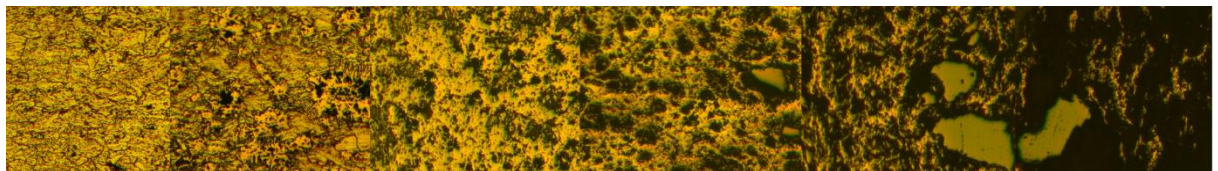
Figure 3: Fe-B/Vc:0.7/n:10 FGM microstructure after 1000°C, 60 minute sintering.

c. *Mechanical evaluations*

Microhardness measurements were done from Fe layer to ceramic dense layer with a Vickers indenter under 1 kg load to get information of their mechanical behaviours. The variation of hardness values were shown in Figure 4 for different sintering time and FGMs. It was seen that general and maximum hardness value was not affected by the sintering time. Hardness of Fe/B samples (max. HV$_1$ 700) were higher than the Fe/B$_4$C samples (max. HV$_1$ 666). Apparent decline of hardness was observed after a certain layer at 4~5th layer for 10 layered samples and 10~11th layer for 20 layered sample, as seen in Figure 4. Increasing of hardness from Fe layer to ceramic dense layer was observed more smoother in 20 layered samples than 10 layered samples. Hardness was decreased suddenly throughout the ceramic dense layer due to the increasing of the porosity and reduction of bonding strength. Secondary boride phases and diffusion areas, especially observed at initial and middle layers of the FGMs, have increased the hardness of samples because of the hardness of this phases 3-9 times higher than Fe matrix.
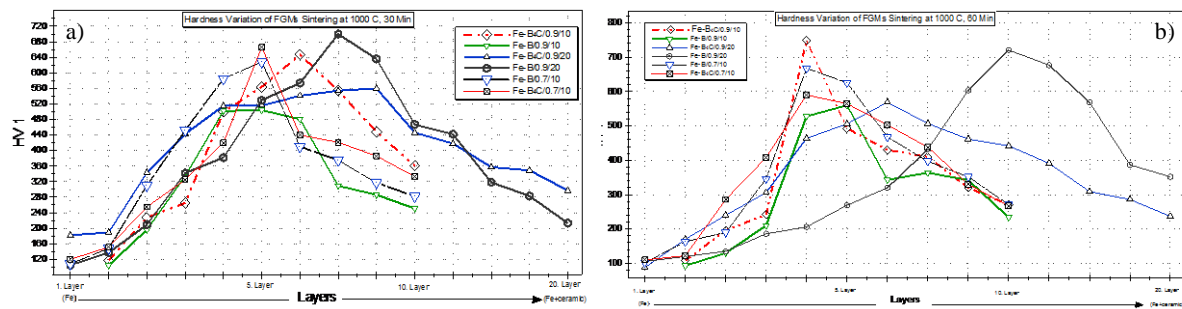
Figure 4: Hardness variation of FGMs sintering at 1000 °C, (a) 30 minutes , (b) 60 minutes.

3. Conclusions

Experimental investigations showed that seperations and cracks were formed in some regions between the layers have high volume fraction of B_4C/B. When the volume fraction of ceramic dense layer ($V_{c\ max}$) increase from 0.7 to 0.9, crack and pore formation was increased. As a result of this study, taking $V_{c\ max}$ 0.4 or 0.5 for ceramic dense layer will sufficient for getting stable microstructural and mechanical distribution. It was observed that B_4C and B particles were completely diffused to Fe matrix at low ceramic density layers. But residual B_4C and B particles were found in high ceramic dense layers. This residual particles have caused to formation of pores between paticle and matrix interface, and decreases the hardness values. Sintering time has been effective in the size of diffusion area, and more residual particles were observed at low sintering time. Secondary boride phases were obrserved in the XRD analysis. This phases have increased the hardness of samples. Transition of hardness from Fe layer to ceramic dense layer was observed more smoother in 20 layered samples than 10 layered samples.

Acknowledgements

References

[1] Mahamood, R.M., Akinlabi, E.T., Shukla, M. and Pityana, S., "Functionally graded material: an overview", *Proceedings of the World Congress on Engineering, London*, 3, 2012.

[2] Sarıkan, B., Balcı, E., Übeyli, M. and Camuşcu, N., "Investigation on the aging behaviour of the functionally gradient material consisting of boron carbide and an aluminum alloy", *Materiali in Tehnologije*, 46 (2012), 393-397.

[3] Sadowski, T., Boniecki, M., Librant, Z. and Nakonieczny, K., "Theoretical prediction and experimental verification of temperature distribution in FGM cylindrical plates subjected to thermal shock", *International Journal of Heat and Mass Transfer*, *50* (2007), 4461-4467.

[4] Turov, Y.V., Khusid, B.M., Voroshnin, L.G., Khina, B.B. and Kozlovskii, I.L., "Gas transport processes in sintering of an iron-boron carbide powder composite", *Soviet Powder Metallurgy and Ceramics*, 28 (1989), 618-622.

[5] Campos, I., Torres, R., Ramirez, G., Ganem, R. and Martinez, J., "Growth kinetics of iron boride layers: dimensional analysis", *Applied Surface Science*, 252 (2006), 8662-8667.

[6] Nowacki, J. and Klimek, L., "Structure and properties of Fe-Fe$_2$B cermets, *Journal of Materials Science*, 27 (1992), 3651-3656.

Friction and Wear Characteristics of MoS$_2$/Cu-Sn Composite Film

Hitoshi Kohri[1], Takayoshi Yagasaki[2]

[1]*School of Advanced Engineering, Kogakuin University, kohri@cc.kogakuin.ac.jp*
[2]*School of Advanced Engineering, Kogakuin University, yagasaki@cc.kogakuin.ac.jp*

Abstract

It is difficult to use an ordinary bearing in a vacuum and/or at a high temperature, because of evaporation or deterioration of the lubricant oil. A solid lubricant like as MoS$_2$ is promising in such condition. Recently, a thin solid lubricant film is often applied on a hard material by PVD or CVD. The thin film is, however, easily removed when the load or friction speed is too high. On the other hand, when the lubricant is dispersed in the surface layer of bearing, it is expected that the solid lubricant exists by abrasion on the surface of the bearing. The aim of this report is to examine friction and wear behavior of the MoS$_2$/Cu-Sn composite film.

The Sn layer dispersed lubricant particles was formed on the Cu substrate by electroless deposition. Then the plated sample was heat treated at 150 °C due to become bronze. Friction properties of composites were determined by using a ball-on-disk type testing machine. The test was performed in a vacuum without oil at the room temperature.

The coefficients of dynamical friction of the composite films were decreased by the lubricant than the one of Cu. The effect of the lubricant was much remarkable in vacuum. From the results of 0.076 ms^{-1} in the sliding speed, the coefficient of dynamical friction of as deposited sample, which is MoS$_2$/Sn, was lower than the one of heat treated sample, which is MoS$_2$/bronze. On the contrary, for the results of 0.12 ms^{-1} in the sliding speed, the coefficient of dynamical friction of heat treated sample was lower than the one of as deposited sample. The wear rates of the composites were much less than one of Cu in a vacuum. The wear rate of heat treated sample was 2.5% less than the one of as deposited sample in both test condition.

Keywords: Friction, Wear, Solid lubricant, Electroless deposition, Composites

1. Introduction

It is difficult to use an ordinary bearing in a vacuum or at a high temperature, because of evaporation or deterioration of the lubricant oil. A solid lubricant like as MoS$_2$ is promising in such condition. Recently, a thin solid lubricant film is often applied on a hard material by PVD or CVD. The thin film is, however, easily removed when the load or friction speed is too high. On the other hand, when the fine lubricant is dispersed in the bearing material, it is expected that the solid lubricant exists by abrasion on the surface of the bearing. In previous works, MoS$_2$/Cu composite blocks were prepared by electroless deposition and hot pressing [1,2]. The relative density was 85 to 95 % which depends on volume fraction of MoS$_2$. This report concluded that the densification of composite was needed due to improve of friction and wear properties. In this study, the MoS$_2$/Cu-Sn composite films, which aimed densification and reduction of the amount of lubricant, were prepared by electroless deposition and heat treatment, and the friction and wear properties of the composite films were investigated.

2. Experimental Procedure

2.1 Fabrication of MoS_2/Cu-Sn composite film

The Sn layer dispersed lubricant particles was formed on the Cu substrate by electroless deposition. The LT-34G (Rohm and Haas Electronic Materials K.K.) was used as electroless Sn plating solution. The plating temperature was 70 °C. The plating time was 20 min. MoS_2 composite samples were prepared by adding MoS_2 powder to plating solution. The concentration of MoS_2 for the plating solution was 0.001 or 0.002 g/ml. Then the plated sample was heat treated due to become bronze. The heat treatment was performed at 150 °C for 3 to 600 s in the air. The crystalline phase was identified by x-ray diffraction (XRD). The chemical state analysis was carried out by x-ray photoelectron spectroscopy (XPS).

2.2 Friction and wear properties

Friction properties of each sample were determined by using a ball-on-disk type testing machine. The ball was made of SUJ-2 and the diameter of the ball was 10 mm. The test was performed in a vacuum without oil at the room temperature. The sliding speed was 0.076 or 0.12 ms^{-1}. The load was 0.98 N. The diameter and width of the wear track was measured by laser microscope. Nominal wear rate was determined from the volume of the wear track, wear distance and the load, though the pressure varies with increasing of the width of the wear track under the constant load. The friction and wear properties of composites were compared with pure Cu and Sn film. The wear track was also observed by optical microscope.

3. Results and Discussion

The Sn layer with 1.11 µm in thickness was formed on the surface of as deposited sample. From the results of SEM observation, XRD and XPS for heat treated sample, bronze phase was confirmed on the surface of a sample heat-treated in 300 s or more. The oxide layer was also confirmed on the surface of a sample heat-treated in 300 s or 600 s. From the results of depth profile for XPS, the thickness of the oxide layer for a sample heat-treated in 300 s was less than 50 nm. Therefore, it was found that the heat treatment in 300 s was suitable for the alloying to bronze.

Figure 1 shows the relationship between sliding distance and the coefficient of dynamical friction. The coefficients of dynamical friction of the composite films were decreased by the lubricant than the one of Cu. The effect of the lubricant was much remarkable in vacuum. From the results of 0.076 ms^{-1} in the sliding speed, the coefficient of dynamical friction of as deposited sample, which is MoS_2/Sn, was lower than the one of heat treated sample, which is MoS_2/bronze.

Figures 2 shows OM images of the ball and the wear track after test of 0.076 ms^{-1} in sliding speed. For MoS_2/Sn, it was suggested that the whole sliding surface was covered by MoS_2 because MoS_2 agglutinated on ahead of the contact area of the ball. Therefore, it was considered that the coefficient of dynamical friction for MoS_2/Sn was lower than the other.

On the contrary, for the results of 0.12 ms^{-1} in the sliding speed, the coefficient of dynamical friction of heat treated sample was lower than the one of as deposited sample as shown in figure 3.
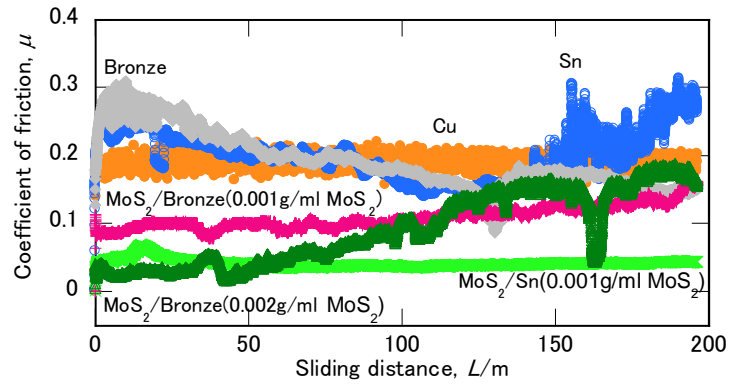
Figure 1: Relationship between sliding distance and the dynamical friction coefficient (sliding speed:0.076 ms^{-1})
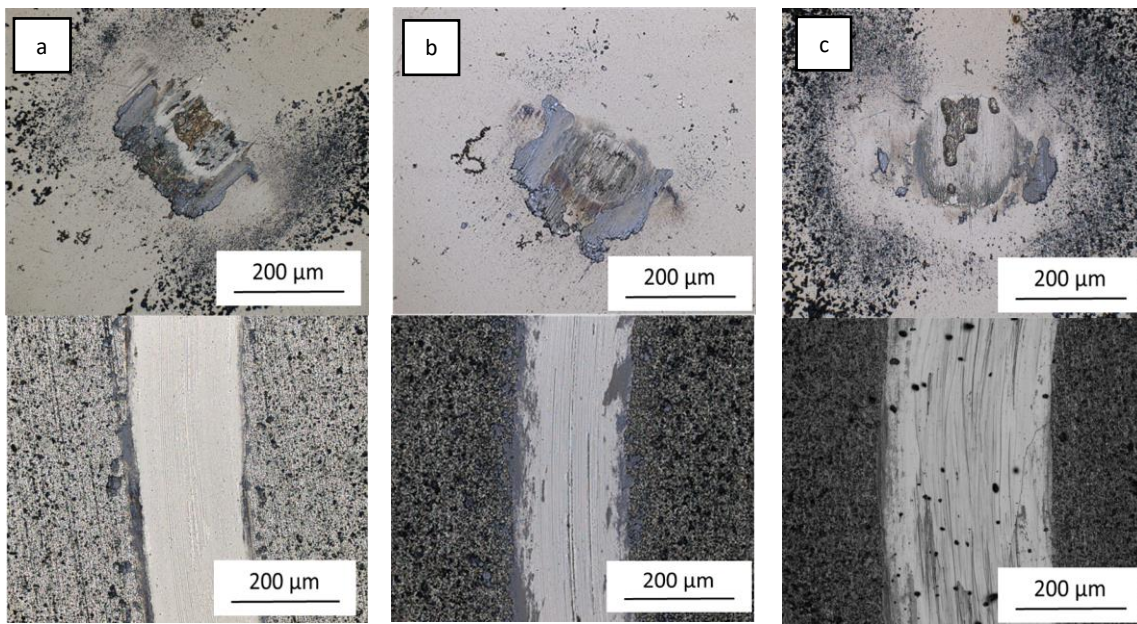
Figure 2: The OM images of the surface of the ball after test (upper) and wear track(lower). (sliding speed: 0.076 ms^{-1}), a: MoS$_2$/Sn (0.001 g/ml MoS$_2$), b: MoS$_2$/bronze (0.001 g/ml MoS$_2$), c: MoS$_2$/bronze (0.002 g/ml MoS$_2$)
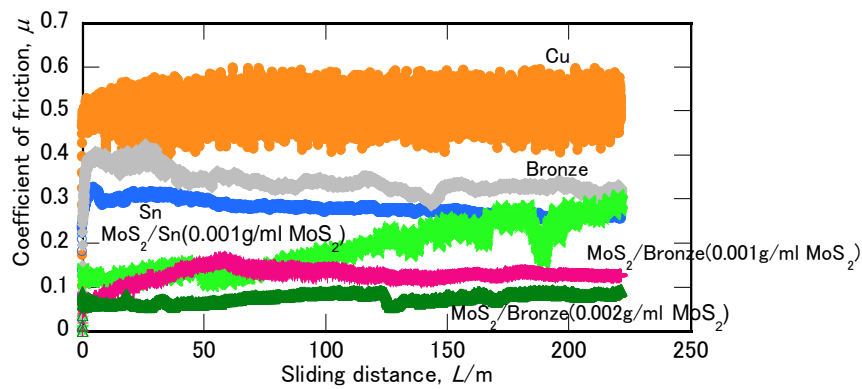
Figure 3: Relationship between sliding distance and the dynamical friction coefficient (sliding speed:0.12 ms^{-1})
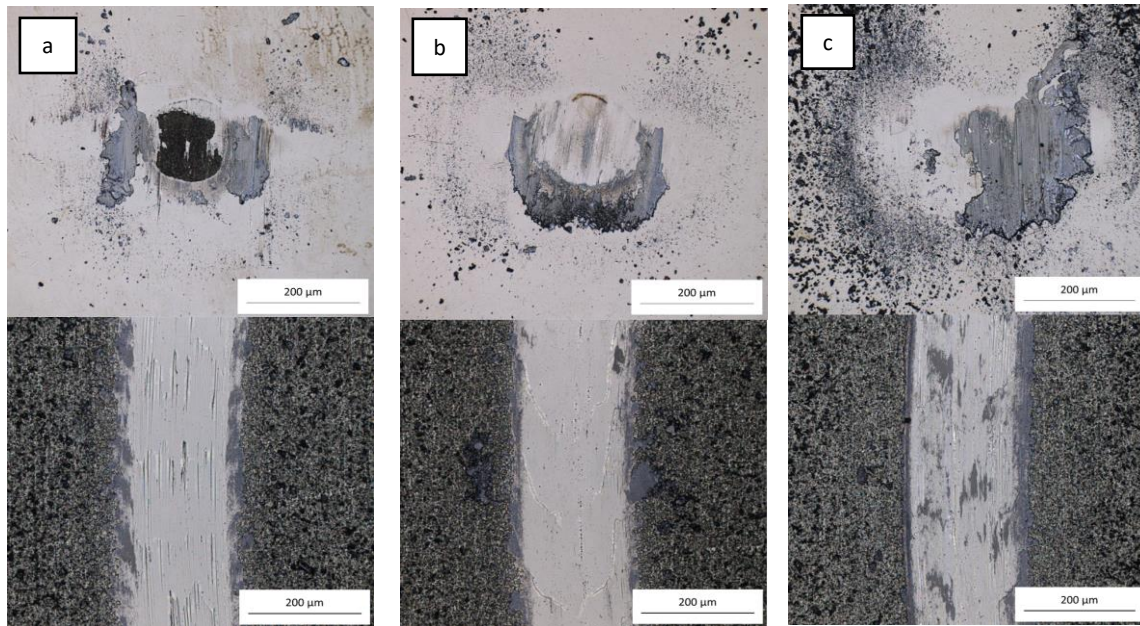
Figure 4: The OM images of the surface of the ball after test and wear track. (sliding speed: 0.12 ms^{-1})
a: MoS$_2$/Sn (0.001 g/ml MoS$_2$), b: MoS$_2$/bronze (0.001 g/ml MoS$_2$), c: MoS$_2$/bronze (0.002 g/ml MoS$_2$)

Figures 4 shows OM images of the wear track and the ball after test of 0.076 ms^{-1} in sliding speed. It was suggested that the Sn matrix was flattened during the test because Sn matrix was more soft than bronze matrix, and MoS$_2$ was pushed out from the sliding surface.

The wear rates of the composites were much less than one of Cu in a vacuum. The wear rate of MoS$_2$/bronze (0.001 g/ml MoS$_2$) was 2.5% less than the one of MoS$_2$/Sn (0.001 g/ml MoS$_2$) in both test condition. However, the wear rate MoS$_2$/bronze (0.002 g/ml MoS$_2$) was larger than the one of MoS$_2$/bronze (0.001 g/ml MoS$_2$). Considering that tendency of the dynamical friction coefficient showed the opposite tendency, it was suggested that the trend of wear rate caused by increase in quantity of detachment of the solid lubricant.

4. Concluding remarks

The coefficients of dynamical friction of the composite films were decreased by the lubricant than the one of Cu. The effect of the lubricant was much remarkable in vacuum. From the results of 0.076 ms^{-1} in the sliding speed, the coefficient of dynamical friction of as deposited sample, which is MoS$_2$/Sn, was lower than the one of heat treated sample, which is MoS$_2$/bronze. On the contrary, for the results of 0.12 ms^{-1} in the sliding speed, the coefficient of dynamical friction of heat treated sample was lower than the one of as deposited sample. The wear rates of the composites were much less than one of Cu in a vacuum.

References
[1] T. Hashimoto, H. Kohri, A. Yumoto and I. Shiota, Advances in Science and Technology Vol. 54 (2008) pp. 174-179
[2] T. Hashimoto, H. Kohri, A. Yumoto and I. Shiota, Materials Science Forum Vols. 631-632 (2010) pp. 465-470

Functionally Graded Cu-ZnS Phosphor and its Applications

Jehong Park[1], Seungchan Cho[2], Akira Kawasaki[3], Kwangjae Park[4],
Kwonhoo Kim[4], Hansang Kwon[1,4]

[1]*Next-Generation Materials Co., Ltd.(NGM),ngm01@ngm.re.kr*
[2]*Korea Institute of Materials Science,sccho@kims.re.kr*
[3]*Tohoku University,kawasaki@material.tohoku.ac.jp*
[4]*Pukyong National University,kwon13@pknu.ac.kr*

Abstract

We describe a functionally graded metal-phosphor adapting the concept of the functionally graded materials (FGMs); copper (Cu) is selected as a metal and Cu- and Cl-doped ZnS (ZnS:Cu,Cl) is selected as a phosphor and FG [Cu]-[ZnS:Cu,Cl] is fabricated by a simple powder process through spark plasma sintering (SPS). The FG [Cu]-[ZnS:Cu,Cl] reveals a dual-structured functional material composed of dense Cu and porous ZnS:Cu,Cl, which is completely combined through six graded mediating layers. FG [Cu]-[ZnS:Cu,Cl] exhibits photo reactivity for 365 nm-UV light. Our FG metal-phosphor concept can pave the way to simplified manufacturing of low-cost and can be applied to UV-light sensor and various electronic devices.

Keywords: Functionally Graded Materials (FGMs); Metal; Phosphor; Spark Plasma Sintering (SPS)

1. Introduction

Zinc sulfide (ZnS) is a well-known II-VI group semiconductor with a bandgap energy of 3.7 eV at room temperature. ZnS is one of the attractive materials in optoelectronic devices with applications such as field emitter, laser diode, and sensor [1-8]. Additionally, ZnS doped with impurities has been used as a traditional phosphor for light-emitting materials in display devices such as electroluminescence devices (ELDs), cathode-ray tubes (CRTs), and field emission devices (FEDs); for instance, Cu- and Cl-doped ZnS (ZnS:Cu,Cl) is an efficient phosphor emitting in the blue-green visible range [9-14]. Recently, nanostructure (NS)-based ZnS has been identified as a high potential candidate for use in photo-sensing materials. However, most of the research on NS-based ZnS has been performed using inefficient methods involving time-consuming processes or complex chemical routes [3-8]. We report functionally graded (FG) metal-phosphor fabricated by a very simple powder process using a spark plasma sintering (SPS) technique [15]. In this research, we employed copper (Cu) and Cu- and Cl-doped ZnS (ZnS:Cu,Cl) as metal and phosphor materials, respectively. Cu and ZnS:Cu,Cl were successfully combined by adapting the concept of the FGM. The fabricated FG [Cu]-[ZnS:Cu,Cl] showed that one side had the intrinsic properties of an electrode and other side had the intrinsic properties of a phosphor within the same bulk material. We investigate the reactivity for ultraviolet (UV)–light as well as the morphology of the FG [Cu]-[ZnS:Cu,Cl].

2. Experimental

High-purity commercial Cu powder (dendrite, 99.99 %) and commercial Cu- and Cl-doped ZnS (ZnS:Cu,Cl, cubic, ~50 µm) were used as a raw materials. Mixtures of Cu and ZnS:Cu,Cl powders containing 5, 10, 20, 30, 50, 70 vol.% Cu in ZnS:Cu,Cl were prepared using a simple ball milling process for 30 min at 200 rpm in air. The pure Cu and ZnS:Cu,Cl powders were not ball-milled. Pure Cu, mixtures of Cu-ZnS:Cu,Cl, and pure ZnS:Cu,Cl powders were stacked layer by layer into a graphite mould with a diameter of 15 mm; 0.2 g of powder was used for each layer. Then the stacked powders were sintered using a customized spark plasma sintering (SPS) system
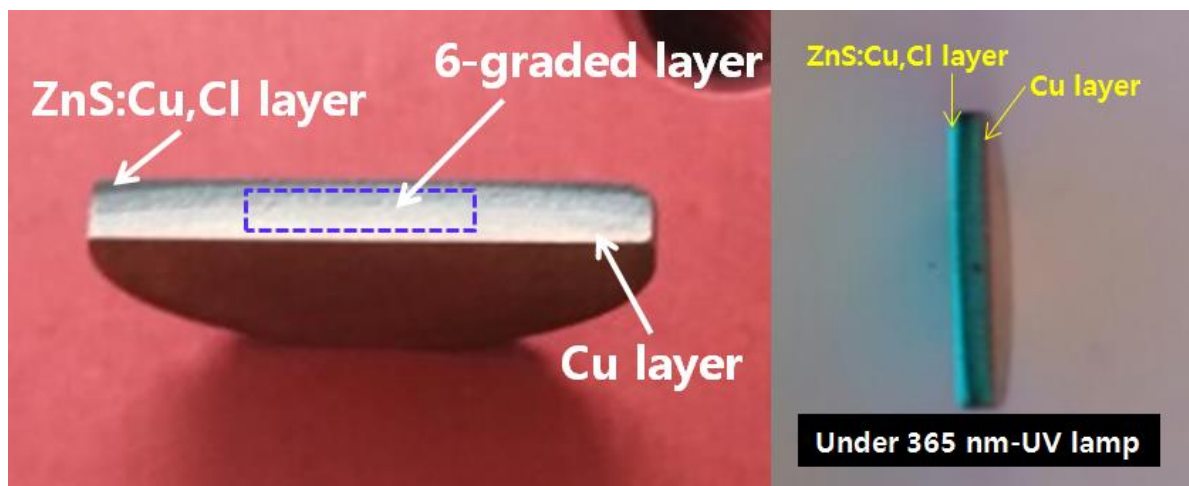
Figure 1: Cross-sectional photograph of FG [Cu]-[ZnS:Cu,Cl].

(Fuji Electronic Industrials Co., Ltd., SPS-321Lx, Japan). The SPS was carried out at 900 °C (heating rate; 100 °C/min) for 5 min of 50 MPa of pressure. The morphology of fabricated FG [Cu]-[ZnS:Cu,Cl] was observed by using a scanning electron microscope (SEM, Tescan, Vega, Czech). Current-voltage (*I-V*) curves of the FG [Cu]-[ZnS:Cu,Cl] were obtained using a Keithley 2400, and a 365 nm-UV source (UVItec Ltd, LF-204.LS, 4W, UK) was used for irradiation at distance of 10 cm between source and sample.

3. Results and Discussion

Figure 1 shows cross-sectional photograph of the FG [Cu]-[ZnS:Cu,Cl. The Cu and ZnS:Cu,Cl layers can be obviously identified when 365 nm- ultraviolet (UV) light was irradiated on the cross-section of the specimen as seen in figure 1. The Cu and ZnS:Cu,Cl were completely combined by graded layer between pure Cu and ZnS:Cu,Cl layers.We observed the cross-sectional morphology of the FG [Cu]-[ZnS:Cu,Cl] using scanning electron microscopy (SEM). Figure 2 shows cross-sectional SEM images of the FG [Cu]-[ZnS:Cu,Cl]. The thickness of the Cu and ZnS:Cu,Cl layers in FG [Cu]-[ZnS:Cu,Cl] were found to be approximately 70 µm and 200 µm, respectively. We confirmed that the density of the Cu layer is higher than that of the ZnS:Cu,Cl layer. We expect that this dual structure of porous-dense material has an advantage in sensor applications [16]. Figure 3 shows the current(*I*)-voltage(*V*) curves for the FG [Cu]-[ZnS:Cu,Cl] in the dark and under 365 nm -UV irradiation. The current increased from 10.34 µA (dark condition) to 20.05 µA at an applied bias of 0.5 V when the FG [Cu]-[ZnS:Cu,Cl] was irradiated by 365 nm -UV light. In our case, the ZnS:Cu,Cl layer functions as the active layer detecting a change in the environment, the porous structure of the ZnS:Cu,Cl expose more active sites to the environment than a dense structure would, and the Cu layer functions as an electrode that transfers electrons captured by the active sites of ZnS:Cu,Cl; the dense structure of the Cu provides more electron mobility than a porous structure would.

4. Conclusions

In this study, the microstructures of Al-Al$_3$Ti FGMs fabricated at 1200 °C from a master alloy of an Al-5 mass% Ti ingot containing 11 vol% Al$_3$Ti platelets in the Al matrix are investigated. Compositional gradient and orientation effects are found in the Al-Al$_3$Ti FGMs. It is found that the mold temperature plays an important role in the solidification behavior by the centrifugal casting. Anisotropic wear resistance is found to be dependent on the direction of the test wear relative to the Al$_3$Ti platelet orientation. Specimen tested along the Al$_3$Ti platelets thickness direction shows the smallest wear resistance among the three orientations due to the ease with which the Al$_3$Ti platelets broke.

Figure 2: Cross-sectional SEM image of FG [Cu]-[ZnS:Cu,Cl] [17].
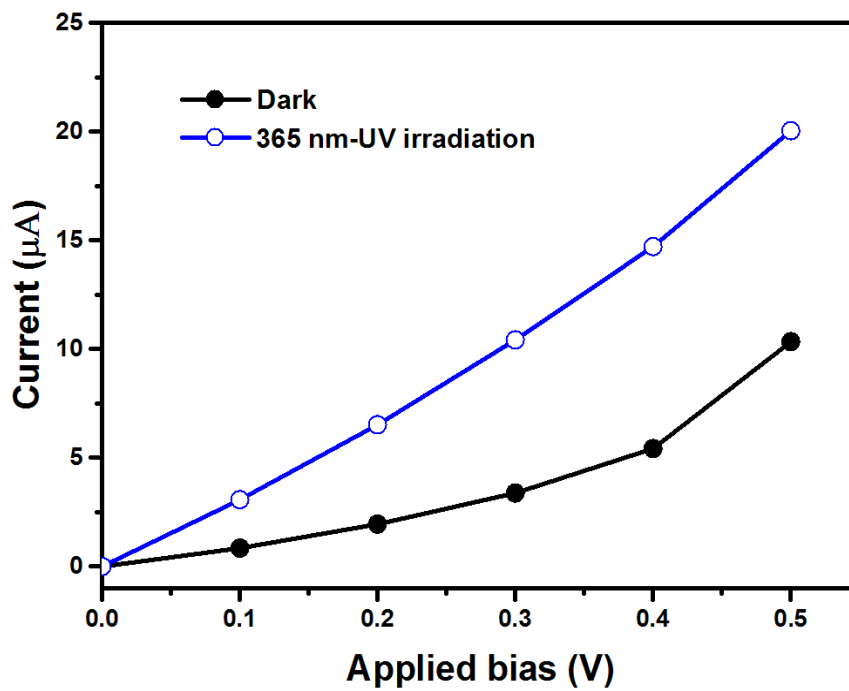
Figure 3: *I-V* curves of FG [Cu]-[ZnS:Cu,Cl] in the dark and under 365 nm UV-lamp irradiation [17].

Acknowledgements

References

[1] X. Fang et al., Adv. Mater., 19 (2007), 2593-96.

[2] Y. Jiang et al., Adv. Mater., 18 (2006), 1527-32.

[3] X. Fang et al., Adv. Mater., 21 (2009), 2034-39.

[4] X. Fang et al., Adv. Funct. Mater., 20 (2010), 500-08.

[5] L. Hu et al., Adv. Mater., 24 (2012), 2305-09.

[6] W. Tian et al., Adv. Mater., 26 (2014), 3088-93.

[7] L. Wang, X. Ma, R. Chen, Y. Q. Yu, L. B. Luo, J. Mater. Sci: Mater. Electron, 26 (2015), 4290-97.

[8] X. Wang et al., J. Mater. Chem., 22 (2012), 6845-50.

[9] C. R. Ronda, J. Alloy Compd., 225 (1995), 534-38.

[10] S. Jacob, J. Yu, B. Frank, A. C. Sue, R. Laurel, J. Phys. Condens. Matter, 22 (2010), 055301.

[11] H. C. Swart, L. Oosthuizen, P. Holloway, G. L. P. Berning, Surf. Interface Anal., 26 (1998), 337-42.

[12] Y. Y. Chen, J. G. Duh, B. S. Chiou, C. G. Peng, Thin Solid Films, 392 (2001), 50-55.

[13] Y. T. Nien, I. G. Chen, C. S. Hwang, S. Y. Chu, J. Phys. Chem. Solids, 69 (2008), 366-71.

[14] W. Chen et al., J. Appl. Phys., 92 (2002), 1950-55.

[15] O. Guillon et al., Adv. Eng. Mater., 16 (2014), 830-49.

[16] M. E. Davis, Nature, 417 (2002), 813-21.

[17] J. Park et al., Sci. Rep., 6 (2016), 23064.

Study on the functionally graded characteristics of biofilms

Makoto Miyaoka[1], Kouich Nakano[2], Toshinari Maeda[3]

[1] *Graduate School of Life Science and Systems Engineering Kyusyu Institute of Technology, miyaoka-makoto@edu.life.kyutech.ac.jp* [2] *Graduate School of Life Science and Systems Engineering Kyusyu Institute of Technology, nakano@life.kyutech.ac.jp* [3] *Graduate School of Life Science and Systems Engineering Kyusyu Institute of Technology, toshi.maeda@life.kyutech.ac.jp*

Abstract

As regarding graded function on biomaterials, for example, we can find it in the graded distribution of fibrovascular bundle or lacuna on the cross-sectional surface of bamboo or seashell. These three dimensional structure is evaluated as the ideal buckling resistance structure for realizing high strength and weight saving. On the other hand, biofilms are used for activated-sludge process in wastewater treatment and producing useful materials in lactic fermentation. It has been observed that the biofilm on the root surface of plants dissolves phosphorus [1]. From the above, we think that biofilms have functionally graded characteristics even though there are few reports about it. So, we investigated the functionally graded characteristics of some biofilms so as to control and utilize biofilms for the industrial use in the future.

Keywords: biofilms, aerobic bacteria, anaerobic bacteria, graded characteristics, flora analysis,

1. Introduction

Graded functions to be seen in biomaterials include graded distribution of bamboo vascular and the graded distribution of the cavity in the section of the shell. The number and tube diameter of the bamboo vascular are distributed from inside to outside on the sectional surface of the bamboo. This structure evaluated as the dynamic anti-buckling structure to realize high strength and weight saving. In addition, the cavity, which is seen in the section of the shell, acts as anti-buckling structure to realize high strength and weight saving also. On the other hand, the biofilm produces useful materials such as the acetic acid fermentation and biofilms are used for activated-sludge process in wastewater treatment for a useful advantage for the human. And it has been observed that the biofilm on the root surface of plants dissolves phosphorus [1]. However, as a fault to give harm to the human, biofilms will easily attach to the wall of aeration tank in the waste water treatment plant and will affect the process efficiency. In addition, it is thought that the biofilm is a film having a graded function characteristic, but there are few study examples. Therefore we performed flora analysis of the biofilm by next-generation sequencer (Miseq) and examined a graded distribution of the biofilm. And we would like to make use for an applied study to utilize biofilm effectively in the future.

2. Functionally graded characteristics that are expected to biofilms

It is about 4.5 billion years ago since the earth was born and it is thought that the primitive microorganisms was born in the first Earth about 3.3 billion years ago. Microbes and the human beings have been concerned with each other for a long time. The human has been received a benefit of fermented food such as cheese or the yogurt from a microbe. But it is relatively these days that humankind noticed the existence of the microbe. The microbe changes an existence form depending on various graded environment in the natural world. The biofilm is aggregate of the microbes occurring generally in wet environment and is one which is in existence form of the microbes. Focusing on oxygen, it is thought that the oxygen density in biofilm shows graded distribution. So we think that an aerobic
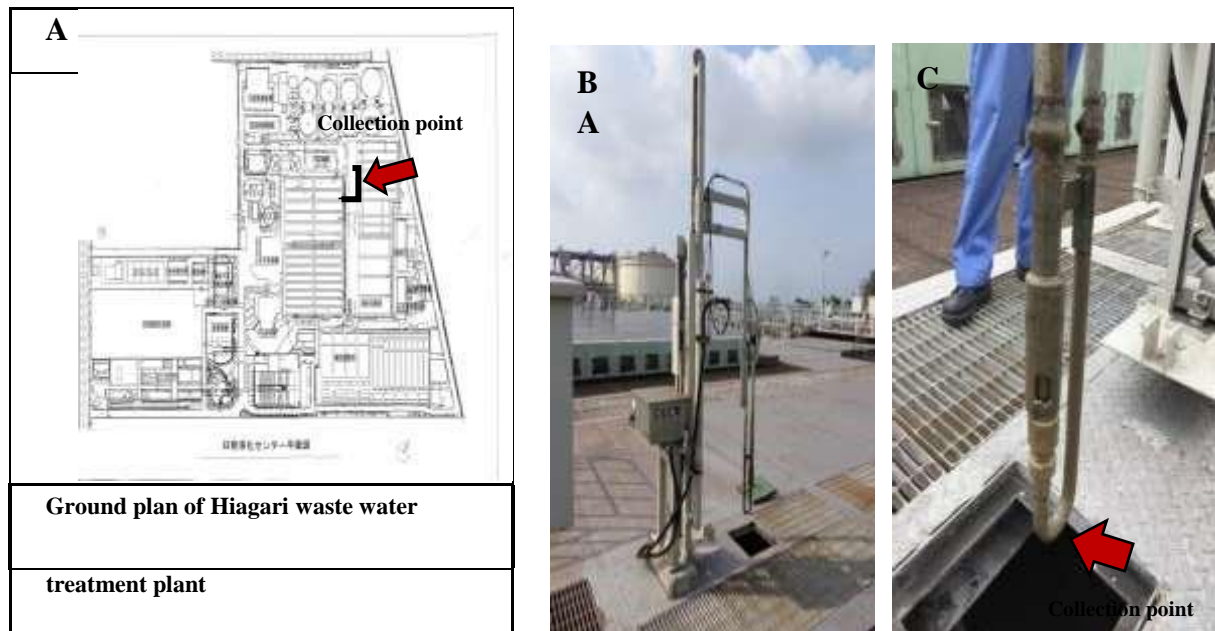
Figure 1: The collection position of biofilms (A: Ground plan of Hiagari waste water treatment plant, B: Overall picture of the oxygen content meter (OR8EFG-ORG-KCl filling type) , C: Enlarged view of the oxygen content meter and picking location of the biofilm)

bacterium and an anaerobic bacterium are graded distributed according to oxygen density. This attracts attention as the reason which can explain micobially influenced corrosion[2] by the production thing of the anaerobic bacterium under the aerobic environment. Focusing on water and nutrient or organic matter, it is thought that these materials are graded distributed from the inside of the biofilm toward the surface. Furthermore, as for the temperature and the light, it is a different value in the surface and the inside of the biofilm, and it is thought that graded area exists as for the middle part. From this and others, it is expected that oxygen permeability, heat shielding characteristic, material permeability, thermal conductivity and others can be graded changed by controlling density or thickness of biofilms.

3. Experimental methods

3.1 The collection of Biofilms

In this study biofilms were collected from the surface of the oxygen content meter (OR8EFG-ORG-KCl filling type) that is submerged in the anaerobic tank of Hiagari waste water treatment plant in Kokurakita-ku, Kitakyushu-city, Fukuoka prefecture. The oxygen content meter is made in Yokogawa Electric Corp Japan and introduced in 2001. This biofilm was picked up from the water of approximately 3m in depth, and the oxygen content in this position was less than 5%. The sampling of the biofilm was carried out with a spatula made of plastic. We moved the biofilm to the laboratory dish immediately and cryopreserved it at -20 degrees Celsius. Figure 1 shows the collection position of biofilms.

3.2 DNA extraction from the biofilm

DNA extraction was executed so as to analyze the flora of the collected biofilm. Collected biofilm was cut into three. DNA extraction positions are shown in Figure 2. We set 6 sampling positions in total. A1, B1, and C1 were set at the surface neighborhood of the biofilm. A2, B2, and C2 were set at the inside of the biofilm. We used Untla Clean Microbial DNA Isolation Kit (MoBio) for the DNA extraction. The measurement of DNA concentration and purity were carried out by using a Nano Drop after DNA extraction. DNA concentration and purity of the sample are listed in Table 1. Usually the concentration of DNA is needed more than 10 ng/µL.
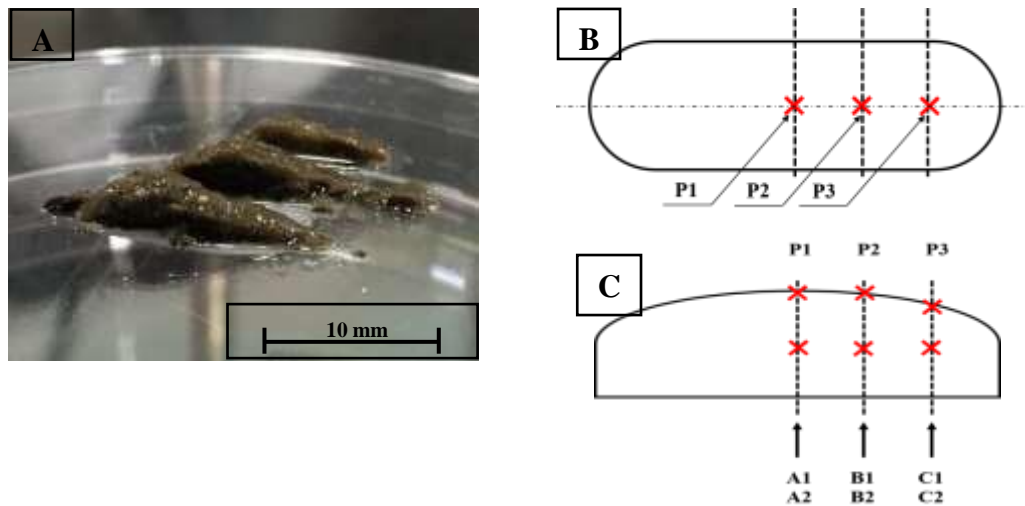
Figure 2: DNA extraction positions (A: Appearance of biofilm which was cut into three, B: Cutting lines, C: Sampling positions)

Table 1 DNA concentration and purity of the sample

Sample No.	A1	A2	B1	B2	C1	C2
DNA concentration (ng/µL)	9.8	15.6	16.4	9.1	18.9	4.4
DNA purity (260/280)	1.66	1.94	1.67	1.93	1.81	2.2

Table 2 The final DNA concentration values measured by using the Qubit

Sample name	A1	A2	B1	B2	C1	C2
DNA concenttation (ng/µL)	4.51	0.366	8.29	0.81	0.491	3.44

3.3 DNA concentration by using PCR & Confirmation of the DNA band by the electrophoresis

As some of the DNA concentration of the samples are very low, PCR (Polymerase Chain Reaction) method are applied so as to increase the concentration of DNA. After concentration treatment of DNA, confirmation of the DNA band was executed by the electrophoresis using a 2.0% agarose gel.

3.4 The final confirmation of the DNA concentration

The final confirmation of the DNA concentration was carried out by using DNA / RNA / protein quantitative measurement device (Qubit® 2.0 Fluorometer made in Thermo Fisher SCIENTIFIC Corp). The final DNA concentration values measured by using the Qubit are listed in Table 2.

3.5 Analysis of the biofilm using a Next-generation sequencer

As a final step, flora analysis was carried out by using next-generation sequencing (Miseq). Its 5 steps are shown below.

(1) Generating a sample sheet for Nextera XT DNA Libraries.
(2) Creating Nextera XT DNA Libries
(3) Preparing the reagent cartridge.
(4) Performing a run on the Miseq.
(5) Analyzing sequencing data in Miseq reporter.
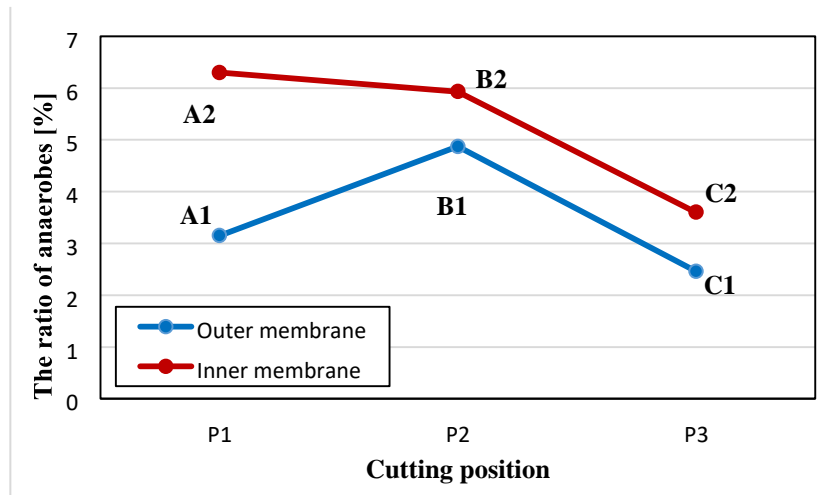
Figure 3: The ratio of anaerobes of an outer layer part and the inner layer part in each cutting position

4. Result & Discussion

We set the total eight kinds of bacteria which indicated high existence ratio from the flora analysis result of each sample as 100%. And we calculated the ratio of anaerobic bacteria for overall bacteria. The ratio of anaerobes of an outer layer part and the inner layer part in each cutting position is shown in Fig.3. As a result, a lot of aerobic bacterias were distributed over the outer layer part more, and there were many anaerobes in the center. In addition, as a result of flora analysis, the Dokdonella, Acinetobacter, Acidovorax, Nitrospira genus existed in an outer layer part and in the center. These bacteria are regarded as a facultative anaerobic bacterium. On the other hand, in case of bottom layer part, the anaerobes such as methanation or the sulfur oxidation bacteria were observed. However, this tendency is regarded as a good result in confirming graded distribution of anaerobes in biofilm.

5. Conclusion

The conclusions obtained in this study are as follows.
- Dissolved O2 content becomes around 5% in the outer layer part of the biofilm, and aerobic bacteria are observed a lot.
- In all cutting positions, the ratios of anaerobic bacterium increased from the outer layer part of the biofilm to the inner layer part, and graded distribution was confirmed.
- Anaerobic methanogen and sulfur-oxidizing bacteria were confirmed in the bottom layer part.

References
[1] Yamaga, F, et al.: Environ. Sci. Tech, 44 (2010), 6470
[2] Anzai Toshio, Nakano Kouichi, Nishio Kazumasa, Matsukawa Kiyotaka, JWS, Vol.23, No.2, (2005), pp.179-185

Decomposition and Recovery Technology of Multi-function Type Print Circuit Board with Substrate a Biodegradable Resin

Arashi Ohmukai[1], Takayoshi Yagasaki[2], Hitoshi Kohri[3], Ichiro Takano[4]

[1] *Graduate school, Kogakuin University, bm15005@ns.kogakuin.ac.jp*
[2] *School of Advanced Engineering, Kogakuin University, yagasaki@cc.kogakuin.ac.jp*
[3] *School of Advanced Engineering, Kogakuin University, kohri@cc.kogakuin.ac.jp*
[4] *Faculty of Engineering, Kogakuin University, ct97912@ns.kogakuin.ac.jp*

Abstract

In recent years, resins (plastics) have been used in large quantities as substrate materials for making printed circuit boards. Problems associated with the disposal of these resin materials—including the exhaustion of landfill areas and generation of toxic gases during disassembly—have long been pointed out. Accordingly, there is much interest from the standpoint of environmental protection in the potential of biodegradable resins that are broken down to water and carbon dioxide by microorganisms as replacements for conventional resins. However, because the dissolution behavior of biodegradable resins in different environments is still poorly understood, methods for collecting and breaking down biodegradable resins have not yet been established.

In this study, polylactic acid (PLA) as a biodegradable resin with high potential for use as a general-purpose material was selected, and carefully examined the decomposition characteristics of PLA, modified at the microstructural level to multi-functionalize it with respect to the end goal of use in printed circuit boards. It was found that the decomposition characteristics of the resin essentially did not change, even when the resin was modified at the microstructural level to improve various functions. It was also found that the rate of decomposition significantly varied depending on the liquid medium used during decomposition (i.e., the decomposition solution). These results demonstrate that microstructural modification and choice of decomposition solution can either promote or inhibit decomposition.

Keywords: Biodegradation, Polylactide acid, Print Circuit Board, Proteinase K

1. Introduction

General purpose resins have the advantage of being inexpensive, lightweight, and easily mass-produced. As a result, these resins have been both made and used in large quantities. The use of resins in printed circuit boards (PCB) for electronic components has increased in conjunction with the miniaturization and elevated precision of such parts. At the same time, the greater quantity of resins contained in these PCBs has resulted in massive quantities of waste materials, the environmental impact of which has become problematic. Furthermore, the recovery of the valuable metals printed on PCBs has also become an issue.

Given these circumstances, there is significant interest in biodegradable resins that can ultimately be degraded into CO_2 and H_2O by environmental microorganisms. In particular, there is a requirement for low environmental impact materials with the potential to replace the general purpose resins currently being used in PCBs. That said, biodegradable resins are currently more expensive and typically exhibit lower heat tolerance than conventional resins. Furthermore, because the dissolution behavior of biodegradable resins is not precisely and clearly

understood, such resins are only found in a limited number of applications at present, and have not yet reached the general use phase.

The present study attempted to improve the mechanical properties and thermal stability of a biodegradable resin by modifying its microstructure, with the goal of making this resin usable in PCBs. This work also investigated the effect of the liquid medium comprising the decomposition solution on the dissolution behavior of a microstructurally-modified biodegradable resin.

2. Experimental

2.1 Preparation of Test Materials

Authors selected polylactic acid (PLA) as a representative biodegradable resin and therefore the primary test material. PLA slabs ($10 \times 10 \times 2$ mm) were prepared using an injection molding machine, and are designated herein as "virgin PLA" samples. Some of these PLA slabs were subsequently heated at 100 °C for 180 min[1], and the resulting thermally-treated material is designated as the "annealed PLA." In an attempt to improve the impact resistance of the polymer, PLA was also mixed with polybutylene succinate (PBS) to create a PLA:PBS polymer blend (60:40). Slabs of this material were prepared having the same shape and dimensions as the virgin PLA and annealed PLA slabs. Finally, a carbonized layer was formed (except for the side portions) on some untreated PLA specimens using Ar^+ ion beam irradiation, followed by the deposition of a Ti thin film(except for the side portions). The above materials were all used as test samples.

2.2 Evaluation

Test samples were subjected to decomposition by either hydrolytic or enzymatic degradation. Hydrolytic degradation was conducted by immersing the test samples in a phosphate buffer (0.05 mol/L), while enzymatic degradation was performed by immersing the specimens in this same phosphate buffer (0.05 mol/L) but with added proteinase K (100 μg/mL). Both degradation trials were conducted with the experimental vessels held in a thermostatic bath maintained at 60 °C[2].

Given the potential for the phosphate buffer to inhibit enzyme activity, in order to accurately assess the effect of enzyme activity on decomposition during the enzymatic degradation trials, we decided to also add to the tris- HCl buffer solution. This should be noted because otherwise the description appears to suggest that no other substances were used during the enzymatic degradation experiment with the tris- HCl buffer (0.1 mol/L), which is believed to have little effect on enzyme activity.

To evaluate the degree of decomposition of each test sample following immersion, their surfaces were inspected using optical microscopy (OM) and scanning electron microscopy (SEM). In addition, the amount of carbon dioxide generated during each decomposition trial was calculated based on measurements of the total organic carbon (TOC).

3. Results and Discussion

OM inspection revealed evidence of much more severe surface dissolution in the case of the annealed PLA compared to the virgin PLA, while the blended specimens exhibited less surface dissolution than the virgin material. The changes in the amounts of carbon dioxide generated as a function of the number of days over which each sample was immersed for the various materials are shown in Fig. 1, while Fig. 2 presents the data for the sample with a Ti thin film. Both figures demonstrate that the annealing treatment increased the rate of decomposition. In addition, the application of the Ti film evidently did not change the rate of degradation up to eight day compared to the virgin PLA, although the Ti-coated specimen showed much faster decomposition after this point. Therefore, surface modification of the resin during deposition of the thin film, as well as the annealing treatment, are both believed to have led to accelerated degradation.
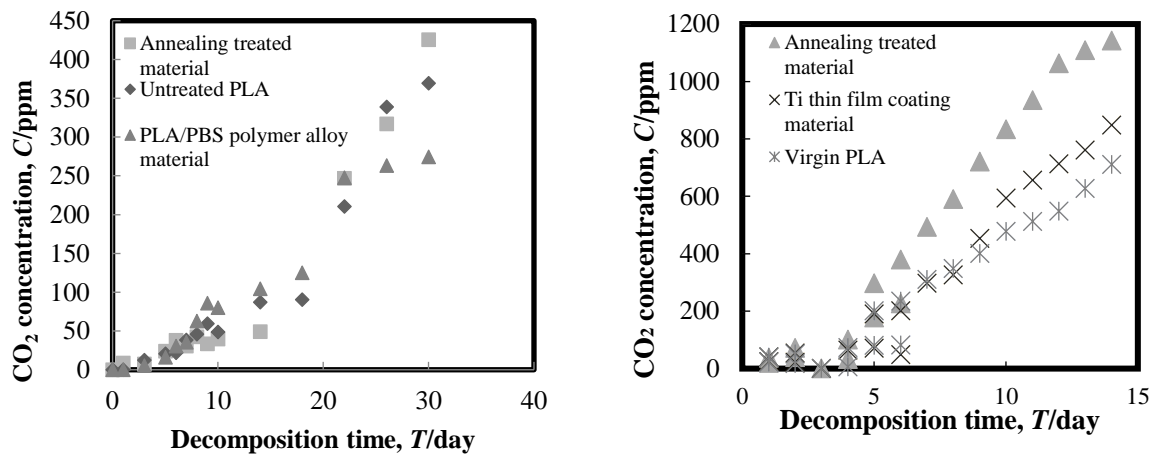
Fig. 1. Carbon dioxide emissions during enzymatic. Fig. 2. Carbon dioxide emissions during enzymatic degradation of various PLA samples .degradation of various PLA samples, including a sample with a Ti film coating.
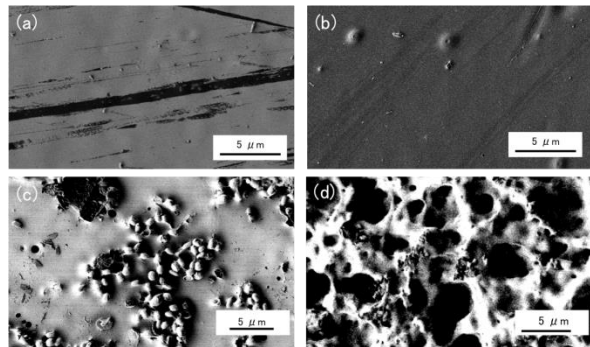
Fig. 3. Dissolution of virgin PLA surfaces 14 days after immersion in (a) phosphate buffer, additive-free, (b) tris-HCl buffer, additive-free, (c) phosphate buffer, enzyme addition, and (d) tris-HCl buffer, enzyme addition.

Closer examination of the dissolved areas indicated that the decomposition occurred in stages, with the chemically weak, amorphous areas dissolving first, followed by the more crystalline regions. In addition, in contrast to the annealed PLA, it was found that the decomposition rate of the polymer blend decreased over time. Based on the observation that the amount of CO_2 generated increased rapidly around nine day of immersion, it is believed that decomposition was accelerated at this point due to the onset of enzymatic degradation in addition to hydrolytic degradation.

SEM images of virgin PLA surfaces after immersion in the various solutions are shown in Fig. 3. Linear dissolution marks are evident on the surfaces of the virgin PLA samples that were immersed in both the phosphate and tris-HCl buffers without the enzyme. These marks are characteristic of the early stages of PLA decomposition, and there are no significant differences between the specimens from the two solutions. Numerous dissolution patches approximately 1 μm in size are observed on the surface of the PLA sample immersed in the phosphate buffer with enzyme, while the decomposition regions on the surface of the PLA sample from the tris-HCl buffer with enzyme are on the order of 5 μm in size. Whereas the dissolution patches generated by the phosphate buffer are highly localized, those on the surface of the PLA immersed in the tris-HCl buffer are more widely distributed and larger. These results confirm that the enzyme-inhibiting effect of the phosphate buffer can be mitigated and decomposition of the PLA can be accelerated using the tris-HCl buffer.

4. Conclusions

This work demonstrated that the dissolution behavior of biodegradable resins can be altered by modifying the microstructure of the material. In addition, given that the liquid medium can have a significant effect on enzymatic activity and, therefore, on the dissolution behavior, it was confirmed that modifying either the microstructure or the enzymatic activity can accelerate or inhibit dissolution.

Acknowledgements

References

[1] K.Hayakawa, T.Yagasaki and H.Kohri, Trans.Mat.Res.Soc.Japan, 38[3], pp. 359-362(2013)

[2] Hideto Tsuji: Science of biodegradable polymer material, Corona Publishing Co. pp. 128-132(2002)

Electromagnetic induced segregation of aluminum alloy cast parts

Bernard Nacke

Institute of Electrotechnology, Leibniz Universität Hannover
nacke@etp.uni-hannover.de

Abstract

The Electromagnetic Induced Segregation (EIS) of cast parts is an innovative technology for diecasting of aluminum alloys. Due to the different action of electromagnetic forces to high and low conductive materials electromagnetic fields can be used for separation of the different materials during the liquid phase before solidification [1]. This principle has been applied during casting of aluminum/silicon alloys cast parts in order to produce a primary silicon concentration gradient during casting. The paper shows the principle of the electromagnetic induced segregation effect, the design of a suitable inductor system for casting of engine blocks using numerical simulation, principle experiments in a pilot casting installation and the realization of the process in an industrial casting production machine. Finally four inductor systems were produced and installed in an industrial casting machine for 8-cylinder engine blocks [2]. Four cylinder bores of the engine block were casted using electromagnetic induced segregation and the other four bores were casted conventionally without electromagnetic treatment. Standard running tests of the casted engine have confirmed a comparable wear resistance compared to conventionally produced engine blocks, but with high advantages due to the fact of graded structures in the engine blocks.

Keywords: functional graded materials, electromagnetic separation, aluminum casting

1. Introduction

In many technical applications Functionally Graded Materials (FGM) promise advantages over conventional materials. Especially in the casting of light metals this technology offers innovative possibilities for wear-resistant but light products. These materials consist of alloy composition gradients within the part, which promote different local properties. The main advantage is the possibility to control the characteristics locally.

Aluminum has eutectic concentration with 12,5 % silicon. The melting point of this alloy is at 577°C. The solubility of silicon at this temperature is 1.65 % and drops to 0,07 % at 300°C. In an alloy with more silicon than this solubility there are mixed aluminum crystals and also silicon crystals. If the alloy cools down slowly the silicon solidifies in the eutectic alloy in the form of square-edged crystals, needles and plates. In the case of a hypereutectic alloy the primary silicon accumulates to big crystals. With specific methods it is possible to decrease the size of the crystals but this reduces the loss of tensile strength and maximum strain only little. This is more disadvantageous at higher silicon concentration. In spite of this reasons alloys with concentrations up to 25 % are used for wear resistant components, for example in the manufacture of internal combustion engines. The primary silicon produces with its hardness of 1400 HV a very good abrasion resistance. Such a high concentration of silicon to increase durability and loading limit is not useful for complete cast parts.

With the technology of *Electromagnetic Induced Segregation* (EIS) a graded structure is generated, that could be adapted to the specific requirement of the product, for example to improve the abrasion resistance of the surface, without changing rigidity inside the material. The process of EIS is based on the different electromagnetic force density between the components of the alloy, that are excited by the electromagnetic field. This is in consequence of the different electrical conductivities of the components. In the electromagnetic field the silicon particles with

lower electrical conductivity are moved to higher flux density. This effect can be influenced by the frequency and the geometry of the electromagnetic field and the maximum flux density.

2. Description of segregation

Considering as example the process of segregation is described for a hollow cylinder. The inductor is located in the center of the cylinder, so that the region of interest is outside of the induction coil. The principle is shown in Figure 1.

To demonstrate the effect of the electromagnetic field on the silicon particles it is necessary to describe the force density. Simplifying the magnetic field of a very long coil is assumed.

The flux density outside the coil is:

$$\vec{B}(r,t) = B_0 \cdot b(r) \cdot \vec{e}_z \cdot \sin(\omega t) \qquad (1)$$

Here b(r) describes the radial decay of the flux density. The induced current density is:

$$\vec{S}(r,t) = S_0 \cdot s(r) \cdot \vec{e}_\varphi \cdot \cos(\omega t) \qquad (2)$$

The current density has only components in azimuthal direction and the amplitude has radial dependence. The electromagnetic force density

$$\vec{f} = \vec{S} \times \vec{B} \qquad (3)$$

is directed radial. For particles with lower conductivity follows with [1]

$$\vec{F}_{em} = -\frac{3}{2}\frac{\sigma_m - \sigma_p}{2\sigma_m + \sigma_p} V_p \vec{f} \qquad (4)$$

that the resulting force on the particles is in negative radial direction. The force depends on the particles volume and the radial coordinate.

magnetic core

⊙ induced current

electromagnetic force

magnetic flux (core)

magnetic flux (melt)

inductor

protection cover

Figure 1: Principle of EIS

If a particle starts to move relative to the aluminum melt, a friction force counteracts the movement. This force depends on the viscosity of the melt, the size of the particle and the relative velocity from particle to the melt. If there is a balance between driving and retarding force, the movement becomes uniform. The flow ends when the melt solidifies, so the segregation varies with solidification time and local temperature distribution. Cooling is yet another parameter to adapt the segregation to the specific requirements of the product. Due to the water-cooled inductor the melt solidifies first on the protection surface of the inductor. In this regions (see Figure 2, domain 1) the time for segregation is very short and there will be nearly no gradient. With larger distance to the surface the solidification time increases and the concentration with it. In Figure 2 this is shown in domain 2. The shape of the silicon concentration in this region can be influenced by the process parameters. Closed to this a depletion zone

Figure 2: Theoretical concentration of primary silicon

will appear where the primary silicon is removed from (3). Far away from the surface there will be a non-affected area because of the limited penetration depth of the electromagnetic field (4).

3. The inductor system

Major task of the inductor system is to excite high magnetic field in the melt to initiate movement of primary silicon. A cooling system has also to be integrated into the inductor to dissipate heat from electric power loss and also to control the solidification of the melt. In Figure 3 the configuration of the developed inductor system is shown. In the center is a magnetic core to concentrate and guide the magnetic field. This core is surrounded by the inductor, which is made of a tube with rectangular shape to make maximum use of the limited space. The cast part is a bushing with graded silicon concentration.

A numerical model is used to calculate electric parameters of the inductor and for the dimensioning of the generator. Also the electromagnetic and thermal field is simulated to calculate the additional induced power. These results are input for the simulation of melt flow and solidification.

The simulations show that the magnetic flux density in the melt is high and uniform enough for the EIS effect. As it is already investigated in preliminary tests a flux density of 180 mT is sufficient for a successful segregation.
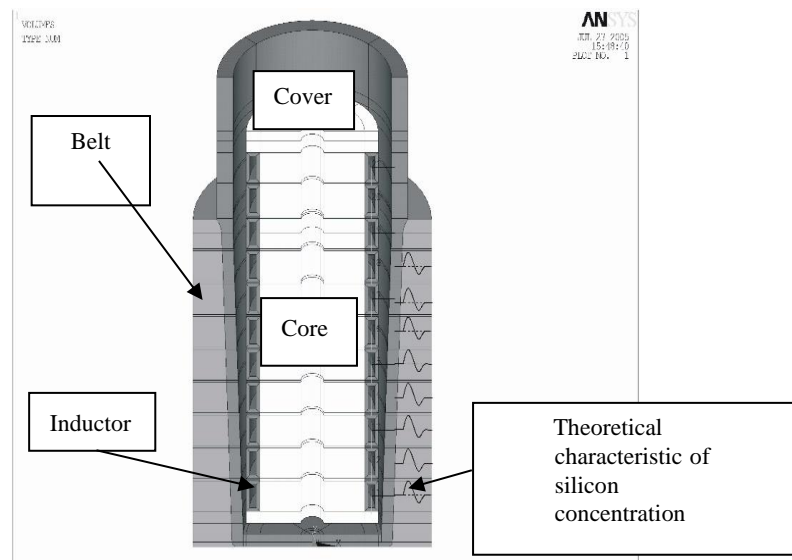
Figure 3: Numerical model of inductor system
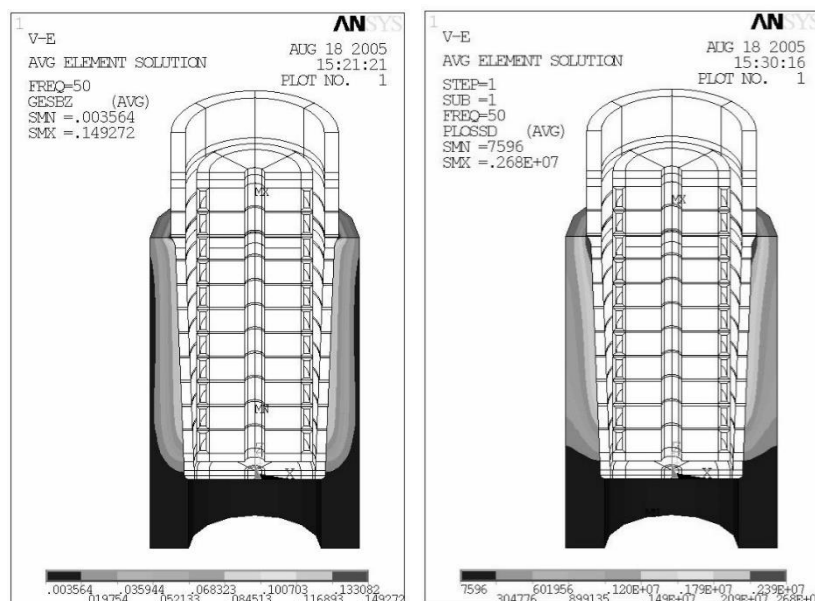
Figure 4: Flux density (left) and Joule heat distribution (right) in the melt

In Figure 4 the distribution of the flux density and the Joule heat is shown, for a radial gradation of primary silicon only the axial component of the magnetic flux density is responsible. The additional energy that is induced into the melt is taken into account in the simulation of solidification. Due to strong axial electromagnetic forces there is a melt flow that influences the segregation of the primary silicon. This flow is important for a good quality of the products, so it has also been simulated to compare between melt velocity and distribution of primary silicon. The results of the melt flow simulation show that regions with nearly no velocity correspond with demixing zones of the primary silicon. These zones have to be avoided by an optimized inductor design.

4.   Casting Results

First castings were carried out in a pilot casting machine at ACCESS in Aachen. The micrograph of the casted bushing in Figure 5 shows the effect of the EIS technology. On the left side there are small crystals of primary silicon that are uniformly distributed without EIS. With the influence of the electromagnetic field the crystals become larger and concentrate on the surface as it is visible at the right micrograph.

Finally, the technology was applied to the casting of a BMW V8 engine which was be assembled and checked on an engine test bench. After this test run the complete engine was disassembled and the walls of the cylinder were inspected. Summarized no difference between engines casted with common technologies and the test engine could be found and the advantages of this new technology prevail, because other regions have less primary-silicon and costs for subsequent machining could be saved.

5.   Conclusions

The EIS technology allows an effective segregation of silicon crystals at the surface of cylinder bores. The silicon content of the used hypereutectic alloy could be reduced without changing properties of the surface. Important process parameters are the temperature of the melt, thermal balance of the die, power and current of inductor, cooling of the sleeves, die-fill time and the casting pressure. With suitable casting parameters it is possible to produce cylinder surfaces by electromagnetic induced segregation that are on a par with common cylinder surfaces.
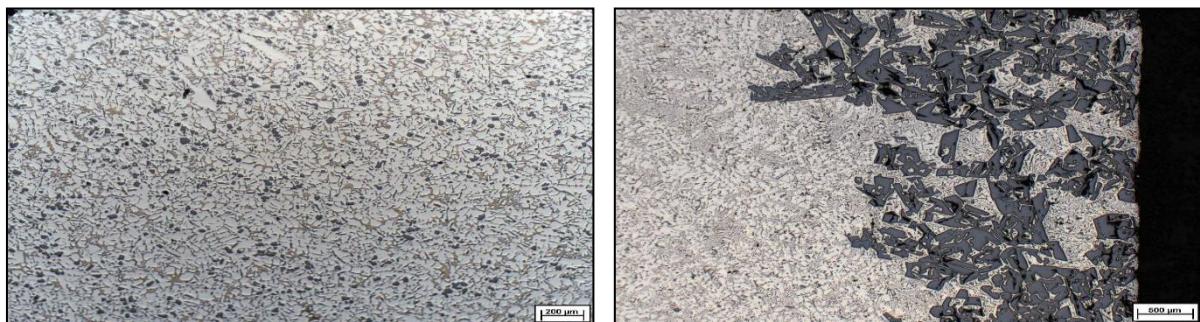
Figure 5: Effect of EIS-technology (left: without, right: with electromagnetic field)

References

[1] Lennov, D; Kolin, A: Magnetohydrodynamic Forces Experienced by Spherical and Symmetrically Oriented Cylindrical Particles, Journal of Chemical Physics 22 (1954)
[2] Aquilar, J.; Grüneberg, C.; Sommer, B.; Niehues, J.; Haimerl, M.; Nacke, B.; Langejürgen, M.: Electromagnetically induced segregation for generation of a gradient microstructure in aluminum castings. Heat processing (3) 2008

Synthesis and Mechanical Properties of Graded TC4 Titanium Alloy via Plasma Activated Sintering

Yi Sun, Guoqiang Luo, Chuandong Wu, Jian Zhang,
Qiang Shen, Lianmeng Zhang*

*State Key Laboratory of Advanced Technology for Materials Synthesis and Processing,
Wuhan University of Technology, Wuhan 430070, China
*corresponding author, Tel.: +86 27 87879468; fax: +86 27 87879468.E-mail address:
luogq@whut.edu.cn*

Abstract

In the present study, graded TC4 titanium alloy with a gradient variation of grain size and shape was successfully synthesized using cryomilling and plasma activated sintering. The microstructures were characterized by OM, SEM and TEM, while the phase compositions were investigated by XRD. To provide insight into the mechanical behavior of the graded TC4 titanium alloy, we measure the compressive strength and micro-hardness on the ambient temperature. Our results show that the graded TC4 titanium alloy has a dense structure with a relative density of 98.32%. The intimate combination between different layers can be observed. The grain sizes show a gradient variation. The phase compositions of each layer change along with the grain sizes. The graded sample exhibits notable mechanical properties, the Vickers micro-hardness, the yield strength and the compression fracture strength of the as-prepared sample reaches 470.9HV, 1229.2MPa, and 2090.3MPa, respectively. The crack initial in fine grain zone, and then grows along grain boundaries.

Keywords: TC4 Titanium Alloy; graded material; cryomilling; plasma activated sintering; mechanical property

1. Introduction

TC4 titanium alloy is widely used in the aerospace, industry, biomedical and other fields due to its high specific strength, excellent corrosion resistance and wide scope of working temperature [1-3]. However, TC4 titanium alloy exhibits weak processability such as sticking phenomenon due to its poor wear resistance and thermal conductivity. Hence, the powder metallurgy which is regarded as a kind of near net shape techniques is a suitable route to synthesize the titanium alloy with excellent properties and low costs. Y. Y. Chen prepared ultrafine grained TiAl intermetallic alloy by spark plasma sintering [3], the results indicated that the enhanced strength can be obtained by reducing the grain size; Y. H. Wei reported that the lamellar grain of TC4 titanium alloy prepared by powder metallurgy method exhibit a relatively low hardness [7].

Inspection of the published scientific literature shows that grain size and morphology are the main factors influencing the strength of metals [4-5]. With the grain size decreasing, the strength of the material increases obviously. However, the toughness and plasticity will be significantly reduced, which limit its comprehensive performance. Therefore, raising its abrasion resistance and hardness of surface, and keeping the high strength of the matrix are the key points of research.

Nowadays, plasma based ion implantation [6-8] and surface Nano-crystallization [9-10] are commonly used in the surface treatment work. The plasma based ion implantation reacts by changing the element composition of the surface, it can obtain an excellent surface strength. However, the process of operation is hard to control, and requires strict reactive atmosphere. Surface Nano-crystallization by Shot Peening is a kind of mechanical surface

Table 1 The structure design of samples

Sample number	Structure information					
	Layer1		Layer2		Layer3	
S1	CG	10mm	/	/	/	/
S2	UFG	10mm	/	/	/	/
S3	UFG	1mm	CG	8mm	UFG	1mm
S4	CG	1mm	UFG	8mm	CG	1mm

strengthening method. But the introduction of impurities in surface may produce adverse effect in some service condition, which requires strict conditions of material.

In view of the above discussion, the objective of the present study was to provide insight into the design of the graded TC4 titanium with gradient variation of grain size and shape. In our study, the graded materials were fabricated by cryomilling and plasma activated sintering. We reported on studies of the microstructure and mechanical properties of the grade materials.

2. Experimental

The raw material is pre-alloyed TC4 titanium alloy powder produced by atomization comminuting process. To facilitate grain size reduction and minimize contamination, the cryomilling was performed in liquid nitrogen (L-N2, with a temperature of 191 ± 5 °C) environment in high speed rotate of 600rpm for 4.5 h, the weight ratio of steel ball and raw materials was 30:1.Table 1 shows the structure information of different samples in this paper, sample 3 and 4 design the different combinations of coarse grain (CG) and ultra-fine grain (UFG).

The vacuum degassing pretreatment is holding 12 hours at the temperature of 350ºC in a vacuum hot-pressing furnace (HP).Typical sintering process began with a heating rate of 100 ºC per minute and held at 900 ºC for 3min in Plasma Activated Sintering (PAS), since the experiment of the early exploration shows that samples produced by this sort of sintering schedule put out high density and better comprehensive performance.

The crystalline phase of the cryomilling and different layer in sintering products were tested by X-ray diffraction (XRD), the microstructure was characterized by Scanning Electron Microscope (SEM) and Transmission electron microscopy (TEM). In terms of mechanical performance, the compression performance was tested by MTS 810 ceramic testing system, and the surface performance was tested by Vickers hardness tester.

3. Result and discussion

3.1 Microstructure

The shape of the raw material powder is spherical as shown in Fig.1 (a), the average diameter of the powder is approximately 40 μm. In the process of cryomilling, powders were broken and get cold welding by continuous hit, finally show the irregular flake in Fig.1 (b). Fig.2 shows the XRD patterns of powder before and after cryomilling process, it shows that the diffraction peaks of the powder after ball milling intensity decrease and the peak width at half height increase at the same time. The size of crystal grain in powders is decreased combine with the Scherrer equation.
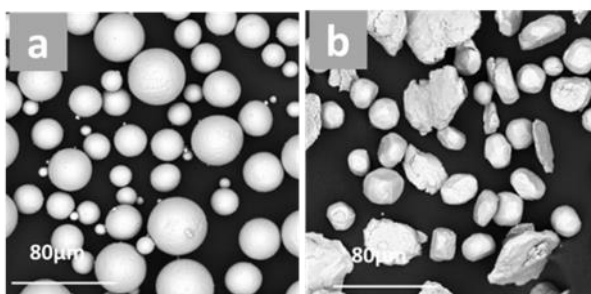
Fig1 Typical SEM images of powder (a) before and (b) after cryomilling
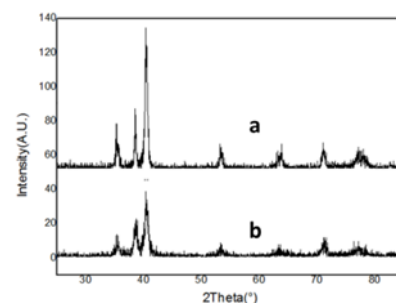
Fig2 XRD patterns of powder
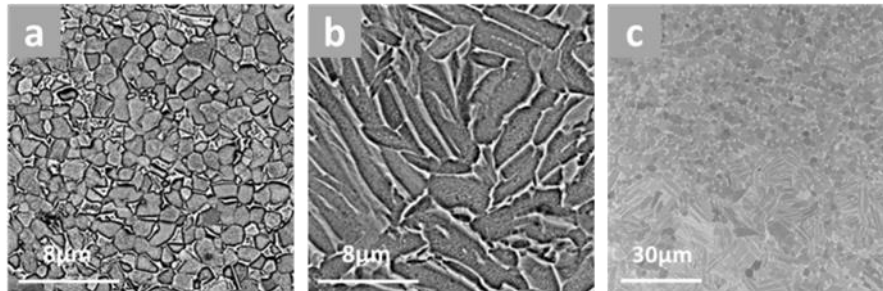
Fig3 Typical SEM images of different area in gradient S-3: (a) Fine grain area; (b) Coarse grain area; (c) Interface between two areas
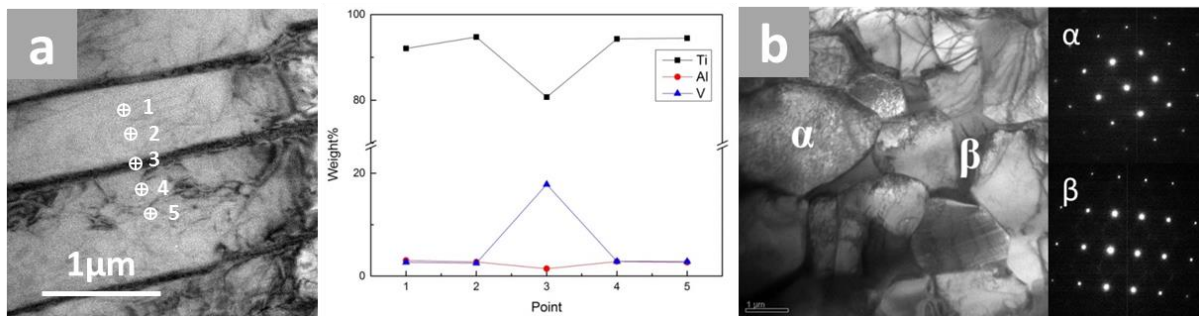
Fig4 Typical TEM images of (a) coarse grain area; (b) fine grain area

The typical SEM images of fine grain layer, coarse grain layer and interface between two layers are shown in Fig. 3(a), (b) and (c), respectively. As shown in Fig.3 (a), the consolidated sample exhibits an equiaxed structure with grain sizes typically in the range of 1-2 μm. The microstructure of grain in coarse area shows typical lamellar crystal with the range of grain sizes reaching 10-12μm in length and xx in width. No visible microcracks or voids were found in the interface between the two layers as shown in Fig. 3c, suggesting that the intimate combination of the interface between different layers can be obtained.. which explains that the gradient structure do not introduce additional imperfections.

TEM analysis was carried out on the sample, Fig.4 (a) and (b) are the coarse zone and fine crystal zone, respectively. EDS and diffraction analysis was carried out on the different regions. The diffraction spot of dark border between two adjacent grains corresponding to cubic, also rich in β phase stable element vanadium, the diffraction spot of crystal grain internal corresponding to hexagonal. TC4 titanium alloy is a kind of α and β bipolar titanium alloy. The content of beta phase mainly affects the brittleness of titanium alloy, and the brittleness and hardness increase with the rising of content.[11-12].

3.2 Mechanical properties

Fig 5 shows the typical compressive engineering stress-strain curves of specimens cut from the graded TC4 titanium alloy samples produced by PAS with different graded structures. The result shows that the four samples have almost the same compressive strength, however, the strain rate and yield strength are quite different. The specimens cut from sample 1 and 3 get higher strain rate relative to those of sample 2 and 4. In addition to the yield strength, the strain of sample 3 is relatively lower than that of sample 1, however, the strain value exhibits higher relative to those of sample 2 and 4.

Fig.6 shows the SEM image of interface and the micro-hardness test results of different area, the fine grain zone on the surface has an obvious role in hardness promotion. The surface fine grain zone has a Vickers hardness of 470.94HV, which is 32.66% higher than the internal coarse crystal zone (355HV).
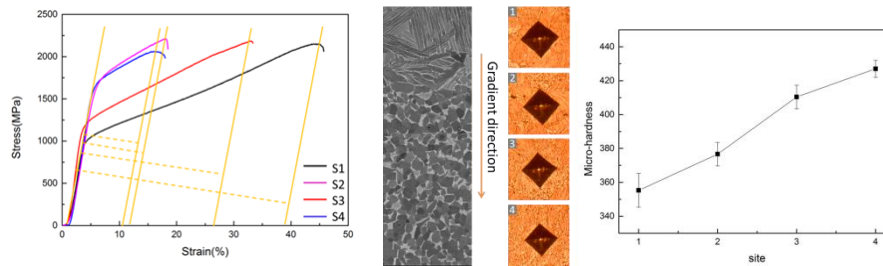
Fig5 Engineering strain-stress curves of samples from S-1 to S-4 Fig6Micro-hardness test result ofS-3

4. Conclusions

The graded TC4 titanium alloy is successfully synthesized by plasma activated sintering, and exhibit enhanced comprehensive strength.

(1) The size of crystal grain in raw material powders is decreased by cryomilling, and the graded TC4 titanium alloy with graded grain size and micro feature is synthesized by as-mentioned process.The laminar coarse grain area with a size at the range from 10 to 12 μm and the equiaxed fine grain area with a size at the range from 1 to 2μm can be observed in the micro feature of graded TC4 titanium alloy.

(2) Coarse and fine grain area in graded TC4 titanium alloy are both constituted by α and β phase, which are the typical structure of TC4 titanium alloy. The βphase can be detected in crystal boundary.

(3) As-prepared graded TC4 titanium alloy maintains the balance between the favorable toughness of coarse grain and the excellent hardness of fine grain area which make the graded sample exhibit notable properties. The Vickers hardness of the graded sample reaches 470.9 HV, the yield strength of 1229.2 MPa, and the compression strength of 2090.3 MPa.

5. Acknowledgements

6. References

[1] T.M.T. Godfrey*, A. Wisbey, P.S. Goodwin, K. Bagnall, C.M. Ward-Close, Materials Science and Engineering A282 (2000) 240–250.
[2] R. Filip*, K. Kubiak, J. Sieniawski, Journal of Materials Processing Technology 133 (2003) 84–89.
[3] Y.Y. Chen, H.B. Yu, D.L. Zhang, L.H. Chai, Materials Science and Engineering A 525 (2009) 166–173.
[4] Hall EO. Proc Phys Soc B, Lond 195164747.
[5] Petch NJ. J Iron Steel Inst 1953 17425.
[6] S. Anand Kumar, S. Ganesh Sundara Raman, T.S.N. Sankara Narayanan, R. Gnanamoorthy, Tribology International 57 (2013) 107–114.
[7] Y.H.Wei, B.S.Liu, L.F.Hou, etc, Journalof Alloys and Compounds, 2006, 452:336-342.
[8] J.W.Ren, A.D.Shan, J.B.Zhang, etc, Materials Letters, 2006, 60: 2076-2079.
[9] S. Jelliti, C. Richard, D. Retraint, T. Roland, M. Chemkhi, C. Demangel, Surface & Coatings Technology 224 (2013) 82–87.
[10] J.J. Jacobs, N.J. Hallab, R.M. Urban, M.A. Wimmer, J. Bone Joint Surg. Am. 88 (Suppl.2) (2006) 99.
[11] X. N. Peng, H. Z. Guo, T. Wang, Z. K. Yao, Materials Science and Engineering A 533 (2012) 55–63.
[12] T. Wang, H.Z. Guo, Y.W. Wang, X.N. Peng, et al., Mater. Sci. Eng. A 528 (2011)2370–2379.

Innovative Preparation of Nano-sized WC/W$_2$C/W Functionally Graded Material (FGM)

Xiaona Ren[1], Min Xia[1*], Qingzhi Yan[1], Changchun Ge[1*]

[1] *Institute of Nuclear Energy and New Energy System Materials, School of Materials Sciences and Engineering, University of Science and Technology Beijing (USTB), Beijing100083, China.*
Corresponding author: Tel: +86-01062334951; E-mail: xmdsg@ustb.edu.cn (Min XIA), ccge@mater.ustb.edu.cn (Chang-chun GE)

Abstract

Functionally gradient material (FGM) is considered as a kind of non-uniform composite functional materials, which is composition-graded or/and structure-graded. Here we first proposed an innovative technology for preparing a kind of nano-sized FGMs, namely WC/W$_2$C/W graded nanorods with diameters of 50nm and less, which consist of WC, W$_2$C and W from the outside to its core. Ammonium metatungstate was encapsulated into the hollow core of nanostructured carbon with hollow macroporous core/mesoporous shell, and then it was reduced in H$_2$ and converted to tungsten nanowire. Through heat treatment at 1300ºC, tungsten in the tube reacted with the carbon shell. Similar to carburization, the outer sphere of nanorod received more carbon and WC formed. And deeper along the radical direction, carbon became less, therefore W$_2$C formed, while tungsten in the core could not react with carbon. Hence the WC/W$_2$C/W graded nanorods formed.

Keywords: WC/W$_2$C/W graded nanorods, mesoporous carbon, graded materials, cemented carbides

1. Introduction

The concept of functionally graded materials (FGMs) was first proposed in Japan to develop ultraheat-resistant materials [1]. Since than FGMs have been worldwide studied by researchers in the fields of metals, ceramics or organic composites to improve physical properties of composites [2]. One of the important applications of FGMs is to lower the sintering temperature of cemented carbide. As known to all that cemented carbides are considered as one of the most important powder metallurgy materials, as they possess excellent mechanical properties and are applied in industry as cutting tools, wear resistance parts, machine components, rock or oil drilling, or press-stamping dies, etc. [3][4]. However, because of the low atomic self-diffusion coefficients, the cemented carbides should be sintered at high temperature and long sintering time, which would enlarge the grain-size. For most cases, metallic binder like Co was applied for the sintering, but the binder phase would lower the hardness of cemented carbides [5]. Therefore, it is a problem to lower the sintering temperature and keep the mechanical properties of cemented carbides at the same time. As known to all, due to the size effects, nano-sized powder always presents special properties, one of them is the much lower melting point than the bulk one [6][7]. Therefore, another way to solve the sintering problem of cemented carbides is to lower the particle size, namely using size graded powder to sintering cemented carbides.

On the other hand, for the hard materials, low toughness is another fatal problem, especially for the cemented carbides. Since, good ductility is very important for cemented carbides in industry. Besides, it is known to all that hardness of the conventional cemented carbides almost determines its wear-resistance [8]. Hence, is there a kind of material which not only could lower the sintering temperature of cemented carbides but also could improve its toughness and keep its mechanical properties at the same time? As for the brittle materials, nanowires are supposed
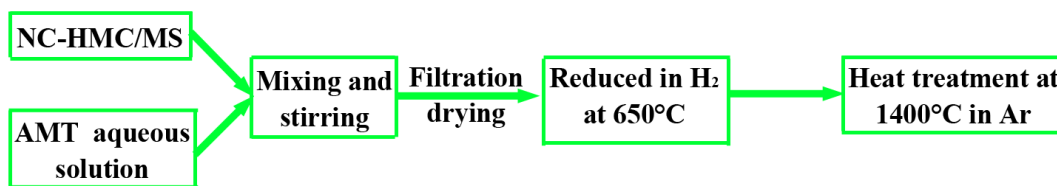
Figure 1. Scheme of the proposed preparation method

to be one of the ideal reinforce phases [9], so introduce tungsten carbide nanowires may solve the issue mentioned before.

It has been reported that tungsten carbide has three crystalline phases: WC, W2C and WC1-x [10]. Among them, W2C is harder than WC [11]–[13] and W2C/WC coating is harder than WC coating[14][15]. Therefore, WC coated W2C nanowires may be the ideal materials for cemented carbides. For the W2C or WC particles, it has been reports that they could be prepared by intermittent microwave heating[16], electron beam induced deposition [17], eutectic solidification [18], electro discharge [19], chemical synthesis [20], temperature-programmed carburization [21][22] or carbothermal reduction[23][24], etc. However, large scale and nano-sized WC or W2C is still hard to be prepared, and nano-sized graded WC/W2C has not been reported as far as we know.

What's more, tungsten carbide is supposed to be excellent green catalyst [10][16][25], but due to the same reason large-scale, nano-sized and shape controllable tungsten carbide is hardly to be prepared. Herein, we proposed a simple method to prepare WC/W2C/W graded nanorods which used nanostructured carbon with hollow macroporous core/mesoporous shell as template.

2. Experiments

Hydrophilic groups modified nanostructured carbon with hollow macroporous core/mesoporous shell (NC-HMC/MS) was first dispersed into the ammonium metatungstate (AMT) aqueous solution. After stirring at room temperature for about 24h, the black solid-liquid mixture was separated through filtration. The obtained black powder was dried in oven for about one night.

The as obtained black powder was AMT encapsulated into the hollow core of NC-HMC/MS. As in most cases the WC or W_2C was obtained from the reaction of W and C, so first of all the AMT should be reduced into tungsten. Hence the black powder was put into Al_2O_3 boat and pushed into the center of quartz tube in the furnace. By reducing at 650ºC in H_2 for 2h, the obtained black powder was tungsten nanowire in NC-HMC/MS. The last step to prepare the WC/W_2C/W graded nanorods was to heat treat the black powder at 1300ºC in Ar for 2h. Scheme of how to prepare WC/W_2C/W graded nanorods was shown in Fig.1

Field emission scanning electron microscopy (FESEM), transmission electron microscopy (TEM) and X-ray diffraction (XRD) were applied to characterize the obtained graded nanorods.

Along with the preparation of WC/W_2C/W graded nanorods, its catalyst activity also has been demonstrated. O-phenylenediamine (OPD) and H_2O_2 were used to detect the peroxidase-like activity of WC/W_2C/W graded nanorods. The photographs and UV absorbance were recorded.

3. Results and discussion

Since the NC-HMC/MS was modified with hydrophilic groups, it could encapsulate materials from water like a capsule or tubular container. However, as shown in Fig.2a, most of the NC-HMC/MS was not side opened, so materials in water should be encapsulated via the mesoprous in the shell (insert of Fig.2a), which is about 4nm (arrows marked in insert of Fig.2a). The mesoporous in shell allow materials fill in the tube by capillary action, as shown in Fig.2, AMT has filled up the tube of NC-HMC/MS and formed nanorods. Length of the nanorods were more than 2μm, and its diameter is circa few tens nanometer which is limited by the diameter of NC-HMC/MS. After reduction in H_2, the AMT nanorods converted to tungsten nanowires as shown in Fig.2c. Because of the size
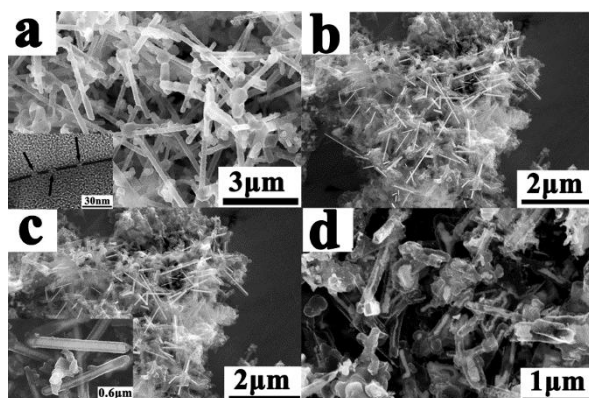
Figure 2. FESEM images of NC-HMC/MS (a), encapsulated AMT (b), tungsten nanowires (c) and WC/W$_2$C/W graded nanorods
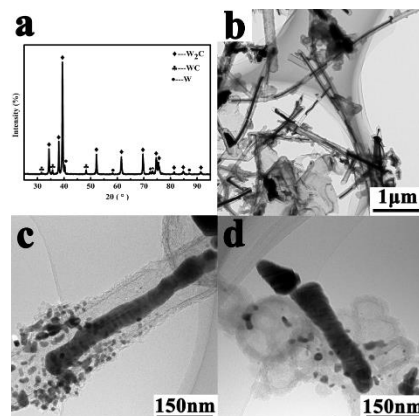
Figure 3. XRD result of the obtained graded nanorods (a), and TEM images of the sample (b), (c) and (d)

and shape confine of NC-HMC/MS, tungsten nanowires formed rather than tungsten nanodots. Again, the growth of tungsten was subjected to the size of NC-HMC/MS, so as shown in the insert of Fig.2.c, diameter of the tungsten nanowires was about dozens nanometer, and the length of AMT nanorods was kept too.

As tungsten and carbon would react at high temperature, the tungsten nanowires within NC-HMC/MS were heat treated at 1300 ℃ in Ar for 2h. After the heat treatment, still black powder obtained and the micro-morphology was kept with nanorods as shown in Fig.2d. The final product has kept the size and shape of its precursor, which must be attributed to NC-HMC/MS.

As aforementioned, the inside tungsten nanowires will react with the carbon shell at high temperature. However, since the carbon react with the inside tungsten is like the way of carburization, so the not all of the tungsten will react with carbon by the same way. That is outer tungsten of the nanowire will receive more carbon, while inner along the diameter direction tungsten will obtained less and less carbon, and at the center of the nanowire, tungsten even could not get any carbon to react. So, from the outside to center of the obtained back powder, it should be WC, W$_2$C and W in order. As the XRD result shown in Fig.3d, the black powder was mainly consisted of W$_2$C, and WC is slightly more than W. The XRD results proved the react mechanism discussed before. From the TEM images, we can clearly see that the WC/W$_2$C/W graded nanorods were confined in the hollow core of NC-HMC/MS and with diameter of circa 50nm.

As shown in Fig.4 the obtained WC/W$_2$C/W graded nanorods showed peroxidase-like activity. Interestingly, the WC nanodots were prepared by the same way of the preparation of WC/W$_2$C/W graded nanorods but with different reaction conditions, the details were shown in our other works. From the UV absorbance results and the photos, we can see that the obtained WC/W$_2$C/W graded nanorods possess peroxidase-like activity and the catalyze efficiency is much higher than WC nanodots.
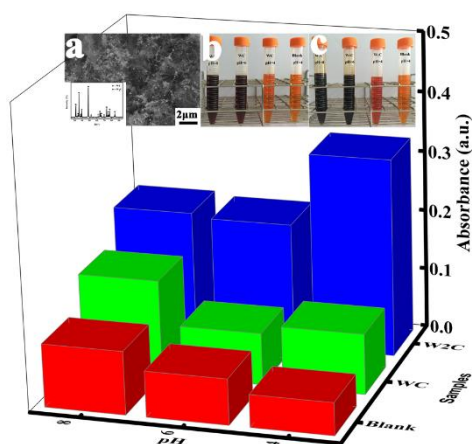
Figure 4. UV absorbance of the catalytic reaction, FESEM of WC nanodots (inserts a), photos of WC catalyzed (insert b) and WC/W$_2$C/W graded nanorods catalyzed

Finally, since the proposed method would not be affected by scale, so how much NC-HMC/MS is dispersed into the AMT solution, how much precursor could be obtained and nearly the same scale of WC/W$_2$C/W graded nanorods would yiled.

4. Conclusion

Utilizing the reaction of W and C at 1300ºC, WC/W$_2$C/W graded nanorods were prepared in NC-HMC/MS. Water soluble AMT was first encapsulated into the hollow core of NC-HMC/MS, and then reduced to W. Due to the confine of NC-HMC/MS, the tungsten nanowires formed. During the heat treatment at 1300ºC in Ar, the carbon shell became react with encapsulated W through infiltration. Since the outer side of W nanowire could react with more C than the inner one, so WC, W$_2$C and W formed along the direction from outer to its center. The formed WC/W$_2$C/W graded nanorods were with diameter of about 50nm. Due to the confine of NC-HMC/MS, the shape of nanorod was kept and the size of graded nanorod was confined within 50nm. The obtained WC/W$_2$C/W graded nanorods showed excellent peroxidase-like activity. Besides, by this simple method, large-scale WC/W$_2$C/W graded nanorods could be prepared for the industry application. Finally, there is still much more work should be done about the mechanical properties of the graded nanorods and the effect of its doping to cemented carbides.

References

[1]   M. Koizumi, M. Niino, MRS Bull. 1995, 20, 19.
[2]   A. Mortenson, S. Suresh, Int. Mater. Rev. 1995, 40, 239.
[3]   M. Eriksson, M. Radwan, Z. Shen, Int. J. Refract. Met. Hard Mater. 2013, 36, 31.
[4]   D.D. Phuong, P. Van Trinh, L. Van Duong, L.D. Chung, Ceram. Int. 2016, 42, 14937.
[5]   H. Taimatsu, S. Sugiyama, Y. Kodaira, Mater. Trans. 2008, 49, 1256.
[6]   J.R. Groza, Int. J. Powder Metall. 1999, 35, 59.
[7]   C. Han, H. Choi, B. Kim, Met. Mater. Int. 2013, 19, 1035.
[8]   I. Konyashin, B. Ries, D. Hlawatschek, Y. Zhuk, A. Mazilkin, B. Straumal, F. Dorn, D. Park, Int. J. Refract. Met. Hard Mater. 2015, 49, 203.
[9]   W. Yang, H. Araki, C. Tang, S. Thaveethavorn, A. Kohyama, H. Suzuki, T. Noda, Adv. Mater. 2005, 17, 1519.
[10]   W.-L. Dai, J. Ding, Q. Zhu, R. Gao, X. Yang, Catal. Vol. 28 2016, 28, 1.
[11]   S.M. Evans, Wear Resistant Drill Bit, Google Patents2002.
[12]   D. Tu, S. Chang, C. Chao, C. Lin, J. Vac. Sci. Technol. A 1985, 3, 2479.
[13]   T.N. Oskolkova, IOP Conf. Ser. Mater. Sci. Eng. 2015, 91, 12019.
[14]   G. Fisher, T. Wolfe, M. Yarmuch, A. Gerlich, P. Mendez, ResearchGate n.d.
[15]   B.H. Kim, D.S. Suhr, Mater. Trans. 2001, 42, 833.
[16]   H. Meng, P.K. Shen, J. Phys. Chem. B 2005, 109, 22705.
[17]   D. Spoddig, K. Schindler, P. Rödiger, J. Barzola-Quiquia, K. Fritsch, H. Mulders, P. Esquinazi, Nanotechnology 2007, 18, 495202.
[18]   Y. Sun, H. Cui, S.X. Jin, C.X. Wang, J. Mater. Chem. 2012, 22, 16566.
[19]   M.R. Shabgard, A.F. Najafabadi, Adv. Powder Technol. 2014, 25, 937.
[20]   U. Kanerva, J. Lagerbom, M. Karhu, A. Kronlöf, T. Laitinen, E. Turunen, Int. J. Refract. Met. Hard Mater. 2015, 50, 65.
[21]   J.-S. Moon, Y.-W. Lee, S.-B. Han, K.-W. Park, Int. J. Hydrog. Energy 2014, 39, 7798.
[22]   Z. Wu, Y. Yang, D. Gu, Q. Li, D. Feng, Z. Chen, B. Tu, P.A. Webley, D. Zhao, Small 2009, 5, 2738.
[23]   C. Liang, F. Tian, Z. Li, Z. Feng, Z. Wei, C. Li, Chem. Mater. 2003, 15, 4846.
[24]   X. Shi, H. Yang, P. Sun, G. Shao, X. Duan, X. Zhen, Carbon 2007, 45, 1735.
[25]   C. Moreno-Castilla, M.A. Alvarez-Merino, F. Carrasco-Marín, J.L.G. Fierro, Langmuir 2001, 17, 1752.

Effect of Number of Layers on the Ballistics Performance of Functionally Graded Sandwich Plates

M. Aydin[1], M. K. Apalak[2], Z. G. Apalak[3]

[1]*Department of Aeronautical Engineering, Erciyes University, Kayseri 38030, Turkey, aydin@erciyes.edu.tr*
[2]*Department of Mechanical Engineering, Erciyes University, Kayseri 38030, Turkey, apalakmk@erciyes.edu.tr*
[3]*Department of Mechanical Engineering, Erciyes University, Kayseri 38030, Turkey, apalakz@erciyes.edu.tr*

Abstract

In this study the damage and deformation mechanisms of functionally graded sandwich plates (FGSPs) which have different layer numbers have been investigated and their performances were compared to each other under ballistics impact loadings. The functionally graded sandwich plate is composed of a mixture of ceramic (SiC) and metal (Al) phases, at a ratio of which is determined by a power-law distribution of the volume fraction. In order to investigate the ballistic performance of FGSPs, a gas gun test system and 0.3 caliber fragment simulating projectiles (FSP) were used. Functionally graded sandwich plates were manufactured by means of the powder stacking-hot pressing method, Their ballistic tests were performed and, contrary to common literature, it was concluded that number of layers in FGSPs has an insignificant effect on the ballistic performance.

Keywords: Functionally graded materials (FGMs), Ballistic performance, Sandwich plates

1. Introduction

Further developments in the design of weapons based on kinetic or chemical energy have mandated the new evolved light and high performance armors. A new idea of material design has concentrated on mechanically functional materials. FGMs are composed of at least two constituents and have continuous composition variation along one or more directions. In general, the most common constituents are ceramic and metal materials whose combinations of their superior properties, such as the toughness, heat resistivity, hardness, can be quite suitable for overcoming the hard, high temperature service environments. FGMs have been applied successfully in specific areas such as space, nuclear, and automotive industries and become an indisputable candidate for defense industries due to their good strength against structural and thermal loadings as well as their advantages in ballistic applications. Therefore, the mechanical responses under ballistic loadings and the material characterization of the functionally graded materials have become a broad research field in last decade [1-3].

2. Experimental Procedure

2.1. Production and design of functionally graded sandwich plates

A functionally graded sandwich plate has a graded layer composed of ceramic and metal constituents between top and bottom metal layers (Fig 2.). Each layer has its own ceramic volume fraction which obeys a power law. The volume fractions of ceramic V_c and metal V_m in the body satisfy the relation

$$V_m + V_c = 1 \qquad\qquad (1)$$

The volume fraction of metal constituent through the plate thickness is defined as

$$V_m(z) = \left(1 - \frac{z}{h}\right)^n \tag{2}$$

where h is plate thickness, and n is exponent value adjusting the composition variation. The FGS plates manufactured for this study embodied a linear volume fraction change (n=1) through the functionally graded region.

In general, functionally graded materials are manufactured via initially obtaining a functionally graded body with powder metallurgy methods and then sintering it [4,5]. The functionally graded sandwich plates used in this study were manufactured with powder stacking-hot pressing method. Functionally graded regions of plates manufactured in four different layer numbers: 5, 10, 15 and 20 layers. Required ceramic and metal amounts for each layer of a sandwich are calculated by the mixture theorem. Volumetric ratios regarding all layers of each FGSP are given in Figure 2. The test specimens were produced a diameter of 90 mm and a thickness of 20 mm. An average of 10 micron-aluminum 6061 powder and an average of 50 micron-silicon carbide powder were used as metal and ceramic constituents, respectively. Homogeneously mixtured powder was laminated under low pressure in the sintering die, sintered in a hot press unit within argon atmosphere under 100 MPa pressure at 600ºC for 90 minutes, and then cooled in the die under controlled pressure.

2.2. Ballistic test system

In order to investigate ballistic performance of FGSPs, a gas gun test system and 0.3 caliber fragment simulating projectiles were used. Specimen plates were fixed to inside of the target chamber, and then shots were conducted. In this study, four different plates were used for testing: 5,10, 15 and 20 layers FGSPs and their layer thicknesses are 3.2 mm, 1.6 mm, 1.06 mm and 0.8 mm respectively. In the ballistic tests, two specimens for each configuration were used and each specimen was used only for one shot. The speed of the bullets used in the tests was measured averagely as 710±5 m/s with optic sensors. For the same type specimen, similar deformations were observed, that it is a good indicator for repetability.

3. Ballistic test results

By designing test procedure as defined above and after conducting shots, no perforation observed at all specimens. Figure 1 and 2 illustrates front and rear surface deformations and penetration and swelling depths under impact of the 0.3 caliber fragment simulating projectile. From the figures, we can conclude that number of layers through the functionally graded region didn't play a substantial role on the projectile penetration depth. More interestingly, an increase in number of layers leaded a slight and insignificant increase in penetration. A similar conclusion can be deduced for swelling depth at the rear surface. Furthermore, from the point of view of interlayer delamination, we observed the least interlayer delamination occured at the plate that have five layers in the graded region.

4. Conclusions

The ballistic tests of the specimens having 5, 10, 15 and 20 functionall graded layers were performed and their penetration and perforation behaviors as well as deformation characteristics were investigated. This study clearly showed that adding more layers through graded region of FGSPs doesn't promise a significantly better ballistic performance. In fact, thick ceramic rich front layers exhibit a more succesful ballistic protection.

References
[1] W. Gooch, B. Chen, M. Burkins, R. Palicka, J. J. Rubin, R. Ravichandran, Development and ballistic testing of a functionally gradient ceramic/metal applique, Materials Science Forum 308 (1999) 614–621.
[2] E. S. C. Chin, Army focused research team on functionally graded armor composites, Materials Science and Engineering: A 259 (1999) 155–161.
[3] S. Quek, V. Lin, M. Maalej, Development of functionally-graded cementitious panel against high-velocity small projectile impact, International Journal of Impact Engineering 37 (2010) 928–941.
[4] B. Kieback, A. Neubrand, H. Riedel, Processing techniques for functionally graded materials, Materials Science and Engineering: A 362 (2003), 81–106.
[5] M. Zhou, J. Xi, J. Yan,Modeling and processing of functionally gradedmaterials for rapid prototyping, Journal of Materials Processing Technology, 146 (2004), 396–402.
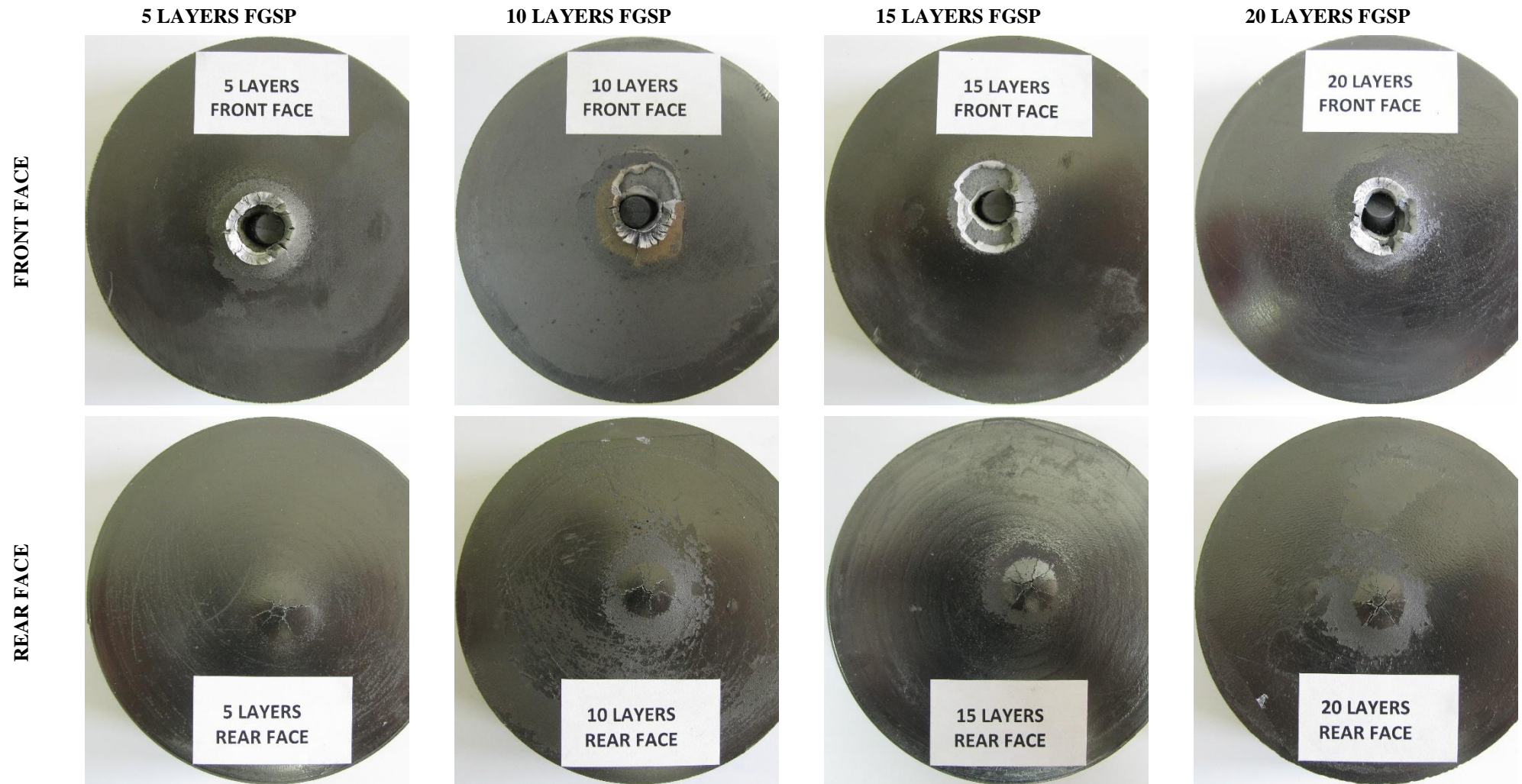
Figure 1. Front and rear-faces deformations caused by a 0.3 caliber fragment simulating projectile.
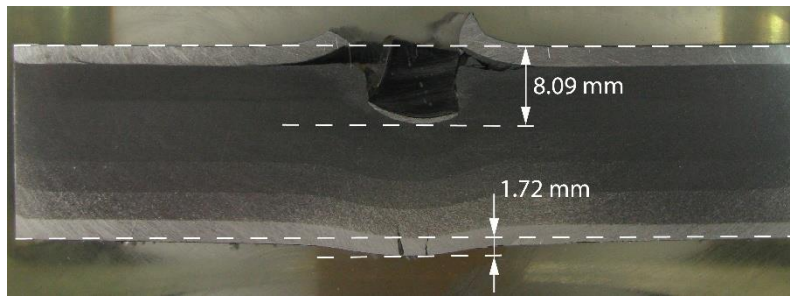
5 Layers Functionally Graded Sandwich Plate
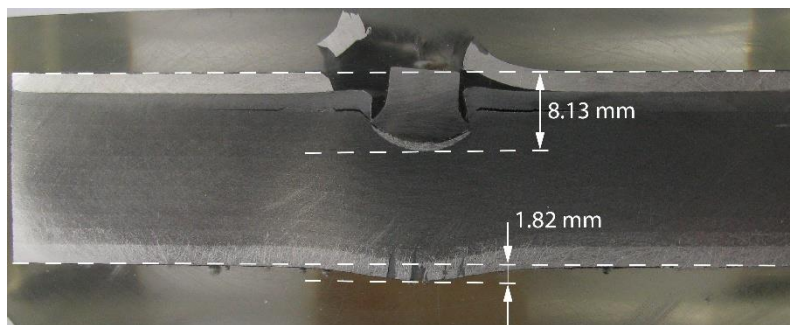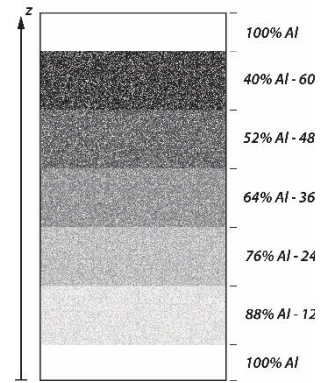
10 Layers Functionally Graded Sandwich Plate
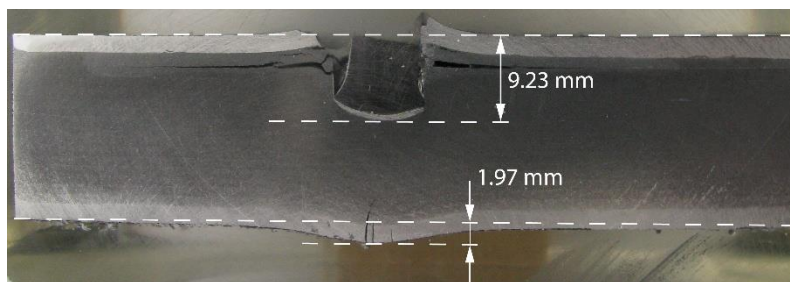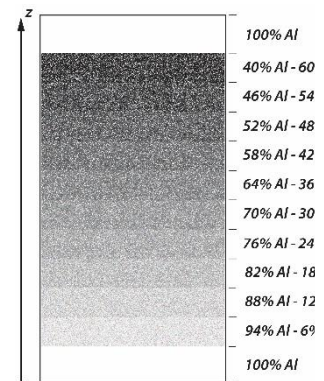
15 Layers Functionally Graded Sandwich Plate
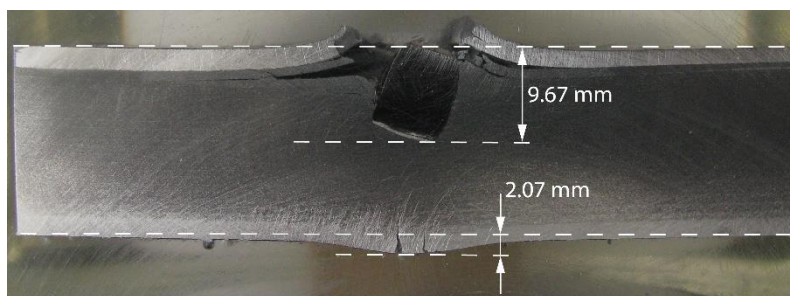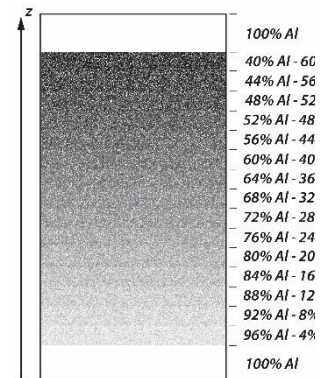
20 Layers Functionally Graded Sandwich Plate
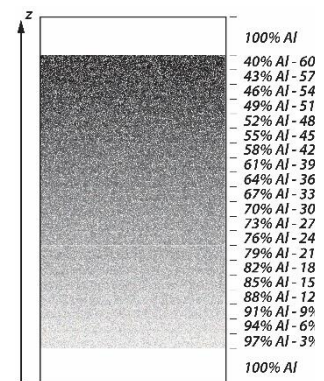
Figure 2. Penetration depth and diameter of tested plates and volumetric ratios of ceramic and metal for all layers of each FGS plates.

Poster

Change in mechanical characterization according to the addition of graphene in functionally graded Cu-ZnO manufactured through spark plasma sintering

Kawngjae Park[1], Jehong Park[2], Seungchan Cho[3], Akira Kawasaki[4]
Kwonhoo Kim[1], Hansang Kwon[1,2]

[1]*Pukyong National University, pkj3678@naver.comrichter*
[2]*Next-Generation Materials Co., Ltd.(NGM), ngm01@ngm.re.kr*
[3]*Korea Institute of Materials Science, sccho@kims.re.kr*
[4]*Tohoku University, kawasaki@material.tohoku.ac.jp*

Abstract

We fabricated a 5-layer functionally graded material using spark plasma sintering, with Cu and zinc oxide (ZnO) powder as the raw materials. The layers comprised 100vol% ZnO, 25vol% ZnO-Cu, 50vol% ZnO-Cu, 75vol% ZnO-Cu, and 100vol% Cu, which were sintered at 700 °C and 50 MPa for 5 min. To obtain a graphene-adapted functionally gradient material (FGM), we added 0.1wt% graphene to each layer and used a hand mill to mix the layers for 30 min, followed by sintering under the same conditions. The mechanical properties of the fabricated FGM bulk materials were analyzed using an optical microscope and a Vickers hardness tester. Thus, we easily fabricated non-sinterable materials that are expected to be applicable in various fields.

Keywords: Spark plasma sintering, Graphene, Mechanical properties, Nanocomposite, Functionally graded materials.

1. Introduction

Functionally gradient materials (FGMs) were proposed in 1984 by material scientists in the Sendai area of Japan as a means of preparing thermal-barrier materials [1–7]. FGM is a novel concept for the realization of innovative properties and/or functions that cannot be achieved with conventional homogeneous materials [1–7]. In its simplest structure, an FGM consists of one material on one side, a second material on the other, and an intermediate layer whose structure, composition, and morphology vary from one material to the other, at the micron level [2, 5]. The FGM was proposed to prepare a new composite by using heat-resistant ceramics on the high-temperature side and tough metals with a high thermal conductivity on the low-temperature side, with a gradual compositional variation from ceramic to metal [1, 5]. Thus, FGMs are composite materials with microscopically inhomogeneous characteristics [1]. The continuous changes in the microstructure of an FGM distinguish it from conventional composite materials [1]. The continuous change in composition results in gradients in the properties of FGMs [1]. There are many methods for fabricating FGMs, such as spark plasma sintering (SPS), chemical vapor deposition, ion plating, ion mixing, plasma spraying, electrodeposition, and powder metallurgy. We employed an SPS process to easily fabricate a non-sinterable bulk material, similar to metal-ceramic materials [4, 6]. Then, we analyzed the effect of adding graphene to a fabricated FGM on the Vickers hardness of the material.
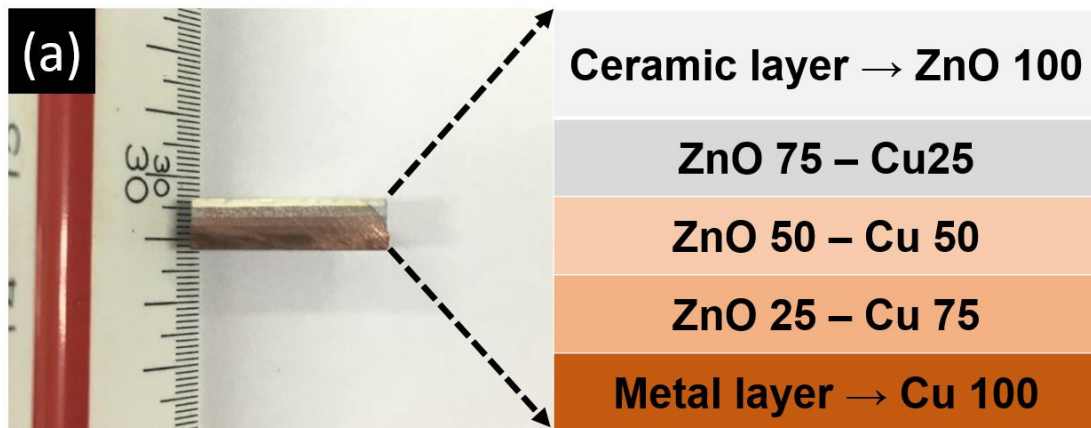
Fig. 1. Cu-ZnO FGM and a mimetic diagram showing the composition of each layer

2. Experimental

Cu powder and ZnO powder were used as raw materials for sintering metal-ceramic materials. The composition of the layers was 100vol% ZnO, 25vol% ZnO-Cu, 50vol% ZnO-Cu, 75vol% ZnO-Cu, and 100vol% Cu. The two raw materials were prepared via ball milling for 30 min at 200 rpm in air. Then, the mixed powder was placed into a graphite mold. The graphite mold was installed in an SPS machine (Fuji Electronic Industrials Co., Ltd., SPS-321Lx, Japan). The powders were sintered at 700 °C and 50 MPa for 5 min. The size of the fabricated Cu-ZnO FGM sample was 15 mm. To obtain a graphene-adapted FGM, we added 0.1wt% graphene to each layer and used a hand mill to mix the layers for 30 min, followed by sintering under the same conditions. The mechanical properties of the fabricated FGM bulk materials were analyzed using an optical microscope (LEICA DM500, LEICA Microsystems (Schweiz) AG) and a Vickers hardness tester (HM-101, Mitutoyo Corporation, Japan). We tested each layer five times and calculated the average.

3. Results and discussions

Fig. 1 shows the cutting plane of the Cu-ZnO FGM fabricated by SPS. As shown in the mimetic diagram on the right side of the figure, the FGM comprised 100vol% ZnO in the upper layer and 100vol% Cu in the lowest layer. This diagram confirms that the mixtures were clearly layered on each other. To examine the cutting plane in detail, we used an optical microscope. Fig. 2 shows an optical microscope image of the cutting plane of Cu-ZnO. Here, as with Fig. 1, each layer is clearly identified. To investigate the effect of graphene reinforcement on the Vickers hardness of the Cu-ZnO FGM, each layer was investigated using a micro Vickers hardness tester.

Fig. 3 shows the Vickers hardness of each layer. When graphene was not added to the Cu-ZnO FGM, ZnO exhibited the highest Vickers hardness. Cu exhibited a lower Vickers hardness than ZnO. As shown in Fig. 3, when the ZnO content was 0 to 50vol%, the Vickers hardness decreased, but when the ZnO content was greater than 50vol%, the Vickers hardness rapidly increased. In the case of the graphene-reinforced Cu-ZnO FGM, all the layers exhibited an increasing Vickers hardness except for the 100vol% ZnO layer. Graphene is the strongest material ever tested, with an intrinsic tensile strength of 130 GPa and Young's modulus of 1 TPa [8]. It is widely used as reinforcement because of its favorable properties [8]. In this study, we investigated two strengthening mechanisms, as follows. First, the graphene acts as a pinning point. In a general grain-growth process, the dislocation moves around in the matrix of the material. However, graphene functions as a pinning point, inhibiting the movement of dislocations [9, 10]. Consequently, the growth of the grain boundary was inhibited and the size of the grains was reduced, strengthening the material. Second, the high speed of the SPS process guarantees a strengthening effect. In the SPS process, the nucleation time is decreased, which inhibits the growth of the grain boundary, strengthening the material. On the other hand, the ceramic layer (100vol% ZnO) exhibited a decreasing Vickers hardness when graphene was added. In future research, we will investigate how the fabricated Cu-ZnO FGM can be strengthened via various mechanisms, such as the Hall-Petch formula, the shear-lag model, the Orowan–Ashby model, and thermal mismatch [11–14].

❖ **Graphene not added**
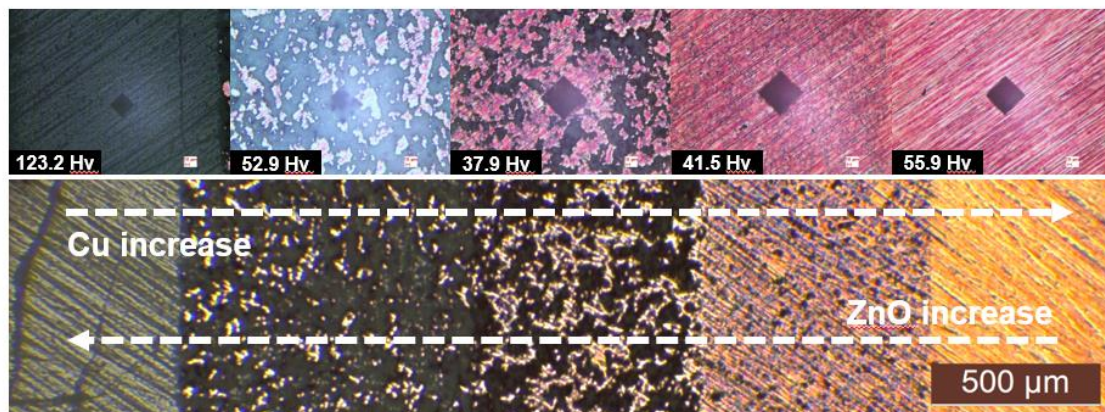
❖ **Graphene added**
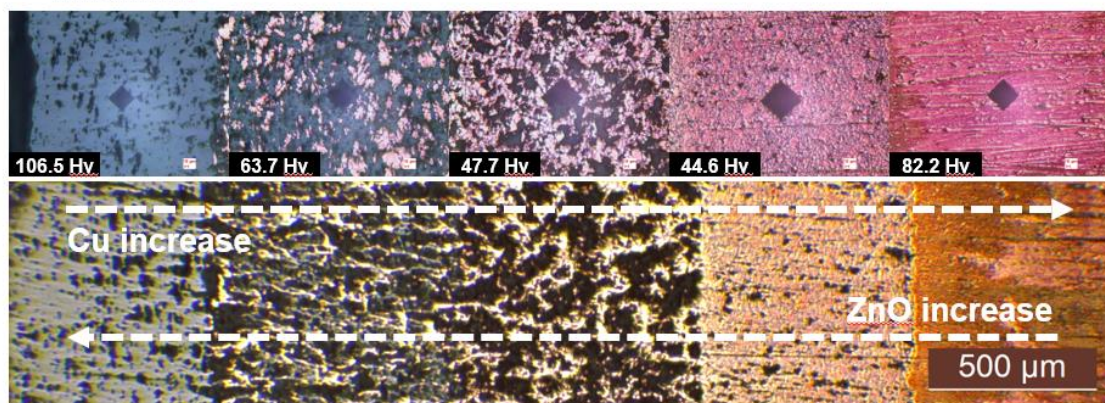
Fig. 2. Vickers hardness and optical microscope images of the Cu-ZnO FGMs with and without graphene
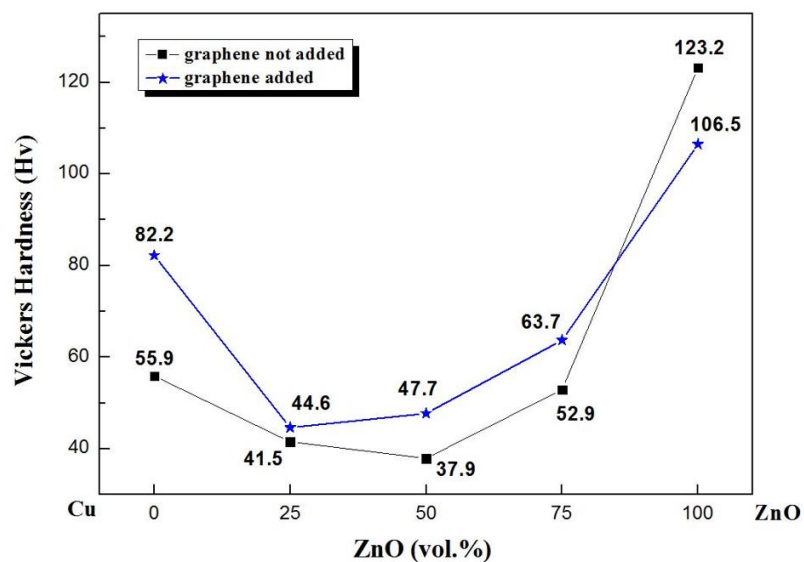
Fig. 3. Vickers hardness with respect to ZnO content with and without graphene added

4. Conclusion

Metal-ceramic composite materials are known as non-sinterable materials, but the results for a bulk Cu-ZnO FGM fabricated by SPS show that the matrices were successfully joined together. This suggests that other non-sinterable materials can easily be fabricated via SPS. In this study, the Vickers hardness of the metal matrix increased when graphene was added, but that of the ceramic (100vol% ZnO) matrix decreased. To investigate this phenomenon, we need more professional and specialized experiment. Metal-ceramic bulk composite materials fabricated through this construction method are expected to be applicable in various fields of industrial engineering.

Acknowledgements

References

[1] M. Koizumi, Composites Part B, 28B (1997), 1-4
[2] A. Kawasaki, R. Watanabe, Ceram. Int., 23 (1997), 73-83
[3] H. Kwon, M. Leparoux, A. Kawasaki, J. Mater. Sci. Technol., 30 (2014), 736-742
[4] J. Park, K. Park, J. Kim, Y. Jeong, A. Kawasaki, H. Kwon, Sci. Rep., 6 (2016), 23064
[5] H. Kwon, C. R. Bradbury, M. Leparoux, Adv. Eng. Mater., 13 (2011), 325-329
[6] W. Y. Lee, D. P. Stinton, C. C. Berndt, F. Erdogan, Y.-D. Lee, Z. Mutasim, J. Am. Ceram. Soc., 79 (1996), 3003-3012
[7] M. Koizumi, M. Niino, MRS Bull., 20 (1995), 19-21
[8] C. Lee, X. Wei, J. W. Kysar, J. Hone, Science, 321 (2008), 385-388
[9] Y. Chen, X. Zhang, E. Liu, C. He, Y. Han, Q. Li, P. Nash, N. Zhao, J. Alloys Compd., 688 B (2016), 69-76
[10] H. Kwon, M. Estili, K. Takagi, T. Miyazaki, A. Kawasaki, Carbon, 47 (2009), 570-577
[11] R. George, K. T. Kashyap, R. Rahul, S. Yamadagni, Scr. Mater., 53 (2005), 1159-1163
[12] X. Long, Y. Bai, M. Algarni, Y. Choi, Q. Chen, Mater. Sci. Eng. A, 645 (2015), 347-356
[13] L. Kurmanaeva, T. D. Topping, H. Wen, H. Sugahara, H. Yang, D. Zhang, J. M. Schoenung, E. J. Lavernia, J. Alloys Compd., 632 (2015), 591-603
[14] M. Li, H. Zhai, Z. Huang, X. Liu, Y. Zhou, S. Li, C. Li, J. Alloys Compd., 628 (2015), 186-194
[15] C. Varvenne, A. Luque, W. A. Curtin, Acta Mater., 118 (2016), 164-176

Reactive Texturing of Y-TZP and Ce-TZP in Magnetic Field

O. Van der Biest[1], D. Vriami[1], E. Beaugnon[2]

[1]Department of Materials Engineering, K.U.Leuven, Kasteelpark Arenberg 44, Heverlee, Belgium
[2]Laboratoire National des Champs Magnétiques Intenses (LNCMI), Grenoble, France

Abstract

Tetragonal zirconia powder cannot be aligned by applying a strong magnetic field during green forming of a powder compact. In prior work we have shown that a strong texture can be achieved in 3Y-TZP by using a reactive texturing technique. One uses a suspension that contains monoclinic zirconia that can be oriented in a strong field during green forming for instance by slip casting. The monoclinic (100) plane is oriented perpendicular to the magnetic field direction. When a mixture of pure monoclinic zirconia powder and 8 mol% yttria co-precipitated zirconia is used, a strong texture of single phase 3Y-TZP is obtained after reactive sintering for 3 hrs at 1650°C. The (001) plane of the tetragonal phase is perpendicular to the magnetic field direction, i.e., the c-axis is aligning parallel to the field. In the strong magnetic field of 17.4 T used in the present work, the texture of the cast green ceramic, can be measured (Lotgering factor f = 0.15) whereas at lower fields texture in the green body is barely discernible. After sintering a Lotgering factor of 0.8 is measured. More detailed analysis of the texture showed a texture index of 32.5.

We attempted to texture Ce-TZP by a similar strategy but with less success. The suspension consisted of a mixture of monoclinic zirconia and nanometric ceria powder. Orienting the monoclinic zirconia particles during slip casting was again clearly achieved with a Lotgering factor of 0.3. calculated from the monoclinic reflections again with the (100) plane normal to the magnetic field. After reactive sintering a single phase tetragonal microstructure is formed if the sintering temperature is chosen high enough. However the resulting Lotgering factor for the 001 reflections was only 0.3 and a texture index of about 3 was measured.

It appears that for successful reactive texturing of zirconia the differences in composition between the monoclinic phase and the phase containing the stabilizing element should be as small as possible.

Si$_3$N$_4$-CMC reinforced with compositionally graded carbon fibers

Christian Richter[1], Karina Mees[1], Monika Willert-Porada[1], Victor Heyer[2], Achim Schmidt-Rodenkirchen[3]

[1]*Chair of Materials Processing, University of Bayreuth, Germany, Christian.richter@uni-bayreuth.de*
[2]*Graduate School 1229, University of Bayreuth, Germany*
[3]*InVerTec e.V., Bayreuth, Germany*

Abstract

Attempts to further improve the high temperature mechanical performance of sintered and in-situ β-Si$_3$N$_4$ fiber reinforced Silicon Nitride ceramic by addition of short carbon fibers as strengthening element independent of in-situ formation of the elongated β -Si$_3$N$_4$-inclusions were not very successful so far. The main obstacles are the mismatch of thermal expansion coefficient (CTE) between C-fiber and Si$_3$N$_4$ – tensile stress builds up at the fiber-matrix interface due to higher CTE of the Si$_3$N$_4$ ceramic - and reactions between Carbon, Oxide additives and Silicon Nitride at sintering temperature. Two processing strategies were mainly followed in the past: infiltration of a carbon template with Si$_3$N$_4$-ceramic precursor followed by pyrolysis of the precursors, and low temperature hot pressing of powder derived C-Si$_3$N$_4$-CMC's. As a new approach, we synthesize compositionally graded C-SiC-Si$_3$N$_4$-coatings on short carbon fibers and consolidate the fibers with the ceramic powder by hot pressing. The matrix powder consists of commercial Si$_3$N$_4$ powder (HC Starck) and in-house synthesized Yb$_2$SiO$_5$ as sintering additive [1,2].

The fibers are coated by Silicon via CVD deposition of Silicon in a fluidized bed reactor. As precursor Silane, SiH$_4$ or Trichlorosilane, HSiCl$_3$ (TCS) are utilized. With TCS as precursor Plasma Enhanced atmospheric pressure CVD is applied while with Silane thermal CVD conditions are used. Transformation of Silicon into SiC and Si$_3$N$_4$ proceeds by subsequent heating of the Si-coated fibers in Nitrogen atmosphere, up to 1500°C at 1 atm N$_2$. The relative thickness of SiC:Si$_3$N$_4$ layers depends upon the morphology and thickness of the original Silicon coating, which is itself strongly depending upon the choice of Si-precursor and CVD reaction conditions as well as fluidized bed process parameters.

In the paper the different Si-coating morphologies obtained from different variants of CVD-coating are discussed with respect to specific surface and reactivity for formation of SiC as well as Si$_3$N$_4$. The phase composition is analyzed by XRD and Raman spectroscopy while the compositional gradients are studied on cross sections of the coated fibers using SEM-EDX and Monte Carlo simulations. The achievable compositional gradients are compared with results of thermodynamic calculations.

[1] M. Knoll, M. Willert-Porada, Synthesis of porous silicon nitride ceramic with a compositional Gradient, Materials Science Forum Vols. 631-632 (2010) pp 477-482. doi:10.4028/www.scientific.net/MSF.631-632.477
[2] P. Pontiller, M. Willert-Porada, High Temperature Behavior of Si$_3$N$_4$ and Yb$_2$SiO$_5$ Coated Carbon Fibers for Silicon-Nitride CMC, Advanced Engineering Materials 16(5), May 2014

Keywords: CVD, fibre reinforced silicon nitride, coating, CMC

Development of a functional glass having antimicrobial activity, non-irritant and low ion elution via silver or copper ion exchange technique

Gyu-In Shim, Seong-Hwan Kim, Se-Young Choi

Department of Materials Science and Engineering, Yonsei University, 50 Yonsei-ro, Seodaemun-ku, Seoul 120-749, Republic of Korea, sychoi@yonsei.ac.kr

Abstract

In this study, we aimed to evaluate the antibacterial and antifungal properties, skin irritation, and elution behavior of silver or copper ions with varying ion-exchanged conditions with respect to its application to display screens and glassware. $AgNO_3$ or $Cu(NO_3)_2$ powders were spread on both sides of aluminosilicate glass, and it was heated to 200–280 °C for 10 min. Under optimized heating conditions at 260 and 250 °C for 10 min, Ag or Cu ion-exchanged glasses showed 99.9% antimicrobial activity against *Escherichia coli*, *Staphylococcus aureus* and *Penicillium funiculosum*. Ag and Cu ions were found to be non-irritant in New Zealand white rabbits. The concentrations of Ag or Cu ions from ion exchanged glasses eluted in drinking water in 24 h at 100 °C were 0.351 µg L^{-1}, 5.654 µg L^{-1}, respectively, which were below the standard acceptable level. The transmittance of ion-exchanged glass was similar to that of parent glass. The antimicrobial activity, skin irritation, elution behavior, and transmittance of Ag or Cu films deposited on glass suggest that these films could be useful in household devices and display devices.

Keywords: antimicrobial activity, skin irritation, elution behavior, silver ion, copper ion

1. Introduction

In the last decade, the use of glassware, and of display screens in applications such as cellular phones and touch panels of medical devices, has risen quite significantly, and there have been many studies about the adverse effects of certain bacteria and fungi on the human body [1-3]. The reproduction of such potentially harmful microbes depends on environmental factors, such as temperature, humidity, and contamination (i.e., transfer of microbes between surfaces). In particular recent studies have suggested that Staphylococcus aureus (gram-positive) and Escherichia coli (gram-negative), which can cause dermatitis, pneumonia, and septicemia, have been detected on the glass surfaces of mobile phones. In addition, Penicillium funiculosum, the spores of which can cause asthma and rhinitis, has been found on display screens. In order to remove harmful bacteria and fungi, washing of product surfaces using isopropyl alcohol is encouraged, but this method does not confer long-lasting antimicrobial activity [4,5]. Therefore, products with potent antimicrobial activity and durability have recently been produced by incorporating Ag and Cu ions into the glass surface as nanosized particles, thus providing a large specific surface area.

However, in recent years there have been growing concerns about the use of metallic ions in materials, due to problems such as a reduced adhesive strength of thin films, skin irritation by eluted Ag or Cu ions, and mammalian cytotoxicity and genotoxicity. Ag ions have toxic properties in the human body, and so the World Health Organization (WHO) has restricted the maximum safe concentration of Ag ions to 100 µg L–1 (Cu ions to 2000 µg L–1). However, there have been only few studies relating to Ag or Cu ion elution from antibacterial glass

products. In this study, we aimed to evaluate the antibacterial and antifungal activities, skin irritation, and elution behavior of Ag- and Cu-ion exchanged glass.

2. Materials and methods

Sheets of aluminosilicate glass composed of 62.4 SiO$_2$–17.4 Al$_2$O$_3$–3.3 MgO–0.2 CaO–0.6 TiO$_2$–12.6 Na$_2$O–3.5 K$_2$O (wt.%) and 0.7 mm thick were used for ion exchange. High purity AgNO$_3$ and Cu(NO$_3$)$_2$ powders were used as the raw materials for ion exchange. AgNO$_3$ or Cu(NO$_3$)$_2$ powders were spread on both sides of aluminosilicate glass, and it was heated to 200–280 °C for 10 min. The antimicrobial activity of the ion-exchanged glass was evaluated against *E. coli*, *S. aureus*, and *P. funiculosum* on the basis of the ISO method 22196. The effect of the Ag and Cu ions on the surface morphology of microorganisms was confirmed by observing the shape of bacterial (*S. aureus*) cells grown on the glass before and after ion exchange using transmission electron microscopy (TEM). The potential for the Ag or Cu ion-exchanged glass to cause skin irritation was evaluated in accordance with the ISO 10993-10 method. Inductively coupled plasma (ICP) atomic emission spectroscopy was used to measure the elution of Ag or Cu ions from the ion-exchanged glass. To confirm whether the Ag and Cu ion concentration in drinking water meets the WHO guideline for maximum safe concentration (Ag 100 µg L^{-1}, Cu 2000 µg L^{-1}), the ion-exchanged glass was placed into drinking water (100 mL) and incubated at 100 °C in a water bath for 24 h.

3. Results and discussion

To make the antimicrobial activity on glass, alkali cations (Na$^+$) from the glass were exchanged with monovalent dopant cations (Ag$^+$ or Cu^{2+}), and then the penetration depth of Ag or Cu ions into the glass surface was confirmed. As a result, Ag ions increased from 2 to 22 µm as the ion-exchange temperature was raised from 250 to 280 °C. The Cu ions also increased from 1 to 5 µm as the temperature was raised from 230 to 260 °C. Figure 1 showed the transmittance of the Ag- and Cu-ion exchanged glass produced by heating at 230-280 °C for 10 min. At the increasing depth of Ag or Cu ion penetration, the transmittance decreased due to the increases the optical absorption. Generally, the transmittance of more than 90% is requared for the screens of display devices.

As shown in Figure 2, Ag or Cu ion-exchanged glasses produced by heating at 250-280 °C for 10 min showed 99.9 % antimicrobial activity against *E. coli*, *S. aureus*, and *P. funiculosum*. We also confirmed that the antimicrobial activity of *E. coli* was higher than that of other *S. aureus*, and *P. funiculosum*, as shown in Figure 3. Because, *S. aureus* have a thicker peptidoglycan layer and *P. funiculosum* cells are larger than the bacteria. Based on these findings and the responses of microbes shown in Figure 4, it was confirm that the Ag ion could lead to inactivation of the microbes. The Ag ions enterand produce oxidative stress in microbial cells, resulting in the retardation of cell recovery, a reduced growth rate, and eventual microbial cell death.

Ag and Cu ions were found to be non cytotoxic in New Zealand white rabbits. The concentration of Ag or Cu ions from thin films eluted in drinking water in 24 h at 100 °C was about 0.351 and 5.654 µg L^{-1}, respectively. Therefore, ion-exchanged glass met the safety limits for Ag or Cu elution into drinking water. The antimicrobial activity, skin irritation, elution behavior, and transmittance of Ag or Cu ion exchanged on glass suggest that these glasses could be useful in household devices and display devices.
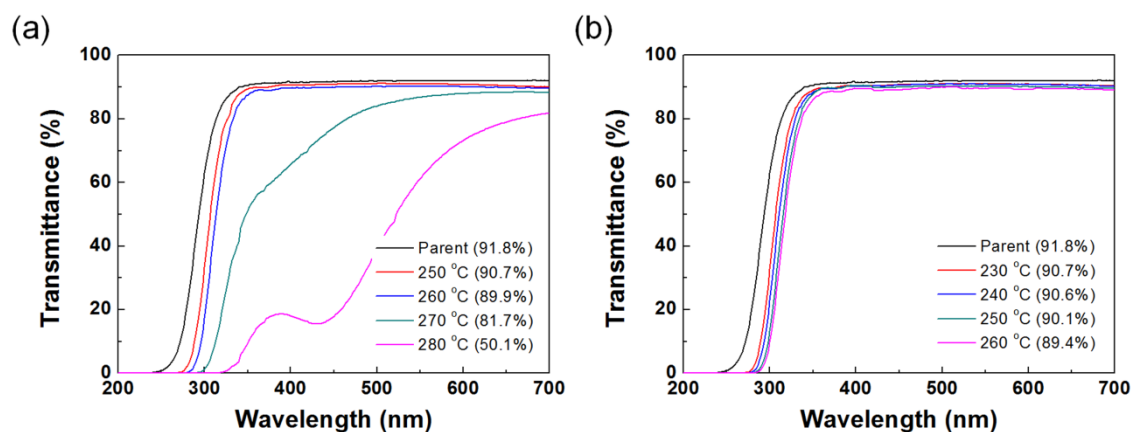
Figure 1: Transmittance of light wavelengths from 200 to 700 nm by parent and ion-exchanged glass varieties that were produced by heating at various temperaturesas for 10 min shown in the presence of (a) Ag-ion exchanged glass and (b) Cu-ion exchanged glass.
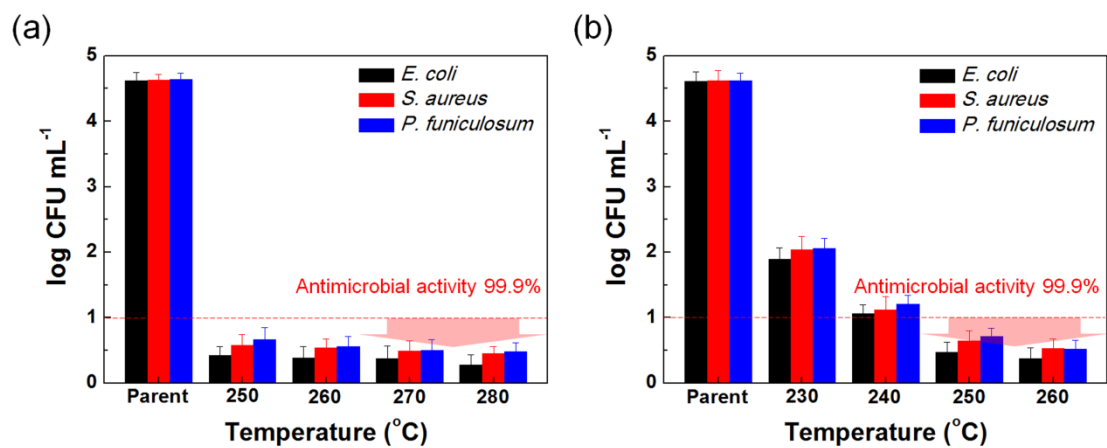
Figure 2: Antimicrobial activity results of the (a) Ag ion-exchanged glasses and (b) Cu ion-exchanged glasses produced by heating to various temperatures against *E. coli*, *S. aureus*, and *P. funiculosum*. Data values are expressed as the mean ± standard deviation of ten replicate tests.
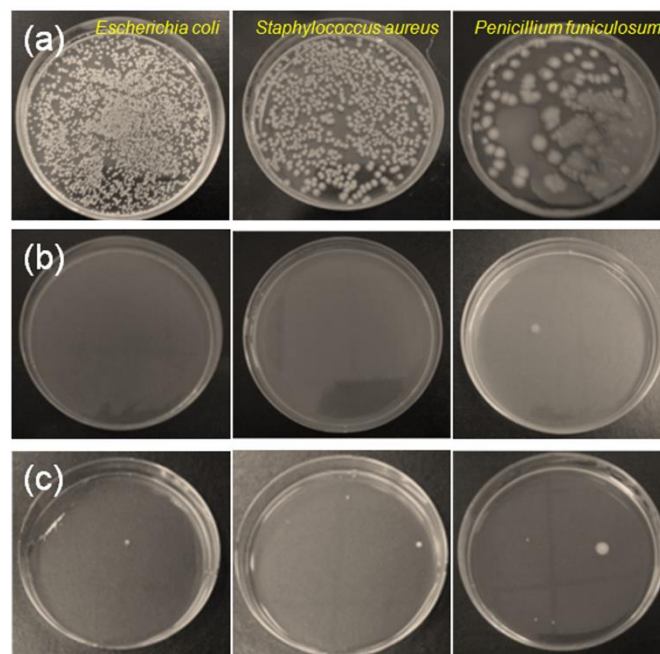
Figure 3: Photographs of bacterial colonies grown on plates of (a) diluted cell suspension mixture containing 10^4 CFU/mL, (b) Ag-ion exchanged glass at 260 °C for 10 min, (c) Cu-ion exchanged glass at 250 °C for 10 min against *E. coli*, *S. aureus*, and *P. funiculosum*.
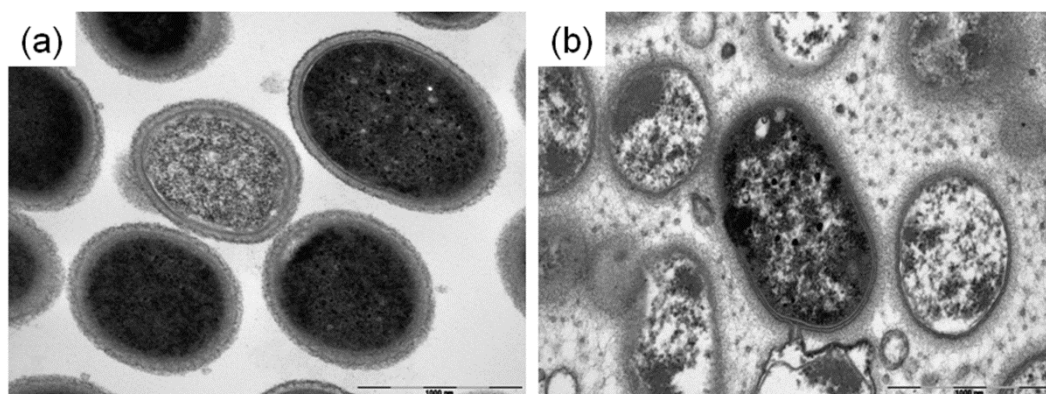
Figure 4: TEM micrographs of (a) untreated *S. aureus* bacteria, and (b) those treated with Ag-ion exchanged glass.

4. Conclusion

Glass was ion-exchanged via the spreading method using $AgNO_3$ and $Cu(NO_3)_2$ powder. Under optimized heating conditions at 260 and 250 °C for 10 min, Ag or Cu ion-exchanged glasses showed 99.9% antimicrobial activity against *Escherichia coli*, *Staphylococcus aureus* and *Penicillium funiculosum*. Ag and Cu ions were found to be non cytotoxic in experimental rabbits. The ion-exchanged glass met the safety limits for Ag or Cu elution into drinking water. Therefore, we developed a novel antimicrobial glass that satisfied all conditions required for use as a display screen, such as light transmittance (90%), antimicrobial activity (99.9%), skin irritation (non-irritant) and elution behavior (WHO guideline). These results suggest that this antimicrobial Ag and Cu ion-exchanged glass can be safely and effectively used for the production of glassware and display industry products such as mobile telephone screens and touch panels.

Acknowledgements

References

[1] Liu L, Liu T, Tade M, Wang S, Li X, Liu S., Enzyme and Microbial Technology, 67 (2014) 53–58
[2] Cheol-Young Kim, Yu-ri Choi, Kwang-Mahn Kim, Se-Young Choi, International Journal of Nanotechnology, 10 (2013), 643–652
[3] Prucek R, Tuˇcek J, Kilianová M, Panáˇcek A, Kvítek L, Filip J, et al., Biomaterials, 32 (2011) 4704–4713.
[3] Gyu-In Shim, Seong-Hwan Kim, Hyeng-Woo Eom, Se-Young Choi, Journal of Industrial Microbiology & Biotechnology, 42 (2015), 735–744
[4] Djeribi R, Boucherit Z, Bouchloukh W, Zouaoui W, Latrache H, Hamadi F, et al., Colloid Surf B 102 (2013), 540–545
[5] Gyu-In Shim, Seong-Hwan Kim, Hyeng-Woo Eom, Kwang-Mahn Kim, Se-Young Choi, Enzyme and Microbial Technology, 72 (2015), 65–71

Fabrication of lightweight and thin bulletproof materials satisfying protective capacity of NIJ level III using strengthened-glass by ion exchange

Gyu-In Shim[1], Seong-Hwan Kim[1], Jong-Kyoo Park[2], Se-Young Choi[1]

[1] *Department of Materials Science and Engineering, Yonsei University, 50 Yonsei-ro, Seodaemun-ku, Seoul 120-749, Republic of Korea, sychoi@yonsei.ac.kr*
[2] *Agency for Defense Development, Bugyuseong daero 488 beon gil, Yuseong-gu, Daejeon 305-152, Republic of Korea, pjkyoo@add.re.kr*

Abstract

This research aims to evaluate the ballistic impact resistance of strengthened glass/polymer composites for application in lightweight and thin bulletproof materials. The flexural strength of regular borosilicate glass increased 2.8 times from 0.241 to 0.835 GPa when the glass is strengthened by the ion exchange process using dispersed concentrated potassium nitrate powder for 10–20 minutes at 560 °C. The ballistic impact test was conducted using a M-16 bullet (5.56 mm diameter, 45 mm length). In the case of laminating the strengthened borosilicate glass, lightweight design transparent bulletproof material with the thickness of 17.05 mm mass per unit of 33.4 kg/m^2, V_{50} 870 m/s, and transmittance of 86.9% that satisfies the NIJ-0101.06 level III was produced. As a result, by laminating the strengthened borosilicate glass with two polycarbonate sheets, the thickness of the bulletproof material was decreased by about 40% from 28.25 to 17.05 mm. This work suggests the world's thinnest transparent bulletproof material by using a strengthened-glass/polymer composite, which can help widen the military applications such as armored vehicles, ballistic plates and helmets.

Keywords: transparent bulletproof material, borosilicate glass, ion exchange, ballistic impact test

1. Introduction

Bulletproof materials play an important role in the defence and civilian industries, and they are used for various applications such as vehicles, vessels, airplanes, ballistic plates and helmets and banking facilities [1,2]. Recently, the lightweight and thin bulletproof materials (e.g. military personnel visors, windows of armoured vehicles and warships) are required to overcome operational capability shortfalls on the battlefield. In order to manufacture thin and lightweight bulletproof material, the strengthened glass is essential. Therefore, when the parent glass in the bulletproof material is replaced with strengthened glass, the thickness of bulletproof material can be reduced. Borosilicate glass is suitable for manufacturing lightweight and thin products as it possesses excellent mechanical properties, low thermal expansion coefficient, and low density. Furthermore, as borosilicate glass has high transmittance in the visible light region, it is used in various applications such as protective windows and optical glass. However, more studies are necessary to improve the mechanical properties by securing the optimal ion exchange conditions of borosilicate glass according to various glass thicknesses. It is also necessary to study the transmittance of ion exchanged glass systematically for bulletproof materials. The purpose of the current study is to evaluate the effects of using strengthened borosilicate glass with thicknesses of 2-10 mm to possibly fabricate lightweight and thin bulletproof materials. A ballistic test was carried out according to NIJ standard (Level III) using live ammunition (5.56 mm M-16 bullet), and the transmittance was measured in the visible light range to determine whether the glass under study could be used to make transparent bulletproof materials.

Table 1: Lamination patterns of bulletproof materials with different types of the strengthened glass.

Specimen code	Material stacking sequence and thickness (mm)								Thickness (mm)	Weight (kg)	Areal density (Kg/m^2)
	G	PVB	MD	PVB	G	PU	PC	PE			
C-1. 17GMGP	10	0.7	0.2	0.7	3	0.1	2	0.35	17.05	3.01	33.41
C-2. 17GMGP	10	0.7	0.2	0.7	2	0.1	3	0.35	17.05	2.92	32.43

2. Materials and methods

To laminate the bulletproof materials, samples of borosilicate glass (Schott-Glas, Germany) with 2–10 mm thickness and 310×310 mm^2 area were prepared. After the entire surface of the glass was covered with KNO$_3$ powder in an alumina tray, the glass and KNO$_3$ powder were heated using an electric furnace at 560 °C for 10–20 min to ensure optimized ion exchange. The transmittance values of the ion exchanged glass and bulletproof materials were measured using an UV/VIS/NIR spectrophotometer (V-570, Jasco, Japan). The scan speed was 400 nm/min over a wavelength range from 200 to 800 nm. The Vickers hardness (H_V) and fracture toughness (K_C) of the parent and the strengthened glass surfaces were measured using a Vickers microhardness tester (MXD-CX3E, Matsuzawa, Japan). The three-point flexural strength (σ_f) was measured using a universal testing machine (H10K-C, Hounsfield, UK). Rectangular specimens 4 mm wide and 36 mm long with various thicknesses were tested. The lamination of bulletproof materials (Table 1) was carried out by using an autoclave (Autoclave KYL-15, Italmatic, Italy). The autoclave was preheated to 90 °C for 1 h and the bulletproof materials were laminated in the autoclave at 130 °C for 3 h. According to NIJ standard-0108.01 (level III), V_{50} of the M-16 bullet must be over 838 ± 15 m/s from a distance of 15 m. Following the MIL-G-5485 standard, the required transmittance depending on the thickness of bulletproof material is confirmed.

3. Results and discussion

As shown in Figure 1, the mechanical properties of the parent and the chemically strengthened borosilicate glasses were evaluated according to the time of ion exchange at 560 °C.

As a result, the Vickers hardness, fracture toughness, and flexural strength of the strengthened borosilicate glass with thickness of 2, 3, 8 and 10 mm exhibited maximum values at 560 °C for each duration of 10, 12, 15 and 17 min, respectively, and increasing the thickness of the glass slightly improved the mechanical properties. The mean ion exchange rate of potassium ions of the borosilicate glass that exhibited the best mechanical performance was 3.0 ± 0.8 μm/min at 560 °C. Therefore, this information is useful for modifying the mechanical properties according to the depth of the compressive stress layer.

The light transmittance of the parent and ion-exchanged borosilicate glass is shown in Figure 3, for glass thicknesses of 2, 3, 8, and 10 mm. Increasing the ion exchange time slightly decreased the transmittance because the penetration depth of the potassium ions increased and, as a result, a compressive stress layer was formed, which increased the index of refraction. Nevertheless, because the transmittance of the strengthened glass was more than 90.9%, it can be applied to transparent bulletproof materials. Figure 3(c) shows the transmittance of two bulletproof materials at a thickness of 17.05 mm. For use as a MIL-standard transparent ballistic material, a transmittance
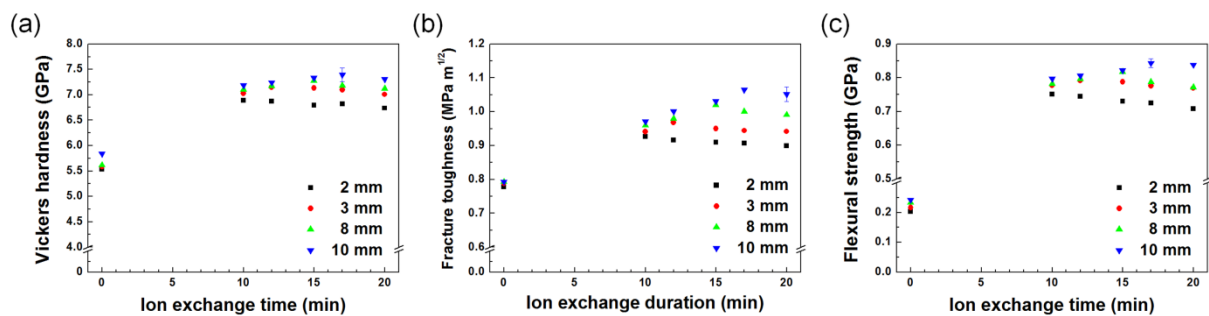
Figure 1: Mechanical properties of the parent and strengthened borosilicate glass at 560 °C with different holding times (air cooling process): (a) Vickers hardness, (b) fracture toughness, (c) three-point flexural strength.
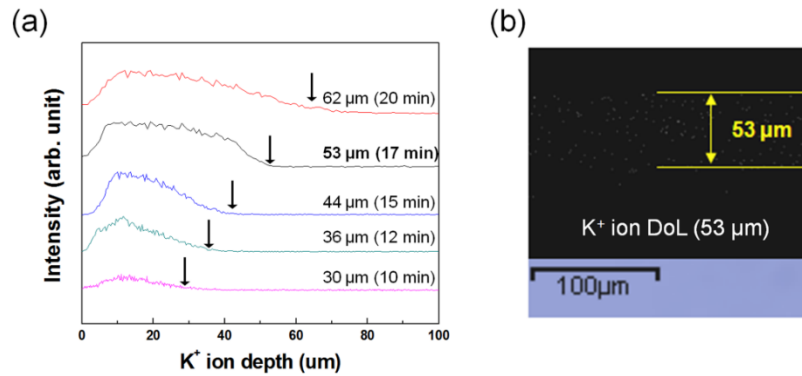
Figure 2: (a) Penetration depth profile of the potassium ions with various ion-exchanged times (10–20 min). (b) EDS mapping analysis of the potassium ions at the optimized ion exchange conditions at 560 °C for 17 min.
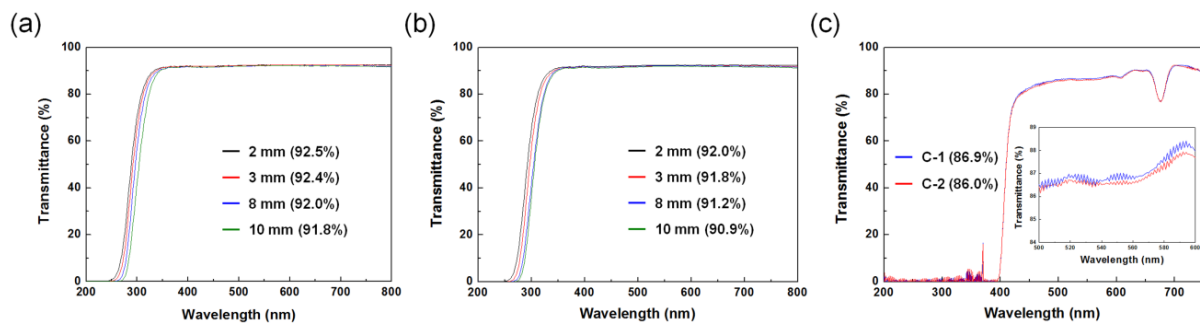
Figure 3: Transmittance with various thicknesses of (a) parent and (b) ion-exchanged borosilicate glasses at the optimized ion exchange conditions at 560 °C. (c) Transmittance of bulletproof materials at a thickness of 17.05 mm.

exceeding 79% at a thickness of 17.05 mm is necessary. Both types of bulletproof material using laminated ion-exchange strengthened glass provide light transmittance exceeding 86.0%, permitting their use as transparent ballistic materials.

The 17GMGP (C-1) bulletproof material shown in Figure 4(a), which was laminated with one PC sheet (2.0-mm thick), one MD film, and two layers of strengthened glass. The V_{50} value of the C-1 bulletproof material was found to be 869.9 m/s, which was slightly higher than that of the bulletproof material of 28.25-mm thick [1]. The 17GMGP (C-2) bulletproof material shown in Figure 4(b), which was laminated with one PC sheet (3.0-mm thick), one MD film, and two layers of strengthened glass. The C-2 type, fragments of the second bullet with a speed of 867.8 m/s penetrated the material, showing as ruptures in the Al witness plate (V_{50} 863.8 m/s). The V_{50} value of the 17GMGP bulletproof material was also slightly higher than that of the bulletproof material of 28.25-mm thick [1]. This is because, the use of thicker glass (10-mm thick) having a high impact resistance was better than the addition of several thin glasses or PC sheets.

4. Conclusion

The flexural strength, fracture toughness, and Vickers hardness of the strengthened borosilicate glass with thickness of 2, 3, 8 and 10 mm exhibited maximum values at 560 °C for each duration of 10, 12, 15 and 17 min, respectively, and ion exchange rate of potassium ions was about 3.0 ± 0.8 μm/min at 560 °C. The V_{50} value of the 17GMGP bulletproof material was found to be 869.9 m/s, which was higher than that of the bulletproof material of 28.25-mm thick (850.0 m/s). As a result, by laminating the strengthened borosilicate glass with two polycarbonate sheets, the thickness of the bulletproof material was decreased by about 40% from 28.25 to 17.05 mm. Therefore, the 17GMGP bulletproof material was found to have the most effective design while being both thin and lightweight due to higher specific energy absorption (0.62-0.63 J/g) than others.
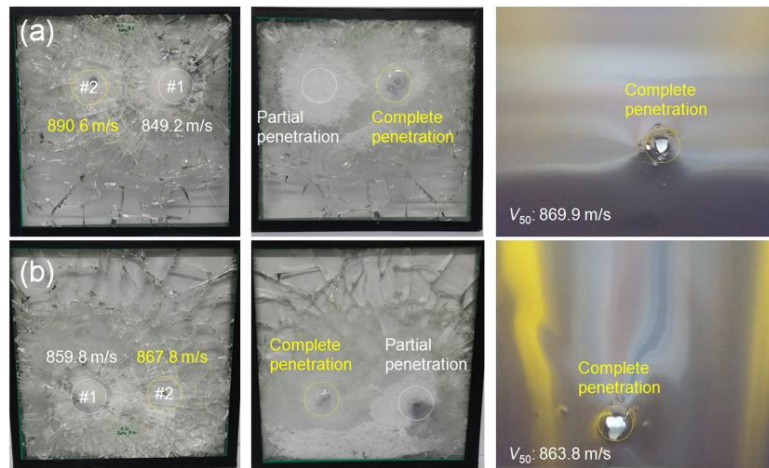
Figure 4: Photographs of the front and back faces and Al witness plate with impact velocity (m/s) of the bulletproof material: (a) 17GMGP (C-1) and (b) 17GMGP (C-2) samples after ballistic test.

Acknowledgements

References

[1] Gyu-In Shim, Hyeng-Woo Eom, Seong-Hwan Kim, Jong-Kyoo Park, Se-Young Choi, Composites Part B, 69 (2015), 44-49

[2] Shim GI, Choi SY. Strengthening method of borosilicate glass, and borosilicate glass strengthened by the same. Korea Patent Application No. 1015380530000, 2015.

Fabrication of functionally graded materials with a high melting point difference for extreme environment application

Zhangjian Zhou , Lin Shi, Changchun Ge

School of Materials Science and Engineering, University of Science and Technology Beijing, Beijing 100083, zhouzhj@mater.ustb.edu.cn

Abstract

Many engineering applications require functionally graded materials (FGM) composed with materials with high melting point difference. But it is difficult to fabricate such FGM, because there is no overlap of sintering temperature ranges between the composed materials. In this paper, fabrication such kind of FGMs with a full compositional distribution (from pure high melting point material to pure low melting point material) by a novel one-step fast sintering technology named as resistance sintering under ultra-high pressure was reviewed and discussed. The sintering of two kinds of typical FGMs was investigated. They are metal/metal FGMs (such as W/Cu and W/Fe FGM) and ceramic/metal FGMs (such as Al_2O_3/Cu FGM). The relative density of the FGMs reached higher than 97% without the addition of any sintering additives only after 1 minute sintering. Microstructure analysis showed that the good grading composition of all FGMs has been obtained, which indicated that the designed composition distribution of the FGM can be preserved very well.

Keywords: FGM, high melting point difference, resistance sintering, ultra-high pressure

1. Introduction

Nowadays, the rapid developments of aerospace and advanced energy industry require components with properties that vary with location in the part for extreme high temperature environments applications. Such extreme environments usually need components that must perform at radically different temperatures at different location in the parts, namely, one side of the component can service in high temperature with complicated particle or heat flux loading, while the other side of the component need very good heat dissipation ability and cooling effect. Functionally graded materials (FGMs), which possess gradients in properties such as high temperature strength or high thermal conductivity, are a potential solution to address these requirements [1, 2].

Usually for the components apply in the extreme high temperature environment, the side facing high temperature needs materials with high melting point, such as refractory metal or ceramic, while the other side needs materials with good thermal conductivity and machinability for effective cooling, usually this kind of material is metal with low melting point, such as Cu. Thus, the development of FGM composed with materials with high melting point difference (hereinafter referred to as HMPD-FGM) is highly interesting. However, the large melting point difference also means there is no overlap of the sintering temperature ranges between these two materials. This makes it difficult to fabricate such FGMs with a full compositional distribution (from 0% to 100%). A logical fabrication method is to form a high melting point material (hereinafter referred to as HMPM) skeleton with graded open pores fist, then perform the infiltration of low melting point materials (hereinafter referred to as LMPM) into the pores. However, it is not easy to fabricate the graded HMPM skeleton which is easy to shrink and distort, especially, it is difficult to acquire a pure HMPM layer with high density. In the author's laboratory, a novel one step sintering technology, named as resistance sintering under ultra-high pressure (RSUHP) has been developed to fabricate HMPD-FGMs[3-6]. In the present work, the related works are reviewed and discussed.

Table 1: Typical materials for HMPD-FGM fabrication

Materials	Melting point (℃)	TC (Wmk)	CTE (10-6/℃)	Purity (%)	Powder size (μm)
W	3410	~ 170	~ 4.5	≥99.5	1~3
Al2O3	2015	~ 20	~ 6.8	≥99.5	1~3
Cu	1083	~ 390	~ 16.5	≥99.5	-200 mesh
Fe	1535	~ 54	~ 17	≥99.5	-200 mesh

2. Materials and Experiments

The typical HMPM usually should show feature of high temperature strength, erosion resistance, low coefficient of thermal expansion (CTE), but low ductility, such as W, Al2O3, while the typical LMPM are mainly metal with good thermal conductivity (TC) and good machinability, but high CTE, such as Cu. According to the composed materials, HMPD-FGMs can be divided into two types: metal/metal FGMs (such as W/Cu and W/Fe FGM) and ceramic/metal FGMs (such as Al2O3/Cu FGM). Table 1 lists the typical materials for HMPD-FGM.

Fig.1 shows the process of RSUHP. HMPM powders and LMPM powders are mechanical mixed with different volume ratios according to the composition design. The mixed powders with different compositions together with two pure materials powders are stacked, layer by layer, and cold pressed in a steel mould to form a green compact with a diameter of 20 mm and a height of 6 mm. For example, for a 6-layered FGM, it includes pure HMPM layer, 80% HMPM +20% LMPM layer, 60% HMPM +40% LMPM layer, 40% HMPM +60% LMPM layer, 20% HMPM +80% LMPM layer and pure LMPM layer, all were volume fraction. The green compact was encapsulated in a pyrophyllite sleeve to form a sample assembly. The sample assembly was sintered in a special experimental setup. The device consists of a pressure vessel, associated electronic system and mechanical press system. First, the mechanical compressive pressure was cubic quasi-isostatic loaded on the FGM green compact, then the alternating current (A.C.) is applied to the sample and the sample was heated mainly by Joule heating. The most important sintering parameters for RSUHP are pressure, power, and current application time. The typical sintering conditions is with pressure of 6-9 GPa, power of 10-20 kW, sintering time less than 1 min [3-6].

3. Results and discussion

3.1. Metal/metal FGMs

Metal/metal HMPD-FGMs can be divided into two types according to the reactivity of the two composed materials. W-Cu is a kind of typical pscudo-alloy. There is no solid solution and reaction between W and Cu. Fig.3 shows the macrophotograph of the sintered 6-layered W/Cu FGM and its cross section backscattering SEM image, in which the W component is white and the Cu is black. Both pictures show a good composition transition. The interfaces between layers are clear and no obvious pores or cracks. This reveals that there has no obvious composition migration during the short sintering time. The relative density of the FGM and pure W layer were higher than 97 % and 96% respectively. The hardness of pure W layer reached more than 500 Hv.

Fe is an important element for structure materials. For W and Fe, brittle intermetallic compounds based interface phases are easy formed during high temperature sintering. A 5 layered W/Fe FGM was fabricated by RSUHP. Fig. 3 shows the W/Fe interface morphology of the 50%W-50%Fe layer in the FGM. Form the left picture it can be
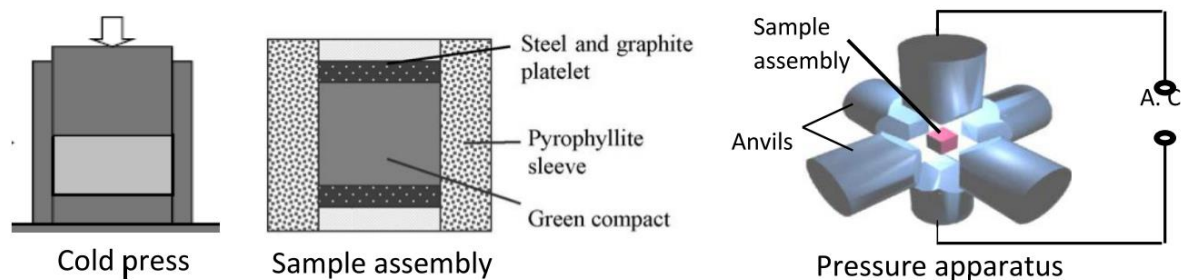
Fig. 1: Flow chart of RSUHP
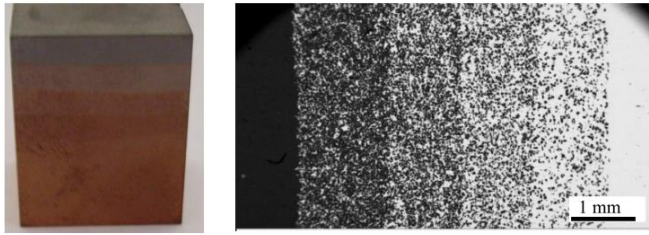
Fig. 2: Macrophotograph and SEM cross section morphology of W/Cu FGM
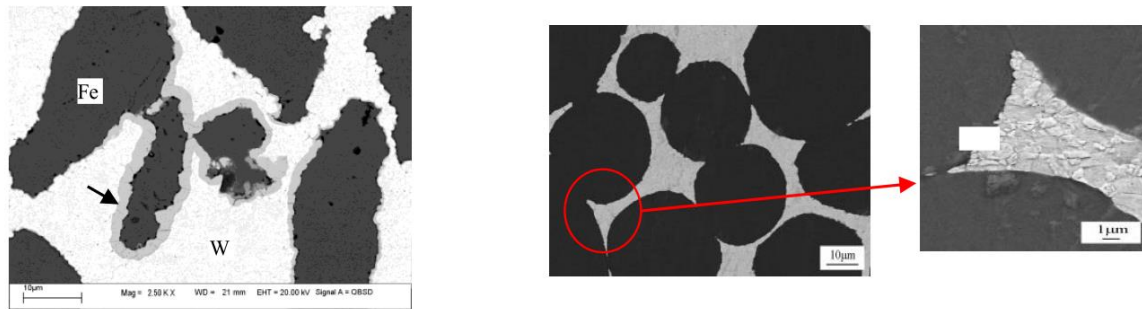
Fig.3: The interface between Fe and W, with reaction layer (left) and without reaction layer (right)
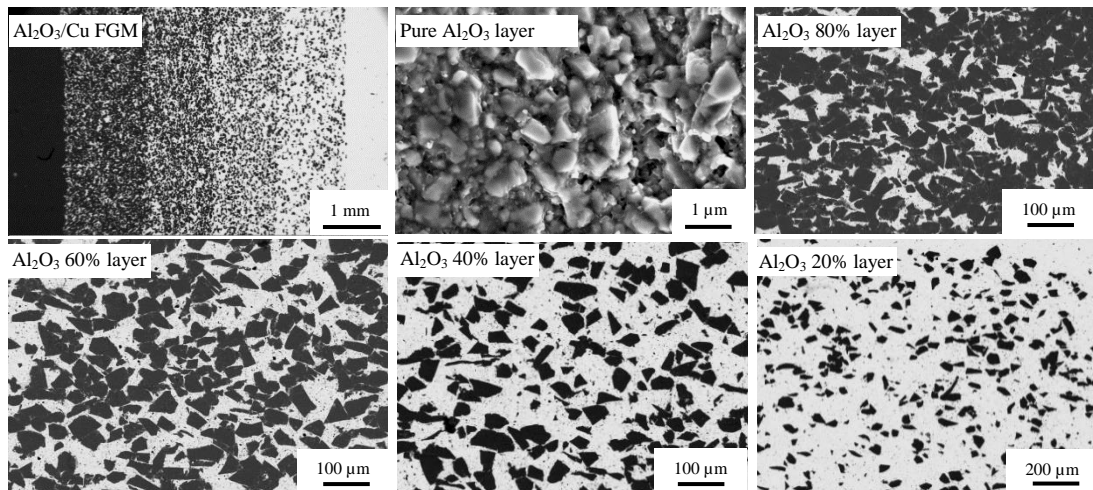
Fig. 4: SEM cross section morphology of Al2O3/Cu FGM, overview and each layers

seen that obvious interface phase formed between W and Fe particles. The phase is Fe7W6 according to EDS and XRD results. But after optimizing the sintering parameters (mainly adjust the power from 12kW to 10kW), the interface phase can be avoided, as seen in the right picture.

3.2 Ceramic/metal FGMs

A six layered Al_2O_3/Cu FGM was fabricated by RSUHP. Fig. 4(a) shows the overview cross-sections SEM morphology of the FGM, a good graded compositional transition can be found. This reveals there had no macro compositional migration during short time sintering. For pure ceramic layer, as shown in Fig. 4(b), it is obvious that ultra-fine Al_2O_3 has been sintered and bonded well together. The average particle size remained about 3μm and no obvious grain growth was observed. In the $Al_2O_3$80Cu 20 layer, isolated Cu particles are dotted in Al_2O_3 matrix just same in the $Al_2O_3$20Cu80 layer, where Al_2O_3 particles are dispersed in the Cu matrix. To the Al_2O_3-60Cu and Al_2O_3-40Cu layers, Cu and Al_2O_3 show a net distribution, but obvious holes can be found.

3.3. Desensification Analysis

When ultra-high pressure was brought to FGM green compact, it can be supposed that particle rearrangement, plastic distortion and sliding will occur quickly in the green compact, especially in the LMPM particles due to its excellent plasticity. Thus a very high density will be obtained especially on the LMPM rich part. But there still have a lot of close pores in the HMPM particles due to its brittle and high hardness thus lacks of plastic deformation and sliding under ultra-high pressure.

When a high voltage is put on the green compact, it can be found that the current is very small at first, then increase along the sintering time. This shows that as the resistance of HMPM are much larger than that of LMPM, the temperature of HMPM would increase quickly due to its high resistivity and simultaneously, surface diffusion would occur to form a neck between particles. The particle size of HMPM powders should be very fine for decreasing the sintering time temperature. At the same time, LMPM would produce very little Joule heat due to its low resistivity, but a mass part of heat would be conducted from HMPM to it owing to its high TC. Based on the above analysis, we can deduce that according to their distinct resistivity difference between two materials, it can be expected that a gradual resistance distribution and thus an elevated temperature zone will be constructed when strong current passes through the FGM green compact. The highest temperature is at HMPM side where Joule heat is generated and the lowest temperature is at LMPM side where heat was transferred by conduction from the other side. For decreasing the sintering time and sintering temperature of HMPM, ultra-high pressure and fine powder are needed, for avoiding the migration of LMPM, very fast sintering time is necessary.

4. Conclusion and outlook

Different kind of FGM composed with high melting point different materials were fabricated by RSUHP in a very short sintering time. The composition design can be maintained very well. Interface reaction can be avoided by choosing proper sintering conditions. Both FGMs and pure high melting point materials layer reached high sintered density. RSUHP is fundamentally different from the conventional sintering, which involves ultra-high pressure consolidation followed by resistance heating. RSUHP is a volumetric heating involving conversion of electric energy into thermal energy, which is instantaneous, rapid and highly efficient, thus time and energy savings. RSUHP has major potential, and real advantages over conventional heating for fabrication of heterogeneous materials with designed structure.

This research is just at the early stages, and it will be a long time before the exact mechanisms and the science behind RSUHP are elucidated. So far, this approach is not attractive for larger parts which require enormous presses that make them noncompetitive. More accurate quantitative modeling of the high pressure compaction process and pressure assisted resistance sintering needs development in the future.

Acknowledgements

References

[1] Beth E. Carroll, Richard A. Otis, John Paul Borgonia, Jong-ook Suh, R. Peter Dillon, Andrew A. Shapiro, Douglas C. Hofmann, Zi-Kui Liu, Allison M. Beese, Acta Materialia 108 (2016) 46-54
[2] Ankit Gupta, Mohammad Talha, Progress in Aerospace Sciences 79(2015) 1-14
[3] Zhangjian Zhou, Juan Du, Shu-xiang Song, et al. Journal of Alloy and Compound, 428(2007): 146-150
[4] Zhangjian Zhou, Changchun Ge, 475-479(2005): 1475-1478
[5] Thomas Weber, Zhangjian Zhou,Dandan Qu, Jarir Akta. Journal of Nuclear Materials, 414 (2011) 19-22
[6] Dandan Qua, Zhangjian Zhou, Jun Tan, Jarir Aktaa, Fusion Engineering and Design 91 (2015) 21-24

Workshop Supplemental Materials

The LaserCUSING® Process

Dr.-Ing. Peter Pontiller-Schymura[1]

[1]Concept Laser GmbH, p.pontiller-schymura@concept-laser.de

How to produce a complex shaped metal part in a single step process starting with metal powders? We will answer this question, and show you how we achieve this goal with our patented LaserCUSING® machines.

You will get an insight view into our machine principles and all necessary steps to realize your desired metallic part will be discussed briefly. Because the laser beam characteristics as well as the scan strategy - how the laser beam moves over the powder bed surface - have a tremendous influence on the part quality, different scan strategies will be presented to achieve the desired result.
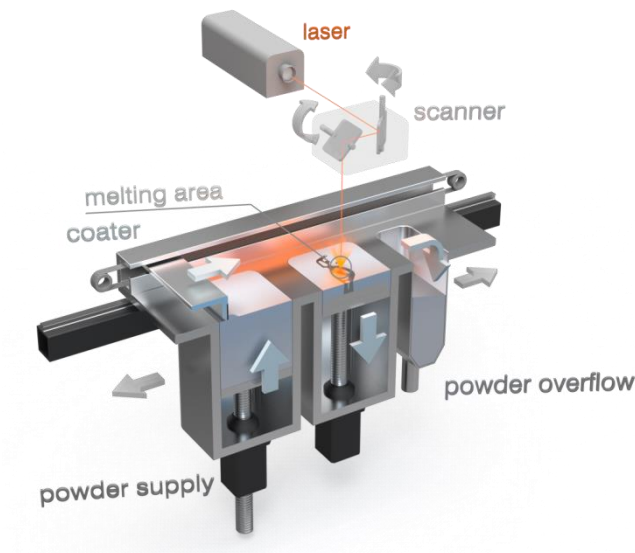
Figure 1: Schematic drawing of the LaserCUSING® process.

Keywords: LaserCUSING®; selective laser sintering; selective laser melting; additive manufacturing; 3D printing; powder bed fusion

Binder Jetting technology to 3D print complex parts in industrial-grade materials

Dr. Sarig Nachum

Fraunhofer-Zentrum für Hochtemperatur-Leichtbau HTL, Bayreuth

Binder Jetting is an additive manufacturing process in which a liquid binding agent is selectively deposited to join powder particles. Layers of material are then bonded to form an object. The job box lowers and another layer of powder is then spread and binder is added. Over time, the part develops through the layering of powder and binder. Binder Jetting is capable of printing a variety of materials including metals, ceramics and composite materials. After the printing procedure the materials are typically cured and sintered and sometimes infiltrated with another material, depending on the application. Hot isostatic pressing may be employed to achieve high densities in solid metals

List of Participants

	Amirpourmolla, Maedeh	The University of Auckland, Auckland	New Zealand
Prof. Dr.	Apalak, Kemal	Erciyes University, Kayseri	Turkey
	Arslan, Kemal	Erciyes University, Kayseri	Turkey
Asst. Prof. Dr.	Aydin, Murat	Erciyes University, Kayseri	Turkey
Prof. Dr.	Boccaccini, Aldo R.	University of Erlangen-Nuremberg, Erlangen	Germany
Dr.	Borovinšek, Matej	University of Maribor, Maribor	Slovenia
	Chajdi, Mohcine	Mohammed V University in Rabat, Rabat	Marocco
Prof. Dr.-Ing.	Choi, Se-Young	Yonsei University, Seoul	Republic of Korea
	Comez, Isa	Karadeniz Technical University, Trabzon	Turkey
	Daszkiewicz, Karol	Gdansk University of Technology, Gdansk	Poland
	DeSimone, Elise	University of Bayreuth, Bayreuth	Germany
	Fatievieva, Yu.	Zaporizhzhe National University, Zaporizhzhe	Ukraine
	Fumio, Ono	Osaka Science & Technology Center, Osaka	Japan
Prof. Dr. Dr. Sci.	Gasik, Michael	Aalto University Foundation, Aalto	Finland
Prof. Dr.	Gbureck, Uwe	University Hospital Würzburg, Würzburg	Germany

Prof.	Ge, Changchun	University of Science and Technology Beijing, Beijing	China
Dr.-Ing.	Gerdes, Thorsten	University of Bayreuth, Bayreuth	Germany
Dr. rer. nat.	Gerlach, Sandra	GRINTECH GmbH, Jena	Germany
Assoc. Prof. Dr.	Gunes, Recep	Erciyes University, Kayseri	Turkey
Research Assist.	Hamamci, Mustafa	Erciyes University, Kayseri	Turkey
Prof.	Hasezaki, Kazuhiro	Tokushima University, Tokushi	Japan
M.Sc.	Haynl, Christian	University of Bayreuth, Bayreuth	Germany
Prof. Dr.	Henriques, Bruno	Federal University of Santa Catarina, Santa Catarina	Brazil
Prof. PhD.	Kawasaki, Akira	Tohoku University, Tohoku	Japan
Prof.	Kirihra, Soshu	Osaka University, Osaka	Japan
Dr.	Kohri, Hitoshi	Kogakuin University, Tokyo	Japan
Prof.	Konyashin, Igor	Element Six GmbH, Burghaun	Germany
Prof. Dr.	Körner, Carolin	University of Erlangen-Nuremberg, Nuremberg	Germany
Professor, CEO	Kwon, Hansang	Pukyong National University, Busan	Korea
Prof.	Lang, Gregor	University of Bayreuth, Bayreuth	Germany
Dr.-Ing.	Leykam, Daniel	University of Bayreuth, Bayreuth	Germany
Prof.	Li, Ling	Wuhan University of Technology, Wuhan	China

Dr.	Lorenzetti, Martina	Jožef Stefan Institute, Ljubljana	Slovenia
Prof.	Luo, Guoqiang	Wuhan University of Technology, Wuhan	China
Dr.	Messerschmidt, Bernhard	GRINTECH GmbH, Jena	Germany
	Miyaoka, Makoto	Kyushu Institute of Technology, Kitakyushu-shi Fukuoka	Japan
Prof.	Mondain Monval	University of Bordeaux, Pessac	France
Prof. Dr.-Ing.	Nacke, Bernard	Leibniz Universität Hannover, Hannover	Germany
Prof. Dr.	Nakano, Kouichi	Kyushu Institute of Technology, Kitakyushu-shi Fukuoka	Japan
Dr.	Oetinger, Stefan	Bosch GmbH, Bamberg	Germany
	Omukai, Arashi	Kogakuin University, Tokyo	Japan
Dipl.-Ing.	Ortmann, Claudia	Mathys Orthopädie GmbH, Mörsdorf	Germany
Prof.	Pan, Wei	Tsinghua University, Beijing	China
Principal Researcher	Park , Jehong	Next Generation Materials Co., Ltd., Busan	Korea
	Park, Kwangjae	Pukyong National University, Busan	Korea
Prof. (Rus.) Dr. habil.	Petrova, Vera	University of Stuttgart, Stuttgart	Germany
Dr.-Ing.	Pontiller-Schymura, Peter	Concept Laser, Lichtenfels	Germany
Dr.	Rauch, Matthieu	Ecole Centrale Nantes, Nantes	France
	Ren, Xiaona	University of Science and Technology Beijing, Beijing	China

M.Sc.	Richter, Christian	University of Bayreuth, Bayreuth	Germany
Prof.	Rocha, Luis Augusto	Universidade Estadual Paulista, Bauru	Brazil
Dr.-Ing.	Rosin, Andreas	University of Bayreuth, Bayreuth	Germany
Prof.	Sanin, Vladimir	Russian Academy of Sciences, Moscow	Russian Federation
Prof.	Sanina, Natalia	Russian Academy of Sciences, Moscow	Russian Federation
Prof.	Santangelo, Christian	University of Massachusetts Amherst, Amherst	USA
Prof. Dr.	Schmauder, Siegfried	University Stuttgart, Stuttgart	Germany
Dr.	Shinohara, Yoshikazu	National Institute for Materials Science, Ibaraki	Japan
Dr.	Sidorenko, Daria	National University of Science and Technology (MISIS), Moscow	Russian Federation
PhD	Souza, Julio	Universidade Federal de Santa Catarina, Florianópolis	Brazil
Dr.-Ing.	Streicher, Alexander	Micro-Epsilon Messtechnik GmbH & Co. KG, Ortenburg	Germany
Prof.	Takahashi, Satoru	Tokyo Metropolitan University, Tokyo	Japan
Prof Dr. ir.	Van der Biest, Omer	K U Leuven, Heverlee-Leuven	Belgium
Prof.Dr.	Van Hecke, Martin L.	Leiden University/LION, Leiden	Netherlands
Dr.	Wang, Chuanbin	Wuhan University of Technology, Wuhan	China
Prof.	Watanabe, Yoshimi	Nagoya Institute of Technology, Nagoya	Japan
Prof. Dr. rer. nat	Willert-Porada, Monika	University of Bayreuth, Bayreuth	Germany

Dr.	Zamulaeva, Evgenia	National University of Science and Technology (MISIS), Moscow	Russian Federation
Dr.	Zhang, Jian	Wuhan University of Technology, Wuhan	China
Prof.	Zhang, Lianmeng	Wuhan University of Technology, Wuhan	China
	Zhang, Ruizhi	Wuhan University of Technology, Wuhan	China
Prof.	Zhou, Zhangjian	University of Science and Technology Beijing, Beijing	China

Industrial Exhibition

GRIN TECH — Gradient Index Optics Technology	GRINTECH GmbH was founded in 1999 as a spin-off of the Fraunhofer Institute for Applied Optics and Precision Engineering in Jena, Germany. Today, GRINTECH is one of the leading manufacturers of gradient index (GRIN) micro-optic lenses and lens systems based on more than 20-years of experience. GRINTECH delivers medical imaging and biophotonic technology, optical metrology and sensor technology to growing markets. GRIN-lenses are miniaturized lenses having extraordinary good optical performance and flat optical surfaces. The optical power of GRIN-lenses is achieved by a refractive index (GRadient INdex) profile fabricated by a non-toxic silver and lithium ion exchange process in glass. Our unique rod and cylindrical micro lenses have typical dimensions from 200 µm to 2 mm. With diffraction-limited numerical apertures up to 0.45. The flat optical surfaces enable an easy assembly to micro-optical lens systems tailored to your specific requirements.
MICRO-EPSILON	Micro-Epsilon is a medium-sized family-run company, which plays a leading role in measurement technology. For more than 45 years we have continuously offered reliable, high performance, unique solutions particularly when high precision measurement or inspection is required. Our product range covers sensors for the measurement of distance and displacement, sensors for IR temperature measurement and color detection, as well as systems for dimensional measurement and defect detection. Innovative products that provide the very highest levels of precision are created through intensive, research and development processes, unique know-how and a broad network of collaborative operations, which are essential for such high performance measurement systems.We understand that our customers are our business partners, which creates a win-win situation for both parties. Our products often provide customers with a genuine competitive advantage. However, this is only the case if the products are higher precision and so provide a clear, decisive competitive edge. With more precision.

CONCEPTLASER	Concept Laser GmbH, which was founded in 2000 by Frank Herzog, is one of the world's leading providers of machine and plant technology for the 3D printing of metal components. The patented LaserCUSING® process – powder-bed-based-laser melting of metals – opens up new freedoms when it comes to configuring components and also permits the tool-free, economic fabrication of highly complex parts in fairly small batch sizes. The company's customers come from many different sectors of industry, for example medical and dental technology, the aerospace industry, toolmaking and mold construction, the automotive industry and the watch and jewelry industry. Concept Laser's 3D metal printers process, among other materials, powder materials of stainless steel and hot-work steels, aluminum and titanium alloys and – for jewlery making – precious metals.
INVERTEC	InVerTec was founded in 1997 as a non-profit organization with the aim of practicing interdisciplinary fundamental research and applied science in the field of combined electrothermal treatment and process intensification. Interdisciplinary R&D projects from a concept to a bench-scale model to the pilot plant scale are carried out in cooperation with our partners in the industry, at institutions and by teams workgroups at the University of Bayreuth. in particular at the chairs in the Faculty for Engineering Sciences. InVerTec provides pilot plants for conceptual and laboratory-scale research, performs experimental work, and does plant engineering. Additionally InVerTec installs and lunches pilot plants at our industrial and institutional partners.

Author Index

Z

Keyword Index